UNIVERSITY OF
LIVERPOOL

Computational Modelling of Transonic Circulation Control

Thesis submitted in accordance with the requirements of
the University of Liverpool for the degree of Doctor in Philosophy
by

Matthew J. Forster

August 2017

Declaration

I hereby declare that this dissertation is a record of work carried out in the School of Engineering at the University of Liverpool during the period from September 2013 to August 2017. The dissertation is original in content except where otherwise indicated.

August 2017

.....

(Matthew J. Forster)

Abstract

This Ph.D. thesis focusses upon computational fluid dynamics simulations of circulation control in transonic freestream speeds for applications to unmanned combat air vehicles. The work addresses Coanda shape designs and their effectiveness for transonic circulation control using supersonic jets, with comparisons against traditional control surfaces. Previous works have thus far only investigated transonic circulation control on elliptical sectioned wings with unrepresentatively thick trailing edges and improvements in performance made by considering elliptical Coanda devices or increasing radii of curvature. In this work, a supercritical aerofoil was first modified to accommodate a small Coanda surface with minimal effects on the base drag and a comparison made between the performance of using several Coanda designs and a hinged control surface. The use of a step was demonstrated to make a circulation control device with a simple converging nozzle as effective as ailerons and flaps up to moderate deflection angles and that the limitations are due to breakdowns in the mean flow in a similar fashion to traditional devices. In addition an optimisation study was performed using modern numerical methods on the contouring of the Coanda surface, which identified a shape that performed well for both transonic and subsonic freestream conditions. Circulation control was then applied to a three-dimensional unmanned combat air vehicle planform and assessed at transonic conditions for use in roll, pitch and yaw control. From the range of conditions investigated the findings suggest that, for a three-dimensional representative geometry, circulation control can match the performance of conventional controls for roll and pitch. The results also suggest that for benign transonic conditions, circulation control can also provide control similar effectiveness to split flaps for yaw control. The findings open up insights into transonic circulation control and hopefully will promote further research in both academia and industry, where a lack of CFD validation quality experimental data for a transonic test case with supersonic blowing prohibits the technology from advancing.

List of Publications

Journal Papers

Forster, M and Steijl, R, "Design Study of Coanda Devices for Transonic Circulation Control," *The Aeronautical Journal*, July 2017, DOI: 10.1017/aer.2017.65.

Conference Papers

Forster, M and Steijl, R, "Numerical Simulation of Transonic Circulation Control," *53rd AIAA Aerospace Sciences Meeting, Kissimmee Florida*, American Institute of Aeronautics and Astronautics, 5th-9th Jan 2015, DOI: 10.2514/6.2015-1709.

Forster, M, Biava, M and Steijl, R, "Optimisation of Coanda Surfaces for Transonic Circulation Control," *6th European Conference for Aerospace Sciences (EUCASS), Krakow Poland*, July 2015, DOI: 10.13140/RG.2.1.3675.8242.

Forster, M, Biava, M and Steijl, R, "Multipoint Optimisation of Coanda Surfaces for Transonic Circulation Control using the Adjoint Method," *8th AIAA Flow Control Conference, Washington DC*, American Institute of Aeronautics and Astronautics, 13th-17th June 2016, DOI: 10.2514/6.2016-3773.

Forster, M and Steijl, R, "Circulation Control for High-Speed Unmanned Combat Air Vehicles," *2016 Applied Aerodynamics Conference, Bristol UK*, Royal Aeronautical Society, July 2016, DOI: 10.13140/RG.2.2.31209.08805.

Acknowledgements

I would like to offer my gratitude for all of the help and advice offered by my supervisor Dr. René Steijl throughout my Ph.D.. My secondary supervisor Prof. Ken Badcock has often offered a voice of reason in our progress meetings together. Dr. Massimo Biava has been invaluable not only for the development of the Adjoint solver that facilitated the optimisation work within this project. Many thanks to Prof. George Barakos for providing the facilities, software and licences to undertake this work, and also to Dr. Mark Woodgate for his support and giving me the keys when I was locked out.

My thanks also extend to Dr. George Hoholis for his prior work on CC, the geometry modifications and building of the initial grid topology for the work involved on the SACCON. The regular meetings with Prof. Clyde Warsop from BAE Systems, Dr. Bill Crowther and his Ph.D. students from Manchester University, as part of the Future Combat Air Systems Focussed Research (FFR) project, often provided a helpful source of critique which shaped the direction of my research. I am also fortunate to have been a participant in the NATO AVT-239 task group, where the wider flow control community offered insights and kindled ideas for future research.

I would like to thank the university staff who often go unthanked for their hard work. In particular Dr. Cliff Addison and Dave Love from the advanced research computing department; Maria White, Lesia Swain and Jack Carter-Hallam from the engineering school; Helen Hall and the inter-library loans department; and building managers Pamela Ambrose, Mark Jewell and Tommy Graham.

In addition, thank you to all the members of the CFD Lab and office who have made the environment an enjoyable place to work: Antonio, Becky, Cathy, Chris, Clement, Dan, Dave, Florent, Fulvio, Gaetan, George, Giampaolo, Giulia, Jade, Luke, Marina, Mark, Mike, Mike, Mikolaj, Neale, Paul, Philipp, Reik, Savio, Sebastian, Sebastiano, Shenren, Simone, Tom and Vladimir. Finally, my thanks and love to Silvia and my family for putting up with me and keeping me sane throughout this time.

This work was jointly funded by the University of Liverpool through the EPSRC Doctoral Training Partnership (grant number 1362153), and BAE Systems as part of the Ministry of Defence FFR programme. The use of the Chadwick HPC facility at the University of Liverpool and the Polaris N8 HPC is greatly appreciated.

Contents

List of Figures

Nomenclature

α	Angle of attack
δ	Control surface deflection angle
A	Wing surface area
c	Chord length
C_d	2D Sectional drag coefficient
C_l	2D Sectional lift coefficient
C_m	2D Sectional pitching moment coefficient
C_D	3D Drag coefficient
C_L	3D Lift coefficient
C_S	3D Side force coefficient
C_l	3D Pitch moment coefficient
C_m	3D Roll moment coefficient
C_n	3D Yaw moment coefficient
C_μ	Momentum coefficient, $\dot{m}_j V_j / q_\infty A$
C_p	Pressure coefficient
$\Delta C_L / C_\mu$	Lift augmentation ratio
$dC_l/dX_\mathbf{n}$	Change in lift coefficient with respect to normal surface displacement
h	Slot height
M	Freestream Mach number
M_j	Jet Mach number

$\dot{m}_j$	Jet mass flow rate
μ	Dynamic Viscosity
ν	Kinematic viscosity
Ω	Vorticity magnitude
P_0	Plenum (total) pressure
P_∞	Freestream (static) pressure
q_∞	Freestream dynamic pressure
r	Coanda radius
Re	Reynolds number
ρ	Density
s	Step height
S_{ij}	i,j component of the mean strain tensor
τ	Reynolds stress tensor
$\bar{u}$	Time average velocity component
u'	Fluctuating velocity component
V_j	Jet velocity magnitude
y^+	Non-dimensional wall distance, $y\sqrt{\frac{\frac{\partial u}{\partial y}}{\nu}}$

Abbreviations

AOA	Angle of Attack
AVT	Applied Vehicle Technology
CC	Circulation Control
CFD	Computational Fluid Dynamics
DTNSRDC	David W. Taylor Naval Ship Research and Development Center
EARSM	Explicit Algebraic Reynolds Stress Model
EXP	Experiment
HMB	Helicopter Multi-Block CFD Code

HSWT	High Speed Wind Tunnel
IBC	Inboard Coanda
MRP	Moment Reference Point
NCCR	Navy Circulation Control Rotor
NPR	Nozzle Pressure Ratio, P_0/P_∞
RANS	Reynolds Averaged Navier-Stokes
SACCON	Stability and Control Configuration
SBLI	Shock Boundary Layer Interaction
TDT	Transonic Dynamics Tunnel
UAV	Unmanned Air Vehicle

Chapter 1

Introduction

1.1 Circulation Control

In aircraft, ailerons have traditionally been used to alter the circulation around the wings to generate additional forces about the wings for flight control. Flaps employ a similar principle and are used as high lift devices for take-off and landing. An alternative method is circulation control (CC) using the Coanda effect; a jet of air is blown over a rounded trailing edge of a wing. CC using blowing offers advantages over devices such as flaps and ailerons, removing the necessity of moving parts, possibly leading to a reduction in aircraft weight [1].

Circulation is defined as the line integral of velocity about a closed loop within a fluid, $\Gamma = \oint \mathbf{v}.d\mathbf{l}$. The Kutta-Joukowski theorem relates circulation to lift and states that the lifting force on a body acts normal to the freestream velocity (U_∞) and is equal to $L = -\rho_\infty U_\infty \Gamma$, where ρ_∞ is freestream density. For aerofoils with a sharp trailing edge in a potential flow, Γ is equal to the amount of circulation necessary to fix the stagnation point at the trailing edge, often known as the Kutta Condition.

The trailing edge separation is not uniquely defined for an aerofoil with a rounded trailing edge. However, in a real viscous flow the separation would be dependent on flow conditions such as Reynolds number, angle of attack, and trailing edge radius. CC utilises the Coanda effect to manipulate the separation point and alter the circulation. An illustration of the streamlines at the trailing edge of a CC aerofoil is shown in Fig. 1.1. With blowing over the upper side of the Coanda surface the stagnation point is moved further around the Coanda as would have been for the unblown case.

The Coanda effect describes the behaviour of a fluid moving tangentially to a convex (typically circular) surface. The flow attaches to the curved surface as a result of the pressure gradients within the jet flow (see Fig. 1.2a). The position of the separation

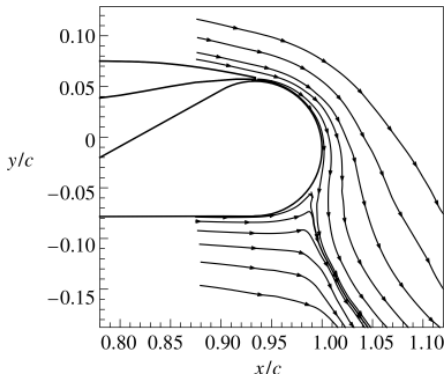

Figure 1.1: Streamlines showing separation point with blowing over Coanda [2].

and stagnation points at the trailing and leading edges of the aerofoil are altered due to blowing a jet over the Coanda surface by an increase in circulation, and therefore lift is increased.

CC requires a high speed jet of air which attaches to the Coanda surface, potentially operating at jet speeds up to 4 times the freestream speed [3–5]. As this high speed jet meets the relatively lower speed air in the freestream, the jet entrains the fluid within the freestream which is then also turned around the Coanda. The entrainment is due to the mixing within a shear layer between the jet and the freestream travelling at significantly different speeds and Mach numbers. Figures 1.2b and 1.2c show simplified schematic diagrams of the flows that occur at the slot exit and just downstream of the slot. The momentum of the jet influences the boundary layer at the trailing edge of the wing and accelerates the local freestream flow.

For aerofoils in the transonic regime, a supersonic Coanda jet is necessary to achieve a significant change in lift. In addition to shear layers there is a possibility of shock boundary-layer interactions occurring on the surface of the Coanda devices, if the jet becomes under-expanded [6]. Depending on the severity of the shock boundary layer interaction, the jet can detach completely from the Coanda surface [7]. At transonic speeds, the shock on the upper surface of the aerofoil also alters the boundary layer flow leading to the CC device at the trailing edge (Fig. 1.2b), which can affect the behaviour of the Coanda jet flow [8].

For an aircraft to successfully use a CC system it would need to be effective over a wide range of flight conditions, including different altitudes. Changes in altitude as well as engine settings will create differences in the pressure ratio the Coanda device is operating at. Therefore, it is crucial to consider the CC device for a wide range of pressure ratios, mainly a range of conditions with under-expansion and, for cases where a converging-diverging nozzle is used, also over-expansion cases.

Studies on transonic freestream CC have shown that the shape of the Coanda surface plays an important role in the effectiveness of the CC device at transonic freestream

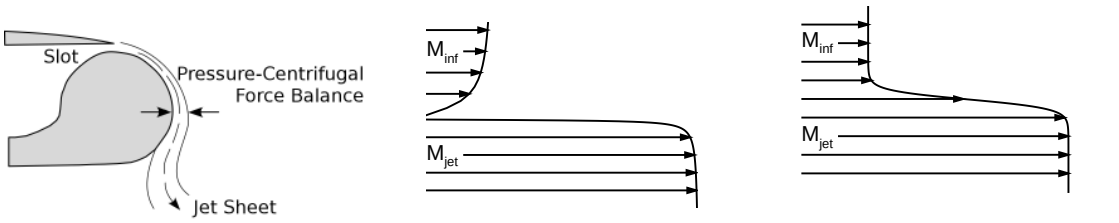

(a) Trailing edge CC [3].

(b) Slot exit flow

(c) Shear layer downstream of slot

Figure 1.2: Schematic of flows at trailing edge.

speeds [3,4,8,9]. Parameters such as the slot height to (local) Coanda radius ratio affect the attachment of the Coanda jet, and the range of blowing rates (and nozzle pressure ratios) for which the jet remains attached to the Coanda. Experimental investigations into elliptical Coanda surfaces have concluded that more eccentric ellipses and smaller slot heights perform most favourably in transonic flows [3, 4, 9].

Alternative methods of promoting supersonic Coanda jet attachment have been studied in conditions without a freestream flow. Converging-diverging nozzles have been shown to increase the detachment pressure ratio [10, 11] by expanding the jet flow further than a converging nozzle and limiting under-expansion. Additionally, the introduction of a step between the Coanda surface and the jet exit of a converging nozzle also increased the detachment pressure ratio [12, 13].

CC using the Coanda effect for use as a means of generating an increase in lift over an aerofoil has been in consideration for at least 60 years [14]. Significant focus was invested on improving the lift of rotor blades with elliptical sections amid development of the X-Wing CC helicopter concept in the early 1980s [15]. The X-Wing concept proposed to take off vertically using the rotor blades, but for forward flight the rotor blades would be fixed and lift generated using circulation control on the rotors. More recently, with concerns over aircraft efficiency and environmental impacts, CC has been studied to improve the lifting capabilities of fixed wing aircraft while keeping within the capabilities of existing airport infrastructures [16]. On fixed wing UAVs, it has been shown in subsonic flight that CC has the potential to replace moving parts for manoeuvrability control [17]. Other active flow control systems are also being studied such as; using sweeping jets to reduce the vertical tail size of commercial aircraft [18,19], blowing over flaps for drag reduction [20], and using plasma actuators for circulation control [21].

Much of the research to date on CC using blowing has investigated flow control devices on aerofoils in the low speed subsonic flight regime. As a result, modern numerical studies on circulation control have heavily relied on these subsonic freestream circulation control experiments [22–25], such as those at the Georgia Tech Research Institute, which were intended specifically for CFD validation and had a trailing edge

radius of approximately 10% chord [25]. This experiment demonstrated significant wall interference and angle of attack corrections to be suitable for CFD simulations [25].

Research of CC in transonic freestreams has produced a handful of experiments and numerical studies, which mostly took place in the 1980s on aerofoil sections intended to be used for helicopter blades on the X-Wing CC concept [4, 5, 8, 26]. Such experiments were conducted in moderate size wind tunnels, which introduced significant wall interference effects [27]. The elliptical X-Wing type sections typically had maximum thicknesses of approximately 15% chord, which do not have the characteristics of a supercritical aerofoil, as would be used on a fixed wing aircraft. A supercritical CC aerofoil has been developed [23], however transonic experiments on this section have not yet been published.

The difference between CC at subsonic and transonic freestream speeds is highlighted in Fig. 1.3, showing the lift obtained by Englar [4] for an elliptical CC aerofoil over a range of Mach numbers. At low speeds, the "Rounded Ellipse" CC aerofoil outperformed the purely elliptical section, however at high speeds this was not the case. Schlecht and Anders [9] found that an elliptical Coanda surface was superior to a biconvex surface for both low subsonic and transonic freestreams, since the separation point of the jet is fixed by the sharp profile of the biconvex Coanda.

Alexander *et. al.* [3] recognised a void in the public domain of data for transonic circulation control aerofoils, specifically those intended for fixed wing aircraft. Experiments were conducted on a 6% thick elliptical aerofoil in the NASA transonic dynamics tunnel for freestream conditions up to $M = 0.84$. Several elliptical Coanda shapes were compared, and it was found that at higher freestream Mach numbers, the Coanda shapes with larger major to minor axis ratios gave a greater ΔC_l. The findings from this experiment will be further discussed in Section 1.3.

Numerical studies of the X-Wing era often used coupled inviscid-viscous solvers [15, 28, 29] or two dimensional Navier-Stokes solvers with algebraic turbulence models [27,30]. There remains a distinct lack of comprehensive numerical studies using modern techniques for transonic circulation control. As a result, fundamental problems such as grid requirements and turbulence modelling remain largely unanswered.

The deficiency in transonic flow control research is also highlighted by Millholen *et. al.* [20] when discussing the fundamental aerodynamics subsonic/transonic-modular active control (FAST-MAC) aircraft model. It is stated that the experiments on the FAST-MAC are unique as it will evaluate flow control strategies at transonic speeds [20]. The FAST-MAC uses a blown flap configuration to enhance lift for take off and landing, and will utilise blowing at cruise for drag reduction.

1.2 Momentum Coefficient

The supply of air for the plenum for circulation control is often taken from bleed air from the jet engine of the aircraft [17]. As a result of this the efficiency of the circulation control device is critical; mass flow taken from the engine reduces the power available for forward thrust. The jet momentum coefficient (C_μ) is often used as a measure of blowing over a circulation control device, which is defined as

$$C_\mu = \frac{\dot{m}_j V_j}{q_\infty A} \tag{1.1}$$

where $\dot{m}_j$ is the mass flow rate through the slot exit and A is the surface area of the aerofoil. In circulation control experiments, $\dot{m}_j$ is usually measured using a flow venturi meter and V_j calculated from isentropic equations using the plenum pressure.

An important and widely used metric for defining the efficiency of a CC system is the lift augmentation ratio $\Delta C_L/C_\mu$. Alexander *et. al.* state that CC performance is considered as "good" for $\Delta C_L/C_\mu > 50$ [3] in a transonic freestream. In their experiments on the 6% thick elliptical wing they found a maximum augmentation ratio of 37 for $M = 0.8$. In addition Abramson and Rogers [8] achieved $\Delta C_L/C_\mu = 27$ at $M = 0.7$ and $\Delta C_L/C_\mu = 10$ at $M = 0.8$ on their 16% thick elliptical aerofoil.

1.3 Effect of Coanda Geometry on Supersonic Coanda Jet Attachment

For Coanda flares and some instances of flow control (such as circulation control in the transonic flight regime) the jet over the Coanda surface is typically supersonic and often under-expanded. The jet expands immediately downstream of the slot exit, followed by a series of shock waves which interact with the free shear layer between the outer flow (either quiescent, or freestream in the case of circulation control) and the jet. These waves also interact with the boundary layer on the Coanda surface, separating the boundary layer in the form of shock boundary layer interactions (SBLIs). At moderate blowing rates, the separation is limited to a recirculation bubble, however for more highly under-expanded jets, the shock waves are strong enough to completely detach (or breakaway) the jet from the Coanda surface [7].

The literature shows that the shape of the Coanda surface has an effect on the attachment of the jet. In transonic freestream flows, experimental studies have mostly investigated the change in lift due to elliptical Coanda devices. Experiments using supersonic jets without a freestream, such as for Coanda flares or for bench tests of Fluidic Thrust Vectoring the focus has been to eliminate the detachment due to under-

expansion of the jet.

1.3.1 In transonic freestream

Of the few investigations into transonic circulation control available in the literature, most were designed such that an assessment of trailing edge geometries could be investigated using the same baseline wing/aerofoil model. Many of these experiments were conducted in relatively small wind tunnels, often with porous or slatted walls limiting their suitability for use as CFD validation cases. Despite this, however, lessons can be learnt from these investigations which are summarised in Table 1.1.

Englar 1970

Englar [4] was one of the first to show the difference between several Coanda geometries for transonic CC at the David W. Taylor Naval Ship Research & Development Center (DTNSRDC). The experiments conducted by Englar on an 8 inch, 15% thick elliptical model in the 12×16 inch tunnel, considered three different trailing edges: a circular (denoted rounded ellipse), elliptical and a jet flap up to freestream Mach numbers of $M = 0.9$.

Figure 1.4 shows the geometries that were considered by Englar. The elliptical and jet flap trailing edge shapes were constructed using the original elliptical aerofoil contour, however the model was truncated by 0.3 inches (3.75% chord) to accommodate the circular Coanda geometry. The circular Coanda geometry had a 4% chord Coanda radius while the ellipse had an aspect ratio of 1.97:1 with 4% chord semi-minor and 7.88% chord semi-major axes. As shown in Fig. 1.4, the slot position for the circular and elliptical Coandas were the same. All geometries had slot heights of 0.01 inches and used a converging nozzle. This corresponds to radius to slot height ratios of 31 for the circular geometry and 120 at the slot exit of the elliptical Coanda device.

Englar found that for $M > 0.7$, C_l when using the elliptical Coanda was twice that of the circular, and a maximum lift augmentation ratio of $\Delta C_l/C_\mu = 43$ was achieved compared with $\Delta C_l/C_\mu = 34$ for the circular device. For subsonic speeds, the circular device was more effective than the ellipse. The jet flap was least effective as a lift augmentation device, as shown in Fig. 1.3.

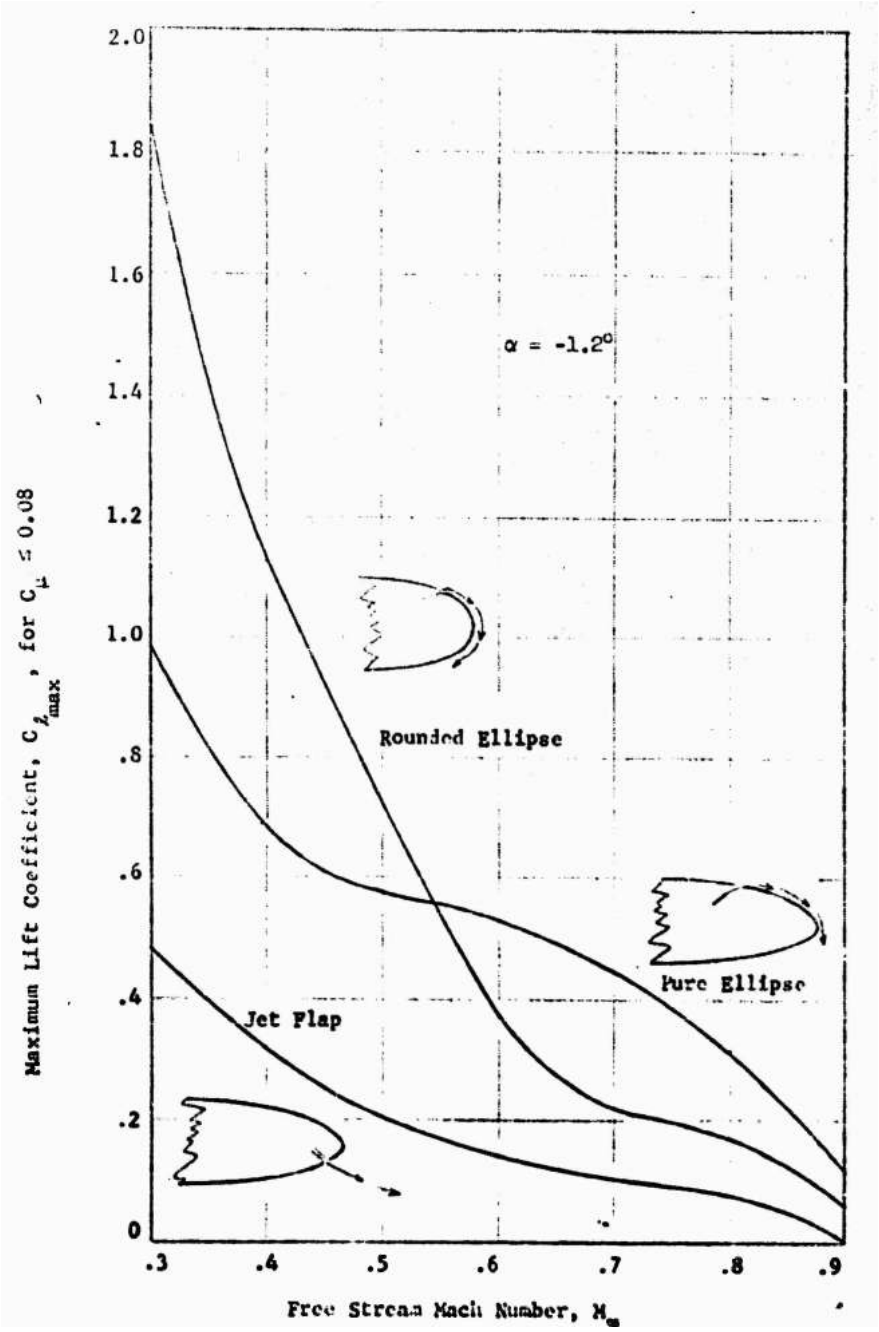

Figure 1.3: Maximum lift obtained by Englar with different Coanda geometries at range of Mach numbers for $C_\mu \leq 0.08$ [4].

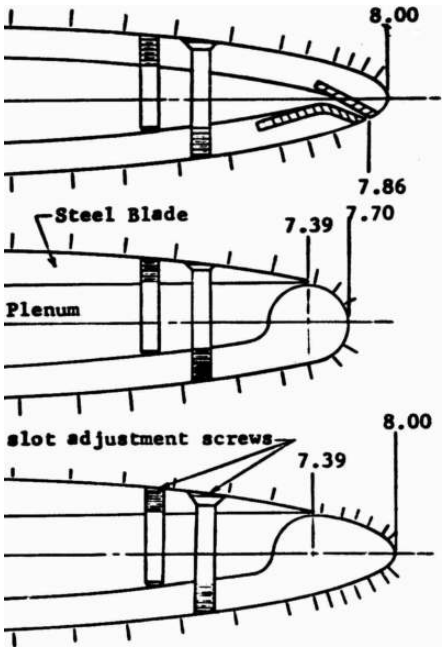

Figure 1.4: Englar trailing edge geometries: Jet flap, rounded ellipse and pure ellipse [4].

Year	Author	Geometry	Re/c ($\times 10^6$)	δ (%c) [1]	Mach	Trailing Edge	R_c (%c) [2]	h (%c) [5]	R_c/h	TH [6]
1970	Englar [4]	15% Elliptical (2D)	$1.5 - 2.5$	1.94%	$0.3 - 0.9$	Circular	3.875%	0.125%	31	7.5%
						1.97:1 Ellipse	15.5% [3]	0.125%	120	7.5%
						Jet Flap		0.125%		
1982	Wilkerson & Montana [5]	16% Elliptical (2D) (NCCR1610-8054)	$3.0 - 5.9$	1.64%	$0.3 - 0.8$	Logarithmic Spiral	2.2% [4]	0.167%	13.2	4.5%
1983	Abramson & Rogers [8]	16% Elliptical (2D) (NCCR1610-8054)	$3.0 - 5.9$	1.64%	$0.3 - 0.8$	Rounded (103XW)	4.6% [4]	0.2%	23	4.5%
						"Displaced Ellipse"	9.9% [4]	0.4%	24.8	4.5%
1983	Wood & Conlon [26]	20% Elliptical (2D)	up to 3.2	1.85%	$0.3 - 0.65$	Circular	$\approx$4%	0.167%	24	8.2%
1987	Spaid & Keener [31]	20% Elliptical (3D) (45° sweep)	$2.3 - 3.2$	1.85%	$0.43 - 0.75$	Circular	4%	0.2%	20	8.3%
2005	Alexander *et. al [3]*	6% Elliptical (3D)	$0.9 - 2.5$	1.94%	$0.3 - 0.84$	1.78:1 Ellipse	5.2% [4]	0.12-0.26%	20-42	3.5%
						2.38:1 Ellipse	9.1% [4]	0.12-0.26%	35-71	3.5%
						2.98:1 Ellipse	14.2% [4]	0.12-0.26%	55-141	3.5%
2007	Schlecht & Anders [9]	6% Elliptical (3D)	$0.9 - 2.5$	1.94%	$0.3 - 0.84$	Elliptical (as above)	5.2-14.2%	0.12%	42-111	3.5%
						2.0:1 Biconvex	3.3%	0.12%	27	3.5%
						2.9:1 Biconvex	4.79%	0.12%	40	3.5%
						3.8:1 Biconvex	6.27%	0.12%	52	3.5%

Table 1.1: Comparing aerofoil geometries, freestream conditions and Coanda shapes for the previous experiments in transonic CC.

[1] Approximate boundary layer height at trailing edge, assuming $\delta \approx 0.37 Re^{-1/5}$.
[2] Radius of curvature at slot.
[3] For ellipses: Max $R_c = 2a^2/b$, where a and b are the semi-major and semi-minor axes, respectively.
[4] As reported in paper.
[5] Slot height.
[6] Approximate thickness of trailing edge.

Wilkerson, Abramson 1982-83

The NCCR1610-8054 model was developed at the DTNSRDC for initial CC research on a 15% elliptical model [5] with focus on the X-Wing CC helicopter concept. This model had an applied camber of 1% and a modified leading edge which reduced the leading edge radius from the initial ellipse [8]. A detachable trailing edge was incorporated into the model which allowed for it to be used for several experimental investigations [5,8,32].

The earliest study using the NCCR1610-8054 model was performed by Wilkerson and Montana [5] where a Logarithmic Spiral shaped Coanda device was used. Here, CC experiments were conducted in the 7 by 10 foot DTNSRDC transonic wind tunnel on the 18 inch chord model. Tests were conducted over a Mach number range of $M = 0.3$ to $M = 0.8$ and Reynolds numbers of 3.0 to 5.93×10^6. The model spanned the width of the wind tunnel. Pressure taps were located along the centre of the aerofoil span with additional measurements taken along the span to verify two dimensionality of the flow.

Figure 1.6 shows the NCCR1610-8054 aerofoil section, the slot was fixed to 98% chord length on the upper surface and had a slot height of 0.1667 % chord. The radius of curvature at the slot exit was 2.2% chord which increased to 4.0% chord at the intersection with the lower aerofoil surface in the shape of a logarithmic spiral (103LS). At the slot exit, the local radius to slot height ratio was 13.2 which increased to 24. Varying blowing rates and angles of attack were investigated with the aim of assessing the high lift capabilities of circulation control at low subsonic speeds while increasing performance in the transonic regime.

The effect of blowing on the lift coefficient of the NCCR1610-8054 with a logarithmic spiral Coanda is shown in Fig. 1.5. For $M = 0.3$ a maximum $\Delta C_l \approx 1.75$ was achieved as the jet Mach number approached $M_j = 1.0$, however the increase in lift plateaued for supersonic blowing. At higher freestream Mach numbers ΔC_l decreased from this maximum following an increase in blowing rate, sometimes considered as a C_μ-stall. C_μ-stall occurred at the jet sonic point for $M < 0.6$, which was attributed to the Coanda geometry design. For $M \geq 0.6$ C_μ-stall occurred while the jet was supercritical, however the flow physics behind the stall was not identified in the report. It is possible that the entrainment of the freestream flow and the increased circulation caused a shock wave on the upper surface towards the leading edge. This shock may have separated the boundary layer to an extent that the Coanda jet was ineffective at increasing lift further. Unfortunately, surface pressure results were not provided for $M \geq 0.6$ with a supersonic jet. Abramson later showed that the presence of a shock on the main aerofoil section did limit CC performance, these findings will be discussed below.

At $M = 0.7$, the maximum lift augmentation ratio of $\Delta C_l / C_\mu \approx 30$ was achieved using the logarithmic spiral Coanda device.

In addition to the tests conducted by Wilkerson and Montana, Abramson and

Rogers [8] also performed experiments on the NCCR1610-8054 aerofoil at the DTNSRDC. The logarithmic trailing edge of the 103LS was replaced with two differing geometries: The 103XW (also called 103RE) had a rounded Coanda surface and was designed such that the aerofoil could be used with the Coanda device on either the leading or trailing edge; The 103DE (displaced ellipse) had an elliptical shaped Coanda device with a larger radius of curvature at the slot exit which decreased towards the trailing edge. All three (103LS, 103XW, and 103DE) aerofoils had the same geometry with the exception of slot heights and Coanda shapes. Most of the results were reported for the 103XW geometry, shown in Fig. 1.7. The local radius to slot height ratios at the slot exit for the 103LS, 103XW and 103DE were 13.2, 23 and 24.8, respectively.

As with the findings of Englar, above, Abramson observed an increase in both available lift due to blowing and the range of momentum coefficients for the geometries with higher radius to slot height ratios. For $M = 0.6$ and $\alpha = 0$, the maximum lift for the rounded 103XW and elliptical 103DE Coanda geometries was approximately $\Delta C_l = 0.2$ above that of the logarithmic spiral 103LS Coanda. At this condition, C_μ-stall occurred at $C_\mu \approx 0.014$ for the 103LS and 103DE, while the lift increased linearly up to $C_\mu = 0.02$ with the 103XW Coanda geometry, as shown in Fig. 1.8.

Higher freestream Mach numbers resulted in a reduced ΔC_l with C_μ-stall occurring earlier. At $M = 0.7$, the 103XW produced a maximum $\Delta C_l \approx 0.5$ at $C_\mu \approx 0.017$ with an angle of attack of $\alpha = 0$ and a $h/c = 0.002$ slot height. Shock waves were present at the leading edge at higher angles of attack, which limited the impact of the Coanda devices. As shock strength increased, the efficiency of the circulation control device reduced, this is shown in Fig. 1.9. This analysis by Abramson also explains the differences seen by Wilkerson on the 103LS Coanda geometry.

Alexander, Schlecht 2005-07

A series of experiments were performed in 2005 on a 6% thick elliptical aerofoil with a 0.75% circular camber [9] in the NASA Transonic Dynamics Tunnel over a range of Mach numbers up to $M = 0.84$. The elliptical section was chosen over the NACA-64A with the justification that the ellipse would produce more desirable pressure distributions [3]. A range of different elliptical Coanda devices were used on this model. It was found that at transonic Mach numbers the Coanda surfaces with larger major to minor axes performed more favourably than smaller elliptical Coanda surfaces; a greater maximum lift was achieved and detachment of the jet was delayed until higher momentum coefficients.

Comparisons were made between geometries of elliptical Coanda devices with different slot heights at freestream speeds of $M = 0.3$ and $M = 0.8$ with Reynolds numbers of $1.0 - 2.5 \times 10^6$ per chord. The baseline aerofoil trailing edge was truncated at 90% chord and replaced with elliptical Coanda surfaces with varying aspect ratios (Fig. 1.10).

At $M = 0.3$ and angle of attack $\alpha = 6$ degrees, it was found that Coandas with the smaller major:minor axis ratio performed favourably, producing a maximum increase in lift coefficient of approximately $\Delta C_l = 0.8$ with blowing on the upper surface. This resulted in a sectional lift augmentation ratio of $\Delta C_l / C_\mu = 28$ with the smaller Coanda consistently outperforming the larger trailing edge geometries over the range of C_μ investigated.

In the transonic flow regime ($M = 0.8$,$\alpha = 3$), it was also found that the smaller slot height was most effective at increasing the lift. In contrast to the low subsonic flow, the larger Coanda was favoured over smaller Coanda geometries. The maximum lift produced by the larger geometry was approximately 30% more than the best case from the $M = 0.3$ experiments. As with the observations made by Englar [4], the increase in lift plateaued over a range of blowing coefficients, which then displayed behaviour of a C_μ-stall. C_μ-stall occurred later with the larger Coandas, suggesting that the smaller Coanda is more prone to detachment. Lift augmentation for the large Coanda with the smallest slot height achieved a maximum value of $\Delta C_l / C_\mu \approx 48$. This is lower than the maximum lift augmentation of the smaller Coanda, however augmentation of the smaller Coanda rapidly decreased to 0, a result of jet detachment.

Schlecht and Anders also performed experiments on this 6% elliptical model [9] in the TDT up to $M = 0.8$. Here, a similar range of elliptical trailing edge devices to the original experiment by Alexander were used. In addition, biconvex Coanda shapes were used which allowed for investigations into using a constant radius of curvature over the Coanda surface. The biconvex shape did however come to a sharp point, forcing the flow to separate where an otherwise rounded Coanda surface jet flow may have attached longer. Several leading edge designs were also considered in this study, which looked at shortening the leading edge and the effect of increasing camber by drooping the nose. It was also found that the larger elliptical Coandas performed better at $M = 0.8$, and that the trend was similar for the biconvex Coandas that the larger radius of curvature was favourable.

The leading edge design had little effects on the lift augmentation at $M = 0.8$. However it was observed that with the smaller leading edge the flow accelerated to a greater extent and so a strong shock was formed at approximately 40% chord, compared with 15% using the original shape at similar blowing rates over the same Coanda devices.

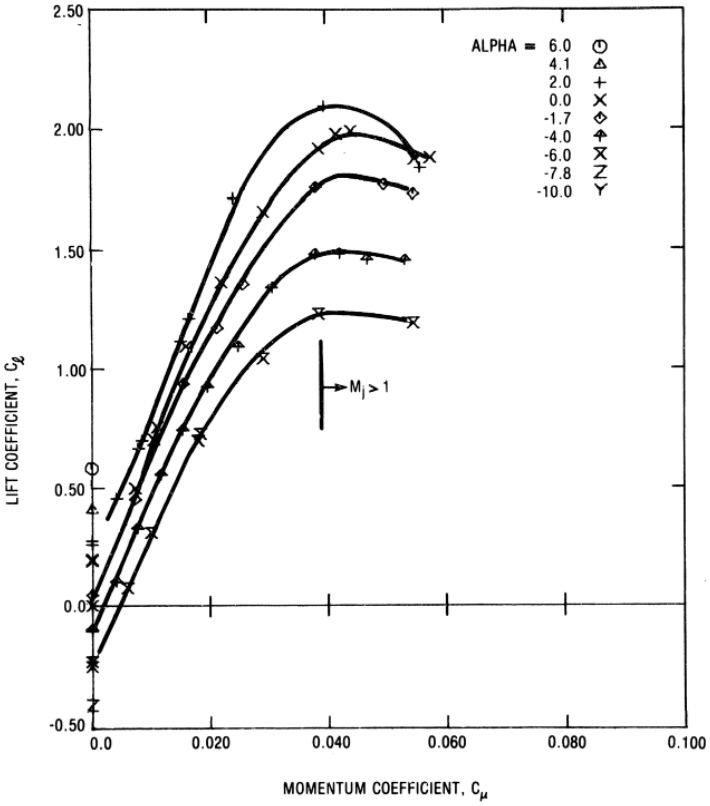

(a) M=0.3.

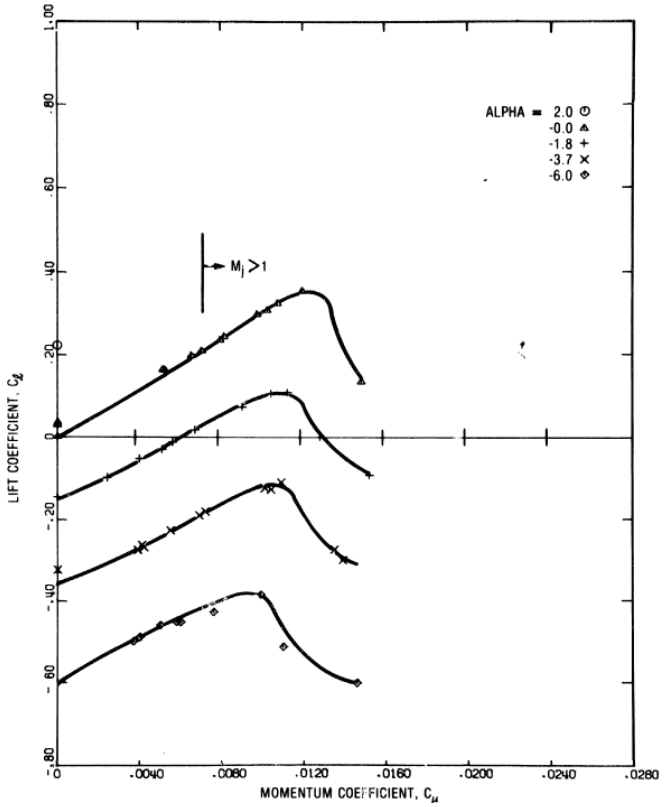

(b) M=0.7.

Figure 1.5: Lift coefficient versus momentum coefficient at a constant freestream Mach number using the 103LS Coanda [5].

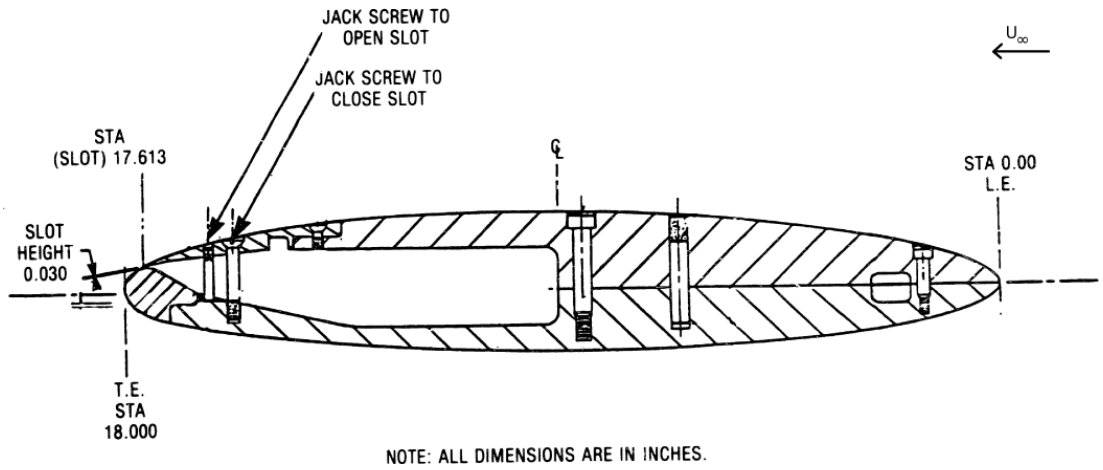

Figure 1.6: NCCR1610-8054 CC aerofoil section [5].

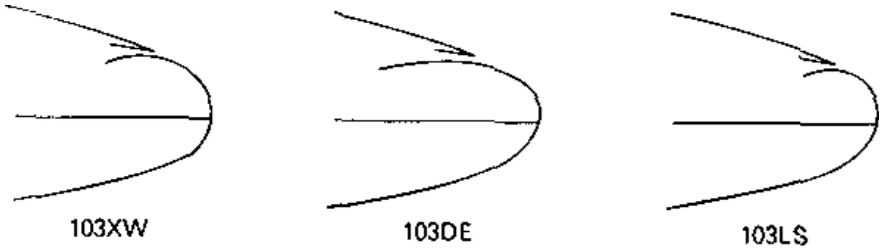

Figure 1.7: NCCR1610-8054 trailing edge geometries, 103LS, 103XW and 103DE [8].

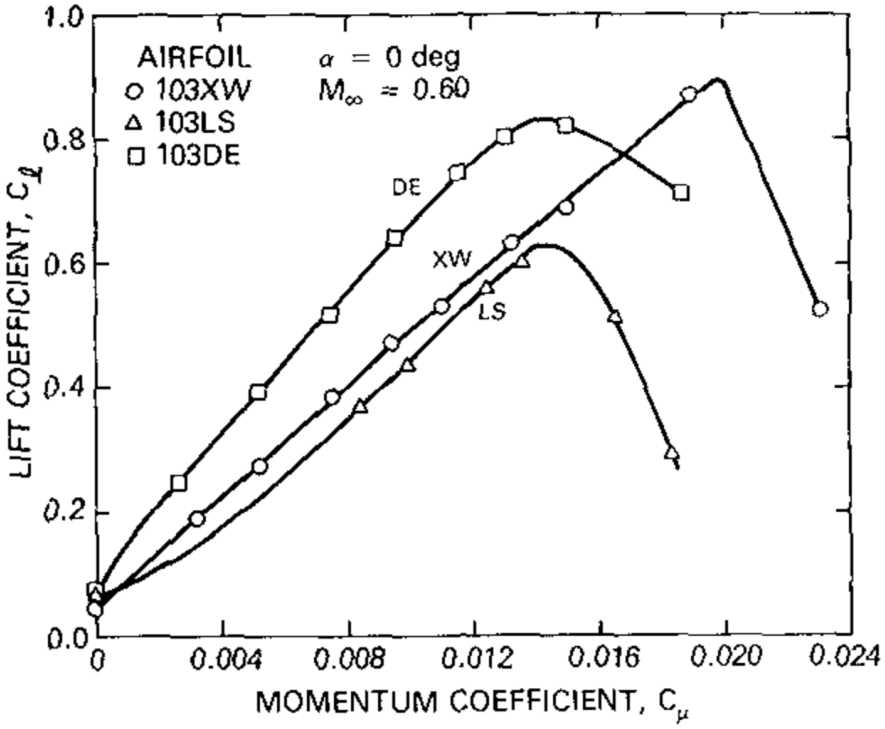

Figure 1.8: Comparison of performance of three Coanda devices at M=0.6 on the NCCR1610-8054 CC model.

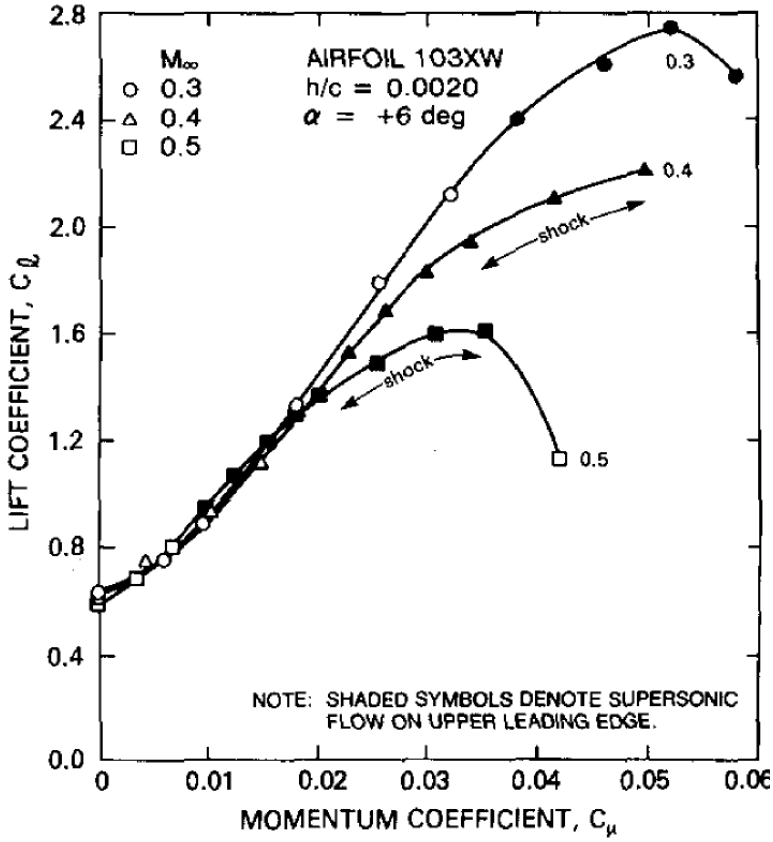

Figure 1.9: Effect of upper surface shock on the NCCR1610-8054 103XW CC experiment [8].

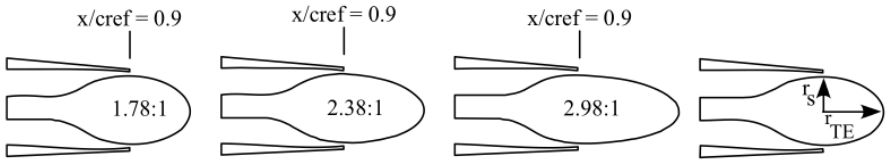

Figure 1.10: Coanda geometries used in the experiment [3].

1.3.2 Without freestream

Stepped Coandas

Much of the research into the supersonic Coanda effect was conducted in a quiescent farfield, focusing upon investigations involving Coanda flares. Coanda flares are designed to provide more efficient combustion of the unusable waste related to extraction of oil and gas. The gas to be combusted is forced at high pressures around a tulip shaped bowl which adheres to the surface due to the Coanda effect (see Fig. 1.11). It is stated that Coanda flares enhance combustion due to the levels of mixing by the turbulence of the jet - due to the higher strain rates associated with convex streamline curvature [6, 34]. At higher pressures however, the jet separates from the Coanda surface in a process known as breakaway or detachment [11].

Experimental studies have shown that introducing a step between the jet exit and Coanda surface can promote attachment at higher pressure ratios by preventing shock induced separation [10, 11]. Carpenter and Smith [10], and Gregory-Smith and Senior [11] have studied the effect of using a step to mitigate the effects of the under-expansion. By introducing a step, the shock waves due to under-expansion interact with the shear layer formed as a result of the step. The step also aids attachment by providing a region of low pressure which turns the jet towards the surface [10].

Figure 1.12 shows Schlieren plots from experiments from a two-dimensional experimental study by Gregory-Smith *et. al.* [11,33], where the nozzle pressure ratio (NPR) is close to the value at which the jet detached from the surface. The unstepped geometry is shown in Fig. 1.11, while the stepped model had the same Coanda radius and slot height. Figures 1.12a and 1.12b show the flowfield before and after breakaway of the jet, where an increase in NPR from Fig. 1.12a saw the jet detach as shown in Fig. 1.12b. For the same slot height and Coanda radius, including a step increased the NPR for which the jet attached by 25% [11].

A diagram of the flow physics of stepped Coanda geometries is shown in Fig. 1.13. As the jet expands, the internal shock waves reflect from a shear layer between the jet and the base-flow region formed by the step. Without the step, these internal shock waves interact with the boundary layer and can promote detachment of the jet.

Carpenter and Smith [6,10] measured the acoustics of supersonic Coanda jets on an axisymmetric Coanda flare with and without a step. The axisymmetric model had a similar profile to the model studied by Gregory-Smith [11] which is shown in Fig. 1.11. Figure 1.14 shows the sound pressure levels for the stepped and unstepped configurations. For the unstepped case, the sound pressure level increases proportionally to the nozzle pressure ratio, which is consistent with theories highlighting the turbulent mixing noise as the principal generator of noise in the flow [6]. Some discrete tones were noted at higher pressure ratios and were attributed to the acoustics of shock-boundary

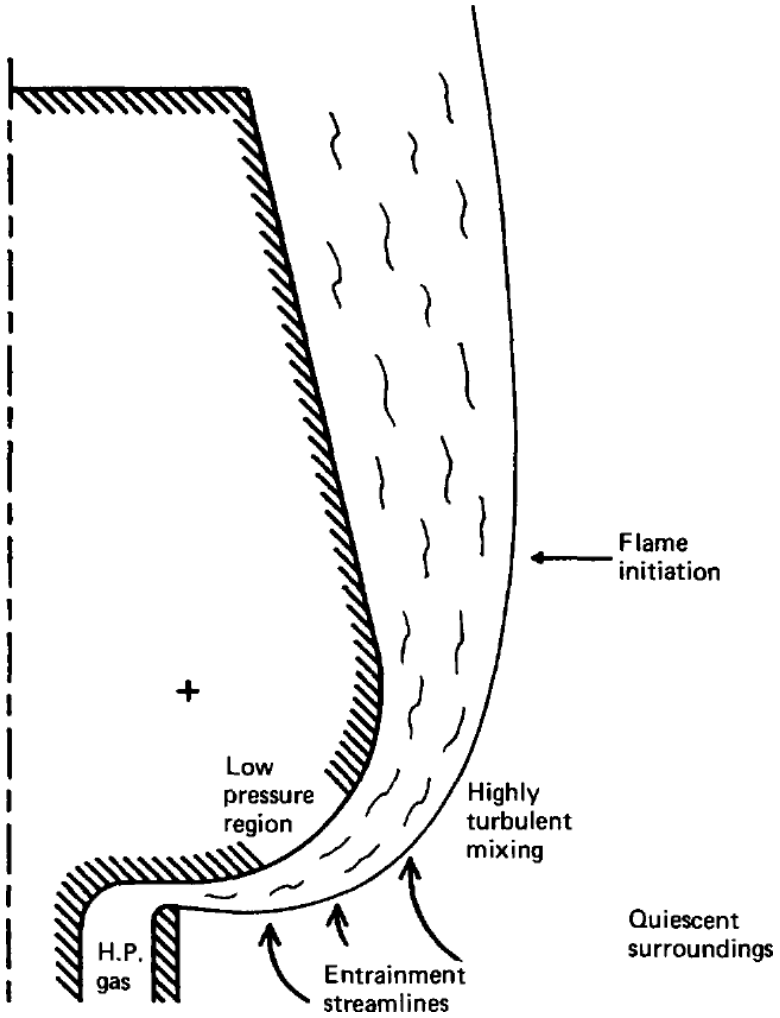

Figure 1.11: Coanda flare geometry [33].

layer interaction.

It was found that the step introduced a significant levels of broadband noise when compared with the case without a step, but there were no noticeable trends in the effect of directivity of the sound waves [10]. The sound pressure levels generally rose with increasing jet velocity. Due to discrete tones being generated as a result of the step, the approximately linear response in sound level to NPR was not observed. At certain nozzle pressure ratios, it appears that the discrete tones were excited close to their natural resonance frequency. The discrete tones can be seen in Fig. 1.14, while the unstepped sound pressure level rises monotonically with NPR the stepped case has steep changes in pressure level. It can be also noted that evidence of breakaway is seen on the unstepped model where the sound pressure drops rapidly at a pressure ratio of $NPR = 6.6$.

There are instances at higher pressures for which the stepped case produced less noise than the unstepped, due to the discrete tones not being produced for certain

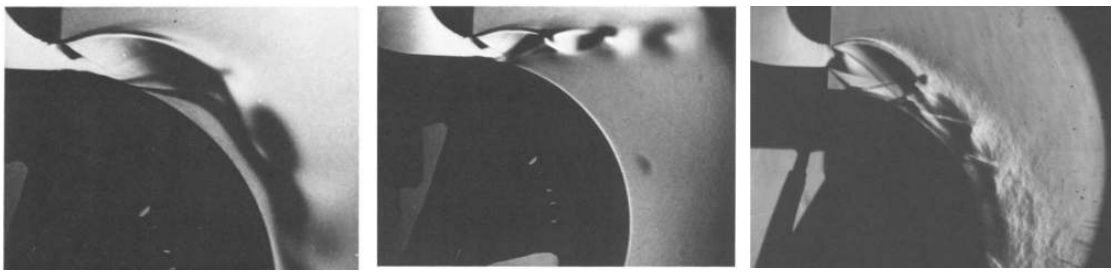

(a) NPR below detachment ratio (b) NPR above detachment ratio (c) NPR above unstepped detachment ratio

Figure 1.12: Schlieren of unstepped [33] (a and b), and stepped [11] (c) supersonic Coanda jets near detachment.

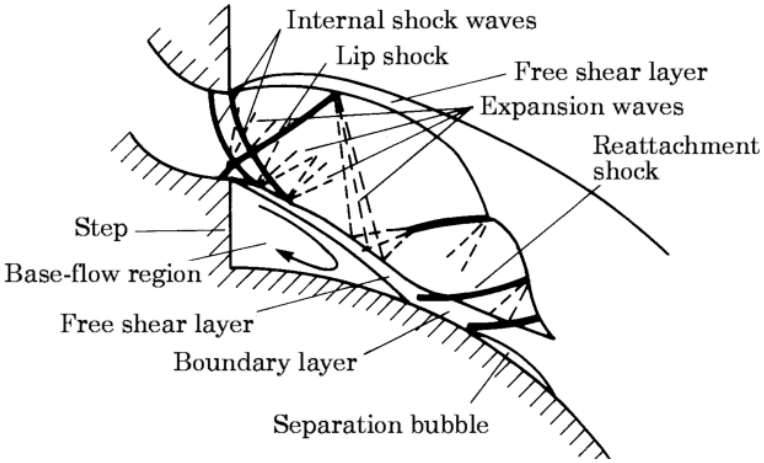

Figure 1.13: Schematic of stepped Coanda geometries. [10]

pressure ratios. This was confirmed by performing a FFT on the frequency spectra, which showed that some tones were not produced throughout the pressure range tested. As step height increased, it was found that the frequency of the tones decreased.

The baseline tones were attributed to periodic fluctuations in the volume of fluid in the recirculation region at the step. As the free shear layer interacts with the wall, fluid will either enter or leave the recirculation region with a frequency equal to that of the waves on the free shear layer between the base flow region and the jet. Figure 1.15 shows the mechanism that generates discrete tones as suggested by Carpenter and Smith; as the shear layer waves interact with the Coanda surface, fluid will either be admitted (a) or ejected (b) from the base flow region. At certain pressure ratios, the periodicity of the oscillations cause acoustic waves to be generated which interact with the shear layer in a self sustaining fashion [10].

Carpenter also proposed that eliminating the larger wavelike structures in the recirculation free shear layer would reduce the acoustic impacts of using a step to delay breakaway. It was found that using a saw-toothed profile on the slot produced stream-

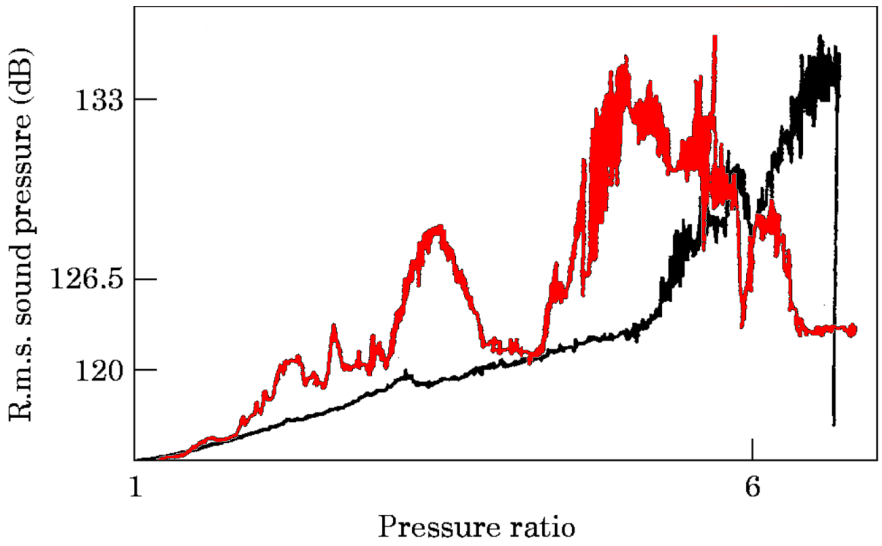

Figure 1.14: RMS sound pressure against jet pressure ratio - no step (black), with step (red). [10].

wise vortices which weakened the shock structure of the jet and enhanced the mixing in the free shear layer. Figure 1.16 shows a schematic of the streamwise vortices over this axisymmetric Coanda flare. No discrete tones were produced when using the saw-tooth step which demonstrated a monotonically increasing sound level with pressure (see Fig. 1.17), reminiscent of the unstepped model as seen in Fig. 1.14. Sound levels were reduced by up to 10dB compared with the unstepped model. Breakaway using a step with a saw-tooth slot profile was also delayed, however the pressure ratio required for breakaway was not observed because the test equipment had reached its maximum operating pressure.

Converging-diverging nozzles

To limit the detachment due to under-expansion of the jet, a converging-diverging nozzle can also be used to expand the flow to the ambient pressure. In experiments on supersonic Coanda jets in still air, Cornelius and Lucius [12] showed that a simple converging-diverging nozzle extends the range of operating pressures at which the Coanda jet remains attached. An adjustable nozzle wall was manufactured to compare the effect of using a convergent-divergent section against an under-expanded jet on the same equipment.

With the under-expanded jet, pressure oscillations are captured on the surface of the Coanda, due to the shock cells within the jet structure. As the pressure ratio is increased, the frequency of the pressure oscillations decreases. An oblique shock is formed on the Coanda surface within approximately 2 slot heights of the jet exit. This oblique shock separates the boundary layer of the jet, and at higher pressure ratios

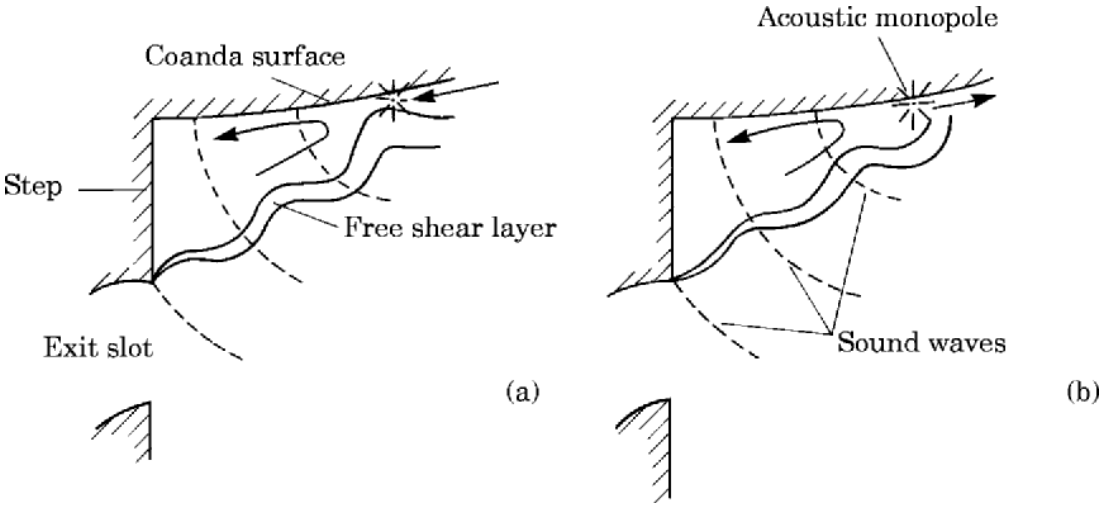

Figure 1.15: Schematic showing production of discrete tones [10].

($NPR \approx 7.6$) the jet detaches from the Coanda.

When the upper wall was extended, the expansion of the supersonic jet was contained between the Coanda surface and the upper wall, preventing the flow from expanding to the Prandtl Meyer angle [12]. As with the under-expanded jet, the frequency of the pressure fluctuations decreased with an increase in plenum pressure. For wall extensions designed to match specific pressure ratios, the jet remained attached up to $NPR \approx 11.5$, where the maximum operating pressure of the equipment was matched. For pressures below the design condition, the jet separated from the upper surface and remained attached to the Coanda surface. At pressures above the design (design $NPR = 7.2$), the jet remained attached up to the operating limit.

Bevilaqua and Lee [13] reported on a method of characteristics design approach which skews the velocity and pressure profile along the jet exit such that the pressure and velocities at the Coanda surface are lower and higher, respectively. Using the radial velocity and pressure profiles of an irrotational vortex at the slot exit, jet attachment was promoted [13]. Figure 1.18a shows the nozzle which generates the desired velocity distribution Bevilaqua proposed, which is shown exaggerated in Fig. 1.18b.

Bevilaqua used a method of characteristics approach to design the wall contours of the nozzle such that the exit Mach number profile matched the vortex associated with the slot height and radius of the equipment. An integral boundary layer method was implemented to help compensate for the viscous effects not catered for by the method of characteristics.

Three nozzles were manufactured and tested over a Coanda surface with a Coanda radius to slot height of 5.0. The first nozzle was a convergent only design, the jet from which detached at NPR=2.6, and reattached when the pressure ratio was decreased to NPR=2.0. Before detachment, the jet sheet was deflected to approximately 120°. The remaining nozzles were a symmetric converging-diverging nozzle, and a "vortex nozzle"

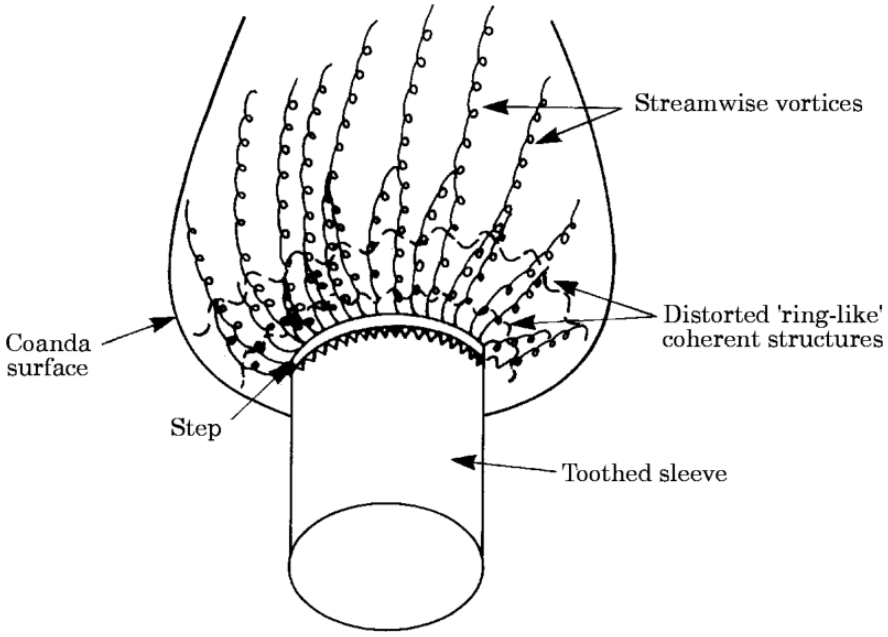

Figure 1.16: Schematic of flow over sawtooth slot exit on axisymmetric Coanda [10].

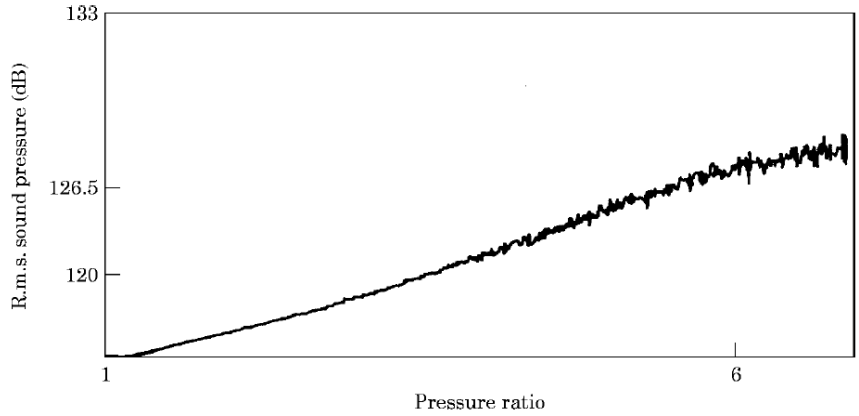

Figure 1.17: RMS sound pressure against jet pressure ratio with saw-tooth profile. [10].

designed using the proposed inverse method of characteristics approach, both designed for NPR=2.5. Both con-di nozzle jets deflected by 150°, however the symmetric nozzle jet separated at NPR=2.7, while the jet designed to have a vortex jet profile separated at NPR=3.0. Both jets observed similar hysteresis effects and reattached at NPR=2.2. Additionally, an approximate 5% increase in thrust was found when using the "vortex nozzle" compared with the symmetric and converging only nozzles in the regime for which the jet remained attached.

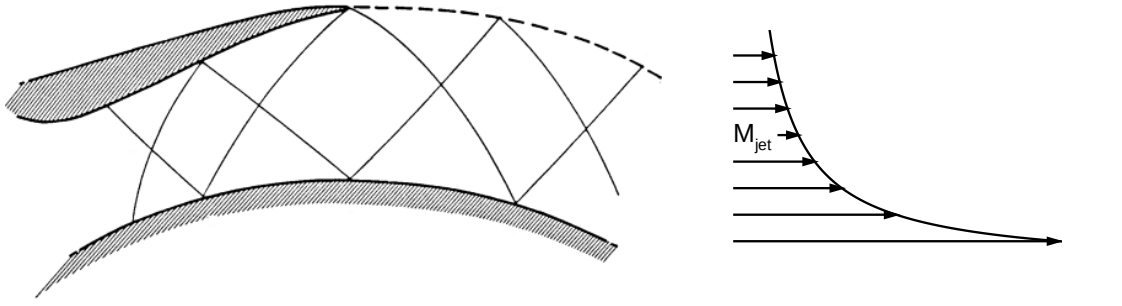

(a) Nozzle designed for irrotational vortex exit profile [13].

(b) Irrotational vortex slot exit profile, $M_j \propto R$.

Figure 1.18: Irrotational vortex theory for attachment of supersonic Coanda jets.

1.4 Sweep Effects on CC

Since the proposed X-Wing demonstrator was intended to have the rotor fixed such that the blades are 45° to the freestream direction, Spaid and Keener investigated the effect on sweep on CC [31, 35]. The wind tunnel model was similar to the model that was earlier studied by Wood in 1983 [26].

This unswept model [26] was elliptical with 20% thickness and 3% camber. The Coanda was circular with a 4% radius and the slot height fixed to a radius to slot height ratio of 24. "2D" Experiments on the original 6 inch chord model were performed in the NASA-Ames 24×24 inch transonic tunnel. With the unswept model, it was found as the angle of attack was increased at $M = 0.65$, the C_μ-stall occurred at higher values of of C_μ. At $\alpha = 0$, maximum lift was achieved at $C_\mu \approx 0.017$, while at $\alpha = -5$ C_μ-stall occurred at $C_\mu \approx 0.013$. For lower speeds, Wood found that the C_μ-stall happened at approximately the same value of C_μ, regardless of angle of attack. This finding can also be observed in the results of the 103LS experiments by Wilkerson [5] (Fig. 1.5), however the effects are less pronounced on the 103LS than the experiment performed by Wood.

The swept model [31, 35] was also a 20% ellipse, but without camber. It was built with a 10 inch chord length and an aspect ratio of 4. The leading and trailing edges were circular, with a 4% radius. The model was mounted in the 6×6 foot NASA-Ames Transonic/Supersonic Wind Tunnel with a sweep angles of 0° and 45°. The experiment was conducted for freestream Mach numbers up to $M = 0.75$.

Measurements of the boundary layer and wake were made using three and five hole pitot tubes. In addition, surface pressures were also measured [35] along the span in positions normal to, and at 45° to the leading edge. Figure 1.19 shows some of the measurements that were taken of the boundary layer and wake. It was found that within the wake a significant outboard flow was present for the swept cases.

Wood performed some analysis of the above mentioned swept case [36]. A compari-

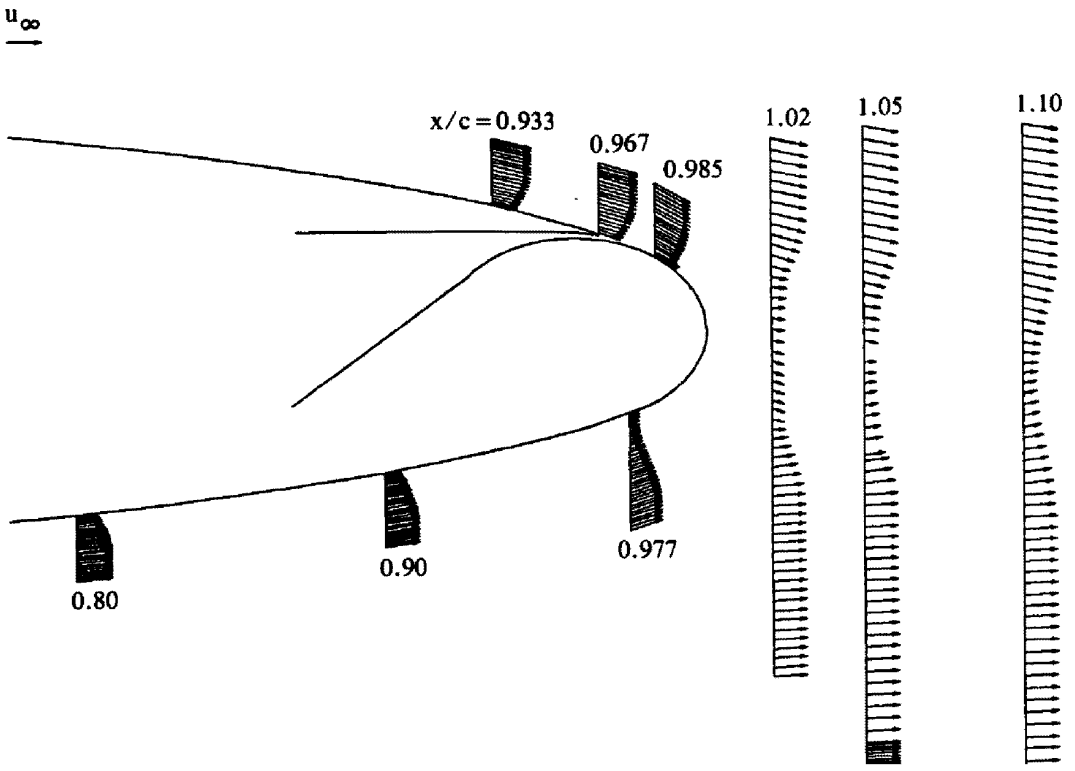

Figure 1.19: Velocity components in the streamwise direction of 45° swept CC model at $M = 0.7$, $\alpha = 0$ and NPR=1.4 [31].

son of the surface pressures for the swept and unswept cases was performed. The effects of sweep were taken into account using simple sweep theory such that surface pressures for the 45° sweep at $M = 0.7$ was compared with the unswept case at $M = 0.5$. Figure 1.20 shows the surface pressures at positions of 70% and 30% span for the swept and unswept cases at equal blowing rates. It was found that the simple sweep theory was applicable to the surface pressures at the 70% span location, Fig. 1.20a, the surface pressures for the swept and unswept cases were in good agreement. The data at the 30% span section highlighted an increase in down wash at the root of the wing since it observed an effectively negative angle of attack with respect to the unswept case. An effect of the relatively large root fairing also appeared to exaggerate a reduction in the lift towards the root that is often observed for swept wings.

Wood concluded that the conventional scaling laws applicable to swept aerofoils are also applicable to swept CC configurations. It was also concluded that two dimensional data sets appear to be an effective tool for estimating load distributions, provided the effects of down wash are known.

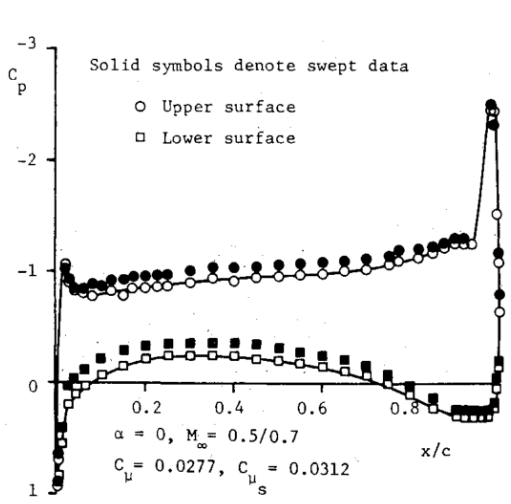

(a) 70% span.

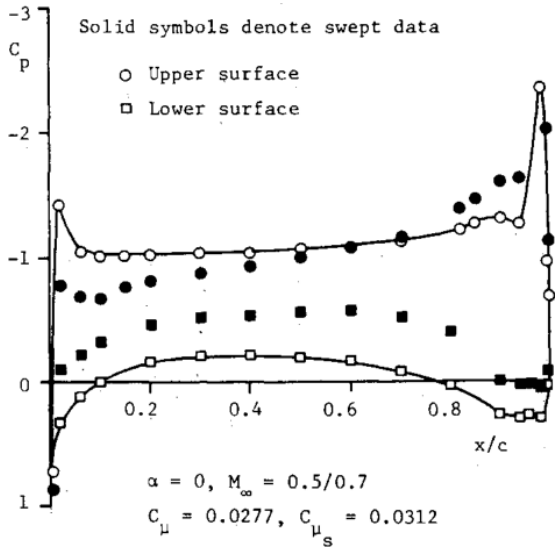

(b) 30% span.

Figure 1.20: Comparison of swept (solid symbols) and unswept (open) at M=0.7 swept and M=0.5 unswept for $C_\mu = 0.03$ [36].

1.5 Numerical Studies on Circulation Control

1.5.1 Subsonic

In 2006, Swanson *et. al.* [37] performed two dimensional RANS simulations of the 16% thick, elliptical 103XW aerofoil [5], however the simulations were limited to $M = 0.6$ at $\alpha = 0.0$. At these conditions, the flow over the aerofoil remained subcritical. It was found that each turbulence model tested (Spalart-Allmaras, Menter SST, Spalart-Allmaras with Curvature Correction and EASM-$k\omega$) failed to predict the pressure distribution over the aerofoil surface at $M = 0.6$. In addition, the separation point of the jet from the Coanda surface was poorly predicted. The SACC model gave reasonable results but only after unrealistic a-posteriori modifications to the baseline model constants [37].

Hoholis [38] validated the employed RANS numerical methods against experiments conducted at the Georgia Tech. Research Institute at $M = 0.1$ [25]. Comparisons between experimental and simulated measurements of the boundary layer and surface pressured showed favourable agreement. For this case the jet remained subsonic at $M_j \approx 0.2$. In addition, after comparing the numerical methods against the SACCON at $M = 0.15$ with flap deflections the use of CC on performing a roll manoeuvre was investigated. For the same conditions as the flap deflection cases (LIB/LOB=$-20°$, RIB/ROB=$+20°$), a Coanda device spanning the wing was designed. Use of the full span CC device generated a stronger rolling moment than the flaps while blowing at NPR=1.2 ($C_\mu = 0.0065$) for $\alpha < 16°$. At higher angles of attack, the highly vortical flow

that caused a "pitch break" in the pitching moment interfered with the effectiveness of the Coanda device, and the roll control available to the CC system was diminished. It was also shown that using two slots covering the outboard and inboard 1/3 span could exceed the efficiency in terms of dC_l/dC_μ of the full span slot by approximately 10%.

Rumsey and Nishino [39] also performed simulations of the Georgia Tech. Research Institute model. Here, a comparison between compressible RANS, and incompressible RANS and LES. For the subsonic freestream and jet ($M_j < 0.64$) considered it was found that an incompressible simulation was suitable. Models that do not account for streamline curvature were found to incorrectly predict the jet separation point, and in some cases the jet wrapped around and remained attached to the lower surface of the aerofoil. Although some models did predict the separation point around the Coanda with reasonable accuracy, it was found that RANS models over predicted the circulation compared with LES.

1.5.2 Transonic

Dvorak and Choi [15] conducted two-dimensional simulations of circulation control aerofoils for both subsonic and transonic flow regimes using the TRACON program. TRACON solved the boundary layer equations for the viscous flow in the boundary layer and then calculated the potential flow in the remainder of the computational domain. For the transonic simulations, the NCCR 1610-8054 circulation control aerofoil [5] was chosen as a validation case.

At $M = 0.7$ without blowing, the TRACON solution gave reasonable results, predicting the location of the shock on the suction surface with considerable accuracy. With blowing at $M = 0.6$ the pressure distribution about the majority of the aerofoil was predicted with good agreement with the experimental results, however the pressure on the Coanda surface was under predicted by TRACON. This under prediction was attributed to the solver being unable to simulate flows of under-expanded jets accurately. Figure 1.21 shows the effect of the blowing coefficient on lift for the numerical simulation and the experimental results of the NCCR 1610-8054 at $M = 0.6$. The peak C_l is predicted correctly at $C_l = 0.4$ when $C_\mu \approx 0.012$. Following the C_μ-stall, the calculated lift decreased at a similar rate to the experiment with further blowing.

1.5.3 Optimisation

Previous optimisation studies of circulation control aerofoils have focussed primarily on improving the efficiency of circulation control for short take-off and landing (STOL) purposes [40]. As such the design conditions were limited to the subsonic flow regime. Many optimisation studies have investigated the effect of blowing rate, jet direction and location of a slot along an aerofoil [40–43] at low speeds. Studies investigating

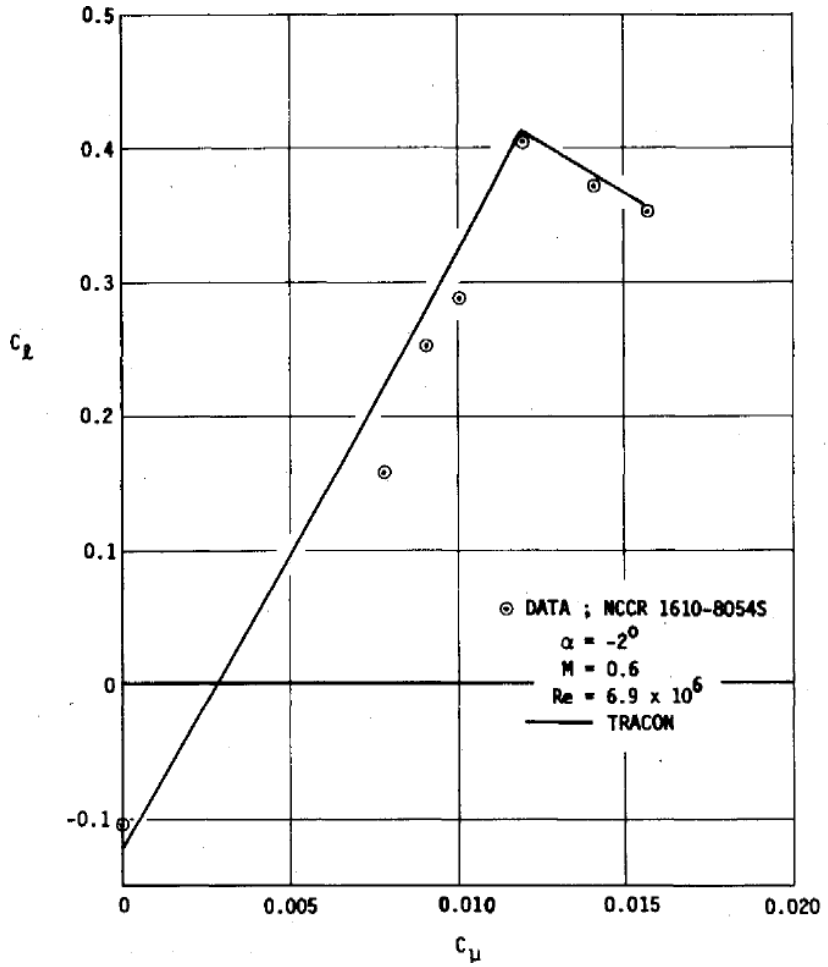

Figure 1.21: Cl vs. C_μ predicted by TRACON [15].

optimisation of the shape of the Coanda surface [44, 45] have been performed, however in these studies both freestream and jet speeds were also designed for sub critical conditions.

Tai *et al.* [45] investigated the effect of the shape of the Coanda surface at the trailing edge of an elliptical aerofoil at a design condition of $M = 0.54$, $\alpha = -2.0°$ and $C_\mu = 0.0071$, using the TRACON coupled inviscid-viscous solver [15]. It was found that an improvement in the lift coefficient of 27% was achieved at design conditions. The resulting design was manufactured and experiments conducted to investigate off-design behaviour of the optimised Coanda shape, which found no discernible improvement for $M = 0.73$ over a range of blowing coefficients.

1.6 Numerical Studies on Aspects of Transonic Circulation Control

1.6.1 Supersonic Coanda without freestream

Sawada and Asami [7] performed Navier-Stokes calculations of the variable wall experiment by Cornelius [12]. Comparisons were made between two different solvers on the converging-diverging geometry, which had a design pressure ratio of 7.2 and was operated on-design at $NPR = 7.17$ and in an over-expanded case $NPR = 5.07$. Tests were conducted in 2D and 3D on an implicit solver with the Baldwin-Lomax turbulence model, and an explicit solver with the Goldberg turbulence model.

For the pressure ratio under the design condition, the pressure oscillation magnitudes gave good agreement to the first shock cell, however the magnitude decays less rapidly than was observed in the experiment for both solvers. Near the design pressure ratio, the agreement was poor for both solvers. The Baldwin-Lomax solver over predicted the magnitude of the oscillations and misrepresented the size of the shock cells, while the Goldberg solver under predicted pressure magnitudes. The failure of the Goldberg solver was attributed to the grid topology, using a grid which included the plenum chamber improved results.

The 2D and 3D solutions gave similar results for much of the Coanda surface, however wall interference effects began to dominate the flow as the angle from the jet exit increased in the 3D calculations. Results were improved for both cases in 3D using the Goldberg model when the pressure data was taken from an off-centre position. For the off design case (moderate over-expansion), disagreement was stated to be due to poor development of the shear and boundary layers [7] as modelled by both schemes. However, near the design pressure ratio it is noted that the results gave better agreement closer to the side walls due to boundary layer separation. This suggests that the boundary layer in this case was possibly more developed than in the experiments.

Sawada and Asami state that while the converging-diverging geometry gives better performance over a range of pressure ratios, "Establishing a sophisticated design method for a nozzle geometry utilising the Coanda effect has yet to be accomplished." [7].

1.6.2 Compressible free-shear layers

As the high speed, supersonic jet meets the freestream, a free shear later forms and follows the jet around the curvature of the Coanda surface. This shear layer influences the mixing and entrainment of the jet and freestream, possibly influencing the circulation about the wing. As shown in Table 1.1, the boundary layer height at the trailing edge

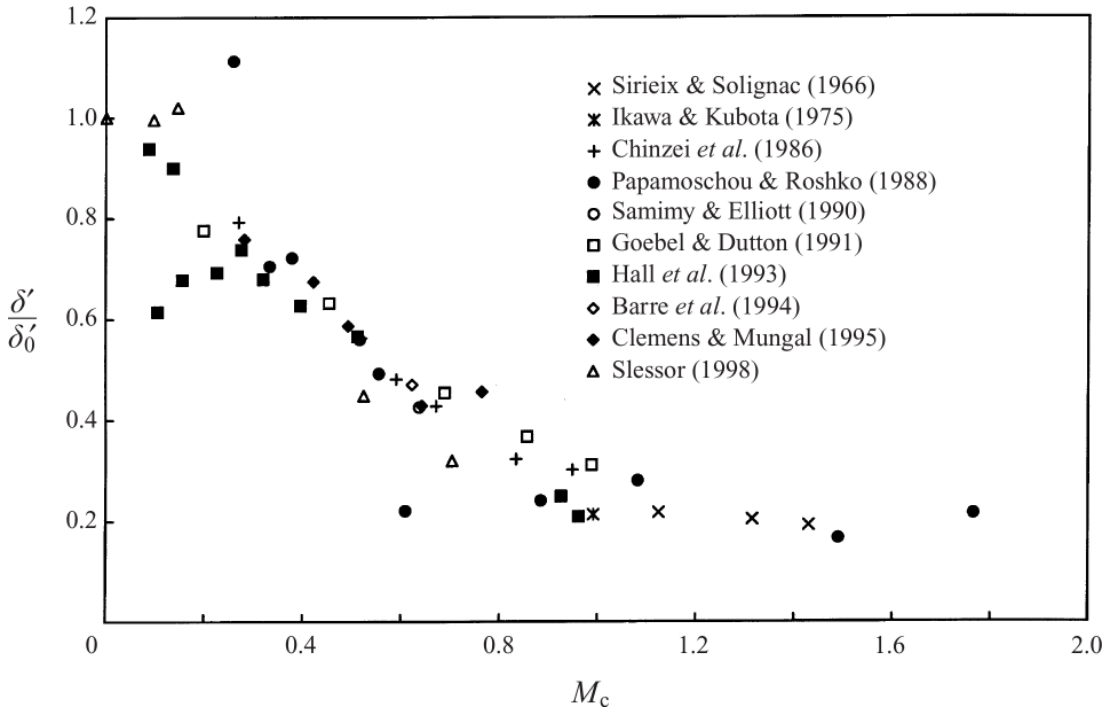

Figure 1.22: Compressible shear layer growth rates vs convective Mach number $M_c = (u_1 - u_2)/(a_1 + a_2)$. [47]

for previous experimental studies was $\approx 2\%$ chord, while the slot height and thus jet width was $\approx 0.15\%$. For use on an aircraft, these boundary layer and slot heights will likely be larger and smaller, respectively. At these scales, to first order approximation, the shear layer will coincide at the interface between the supersonic flow within the jet and the low subsonic flow of the near–wall boundary layer.

Figure 1.13 shows the schematic structure of the structure of supersonic Coanda jets. Here the reflections of shock and expansion waves on the shear layers are shown. For numerical simulations of supersonic Coanda jets, the understanding of the modelling of highly compressible shear layers is required. Inaccurate modelling of the shear layer could determine an incorrect distribution of reflected shocks on the Coanda surface, and in turn may influence predictions of local jet separation and breakaway.

There has been considerable research in the area of compressible shear layers [46–50]. The behaviour of a compressible shear layer is often considerably different to their analogous incompressible type. The convective Mach number $M_c = (u_1 - u_2)/(a_1 + a_2)$ describes the compressibility of the shear layer [46]. As the difference in speeds between fluids across the shear layer increases, the convective Mach number increases, the shear layer spreading rate decreases. Figure 1.22 shows the effect of convective Mach number on shear layer growth rate, for $M_c > 1.0$ the shear layer growth reduces to approximately 20% of that of an incompressible shear layer [47].

Vreman *et.al.* [48] performed DNS on compressible shear layers and found that

the reduced growth rate due to compressibility was not due to dilatation–dissipation and pressure–dilatation but instead due to the pressure–strain relationship. It was also observed that as M_c increased, the anisotropy between Reynolds stresses also increased.

The modelling of compressible shear layers using traditional RANS turbulence models presents difficulties because these models were typically designed and calibrated using measurements from turbulent flat plate and incompressible shear layers. These models also do not model terms in the Reynolds equations such as as the pressure–strain relationship. Several numerical studies have investigated the modelling of compressible shear layers and have found that turbulence models such as the k-ω over predict the spreading rate. The k-ϵ is often considered to outperform the k-ω turbulence model in terms of spreading rate but still fails to capture the anisotropy in the shear layer [49]. This lack of agreement appears to be due also to the Boussinesq approximation [49,51], which describes the linear isotropic relationship between turbulent viscosity and the shear stress.

Gomez and Girimaji [49] present their work on numerical modelling against 2D compressible shear layer experiments performed by Goebel and Dutton [50]. An Explicit Algebraic Reynolds Stress Model (EARSM) is presented and compared with the k-ϵ using Ansys Fluent. Their EARSM provides an explicit second moment closure of the RANS equations while retaining similar costs of the k-ϵ two equation model. For $M_c = 0.2$, the k-ϵ model performed well in terms of predicting the velocity and Reynolds stress profiles across the shear layer, in addition to predicting the spreading rate within 5% of the measured value. However as M_c increased to $M_c = 1.0$, the k-ϵ model could only predict the velocity profile well, while the EARSM also predicted the increased anisotropy within the shear layer. Here the shear layer growth was over predicted by 63% using k-ϵ and the proposed EARSM growth rate was within 6.2%.

1.6.3 Shock boundary layer interactions

Shock boundary layer interactions (SBLIs) occur in many high speed flows such as transonic wings, Scramjet engines, and also supersonic Coanda jets. The breakaway of supersonic Coanda jets has been attributed to effects due to SBLI [7].

DeBonis [52] discussed CFD results from the SBLI prediction workshop, and illustrated that two-equation turbulence models such as the k-ω SST give reasonable predictions in the mean flow, however the Reynolds stresses are poorly predicted compared with scale resolving simulations such as LES.

Georgiadis [53] showed that modifying the viscous limiter of the k-ω SST model to improve predictions of the separated region due to the strong adverse pressure gradient found in SBLI. Increasing the model constant from $a_1 = 0.31$ to $a_1 = 0.355$ reduced the size of the separation bubble to within 10% of the experiment for a $M = 2.25$ SBLI.

Barakos [54] investigated the use of non-linear eddy viscosity turbulence models

for shock boundary layer interactions over a bump geometry in transonic flows. It was found that the cubic non-linear k-ϵ models performed favourably compared with the k-ϵ and k-ω SST models in predicting the anisotropy in the flow, however the anisotropy was underpredicted compared with experiments. It was noted that the k-ω SST model also produced reasonable results.

1.7 NATO AVT-239: Innovative Control Effectors for Manoeuvring of Air Vehicles

As part of the NATO Science and Technology Organisation (STO) Applied Vehicle Technology (AVT) task group AVT-161 [55], the Stability and Control Configuration (SACCON) UCAV demonstrator was designed and developed to provide a platform for static and dynamic experimental and numerical measurements [56]. Within AVT-161 and the follow on task group AVT-201 [57], low speed and transonic wind tunnel experiments were conducted at several facilities [58]. These experiments were complemented by numerical simulations to assess the predictions of the highly non-linear aerodynamics due to the complex vortex interactions of the 53° swept lambda wing planform.

High speed, transonic experiments of the SACCON were conducted in the BAE Systems' High Speed Wind Tunnel (HSWT) and the DNW Transonic Wind Tunnel (TWG) at freestream speeds up to $M = 0.9$ at a range of incidence and sideslip angles [59]. The model (DLR-F17) had control surfaces on the left hand side of the wing which included inboard and outboard flaps and split flaps. Simulations by Coppin and Birch [60] and Kennett *et. al.* [61] into the use of control surface deflections showed that RANS predictions were in reasonable agreement with experimental results for the range of conditions presented, with the main focus upon $M = 0.7$.

Following the successes of the AVT-161 and AVT-201, several other AVT task groups have been formed to investigate multi-disciplinary design requirements for future UCAVs. Of these task groups, AVT-239 [62] is investigating the use of novel control effectors such as circulation control, sweeping jets and fluidic thrust vectoring. The group aims to identify the capabilities of novel controls for three segments of a mission profile: Cruise at low–moderate incidence angles; high speed and high manoeuvrability; and take-off and landing. Currently the focus is on the cruise portion of the mission, with the three segments to be completed by 2019. The findings of the AVT-239 will be presented in a special session at one of the AIAA conferences (Scitech or Aviation) and as a NATO STO technical report. The author is part of this group where work is ongoing. The contributions of the author to the AVT-239 are included in this thesis.

Previous work on circulation control and the SACCON was performed by Hoholis *et. al.* [63], who used circulation control to induce a rolling moment to the SACCON

at low freestream speeds ($M = 0.145$). With subsonic blowing over the Coanda surface, the rolling moment was found to exceed that of 20° flap deflections at angles of attack at which the aerodynamic behaviour is linear. At high angles of attack, highly vortical flow reduced the effectiveness of the circulation control device.

1.8 Summary of Surveyed Literature

In all of the circulation control experiments using a transonic freestream available in the literature the models have had elliptical aerofoil sections. This may have been due to the aims of the project which funded the research, such as the case for the X-Wing era experiments. Practicalities such as providing a supply of air for the jet, wind tunnel size restrictions and manufacturing constraints limiting the minimum available slot height may also have influenced the choice of aerofoil section in CC experiments. These aerofoil sections are not representative of geometries that would be used on an aircraft, however the experiments have provided useful insights into the effect of Coanda radius to slot height ratio, Coanda geometries and the achievable lift augmentation ratios with a transonic CC system.

From these experiments, the results suggest that larger radii to slot height ratios allow for a wider range of blowing rates for which the jet remains attached when the freestream is transonic. This increase in r:h was achieved by decreasing the slot height for a given Coanda geometry, and also by modifying the Coanda geometry to increase the local radius of curvature at the slot exit. This generality is consistent with the findings of Englar [4], Abramson [8] and Alexander [3] as described above. Maximum lift augmentation ratios of 20-50 were observed for freestream Mach numbers of $M > 0.6$ for all experiments.

For supersonic Coanda jets without a freestream, the limiting factor pertinent to jet attachment is the shock boundary layer interaction if the jet is under-expanded. Two approaches have been considered to increase the range of operating conditions for which the jet remains attached. Gregory-Smith and Carpenter found that an approximate 25% increase in the nozzle pressure ratio that caused detachment was achievable using a small step between the jet slot exit and the Coanda surface. The step provided a region for which the jet expanded and the shock waves interacted with a shear layer rather than the Coanda surface boundary layer. Converging diverging nozzles can also extend the operating limit, as seen by Cornelius in their experiments on supersonic Coanda jets in still air. Bevilaqua approached the problem of jet detachment by designing a converging diverging nozzle using the Method of Characteristics such that the jet exit velocity profile matched the profile of an irrotational vortex of the same dimensions.

In addition to having relatively few experiments of CC in transonic flow conditions, the literature has a significant shortage of numerical studies of transonic CC and super-

sonic Coanda jets. Results for low speed CC suggest that numerical modelling is fairly well understood, which is aided by the availability of experimental work suitable for validation. The results from the Georgia Tech Research Institute was able to provide measurements of the jet around the Coanda in addition to quantitative measurements of the freestream flow. This highlighted the wall interference of the experiment which was needed to be known for accurate simulations. Findings from Hoholis have shown that CC in the subsonic regime is capable of producing roll, pitch and yaw using a subsonic jet.

Aspects of transonic CC such as transonic aerofoils, compressible shear layers and shock boundary layer interactions have been successfully modelled using RANS turbulence models. The use of EARSM and SST models for compressible shear layers and shock boundary layers interactions, respectively, suggest that with it may be feasible to predict transonic CC flows with confidence in the accuracy.

1.9 Aims and Objectives

This work intends to address the following aims:

- The fundamental aim of this Ph.D. thesis is to increase the understanding of circulation control in transonic flows using a supersonic Coanda jet.
- Assess CFD capabilities to predict CC in transonic conditions.
- Develop an insight into which geometries and configurations of Coanda devices are suitable/optimal for CC in transonic flows.
- Develop understanding of the effect of Coanda actuators on a representative full aircraft geometry.

To meet these aims, an investigation into the computational challenges and modelling requirements is necessary. This includes investigating the grid strategies, turbulence modelling and boundary conditions necessary to perform reliable simulations of transonic CC and supersonic Coanda jets. Validation of the numerical methods will be made between experimental data available in the literature.

In order to address and develop an insight into the effect Coanda device configurations have on the performance of CC, a design study will be conducted to investigate the appropriate shapes that are effective for transonic CC. This will extend the knowledge from previous experimental works conducted on Coanda geometries by assessing the performance of devices that have currently only been considered for conditions without a freestream. In addition, the use of numerical tools such as aerodynamic shape optimisation may provide an insight into geometries that have yet to be considered.

Using the knowledge developed regarding modelling and Coanda geometric aspects, it will then be possible to apply this knowledge to investigate the use of CC on a representative aircraft geometry. An assessment and comparison of the capabilities of CC compared with traditional control devices will help broaden the body of knowledge on transonic circulation control.

1.10 Thesis Outline

This work is formed of seven chapters including the current introduction chapter. The fundamental equations and numerical methods employed are described in Chapter 2.

The methods are then compared with several experiments to establish that the methods are appropriate for modelling supersonic Coanda jets and transonic circulation control in Chapter 3.

An analysis of circulation control applied to a transonic supercritical aerofoil follows in Chapter 4. Simulations of circulation control and a deflected aileron which are compared for the same aerofoil section, in addition a study into the effect of altering the shape of the Coanda device is made to improve circulation control performance.

The 5th Chapter describes the results of a formal optimisation study on the Coanda shape using the Adjoint method.

Simulations of transonic CC on the SACCON UCAV demonstrator are presented in Chapter 6, where the (ongoing) contributions by the author to the NATO AVT-239 are reported.

Finally, a summary of the findings along with conclusions and recommendations for future work is made.

Chapter 2

Numerical Methods

The Helicopter Multi-Block (HMB) CFD code [64–67] is used for this work. The code has been validated for a number of applications, including helicopters; wind turbines; turboprops; and high-speed unmanned combat aerial vehicles [67–69]. In addition, validation of the solver and boundary conditions for subsonic CC has been conducted by Hoholis [38].

HMB solves the compressible, unsteady Reynolds-averaged Navier-Stokes equations on block-structured grids using a cell-centred finite-volume method for spatial discretisation. The solver has a library of turbulence closures which includes several one- and two- equation turbulence models [70–73]. Turbulence simulation is also possible using Large-Eddy and Detached-Eddy Simulation. As part of this work, a non-Boussinesq version of the k-ω model (EARSM) [74, 75] was implemented into HMB to assess the capabilities of the anisotropic turbulence modelling of supersonic Coanda jets.

The convective fluxes are evaluated using Osher's upwind scheme for its robustness, accuracy, and stability properties. MUSCL variable extrapolation is used to provide second-order accuracy with the Van Albada limiter to prevent spurious oscillations around shock waves. An implicit time-integration method is employed, and the resulting linear systems of equations are solved using a pre-conditioned Generalised Conjugate Gradient method. For unsteady simulations, an implicit dual-time stepping method is used, which is based on Jameson's pseudo-time integration approach [76].

A discrete adjoint solver is also embedded into HMB [77] to provide flow derivatives for flight dynamics and optimisation.

2.1 Navier–Stokes Equations

For compressible, viscous flows the Navier-Stokes equations for continuity, momentum and energy, respectively are given by:

$$\frac{\partial \rho}{\partial t} + \frac{\partial}{\partial x_j}\left[\rho u_j\right] = 0 \tag{2.1}$$

$$\frac{\partial}{\partial t}\left(\rho u_i\right) + \frac{\partial}{\partial x_j}\left[\rho u_i u_j + p\delta_{ij} - \tau_{ji}\right] = 0, \quad i = 1, 2, 3 \tag{2.2}$$

$$\frac{\partial}{\partial t}\left(\rho e_0\right) + \frac{\partial}{\partial x_j}\left[\rho u_j e_0 + u_j p + q_j - u_i \tau_{ij}\right] = 0 \tag{2.3}$$

For a Newtonian fluid the viscous stress is given by:

$$\tau_{ij} = 2\mu S^*_{ij} \tag{2.4}$$

Where the trace-less viscous strain-rate is defined by:

$$S^*_{ij} \equiv \frac{1}{2}\left(\frac{\partial u_i}{\partial x_j} + \frac{\partial u_j}{\partial x_i}\right) - \frac{1}{3}\frac{\partial u_k}{\partial x_k}\delta_{ij} \tag{2.5}$$

The heat-flux, q_j, is given by Fourier's law:

$$q_j = -\lambda \frac{\partial T}{\partial x_j} \equiv -C_p \frac{\mu}{Pr}\frac{\partial T}{\partial x_j} \tag{2.6}$$

Where the laminar Prandtl number Pr is defined by:

$$Pr \equiv \frac{C_p \mu}{\lambda} \tag{2.7}$$

To close these equations it is also necessary to specify an equation of state. Assuming a calorically perfect gas the following relations are valid:

$$\gamma \equiv \frac{C_p}{C_v} \quad , \quad p = \rho R T \quad , \quad e = C_v T \quad , \quad C_p - C_v = R \tag{2.8}$$

Where γ, C_p, C_v and R are constant. The total energy e_0 per unit mass is defined by:

$$e_0 \equiv e + \frac{u_k u_k}{2} \tag{2.9}$$

2.2 Reynolds Averaged Navier–Stokes Turbulence Modelling

Turbulence is a three-dimensional time dependant problem, however in many engineering situations the temporal fluctuations associated with turbulent flow are not of interest. The variables of the governing equations are decomposed into time averaged and fluctuating components, for example $u = u' + \bar{u}$. This decomposition is substituted into the Navier-Stokes equations which results in the Reynolds Averaged Navier-Stokes (RANS) equations (equation 2.10). These are identical to the steady state Navier-Stokes equations with the exception of the spatial derivative of the fluctuating velocity components, known as the Reynolds stresses. The RANS equations are given by;

$$\frac{\partial}{\partial t}(\rho\bar{u}_i) + \frac{\partial \rho\bar{u}_j\bar{u}_i}{\partial x_j} = -\frac{\partial \bar{p}}{\partial x_i} + \frac{\partial}{\partial x_j}[\mu\left(\frac{\partial u_i}{\partial x_j} + \frac{\partial u_j}{\partial x_i}\right) - \rho\overline{u_i'u_j'}] \tag{2.10}$$

where $-\rho\overline{u_i'u_j'}$ is the Reynolds stress tensor, τ_{ij}.

The Reynolds stress tensor is a function of the fluctuating velocity components which are unknowns in the RANS equations and introduce an additional 6 terms to be solved. In 1877, Boussinesq stated an assumption that the turbulent shear stresses are proportional to the mean strain rate by a turbulent eddy viscosity μ_t. This is often known as a first order (or approximate) closure to the RANS equations.

The Boussinesq assumption is known as:

$$\tau_{ij} = 2\mu_t\left(S_{ij} - \frac{1}{3}\frac{\partial u_k}{\partial x_k}\delta_{ij}\right) - \frac{2}{3}\rho k\delta_{ij} \tag{2.11}$$

where:

$$S_{ij} = \frac{1}{2}\left(\frac{\partial u_i}{\partial x_j} + \frac{\partial u_j}{\partial x_i}\right) \tag{2.12}$$

is the mean strain tensor and k is the turbulent kinetic energy. Many RANS turbulence models utilise the linear Boussinesq eddy viscosity assumption when modelling the Reynolds stresses. The Wilcox k–ω [70] and Menter k–ω SST [71] models described below are of the linear eddy viscosity type. These models solve one transport equation for each of the turbulent kinetic energy k, and the turbulent length scale ω.

Some turbulence models however do not use this assumption and instead calculate the Reynolds stresses directly, known as second order or second moment closure turbulence models. Models of this type, such as the full Reynolds stress model solve a transport equation for each of the 6 components of τ_{ij}. To do so an additional 22 unknowns must be modelled first [78]. The Explicit Algebraic Reynolds Stress Models (EARSMs), such as the model of Hellsten, Wallin, and Johansson [74, 75, 79] described below forgoes these additional equations. Instead EARSMs solve algebraic equations

for τ_{ij} while retaining the physical nature of the full RSM.

2.2.1 Wilcox k–ω model

The basic equations for this two-equation model developed by Wilcox [70] are:

$$\frac{\partial(\rho k)}{\partial t} + \frac{\partial(\rho u_j k)}{\partial x_j} = \mathcal{P} - \beta^* \rho\omega k + \frac{\partial}{\partial x_j}\left[\left(\mu + \sigma_k \frac{\rho k}{\omega}\right)\frac{\partial k}{\partial x_j}\right] \tag{2.13}$$

$$\frac{\partial(\rho\omega)}{\partial t} + \frac{\partial(\rho u_j \omega)}{\partial x_j} = \frac{\gamma\omega}{k}\mathcal{P} - \beta\rho\omega^2 + \frac{\partial}{\partial x_j}\left[\left(\mu + \sigma_\omega \frac{\rho k}{\omega}\right)\frac{\partial \omega}{\partial x_j}\right] \tag{2.14}$$

and the turbulent eddy viscosity is computed from:

$$\mu_t = \frac{\rho k}{\omega} \tag{2.15}$$

$$P = \tau_{ij}\frac{\partial u_i}{\partial x_j} \tag{2.16}$$

2.2.2 Menter k–ω SST model

The k–ω Shear Stress Transport (SST) model was developed by Menter in 1994 and is a derivation of the BSL k–ω model, both models were introduced in Ref. 71. The SST included a limiter of the turbulent viscosity μ_t, described below. Otherwise the underlying models of the BSL and SST are the same. In the near wall region the models behave in the same way as the Wilcox k–ω model above while further away from the wall the model blends into the k–ϵ model utilising the free shear capabilities of the k–ϵ model. This two-equation model is given by the following:

$$\frac{\partial(\rho k)}{\partial t} + \frac{\partial(\rho u_j k)}{\partial x_j} = \mathcal{P} - \beta^* \rho\omega k + \frac{\partial}{\partial x_j}\left[(\mu + \sigma_k \mu_t)\frac{\partial k}{\partial x_j}\right] \tag{2.17}$$

$$\frac{\partial(\rho\omega)}{\partial t} + \frac{\partial(\rho u_j \omega)}{\partial x_j} = \frac{\gamma\omega}{k}\mathcal{P} - \beta\rho\omega^2 + \frac{\partial}{\partial x_j}\left[(\mu + \sigma_\omega \mu_t)\frac{\partial \omega}{\partial x_j}\right] + 2(1 - F_1)\frac{\rho\sigma_{\omega 2}}{\omega}\frac{\partial k}{\partial x_j}\frac{\partial \omega}{\partial x_j} \tag{2.18}$$

The turbulent eddy viscosity is computed from:

$$\mu_t = \frac{\rho a_1 k}{\max(a_1\omega, \Omega F_2)} \tag{2.19}$$

Each of the constants is a blend of an inner (1) and outer (2) constant, blended via:

$$\phi = F_1\phi_1 + (1 - F_1)\phi_2 \tag{2.20}$$

where ϕ_1 represents constant 1 and ϕ_2 represents constant 2. Additional functions are given by:

$$F_1 = \tanh\left(\arg_1^4\right) \tag{2.21}$$

$$\arg_1 = \min\left[\max\left(\frac{\sqrt{k}}{\beta^*\omega d}, \frac{500\nu}{d^2\omega}\right), \frac{4\rho\sigma_{\omega 2}k}{\mathrm{CD}_{k\omega}d^2}\right] \tag{2.22}$$

$$\mathrm{CD}_{k\omega} = \max\left(2\rho\sigma_{\omega 2}\frac{1}{\omega}\frac{\partial k}{\partial x_j}\frac{\partial \omega}{\partial x_j}, 10^{-20}\right) \tag{2.23}$$

$$F_2 = \tanh\left(\arg_2^2\right) \tag{2.24}$$

$$\arg_2 = \max\left(2\frac{\sqrt{k}}{\beta^*\omega d}, \frac{500\nu}{d^2\omega}\right) \tag{2.25}$$

where d is the distance from the field point to the nearest wall, and $\Omega = \sqrt{2W_{ij}W_{ij}}$ is the vorticity magnitude, with

$$W_{ij} = \frac{1}{2}\left(\frac{\partial u_i}{\partial x_j} - \frac{\partial u_j}{\partial x_i}\right) \tag{2.26}$$

2.2.3 Explicit algebraic Reynolds stress model

The EARSM turbulence model of Hellsten, Wallin, and Johansson [74, 75, 79] was implemented into HMB. This turbulence model is based upon the Menter BSL $k - \omega$ turbulence model [71], it however does not follow from the Boussinesq eddy viscosity assumption. Instead the Reynolds Stress Tensor τ_{ij} is given by Eq. (2.27), where $a_{ij}^{(ex)}$ is termed the Reynolds Stress anisotropy tensor and is calculated from an algebraic second moment closure of the Reynolds Stress equations. Equation (2.27) can be simply reduced to the linear Boussinesq formulation with an additional anisotropy term Eq. (2.28).

$$\tau_{ij} = 2\mu_t\left(S_{ij} - \frac{1}{3}\frac{\partial u_k}{\partial x_k}\delta_{ij}\right) - \frac{2}{3}\rho k\delta_{ij} - a_{ij}^{(ex)}\rho k \tag{2.27}$$

$$\tau_{ij} = \tau_{ij}^{Boussinesq} - a_{ij}^{(ex)}\rho k \tag{2.28}$$

The Reynolds Stress anisotropy tensor is given by:

$$a_{ij}^{(ex)} = \beta_3 \left(W_{ik}^* W_{kj}^* - \frac{1}{3} II_\Omega \delta_{ij} \right) + \beta_4 \left(S_{ik}^* W_{kj}^* - W_{ik}^* S_{kj}^* \right) + \beta_6 \left(S_{ik}^* W_{kl}^* W_{lj}^* + W_{ik}^* W_{kl}^* S_{lj}^* - II_\Omega S_{ij}^* - \frac{2}{3} IV \delta_{ij} \right) + \beta_9 \left(W_{ik}^* S_{kl}^* W_{lm}^* W_{mj}^* - W_{ik}^* W_{kl}^* S_{lm}^* W_{mj}^* \right) \quad (2.29)$$

Where:

$$S_{ij}^* = \frac{\tau}{2} \left(\frac{\partial u_i}{\partial x_j} + \frac{\partial u_j}{\partial x_i} \right) \quad (2.30)$$

$$W_{ij}^* = \frac{\tau}{2} \left(\frac{\partial u_i}{\partial x_j} - \frac{\partial u_j}{\partial x_i} \right) \quad (2.31)$$

$$\tau = \frac{1}{\beta^* \omega} \quad (2.32)$$

The two-equation model is given by the following:

$$\frac{\partial (\rho k)}{\partial t} + \frac{\partial (\rho u_j k)}{\partial x_j} = \mathcal{P} - \beta^* \rho \omega k + \frac{\partial}{\partial x_j} \left[(\mu + \sigma_k \mu_t) \frac{\partial k}{\partial x_j} \right] \quad (2.33)$$

$$\frac{\partial (\rho \omega)}{\partial t} + \frac{\partial (\rho u_j \omega)}{\partial x_j} = \frac{\gamma \omega}{k} \mathcal{P} - \beta \rho \omega^2 + \frac{\partial}{\partial x_j} \left[(\mu + \sigma_\omega \mu_t) \frac{\partial \omega}{\partial x_j} \right] + \sigma_d \frac{\rho}{\omega} \max \left(\frac{\partial k}{\partial x_k} \frac{\partial \omega}{\partial x_k}, 0 \right) \quad (2.34)$$

The ω equation above is of a similar form to Menter's BSL equation, with a different formulation of the source term $\sigma_d \frac{\rho}{\omega} \max \left(\frac{\partial k}{\partial x_k} \frac{\partial \omega}{\partial x_k}, 0 \right)$ (Eq. (2.34)). Here σ_d varies between $\sigma_d = 0.4$ and $\sigma_d = 1.0$ depending upon the wall distance and the gradients of k and ω in a similar way to the blending function of the BSL $k - \omega$ model. Other than this source term, this EARSM baseline model equations are identical to the Wilcox $k - \omega$ model above (Eqs. (2.13) and (2.13)).

In addition to the anisotropic element $a_{ij}^{(ex)}$ of τ_{ij}, the turbulent eddy viscosity μ_t is scaled by a variable C_μ, which is determined by the strain and rotation tensors. This is given by Eq. (2.35) where $\beta^* = 0.09$.

$$\mu_t = \frac{C_\mu}{\beta^*} \frac{\rho k}{\omega} \quad (2.35)$$

The variable coefficient C_μ is obtained from:

$$C_\mu = -\frac{1}{2}\left(\beta_1 + II_\Omega \beta_6\right) \tag{2.36}$$

Furthermore,

$$\beta_1 = -\frac{N\left(2N^2 - 7II_\Omega\right)}{Q}\beta_3 = -\frac{12(IV)}{NQ} \tag{2.37}$$

$$\beta_4 = -\frac{2\left(N^2 - 2II_\Omega\right)}{Q}\beta_6 = -\frac{6N}{Q}\beta_9 = \frac{6}{Q} \tag{2.38}$$

$$Q = \frac{5}{6}\left(N^2 - 2II_\Omega\right)\left(2N^2 - II_\Omega\right) \tag{2.39}$$

$$II_\Omega = W^*_{kl}W^*_{lk}IV = S^*_{kl}W^*_{lm}W^*_{mk} \tag{2.40}$$

and N is obtained from the solution of a cubic equation. The solution is given by:

$$N = \frac{A'_3}{3} + \left(P_1 + \sqrt{P_2}\right)^{1/3} + \mathrm{sgn}\left(P_1 - \sqrt{P_2}\right)\left|P_1 - \sqrt{P_2}\right|^{1/3} for P_2 \geq 0 \tag{2.41}$$

$$N = \frac{A'_3}{3} + 2\left(P_1^2 - P_2\right)^{1/6}\cos\left[\frac{1}{3}\cos^{-1}\left(P_1/\sqrt{P_1^2 - P_2}\right)\right] for P_2 < 0 \tag{2.42}$$

where

$$P_1 = \left[\frac{A'^2_3}{27} + \left(\frac{9}{20}\right)II_S - \frac{2}{3}II_\Omega\right]A'_3 \tag{2.43}$$

$$P_2 = P_1^2 - \left[\frac{A'^2_3}{9} + \left(\frac{9}{10}\right)II_S + \frac{2}{3}II_\Omega\right]^3 \tag{2.44}$$

$$A'_3 = \frac{9}{5} + \frac{9}{4}C_{diff}\left[\max\left(1 + \beta_1^{(eq)}II_S, 0\right)\right] \tag{2.45}$$

$$II_S = S^*_{kl}S^*_{lk} \tag{2.46}$$

$$\beta_1^{(eq)} = -\frac{6}{5}\left[\frac{N^{(eq)}}{\left(N^{(eq)}\right)^2 - 2II_\Omega}\right] \tag{2.47}$$

$$N^{(eq)} = \frac{81}{20}C_{diff} = 2.2 \tag{2.48}$$

2.3 Adjoint Equations

For aerodynamic optimisation and flight dynamics simulations, aerodynamic derivatives are often required. A simple approach to providing these derivatives is via finite differencing. However this results in many full flow solutions for the derivative around one point when using finite differences. Finite differences can be especially prohibitive for optimisation purposes where the geometry is defined by multiple parameters.

The Adjoint form of the Navier-Stokes equations offer an efficient way to obtain aerodynamic derivatives with respect to variables $\boldsymbol{x}$ such as the angle of attack, Mach number and also design variables for aerodynamic shape optimisation. A cost function I is typically defined for optimisation as a combination of the forces and moments about the geometry of interest, such as C_L/C_D. For flight dynamics, the cost function is called as the functional of the flow solution and is taken as the aerodynamic force or moment of interest.

The gradient of the cost function ($dI/d\mathbf{x}$) is obtained by solving the sensitivity equation in adjoint form [80, 81]. The principle is to formulate the cost function I in terms of the flow variables $\boldsymbol{W}$ and design variables $\boldsymbol{x}$, i.e. $I = I(\boldsymbol{W}(\boldsymbol{x}), \boldsymbol{x})$. The flow variables are found as solutions to the Navier–Stokes equations, written in compact form as

$$\boldsymbol{R}(\boldsymbol{W}(\boldsymbol{x}), \boldsymbol{x}) = 0. \tag{2.49}$$

where $\boldsymbol{R}$ is the residual error of the flow solution. Taking the derivative of I with respect to $\boldsymbol{x}$ we obtain:

$$\frac{\mathcal{D}I}{\mathcal{D}\boldsymbol{x}} = \frac{\partial I}{\partial \boldsymbol{x}} + \frac{\partial I}{\partial \boldsymbol{W}} \frac{\partial \boldsymbol{W}}{\partial \boldsymbol{x}}, \tag{2.50}$$

which represents the tangent form of the sensitivity equation. All the partial derivatives appearing on the right-hand side can be computed with limited effort with the exception of $\partial \boldsymbol{W}/\partial \boldsymbol{x}$, which represents the variation of the flow variables with respect to the independent input parameters. This last term may be obtained by differentiating the governing equations (Eq. (2.49)), to yield the following linear system for the unknown $\partial \boldsymbol{W}/\partial \boldsymbol{x}$:

$$\frac{\partial \boldsymbol{R}}{\partial \boldsymbol{W}} \frac{\partial \boldsymbol{W}}{\partial \boldsymbol{x}} = -\frac{\partial \boldsymbol{R}}{\partial \boldsymbol{x}}. \tag{2.51}$$

The solution of Eq. (2.51) must be solved for each design variable to compute the sensitivities, since the right-hand side of Eq. (2.51) depends upon $\boldsymbol{x}$. Therefore, the computational cost scales with the number of design variables. The sensitivity problem (Eqs. (2.50) and (2.51)) can be recast in dual form by introducing the adjoint vector

variable $\boldsymbol{\lambda}$ as the solution of the following linear system:

$$\left(\frac{\partial \boldsymbol{R}}{\partial \boldsymbol{W}}\right)^{\mathrm{T}} \boldsymbol{\lambda} = -\left(\frac{\partial I}{\partial \boldsymbol{W}}\right)^{\mathrm{T}}. \tag{2.52}$$

Substituting equation Eq. (2.52) into Eq. (2.50) and using matrix algebra we obtain:

$$\frac{\mathcal{D}I}{\mathcal{D}\boldsymbol{x}} = \frac{\partial I}{\partial \boldsymbol{x}} + \boldsymbol{\lambda}^{\mathrm{T}} \frac{\partial \boldsymbol{R}}{\partial \boldsymbol{x}}. \tag{2.53}$$

The computational cost of the dual sensitivity problem (Eqs. (2.52) and (2.53)) scales with the number of outputs, since the right-hand side of Eq. (2.52) depends on I, but it is independent of the input parameters [82]. The adjoint form of the sensitivity equation is therefore particularly efficient for aerodynamic optimisation applications, where typically the number of cost functions is small while the number of design variables is large [83, 84].

The linear system (2.52) for computing the adjoint variable is solved with a Krylov-subspace solver, namely the Flexible Generalised Minimum Residual with deflated restarting (FGMRES-DR) [85]. The flexible formulation allows to precondition the outer GMRES iterations with a nested Krylov-subspace method, which in the current implementation can be either restarted GMRES [86] or GMRES-DR [87]. The nested solver uses in turn an ILU(k) preconditioner [88], which is decoupled on each processor in parallel computations. The use of the nested preconditioner increases the robustness of the method, especially if a large number of processors is used, where the decoupled ILU(k) preconditioner alone would lead to stall of the solver for tough cases.

The implementation of the nested Krylov-subspace solver does not require the Jacobian matrix J, but only the matrix-vector product $J^{\mathrm{T}}\boldsymbol{v}$. Therefore, J is never stored explicitly, and the product $J^{\mathrm{T}}\boldsymbol{v}$ is computed by means of automatically differentiated code of the residual function. Further details about the application of automatic differentiation to the the HMB CFD solver are given in Ref. 77.

2.4 Nondimensionalisation

HMB solves the nondimensional RANS equations, as such the computational grids are built such that a unit length in the grid is equal to the reference length of the model, typically the chord. Reference conditions of Mach and Reynolds number per reference length are provided as inputs to the solver. At the farfield the velocity magnitude is set to 1, and the components of velocity are determined by the incidence and sideslip angles. The pressure is scaled relative to the dynamic pressure at the freestream, while the density is scaled by freestream conditions. The procedure for all quantities used is

as follows:

$$x = \frac{x^*}{L^*}, \qquad y = \frac{y^*}{L^*}, \qquad t = \frac{t^*}{L^*/V_\infty^*},$$

$$u = \frac{u^*}{V_\infty^*}, \qquad v = \frac{v^*}{V_\infty^*}, \qquad \mu = \frac{\mu^*}{\mu_\infty^*},$$

$$\rho = \frac{\rho^*}{\rho_\infty^*}, \qquad p = \frac{p^*}{\rho_\infty^* V_\infty^{*2}} = \frac{p^*}{\gamma M^2}, \qquad T = \frac{T^*}{T_\infty^*}, \qquad e = \frac{e^*}{V_\infty^{*2}}. \tag{2.54}$$

where starred values indicate dimensional quantities.

2.5 Reservoir Boundary Condition

A reservoir boundary condition is used to set the desired pressure and density ratios based on the assumption that the supply has been isentropically compressed. Here, the nozzle pressure ratio (NPR) is fixed and the momentum coefficient (C_μ) is calculated a posteriori by integrating the solution along the slot exit. The pressure and density are fixed using the isentropic flow relations:

$$\frac{p_0}{p_\infty} = (1 + \frac{\gamma - 1}{2} M^2)^{\frac{\gamma}{\gamma - 1}} \tag{2.55}$$

$$\frac{\rho_0}{\rho_\infty} = (1 + \frac{\gamma - 1}{2} M^2)^{\frac{1}{\gamma - 1}} \tag{2.56}$$

$$p_0 = \frac{NPR}{\gamma M_\infty^2} (1 + \frac{\gamma - 1}{2} M^2)^{-\frac{\gamma}{\gamma - 1}} \tag{2.57}$$

since p_∞ is set to $p/(\gamma M_\infty^2)$ at the farfield boundary.

$$\rho_0 = NPR^{\frac{1}{\gamma}} (1 + \frac{\gamma - 1}{2} M^2)^{-\frac{1}{\gamma - 1}} \tag{2.58}$$

Force contributions of pressure and momentum from this internal reservoir boundary face are included in the calculation of the total forces and moments, following the approach presented by Min *et. al.* [89] whereby $C_d = C_d|_{\text{ext surfaces}} - (\dot{m}_j V_j + P_j A_j)/q_\infty A$.

In this work, the pressure and viscous terms are calculated on the external and internal solid surfaces of the wing. Contributions due to the momentum addition of the jet are considered at the reservoir boundary in the force calculation. As such, the drag coefficient calculation is:

$$C_d = C_d|_{\text{all surfaces}} - \frac{\dot{m}_{res} V_{res} + P_{res} A_{res}}{q_\infty A} \tag{2.59}$$

Figure 2.1 shows an illustration of the surfaces considered for the calculation of the forces and moments.

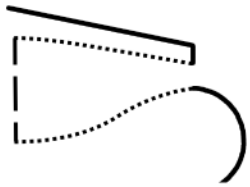

Figure 2.1: Diagram of trailing edge of circulation control aerofoil. The solid lines are considered as external surfaces, dotted lines are the internal plenum surfaces and the dashed line is the reservoir boundary condition.

2.6 Gradient Based Optimisation

Gradient based optimisation is an efficient and widely used method for aerodynamic shape optimisation problems, since it minimises the required number of flow solutions compared with other methods such as genetic algorithms. Gradient methods however require the derivatives of an objective function with respect to the design variables, which can be extremely expensive to compute when high fidelity CFD is employed. Gradient methods march along a direction, performing a one-dimensional minimisation before recomputing a new direction. Formally, the local minimum of the function is found when the gradient is zero.

Using the solution of the adjoint equations to provide gradients is a popular approach, as the cost of solving the adjoint equations is nearly independent of the number of design variables and scales only based on the number of cost functions required, as described in Section 2.3 above. To utilise the adjoint solver in HMB, an optimisation framework was developed in collaboration with Dr. Biava, a post-doctoral researcher within the CFD Lab. The process of parametrising and deforming the surface, and subsequently interfacing with HMB and the optimiser was developed.

Within the optimisation process, the Sequential Least Squares Quadratic Programming (SLSQP) optimisation algorithm [90,91] from the NLopt optimisation library [92] is used to generate new shape designs to find a minimum of the objective function. The

SLSQP uses the Broyden-Fletcher-Goldfarb-Shanno (BFGS) algorithm to update the approximation of the Hessian matrix. The optimisation algorithm is implemented in a separate tool, and it is interfaced with HMB using files for data exchange.

2.6.1 Optimisation routine

Figure 2.2 summarises the design optimisation procedure. After the first calculation of the base flow and adjoint solutions for the initial design, the optimisation algorithm provides a new set of design variables ($\mathbf{x}$). The design variables then parametrically define the updated surface which is passed into the CFD solver. The surface displacements in turn drives the volume mesh deformation.

To reduce computational expenditure the adjoint sensitivity equations (for $dI/d\mathbf{x}$) are only computed when necessary, providing both objective function (I) and its gradient ($dI/d\mathbf{x}$) to the optimiser. During the one-dimensional minimisation within the BFGS procedure, the gradients are not required and therefore the adjoint solution is not calculated, reducing the expense of the optimisation step by approximately 50%.

The multipoint problem is composed of a weighted sum of the individual objective functions (I_i) as proposed by Reuther *et. al.* [93]:

$$I = \sum_{i=1}^{n} \lambda_i I_i \tag{2.60}$$

where n is the number of design points to be evaluated.

The optimisation process is considered complete when either the gradient or the change in design variables between steps falls below a relative tolerance, in this study we seek a maximum tolerance of 1×10^{-3}.

2.6.2 Mesh deformation

The deformation of the volume grid is achieved by an Inverse Distance Weighting (IDW) method [94]. IDW is an interpolation method that calculates the displacement of a given volume point using a weighted average from a set of known sample surface point displacements. The influence of a surface point to a given volume point is proportional to the inverse of the distance between the surface and volume point.

The position of points belonging to parametrically deformed surfaces are provided to the CFD solver. Displacement within the remainder of the domain are then interpolated by the IDW method from these sample surface points, such that the grid deformation does not deteriorate the grid quality and does not lead to invalid cells (*e.g.* negative volumes).

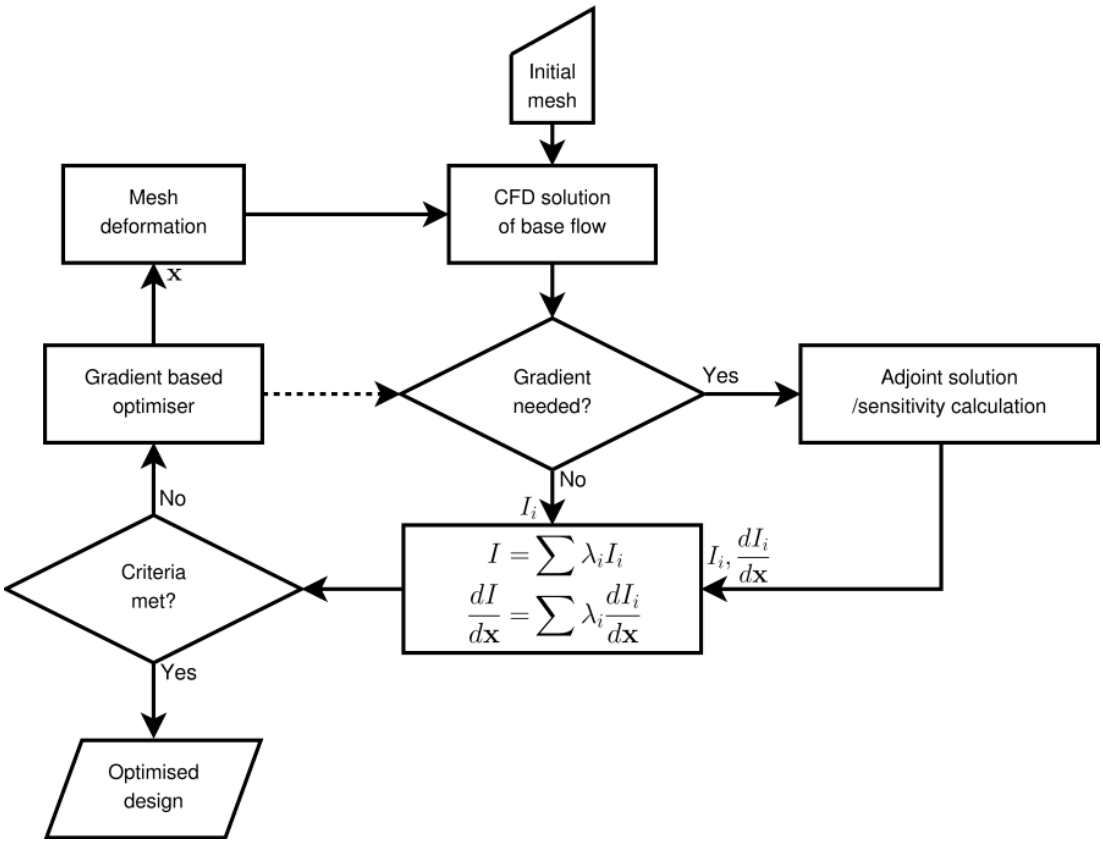

Figure 2.2: Flow chart of the multipoint optimisation process.

2.7 Meshing Approach

Block structured grids were generated using Ansys ICEM-CFD which were then exported as a Multiblock grid and subsequently converted to the appropriate format for HMB. HMB uses a one-to-one mapping of cells between block faces, and parallelisation is performed by assigning a number of blocks to each core with a minimum of one block per core. As a result it is important to generate a mesh with a sufficient number of blocks for load balancing, and to balance the number of cells contained within each block for parallel efficiency. For the cases considered within this thesis, a maximum of approximately 50,000 cells per block was typically used.

Figure 2.3 illustrates the meshing approach employed here. In Fig. 2.3a the detail of the blocking around the Coanda surface is shown. Black lines here represent the solid walls while the coloured lines are block edges. For CC cases without blowing, the plenum is not modelled and instead the slot exit is considered as a wall. An 'O' grid topology was typically used in the CC cases, with additional blocks used to form the plenum and regions near the Coanda. 332 blocks are used in the grid shown in Fig. 2.3b, which corresponds to the SACCON with blowing over upper and lower Coanda surfaces

on the inboard half of the left wing. To generate this grid two half span left wing grids were built; with and without blowing slots which had 168 and 164 blocks, respectively. These grids were merged using a modified grid mirroring utility tool.

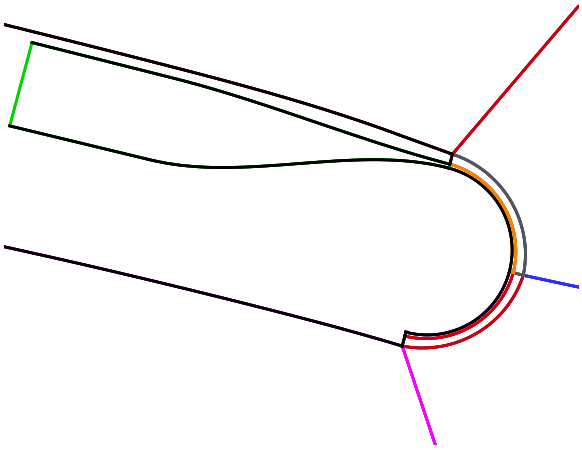

(a) Near Coanda surface.

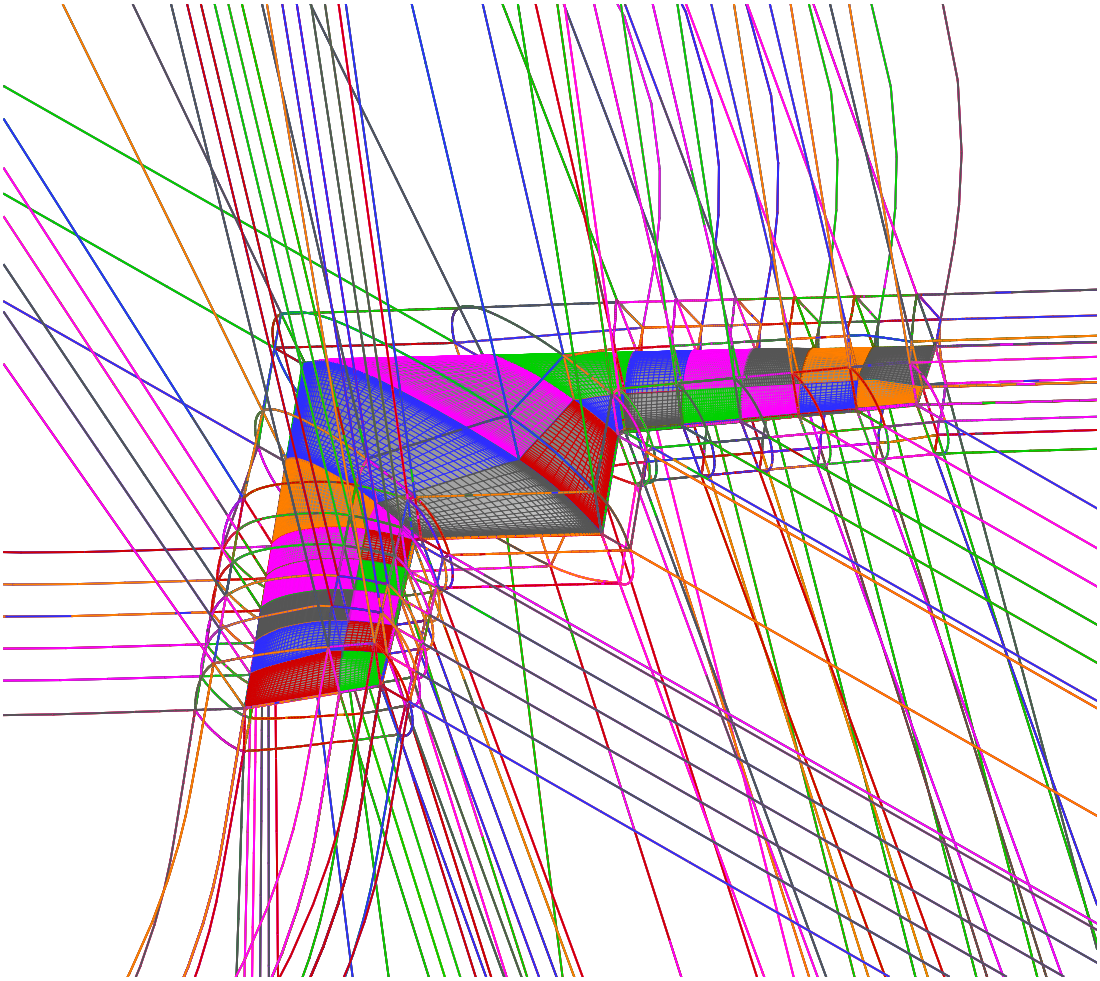

(b) Over 3D UCAV body.

Figure 2.3: Examples of blocking strategy for CC.

Chapter 3

Validation

HMB has been extensively tested and validated for a number of applications including validation of the solver and boundary conditions for CC which was conducted by Hoholis [38]. The work of Hoholis however focussed upon CC for low speed freestream conditions in addition to subsonic jet blowing. For this reason this chapter contains comparisons between numerical simulations using HMB and experimental studies found in the literature with focus on CC in the transonic regime and with supersonic Coanda jets.

Two simulation cases are considered here: an elliptical-sectioned semispan wing in a $M = 0.8$ freestream as investigated experimentally by Alexander *et. al.* [3], and a study of supersonic Coanda jets without a freestream from Gregory-Smith *et. al.* [11,33]. The latter of these two experimental studies also investigated the use of a step as a means of promoting supersonic jet attachment to the Coanda surface [11].

3.1 NASA 6% Transonic Circulation Control

The results within this section were presented in Ref. 95.

Alexander *et. al.* [3] performed a range of experiments on an elliptical aerofoil with a thickness of 6% chord and 0.75% camber (Fig. 3.1). The span of the wing model

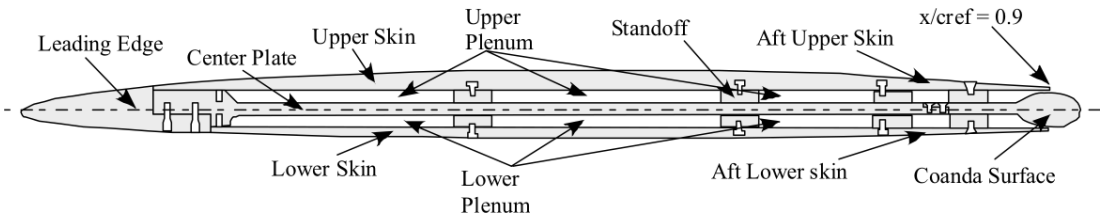

Figure 3.1: Schematic of the NASA 6% elliptical circulation control aerofoil [3].

was 2 chord lengths, with an end plate at 1 chord length in diameter. Comparisons were made between geometries of elliptical Coanda surfaces with different slot heights with emphasis on freestream speeds of $M = 0.3$ and $M = 0.8$ at Reynolds numbers of $1.0 - 2.5 \times 10^6$ per chord, respectively. The baseline aerofoil trailing edge was truncated at 90% chord and replaced with elliptical Coanda surfaces with varying aspect ratios as was shown in Fig. 1.10.

An extensive set of results were published in a NASA technical report following the experimental investigations [3]. The report presents surface pressure coefficients taken at the midspan section of the wing. The lift coefficient was presented as a sectional lift coefficient from integrating the surface pressures along this midspan section, while the drag was measured using a wake rake and including the thrust effect of the jet by $C_d = C_{d\ rake} - C_\mu(V_\infty/V_{jet})$.

Since the only unblown configuration published was for the largest 2.98:1 elliptical Coanda surface with a slot height to chord ratio of 0.12%, the numerical studies presented here have been conducted solely on this geometry. The geometry used was based upon descriptions in reports of the model regarding this dataset [3, 9, 96] and experimental data was digitised from plots in Ref. 3. Small errors due to the interpretation of the model descriptions and limited accuracy of digitising the published data can be expected. In addition, it is stated in the technical report that the data presented was unmodified. It is possible that some flow angle or Mach number corrections from wall interference or blockage effects may be required. For the present study, the freestream conditions given in the report (also Table 3.1) are used for the simulations.

To minimise the finite span effects in the experiments, an end plate was used on the model which is shown in Fig. 3.2. An investigation into the finite span effect was carried out, which compared results between experiments using a "t/2" rounded wingtip and the endplate. The wingtip was circular with a diameter equal to the local aerofoil thickness. It was shown that the endplate did not produce a strong effect as the $C_l - \alpha$ behaviour was similar for both configurations. This suggests that the three dimensional effects of the "t/2" wingtip were still present in the endplate case, and that modelling the wing as a finite span is crucial to generating accurate solutions.

At 5% from the leading edge, a boundary layer trip strip was placed on the upper and lower surfaces to promote turbulent transition of the boundary layer. The trip strip consisted of epoxy dots with diameters of 0.13% chord which extended 0.05% chord into the boundary layer ($y^+ \approx 45$). This trip was not modelled in the simulations, where a fully turbulent flow is assumed.

The majority of simulations for this case were conducted using the k-ω, and k-ω SST models. For comparison there are some additional simulation results using the EARSM. In line with the experiments, surface pressures from simulations were taken at the midspan section. The sectional lift and drag coefficients were computed also

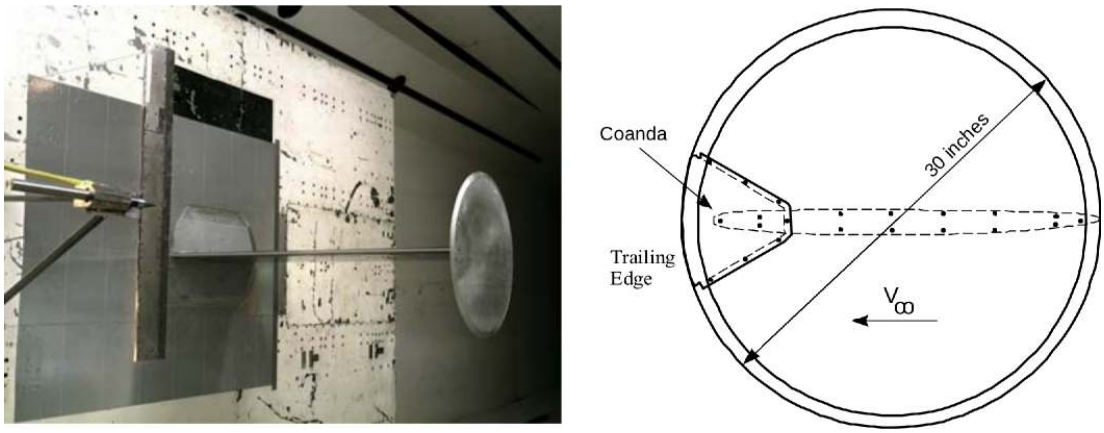

Figure 3.2: End plate diagram and experimental model photo in the NASA TDT wind tunnel [3].

along the midspan, taking into account the pressure, friction of all wall surfaces and additionally the pressure and momentum at the plenum boundary.

3.1.1 Boundary and initial conditions

Figure 3.3 shows the domain and boundary conditions used for the simulation, with parts highlighted in separate colours. The cylindrical farfield is 10 chords from the centre of the aerofoil in the radial direction and 7 chord lengths from the root in the spanwise direction. In comparison, the TDT upper and lower walls are 3.2 chord lengths from the centre of the aerofoil with the side wall 5.2 chord lengths from the root. A similar CFD study [96] used a cuboid shape domain with edges of length $22 \times 22 \times 10$ chord with the model in the centre of the domain.

The freestream flow conditions are summarised in Table 3.1. The Reynolds number is based upon the original chord length of the unmodified ellipse. All plots shown have been rescaled with the maximum length of the modified aerofoil with the elliptical Coanda device.

Table 3.1: Freestream flow parameters used in the simulations of the NASA 6% experiment.

Freestream Mach	0.3	0.8
Reynolds Number	1.0×10^6	2.5×10^6
Angle of Attack	3.0° & 6.0°	3.0°

3.1.2 Multiblock structured grid

Conclusions from preliminary two-dimensional studies suggested that the full 3D model geometry is required to be modelled for the simulations. Flow angle corrections were

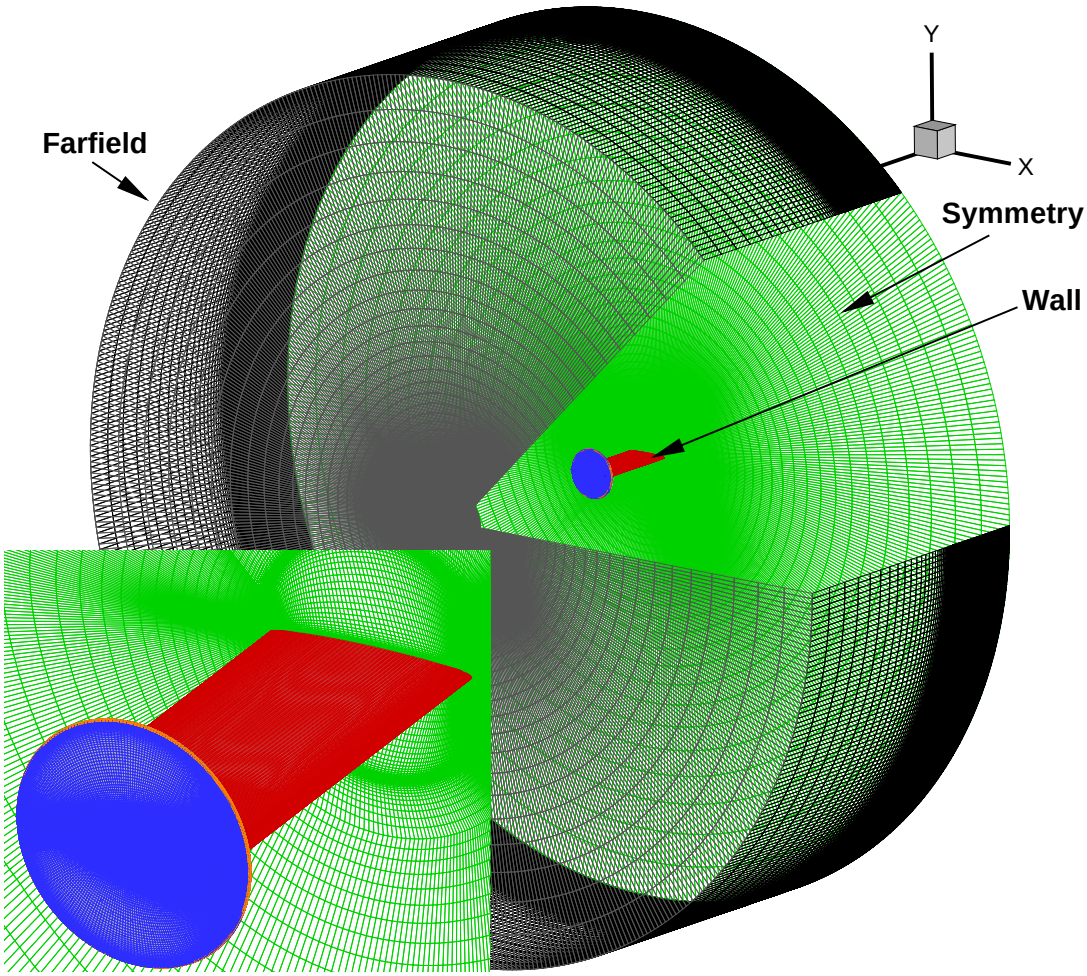

Figure 3.3: View of the computational domain showing the boundary conditions used.

necessary to achieve a fair agreement in two-dimensional cases without blowing, which is a manifestation of finite span and possibly wall interference effects. These two-dimensional simulations provided the initial guidelines for the topology and grid spacings for the following three-dimensional simulations.

The geometry allowed for an 'O'-type grid topology to be created, which can be seen in Fig. 3.4. The end plate is also shown in Fig. 3.4 which is 1.1 chord in diameter. Whilst the experimental setup had an end plate with a diameter of 1.0 chord, enlarging the plate for the simulations allowed for the structured blocks to wrap around the leading edge of the aerofoil while also resolving the flow around the end plate.

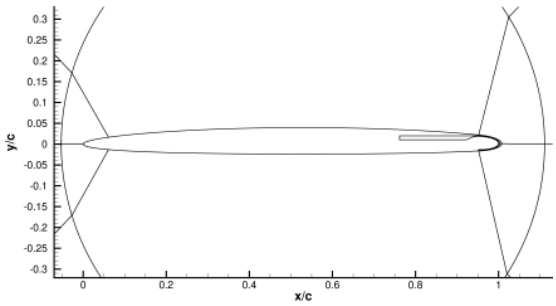

Figure 3.4: View of circular end plate and blocking topology in the near-field.

Grid refinement

Cruz and Anders [96] performed a study on the same baseline model but with the trailing edge designed to be used as a jet flap. A grid refinement study was conducted on this jet flap configuration which concluded that approximately 20×10^6 cell volumes were adequate to resolve the flow using an unstructured grid [96].

In preliminary two-dimensional investigations of the current study, a grid refinement study was performed which found that 384 cells around the aerofoil, 128 over the Coanda surface and 64 in the wall normal direction were adequate to resolve the flow for both unblown and blown configurations. This distribution was applied to the three dimensional grid, with 256 cells over the span of the aerofoil, 33 over the breadth of the end plate, and 64 between the end plate and the farfield. The total grid size for the finest grid with and without blowing were 27×10^6 and 28×10^6, respectively on a multi-block structured grid with approximately 230 blocks. The first grid point for the mesh had a wall-normal spacing of $y^+ \approx 1.0$ over most of the solid walls to resolve the viscous sub-layer of the boundary layer, but $y^+ \approx 2.0$ in the radial direction of the end plate to reduce computational expense.

This grid was coarsened such that the total number of cells were approximately halved between the fine and medium, and the medium and fine grids respectively (shown in Table 3.2). A refinement factor of approximately 0.8 along each block edge was used for each successive grid. The wall normal initial sizes on wall faces were retained from

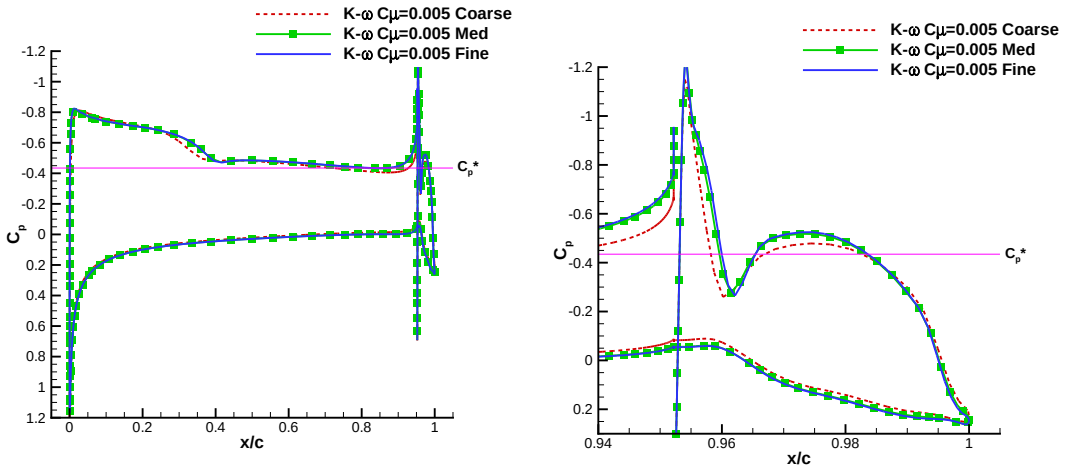

(a) Pressure distribution over the main aerofoil surface.

(b) Distribution over the Coanda surface.

Figure 3.5: Coefficients of pressure with blowing at $C_\mu \approx 0.0051$ for block structured grids with approximately 7 , 14 and 28×10^6 cells, using the standard $k-\omega$ turbulence model.

the fine grid. Along the nozzle exit, the fine grid has a uniform distribution of 64 cells with a height of $y^+ \approx 1.5$, determined from the freestream conditions. A uniform distribution was also maintained for the medium and coarse grids which gave a cell height along the slot of $y^+ \approx 1.9$ and $y^+ \approx 2.4$, respectively.

Figure 3.5 shows the results of the grid refinement study; which compares pressure coefficients between the coarse, medium and fine grids with blowing at $C_\mu = 0.0051$ at $M = 0.8$. There is negligible difference in the pressure distribution between the medium and fine grid on the upper surface of the aerofoil and the Coanda surface. As shown in Fig. 3.5a the shock position is predicted further towards the leading edge with the coarsest mesh, this is possibly due to the boundary layer being under resolved and as a result artificially high turbulent viscosity levels were produced. From this study, it was concluded that the resolution of the medium grid is sufficient to achieve grid independent results.

Splitter plate

Table 3.2: Grid sizes used throughout the study of the NASA test case.

Grid	Blown	Unblown
Coarse	6.94×10^6	
Medium	13.93×10^6	13.41×10^6
Fine	28.31×10^6	27.26×10^6
Visc Splitter	24.12×10^6	23.50×10^6

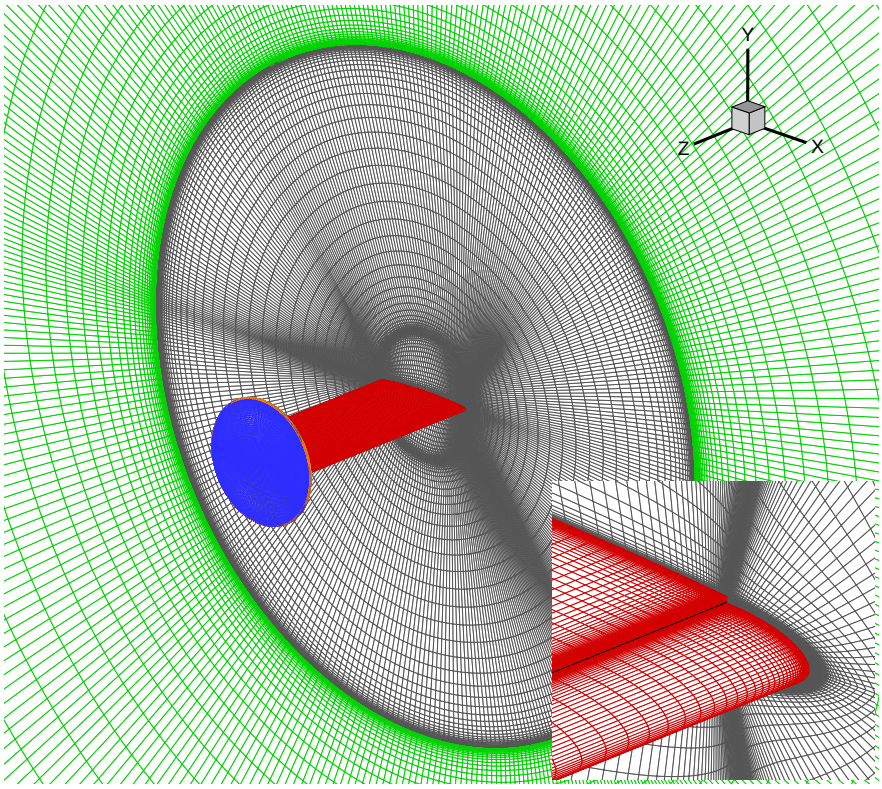

Figure 3.6: Grid including the viscous splitter plate.

The study on a jet flap configuration by Cruz and Anders [96] suggested that modelling of the viscous wall of the splitter plate was necessary for more accurate solutions. Starting from the medium grid described above, a circular splitter plate with a diameter of 6 chord lengths was incorporated. The original technical report [3] did not include the dimensions of the rectangular splitter plate used at NASA Langley, however Cruz and Anders [96] used a circular splitter plate with a 3 chord diameter. Including a larger splitter plate should create a thicker boundary layer on the splitter plate and so the effect of the splitter will be magnified.

The densities of the medium grid over the aerofoil and end plate were maintained for the grid with the splitter plate included. However, in order to resolve the flow over the splitter plate, the mesh required some refinement to account for the viscous effects of the splitter plate. Table 3.2 summarises the total cell count of the grid including the viscous splitter plate. The first cell normal to the splitter plate and along the circular edge had a length of $y^+ \approx 1.0$, this refinement can be seen in Fig. 3.6.

Figure 3.7a shows the effect of simplifications to the simulation. The unblown results show that modelling the flow as a two–dimensional problem is a poor assumption to replicate the experiment, since the shock position is poorly predicted and a large angle of attack correction was needed. With a splitter plate, the upper surface shock position moves forwards, bringing the predicted pressure distribution closer to the experimental

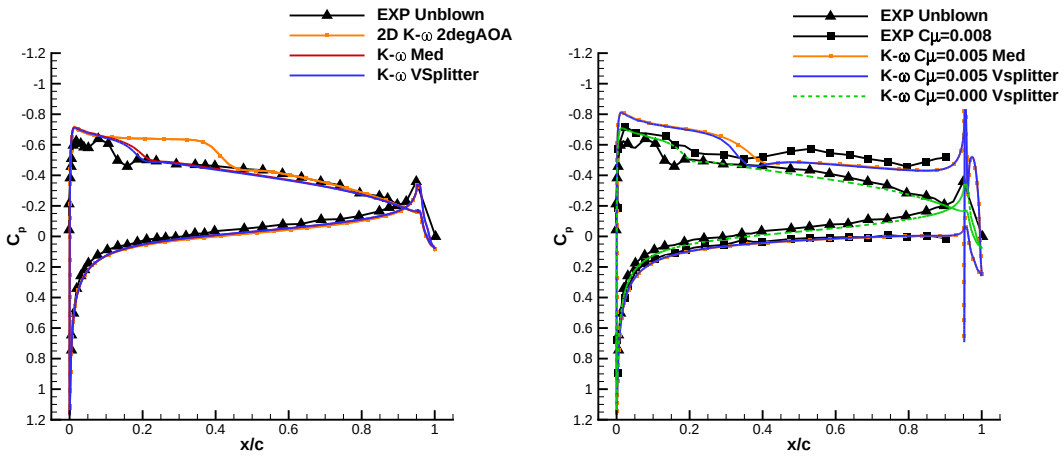

(a) Unblown case, comparing 2D and 3D simulations and the effect of a splitter plate.

(b) Comparing the effect of a splitter plate with blowing at $C_\mu \approx 0.0051$.

Figure 3.7: Pressure coefficients comparing the impact of simplifications to the model, with freestream conditions at $M = 0.8$ and $\alpha = 3.0$.

data. This is also the case for the lower surface pressure coefficients. The effects of the viscous splitter wall is highlighted in Fig. 3.8, which shows that the iso-contours of critical C_p* curve towards the viscous wall. The shock strength also appears to be lessened with modelling of the splitter plate. Although the blowing rate from the simulation is less than that shown from the experiment, the shock position moved further aft due to blowing than the experimental result, as shown in Fig. 3.7b. The effect of the splitter plate is more pronounced when blowing over the Coanda surface, the shock position on the upper surface of the aerofoil moves towards the leading edge by approximately 5% chord. Modelling the splitter plate seems to have little effect on the pressure distribution on the Coanda surface on sections about the mid span position where the experimental data was measured. It is expected that the overall predicted flow with the splitter plate is closer to the experiment, due to the effect of the splitter plate shown in Fig. 3.8. The results from Fig. 3.7 show that modelling this experiment with greater fidelity gives better agreement.

3.1.3 Results

Without blowing

Figure 3.9 shows the surface pressure coefficients about the mid span section of the aerofoil at Mach numbers 0.3 and 0.8 for an angle of attack at 6° and 3°, respectively. At $M = 0.3$ the lower surface pressure distribution gives good agreement with the digitised experimental data. The suction of the upper surface is over-predicted slightly in the leading 20% of the section, while the rear 80% gave more favourable agreement.

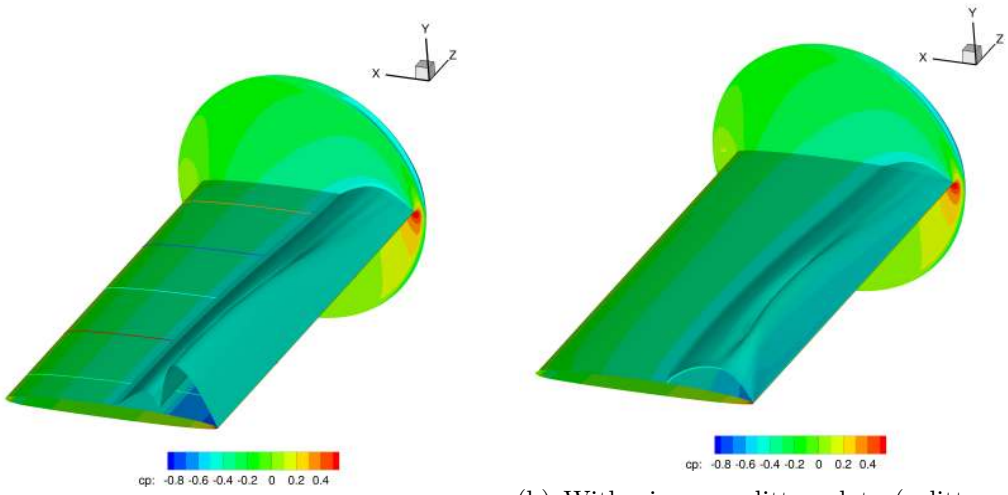

(a) Using symmetry plane.

(b) With viscous splitter plate (splitter plate not shown).

Figure 3.8: Isosurfaces of pressure coefficient at critical $C_p* \approx -0.43$ for $M = 0.8$, without blowing.

For $M = 0.8$, the simulated results show a slightly higher pressure level over the lower surface than the experiment, as shown in Figure 3.9. The difference in pressure coefficient appears to be constant over the aerofoil chord, possibly suggesting that some of the difference may be due to a slight angle of attack deviation, or perhaps a discrepancy in aerofoil shape. A shock is predicted on the upper surface at approximately 20% chord, while experimentally it is captured at 10%. This may be due to an under-prediction of the turbulence on the aerofoil upper surface. Figure 3.9 also shows the critical pressure coefficient for $M = 0.8$. The experimental model included a boundary layer trip strip [3] which promoted turbulent transition of the boundary layer and hence an increase in boundary layer thickness. This tripping effect was not modelled in the current study.

Low speed circulation control

With blowing and a $M = 0.3$ freestream, the predicted pressure coefficient on the lower surface for blowing at $C_\mu = 0.0343$ falls between the experimental data for $C_\mu^{exp} = 0.016$ and $C_\mu^{exp} = 0.054$, as shown in Fig. 3.10a. The upper surface has an over-prediction of the suction towards the leading edge, which results in a lower C_p than the experimental case at $C_\mu^{exp} = 0.054$. On the Coanda surface (Fig. 3.10b), the pressure distribution follows the trends of the experiment with blowing at $C_\mu^{exp} = 0.029$ and 0.042. A peak in pressure at approximately $x/c = 0.96$ is captured with reasonable accuracy by the simulation, the shift of this peak is also predicted for the higher blowing rate of $C_\mu = 0.058$.

Figure 3.11 shows a comparison of the predicted lift and drag coefficients compared

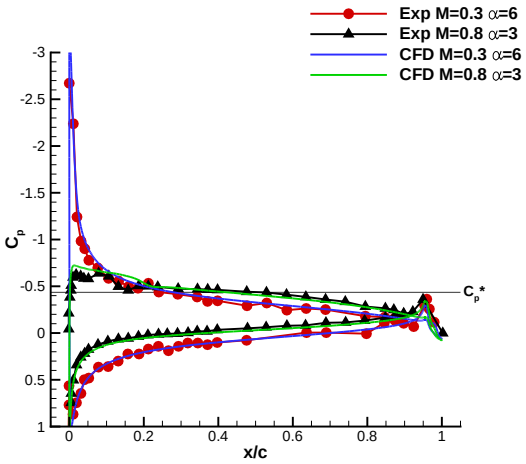

Figure 3.9: Unblown simulated vs experimental pressure coefficients for Mach 0.3 and 0.8 using the fine grid without the splitter plate.

with the experimental results for $\alpha = 3$ and $\alpha = 6$. Qualitatively, the predicted behaviour follows the trends as seen in the experiment. The drag coefficient was calculated in the experiments to include the thrust effects of the jet, as such the drag coefficient is seen to decrease with increasing jet blowing. For the numerical simulations the approach of Min *et. al.* [89] is followed here as given by Eq. (2.59). The lift coefficient, as shown in Fig. 3.11a, is in reasonable agreement with the experiment. The plateauing of the lift coefficient observed in the experiment is not completely captured by the CFD predictions. A shift in the positive C_μ axis appears to be the cause of this issue, which is also apparent in the drag coefficient behaviour (Fig. 3.11b). This shift may be explained by a small difference in the detail of the slot geometry. An over prediction of the baseline drag ($C_\mu = 0$) contributes to the relatively poor agreement in the predicted drag behaviour. However, the slope of the drag coefficient with respect to C_μ follows the trends of the experiment.

Transonic circulation control

Contours of Mach number along the centre span for the unblown and blown cases are shown in Fig. 3.12. The favourable pressure gradient caused by blowing over the Coanda appears to have reduced the thickness of the boundary layer on the upper surface of the aerofoil. Figure 3.12d shows the Mach contours for blowing at $C_\mu = 0.0051$, where the jet can be seen to be under expanding. A small separation bubble is present near the slot exit, caused by a shock wave due to the expansion of the jet flow. This separation bubble increases with further blowing. The Coanda flow re-attaches following the separation bubble, however it is expected that the jet will break away from the Coanda surface due to this shock for higher plenum pressure ratios.

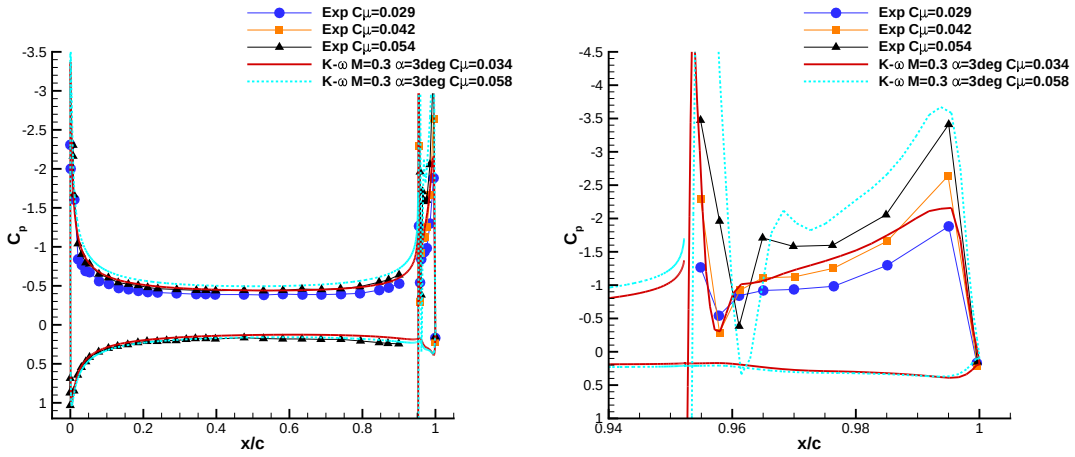

(a) Aerofoil surface.

(b) Coanda surface.

Figure 3.10: Comparing simulated pressure distribution at freestream conditions $M = 0.3$ and $\alpha = 3$ using the grid with the splitter plate.

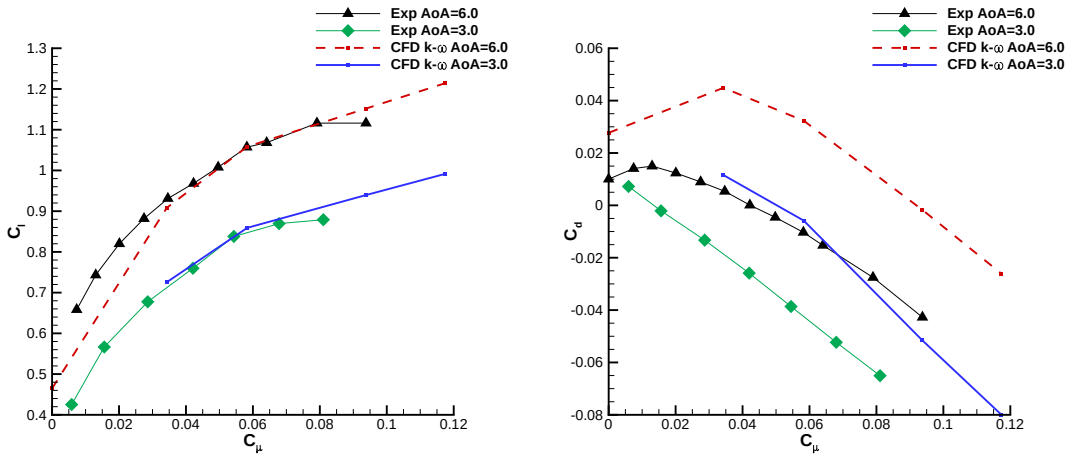

(a) Lift coefficient.

(b) Drag coefficient.

Figure 3.11: Sectional lift and drag coefficients versus C_μ for $M = 0.3$

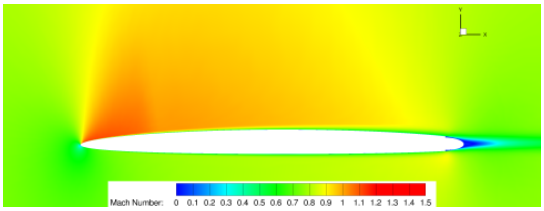

(a) Without blowing.

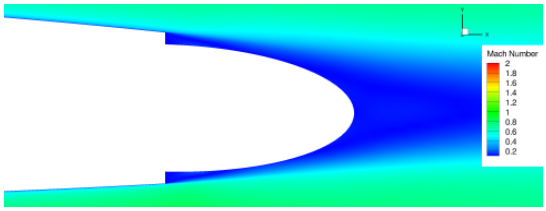

(b) Without blowing.

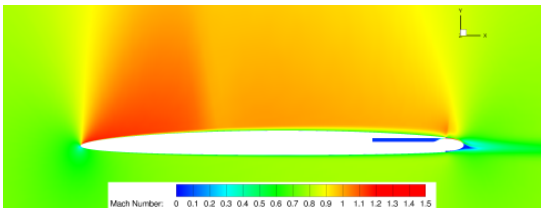

(c) Blowing at $C_\mu = 0.0051$.

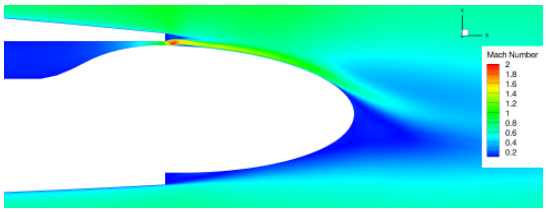

(d) Blowing at $C_\mu = 0.0051$.

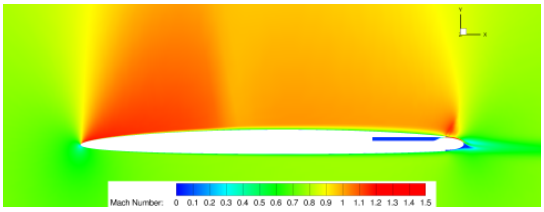

(e) Blowing at $C_\mu = 0.0069$.

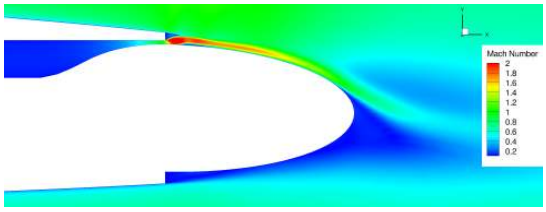

(f) Blowing at $C_\mu = 0.0069$.

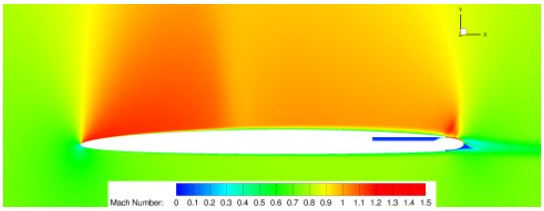

(g) SST blowing at $C_\mu = 0.0069$.

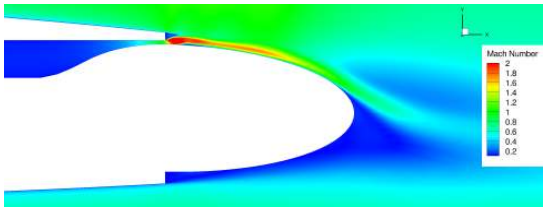

(h) SST blowing at $C_\mu = 0.0069$.

Figure 3.12: Contours of Mach number near the Coanda surface on the midspan slice for $M = 0.8$ and $\alpha = 3$, with the viscous splitter plate.

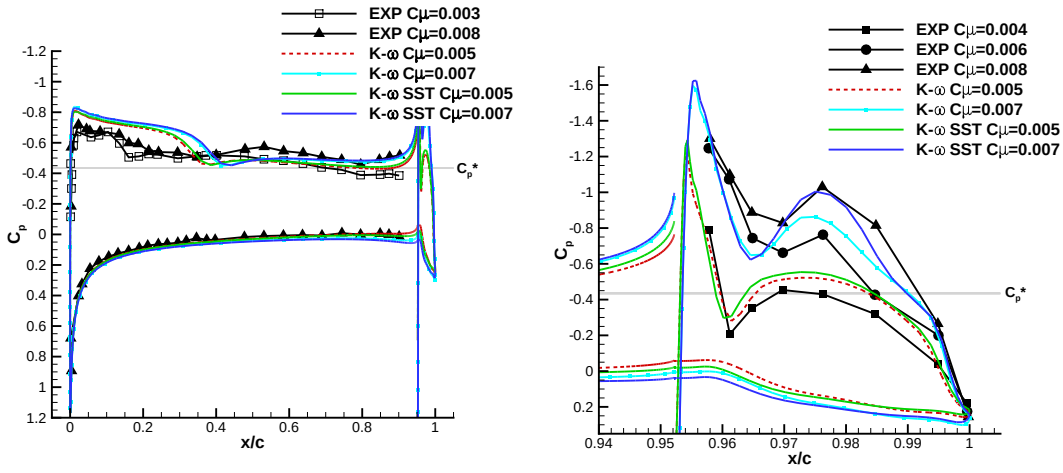

(a) Pressure distribution over the main aerofoil surface.

(b) Distribution over the Coanda surface.

Figure 3.13: Coefficients of pressure with blowing on the grid with the viscous splitter wall.

Figure 3.13 shows that there is little difference between the standard and the SST $k-\omega$ models at low blowing rates on the aerofoil surface. With blowing, the shock moves towards the trailing edge in both the experiment and with the numerical simulations, however the predicted shock location is approximately 20% chord further aft than was found in the experiment (Fig. 3.13a).

Figure 3.13b shows the pressure coefficient distribution over the Coanda surface with blowing. At $C_\mu = 0.0051$, the pressure over the upper surface of the Coanda resembles the distribution measured in the experiment with $C_\mu^{exp} = 0.004$. As the blowing rate increased to $C_\mu = 0.0069$, the pressure distribution over the Coanda surface is within the bounds of the experiment of C_μ^{exp} between 0.006 and 0.008.

For higher momentum coefficients, a difference between turbulence models appears on the Coanda surface (Fig. 3.13b), due to the effect of a difference in the detachment behaviour of the jet from the Coanda surface. Although the models are typically known to produce differences in behaviour in shock-boundary layer interactions: the standard $k-\omega$ model typically under-predicts the size of a separation bubble while the SST tends to over-predict the bubble size [52, 53], the shock boundary layer interaction created by the under-expansion of the jet did not significantly create differences between the models. The behaviour of the SST model in regions away from walls is similar to the $k-\epsilon$ model [71], which tends to perform well in free shear layers [97], which for the jet created over the Coanda surface could be expected to lead to a difference in the shock-shear layer interaction in the under-expanded jet.

A comparison of the behaviour of the EARSM, SST and $k-\omega$ turbulence models is shown in Fig. 3.14. On the main aerofoil section, the EARSM predicts a shock that

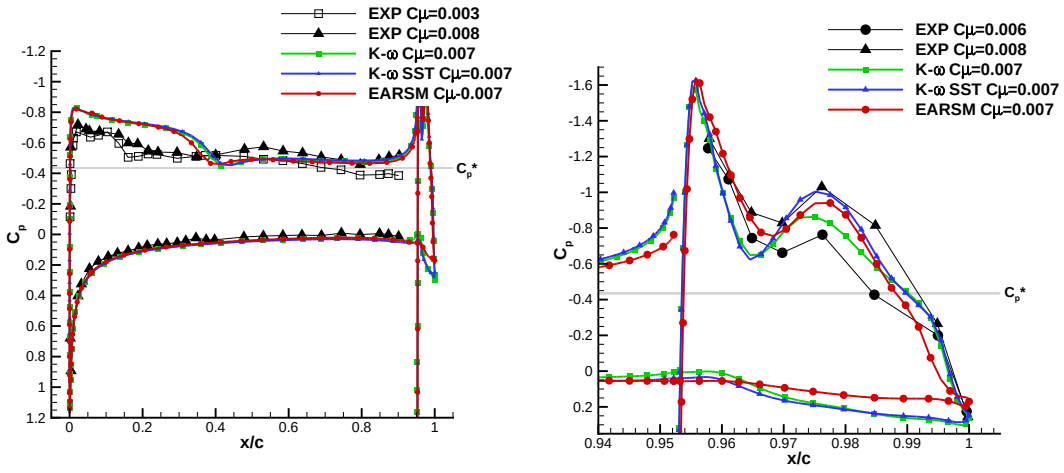

(a) Pressure distribution over the main aerofoil surface.

(b) Distribution over the Coanda surface.

Figure 3.14: Coefficients of pressure with blowing at $C_\mu = 0.007$ between EARSM, SST and $k-\omega$ turbulence models.

is forward of the SST and $k-\omega$ predictions, however the agreement with experiments in terms of shock position is still poor. Figure 3.14b shows the surface pressures on the Coanda surface, here the EARSM predicted a better pressure distribution in terms of the shock position at $x/c \approx 0.97$, however the three models perform similarly. Lower surface pressure coefficients were not presented in the report for this blowing rate, so an assessment of the accuracy of the predictions here is not possible.

Figure 3.15 shows a comparison between the experimental loads from Alexander *et. al.* and the predicted results. The lift coefficient is predicted well (Fig. 3.15a), demonstrating the onset of the stall behaviour of the jet. The lift augmentation $\Delta C_l/C_\mu$ however is slightly over predicted when compared with the experiment. The drag coefficient is predicted too high without blowing. However it was expected that with blowing the drag would decrease as was observed in the experiments. With blowing from CC, the shock moved significantly further aft which increased the lift, but also increased the drag due to the contribution of the body axis vertical force to the wind axis oriented drag. For an angle of attack of 3°, 5.23% of the vertical (with respect to the body axis) force contributes to the drag coefficient. Since the drag coefficient is small relative to the lift, this contribution has a large impact on the calculation of drag.

Shock capturing

Figure 3.16 shows the same data as Fig. 3.15 using symbols only, however body axis force coefficients are also shown as lines. A negligible difference between the lift and normal force coefficients was found, as shown in Fig. 3.16a. However, when converting

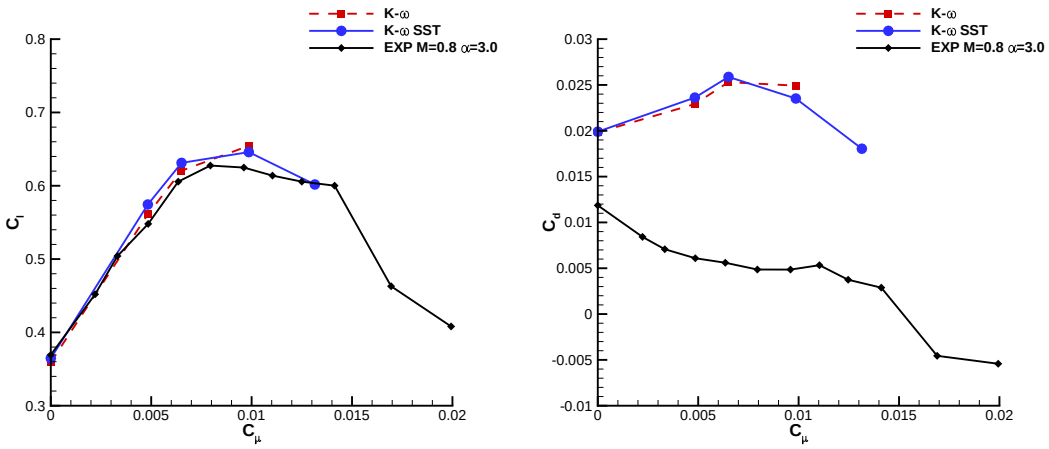

(a) Sectional lift coefficient

(b) Sectional drag coefficient

Figure 3.15: Sectional loads comparing predicted and experimental data with respect to the blowing rate C_μ.

the drag coefficient to the tangential force coefficient, the difference is approximately 0.02 for the case without blowing. Figure 3.16b shows that although the baseline tangential force was predicted inaccurately, the reaction of the force due to blowing decreased at a comparable rate to the experiment.

The poor capturing of the shock position had a significant effect on the prediction of the drag response with respect to blowing. The simulations performed here are more representative of a model in free air, while the experiment introduced blockage effects due to the wind tunnel. A closer agreement to the experimental results would be expected if the wind tunnel walls were modelled and resolved by the grid. Here, it would then be necessary to also have information about the wind tunnel wall boundary layers, inflow conditions and the behaviour of the flow through the slotted walls in the TDT. Researchers at NASA recently performed comparisons between CFD and experiments on a transonic aeroelastic test case in the TDT, and found that modelling the full wind tunnel geometry accounting for the slatted walls was necessary for accurate simulations [98].

3.2 Gregory-Smith Experiments - Stepped Supersonic Coanda Jets in Still Air

The experiments by Gregory-Smith [11] and Carpenter [10] provide the only examples of using a step to passively promote attachment of a supersonic jet to a Coanda surface. For this reason and since the two-dimensional model geometry by Gregory-Smith is well defined and has adequate flow visualisation and wall surface pressure measurements,

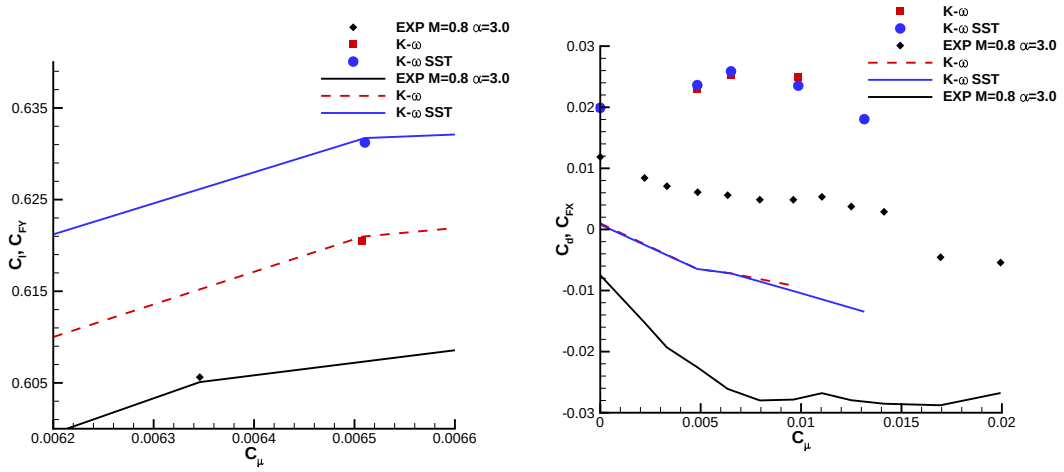

(a) Sectional lift and normal force coefficients

(b) Sectional drag and tangential force coefficients

Figure 3.16: Comparison of the wind (C_l,C_d in symbols) and body (C_{FY},C_{FX} in lines) axis force coefficients with respect to the blowing rate C_μ. Force coefficients were computed by $C_{FY} = C_l\cos(\alpha) + C_d\sin(\alpha)$ and $C_{FX} = -C_l\sin(\alpha) + C_d\cos(\alpha)$.

the experiments provides a useful validation test case to assess modelling requirements of predicting stepped supersonic Coanda jets.

Gregory-Smith [33] presented experimental work on a quasi–two dimensional planar Coanda model, which was shown in Fig. 1.11. The model had a $30mm$ circular Coanda radius for 100° from the slot exit, followed by a planar surface angled at 10° to match the local surface gradient. Two separate converging nozzles were manufactured, however surface pressures were shown from experiments using 'Nozzle A' which had a $8.1mm$ radius lip. The majority of results were published for a slot height of 4mm, giving a radius to slot height ratio of 7.23.

Following the studies of Gregory-Smith and Gilchrist [33], Gregory-Smith and Senior [11] investigated the effects of including a step between the slot exit and the Coanda surface. Results were published for a Coanda radius to slot height ratio of 7.5 and $step/radius = 0.05$, corresponding to a $4mm$ slot and a $1.5mm$ step for a $30mm$ radius. Although not explicitly stated in Ref. 11, the stepped model Coanda surface had the same dimensions as the earlier unstepped geometry [33], but modifications were made to incorporate a step [99].

In the experiments conducted by Gregory-Smith *et. al.*, the nozzle pressure ratio was defined as $NPR = p_\infty/p_0$ which is contrary to the typical definition of $NPR = p_0/p_\infty$ used in CC. To remain consistent with the published data, the nozzle pressure ratios in this section are presented as $NPR^{-1} = p_\infty/p_0$. Measurements of the surface pressures were conducted for both cases over a range of nozzle pressure ratios. Schlieren images and interferometry were also published for selected cases in the reports. For the models described above, detachment occurred at NPR^{-1}=0.251 for the unstepped

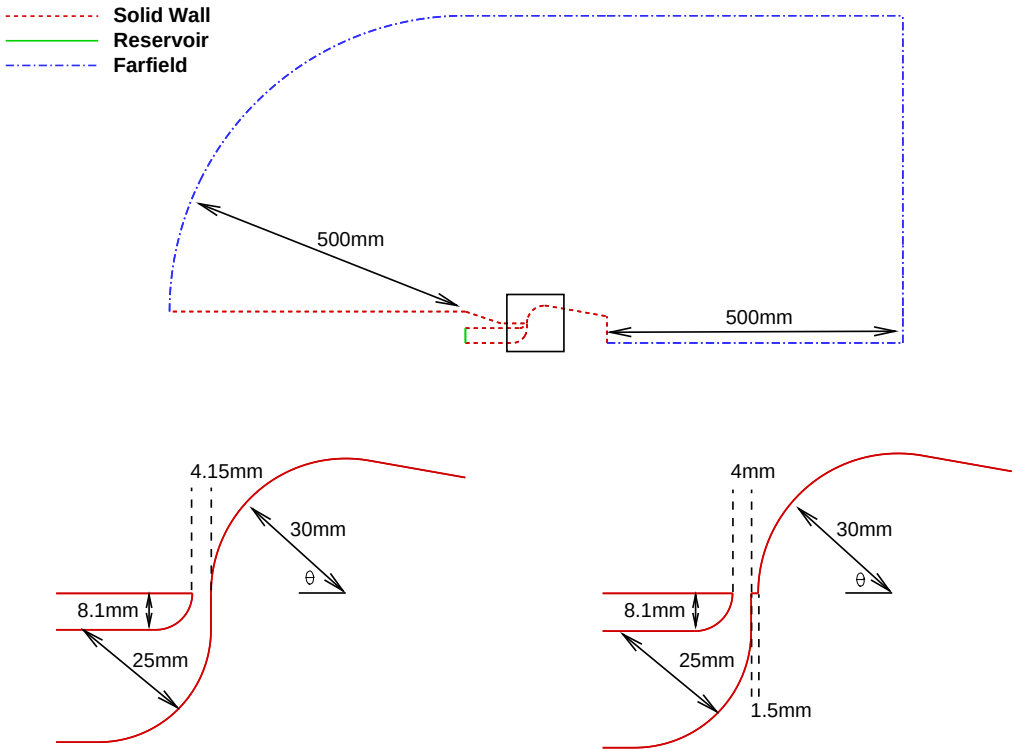

Figure 3.17: Boundary conditions and model geometry.

model [33], while with the step the jet remained attached until NPR^{-1}=0.203 [11].

3.2.1 Model and boundary conditions

Inset into Fig. 3.17 shows the model detail for the unstepped and stepped models considered in the present work. The unstepped model uses the same dimensions as 'Nozzle A' from Gregory-Smith [33] with a $4.15mm$ slot and $30mm$ radius, as described above. The stepped case is geometrically identical to the unstepped model, but with a $4mm$ slot and a step of $1.5mm$, as was used in Ref. 11.

A schematic of the boundary conditions used in the numerical simulation is shown in Fig. 3.17. A characteristic based farfield condition was placed at $500mm$ from the model. This condition allows for mixed sub–and–supersonic flow across the boundaries and fixes the necessary characteristic waves for subsonic outflows and inflows [100]. Solid no-slip walls were modelled for all walls, including the 'upstream' horizontal section leading towards the model from the left of the diagram. The 'downstream' horizontal section was set as a farfield to allow for the flow to exit the domain in the event that the jet remains attached to the planar wall of the model.

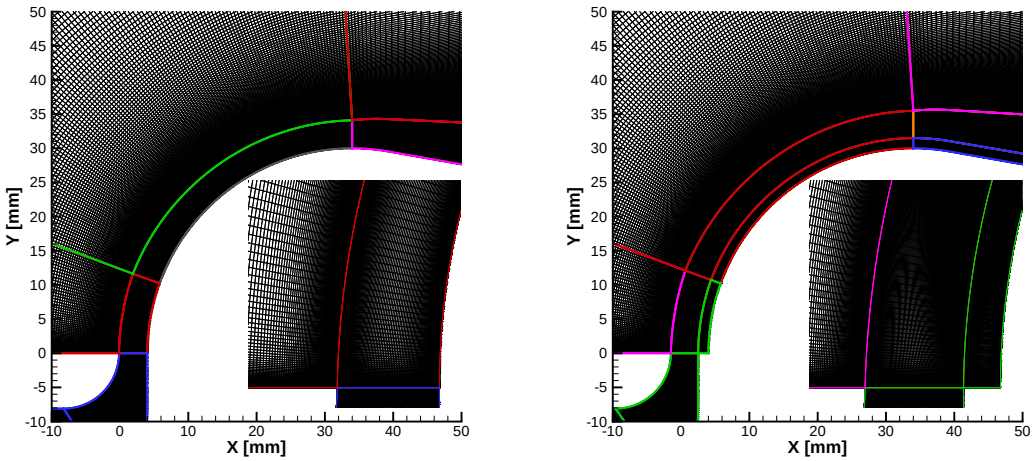

(a) Unstepped (b) Stepped

Figure 3.18: Computational grids for stepped and unstepped supersonic Coanda simulation without a freestream.

Grids

Figure 3.18 shows the grids and multiblock block structure in the vicinity of the Coanda surface for the cases with and without a step. A $y^+ = 1$ based on the Reynolds number at the slot height was employed at the nozzle exit and normal to all solid wall surfaces. The grid had 256 cells across the slot, 128 along the height of the step and 256 cells over the first 90° from the slot exit. The resulting grid had approximately 900,000 cell volumes in total.

Simulation conditions

Simulations were conducted at a Reynolds number per slot height of $Re = 1.5e^5$ and the grid length scaled to the slot height. The reference Mach number for simulations was $M = 1.0$, which is used to define the farfield pressure as $1/\gamma M^2$. The reference velocity for this choice of parameters corresponds to the speed of sound at the conditions in the farfield ($\approx 340ms^{-1}$), rather than the speed of sound at the slot exit.

Unsteady RANS simulations were conducted due to difficulties with convergence using steady state simulations. A non-dimensional time step of 0.1 was used corresponding to a physical time step of approximately $1.18e^{-6}$s, or a frequency of 850kHz. By contrast, Carpenter [10] measured the frequencies on a similarly proportioned axisymmetric model up to 80kHz.

Within each time step iteration the solution residual was reduced to $1e^{-3}$ and the result considered converged when the distribution of pressure on the Coanda surface is unchanged or periodic between solutions across approximately 3000 time steps. The focus of this study was the baseline time averaged flowfield to assess and validate the

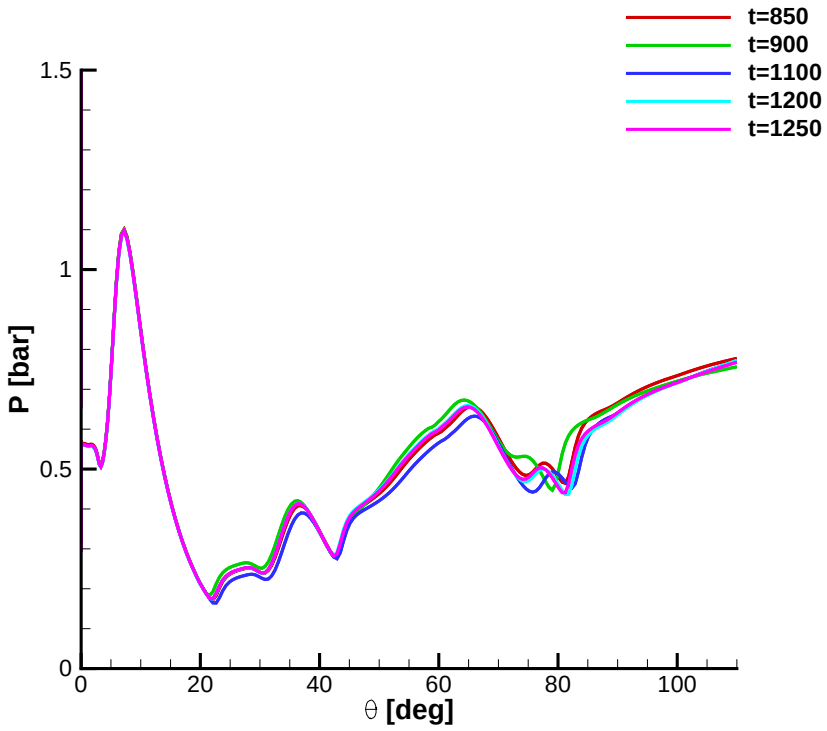

Figure 3.19: Snapshot of surface pressures over stepped geometry at $NPR^{-1} = 0.235$ during unsteady simulation.

turbulence modelling aspects of supersonic Coanda jets, rather than the local unsteady behaviour due to shocks and/or shear layer fluctuations. An example of the surface pressure on the Coanda walls with respect to nondimensional time step is shown in Fig. 3.19. Some unsteadiness is evident in Fig. 3.19, however for the purposes of evaluating surface pressures with the experimental data, the fluctuations remain within acceptable bounds.

A moderate and low NPR^{-1} case was considered here for comparison with the experimental results with and without a step. The low NPR^{-1} case for each geometry case correspond to the conditions at which the jet was near detachment during the experimental investigations. For these conditions surface pressures are available from the available publications, in addition to qualitative results such as interferogram and Schlieren plots. Comparisons were made between simulations using the Wilcox k-ω, Menter k-ω SST and EARSM turbulence models.

The plenum boundary condition provides a static (time independent) nozzle pressure ratio. Each simulation at a new NPR was initialised using the solution from a previous simulation, as such the pressure ratio does not continuously vary as highlighted in Fig. 3.20. Preliminary simulations concluded that due care was necessary with regards to increasing the plenum pressure (decreasing NPR); if the change in NPR is too large the jet can prematurely detach from the surface. As such, a substantial sweep of NPR

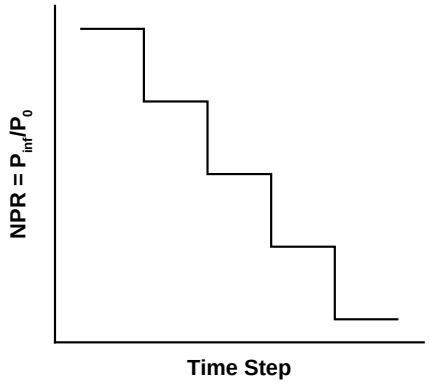

Figure 3.20: Example of setting plenum boundary condition.

cases were simulated to arrive from the moderate to the low NPR case.

3.2.2 Results

Without step

Figure 3.21 shows a comparison between measured and simulated surface pressures over the stepped and unstepped Coanda surfaces. Without the step a separation point occurred at 20° and 30° in the simulations indicated by a sharp change in surface pressures (Figs. 3.21a and 3.21c), this however was captured by the surface pressure measurements in the experiments. The EARSM model follows the unstepped experimental data points with reasonable accuracy with the exception of a local peak in pressure around 80° for both pressure ratios presented in Figs. 3.21a and 3.21c.

Figure 3.22 shows Mach contour lines for the unstepped case at NPR^{-1}=0.257. Here the Mach contours for the three different turbulence models are shown overlaid. The separation bubble in the EARSM simulation spanned approximately 50° from the initial separation point just before 25°. For the linear k-ω and SST Boussinesq models, the separation bubble was approximately 30°. In addition the separation point using the k-ω and SST was at 30° from the slot exit.

Solid black lines in Fig. 3.22b show the approximate path line for shock waves from these simulations. The oblique shock from the separation point using the EARSM model reflected from the shear layer at approximately 40°, this then reflected from the separation bubble at 55°. Contrary to this, the smaller separation bubble that was predicted using the linear models allowed the reflected shock to interact with the boundary layer at 60°, which is visible in the surface pressures of Fig. 3.21c.

Mach contours digitised from an interferogram were presented in Ref. 11 and are shown in Fig. 3.23 alongside Mach contours from the EARSM simulation at $NPR^{-1} \approx$ 0.3. The sonic line and separation point is predicted well by the simulation, while the

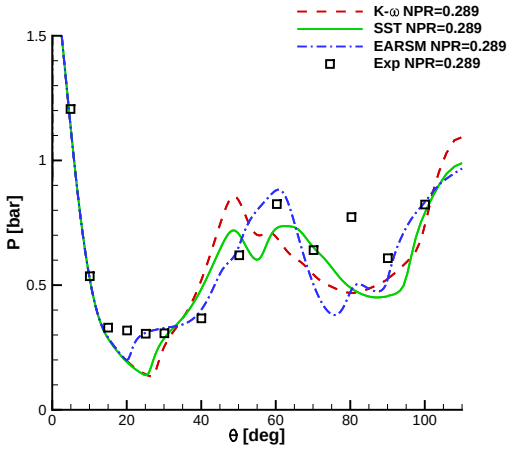

(a) NPR^{-1}=0.289 with unstepped model.

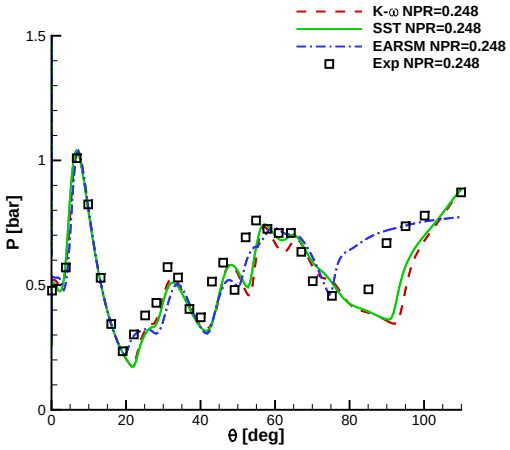

(b) NPR^{-1}=0.248 with stepped model.

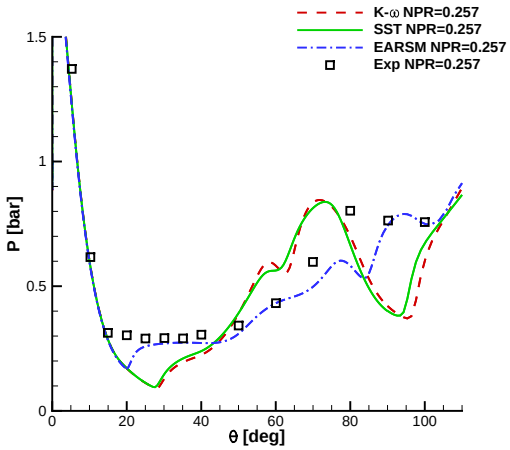

(c) NPR^{-1}=0.257 with unstepped model.

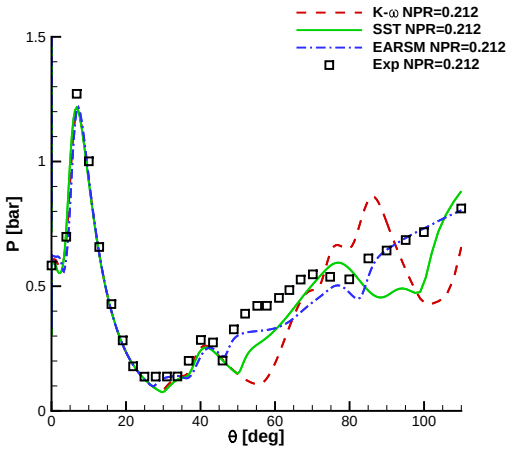

(d) NPR^{-1}=0.212 with stepped model.

Figure 3.21: Surface pressures for unstepped and stepped geometries at moderate (a, b) and low (c, d) nozzle pressure ratios. Low pressure ratios here correspond to the published surface pressure data for which the jet was close to detachment.

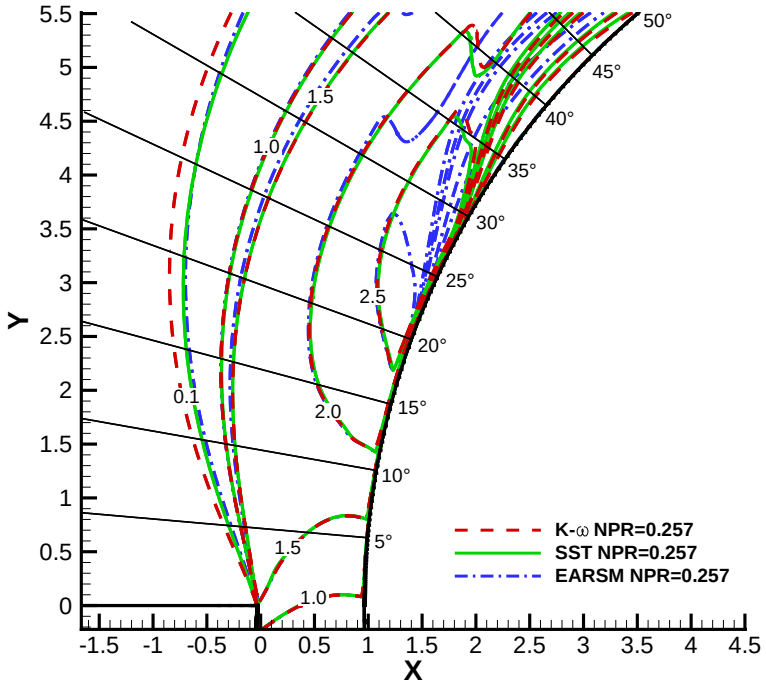

(a) Near slot exit

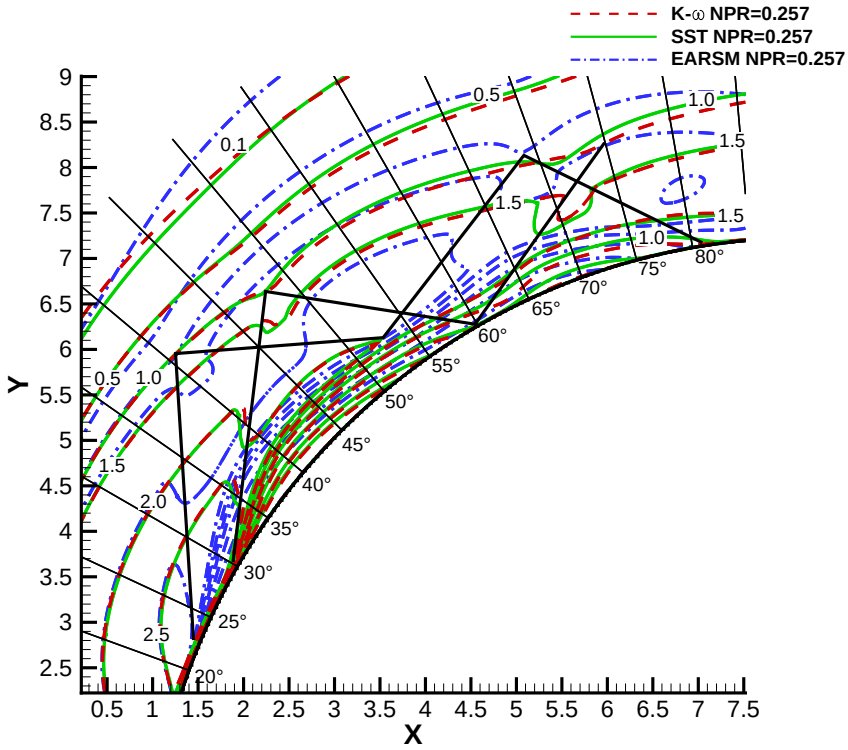

(b) From 20° to 85°

Figure 3.22: Comparison of Mach contours for three models without step $NPR^{-1} = 0.257$.

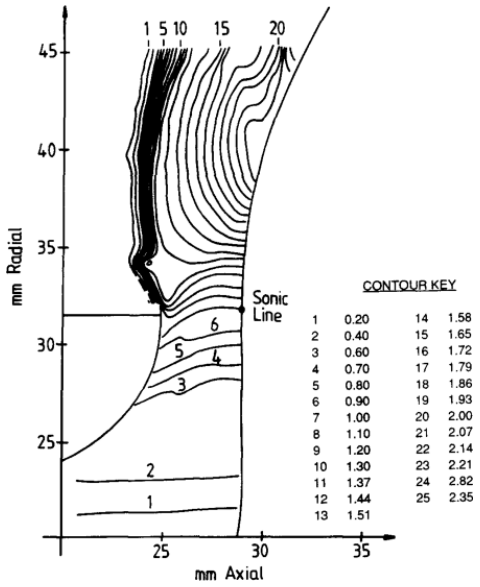

(a) Experiment

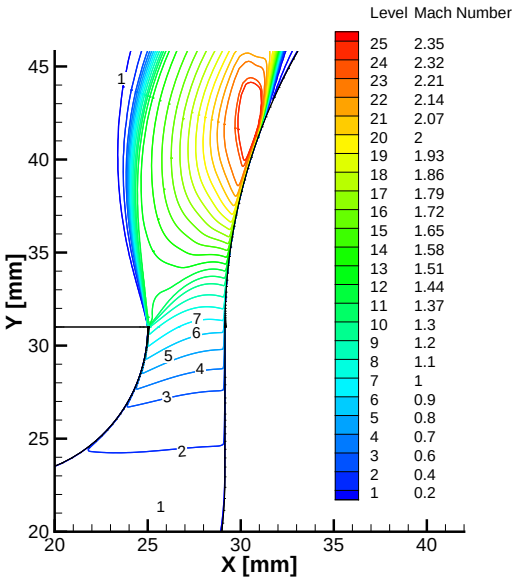

(b) EARSM

Figure 3.23: Comparison of Mach contours with experiment from digitised interferogram $NPR^{-1} \approx 0.3$.

experimental instantaneous image appears to have captured some vorticity or unsteadiness near the slot lip that was not present in the simulation.

With step

At $NPR^{-1} = 0.248$ all three turbulence models considered performed similarly up to 75° as shown in Fig. 3.21b. Contour plots of the flowfield are shown in Fig. 3.24, the reflections of waves between the Coanda boundary layer and shear layer are visible, as is the separation bubble that forms at approximately 30°.

At NPR^{-1}=0.212 small differences in the shear layer and shock boundary layer interactions in the first 30° contributed to larger differences further downstream. Figure 3.25 illustrates the differences between the predictions of the Coanda jet profile for each turbulence model. At 5° the expansion of the jet reached the Coanda surface, and a "reattachment shock" (Fig. 1.13) reflected towards the free shear layer. Differences in this reattachment shock were due to differences in the base flow shear layer and the attachment point of the jet (see Fig. 3.21d at 5°), the EARSM predicted an attachment point later than the $k-\omega$ and SST models.

Figure 3.25 also shows that the EARSM predicted a slower growth rate of the free shear layer, which is evident by the difference in length between the Mach contours at $M = 0.1$ and $M = 1.5$.

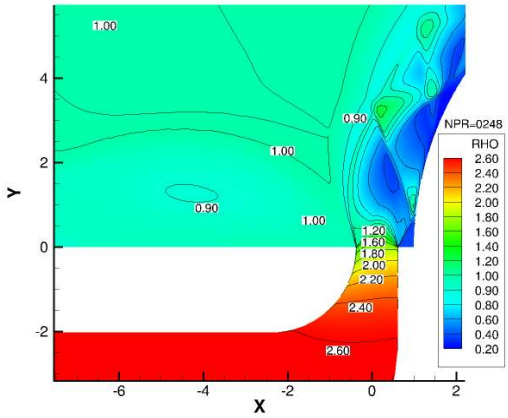

(a) Density $\rho = \rho^*/\rho^*_\infty$ ($\rho_\infty = 1$)

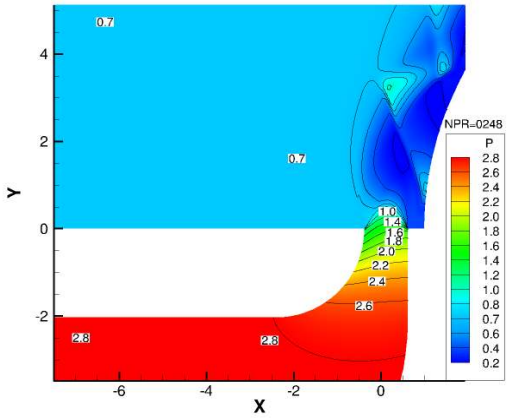

(b) Pressure $P = P^*/\gamma M^2_{ref}$ ($M_{ref} = 1$, $P_\infty = 1.0/\gamma$)

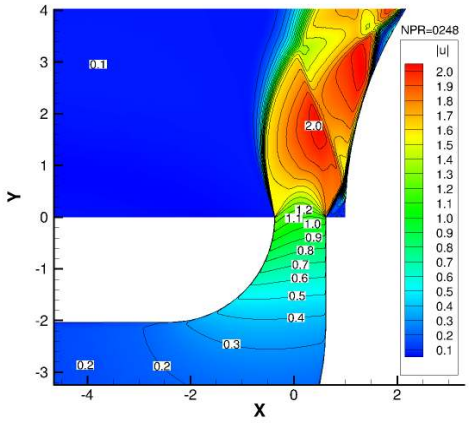

(c) Velocity Magnitude $u = u^*/u^*_{ref}$ ($u_{ref} = a_\infty$)

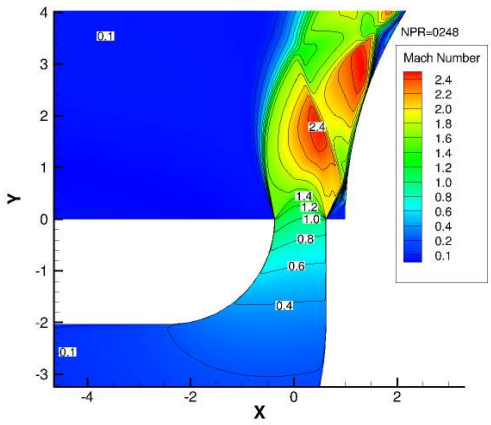

(d) Mach Number

Figure 3.24: Nondimensional Contour plots for NPR^{-1}=0.248.

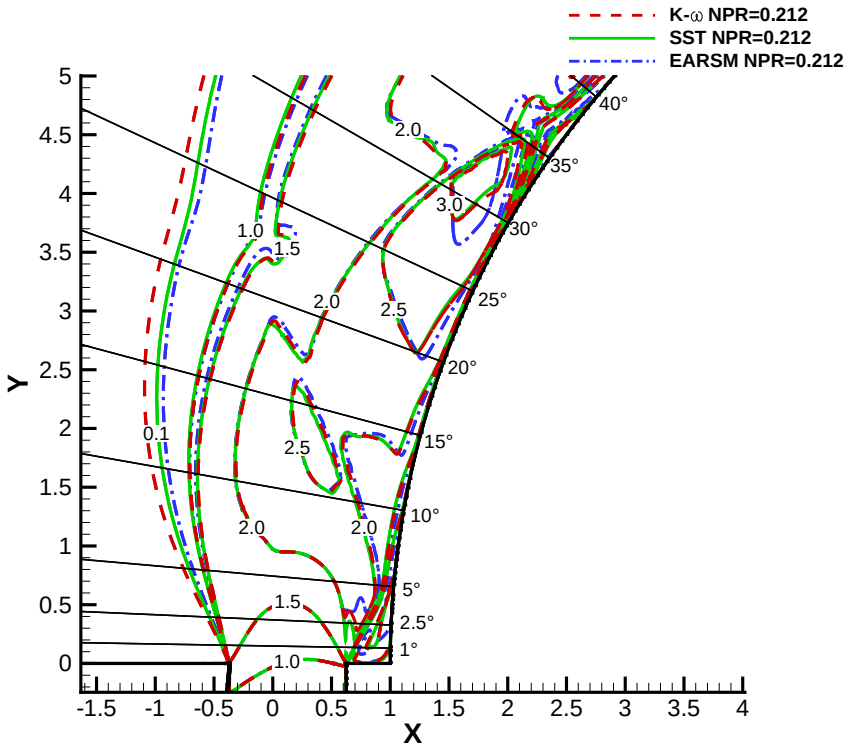

(a) Near slot exit

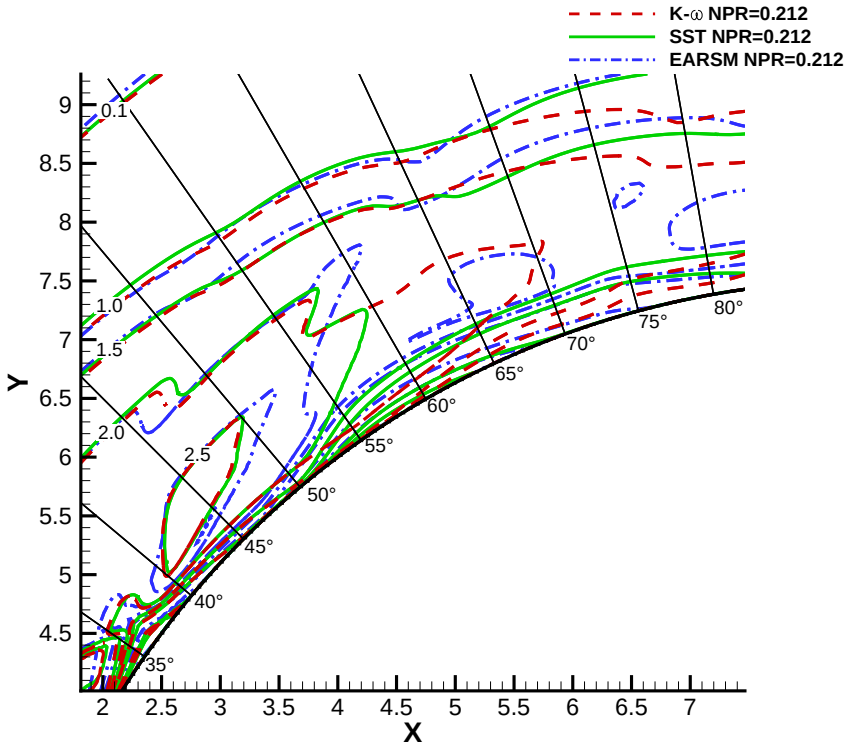

(b) From 35° to 80°

Figure 3.25: Mach contours near slot with step NPR^{-1}=0.212.

Reynolds stresses and viscous limiters

Figures 3.26 to 3.29 shows Mach and Reynolds stress profiles of the jet along slices normal to the Coanda surface at 5°, 20°, 25° and 35° for NPR^{-1}=0.257. As also shown in Fig. 3.22a, the significant difference between the three turbulence model predictions is in the growth rate of the free shear layer up to 20°. Here the difference in Reynolds stresses $u'u'$ and $v'v'$ at 5° highlight the anisotropy of in the EARSM turbulence model, here the anisotropy is the most pronounced. The difference in Mach profiles of the EARSM in Fig. 3.28 and the k-ω and SST models in Fig. 3.29 show the delay in prediction of the separation bubble by approximately 10°. The difference in the prediction of the separation bubble prediction is likely due to the anisotropy and highly variable coefficient of μ_t near the wall, rather than the free-shear layer anisotropy. Figure 3.30 shows the jet profile at 60°, here the separation predicted by the EARSM and the attachment by the other models is shown in the Mach contours.

The change in the limiter of the turbulent viscosity for the unstepped NPR^{-1}=0.289 case at 5° from the slot is shown in Fig. 3.26e. Here, while the coefficient of μ_t in the EARSM varies between 0.4 and 0.6, the limiter in the SST model is equal to 1 everywhere except the first 0.1mm from the Coanda surface. Later around the Coanda surface, this value is equal to 1 for all other positions around the Coanda surface.

Prediction of jet detachment

In the experiments, detachment occurred at $NPR^{-1} = 0.251$ for the unstepped model while with the step the jet remained attached until $NPR^{-1} = 0.203$. The plenum pressure for successive simulations was increased (decreasing NPR^{-1}) until detachment of the jet occurred. The method of increasing the plenum pressure that was used is shown in Fig. 3.20.

Figure 3.31 shows the surface pressures for the unstepped model. Here the SST model predicted a detachment at $NPR^{-1} \approx 0.227$, while the EARSM detachment occurred at $NPR^{-1} \approx 0.247$, corresponding to 10% and 2% error with the experimental observations, respectively. The k-ω model had failed to detach for $NPR^{-1} = 0.247$, but simulations were not continued to find the exact detachment point. With the step, the EARSM model predicted detachment with a 3% error with the experiment at a higher NPR^{-1} than the experiment (lower plenum pressure), while the SST remained attached until approximately 4% below (higher plenum pressure) the experimental detachment point of $NPR^{-1} = 0.203$ as shown in Fig. 3.32.

For both stepped and unstepped cases, a sudden change in surface pressures highlights that the attachment of the jet is a binary mechanism whereby the jet is either completely attached to, or detached from the Coanda surface but without an intermediate state. Other supersonic Coanda studies have observed a hysteresis in the jet

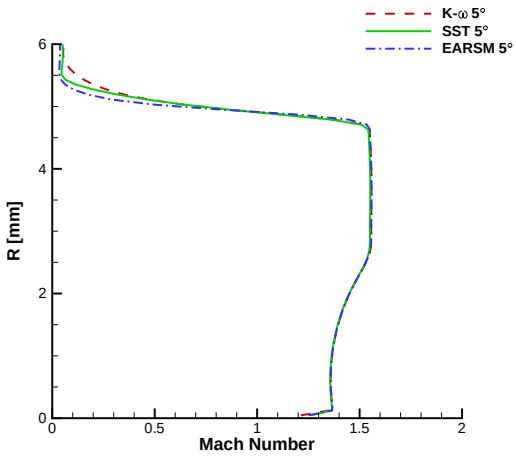

(a) Mach Number

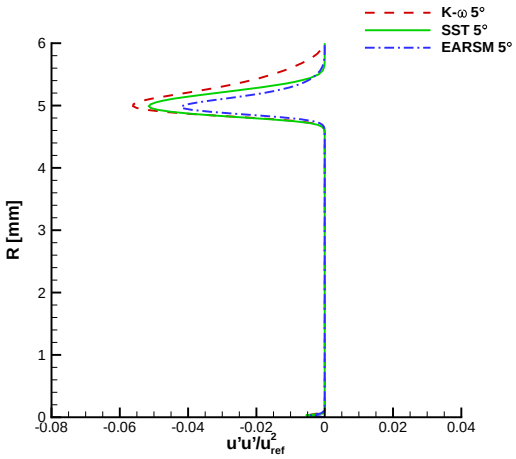

(b) $u'u'/u_{ref}^2$

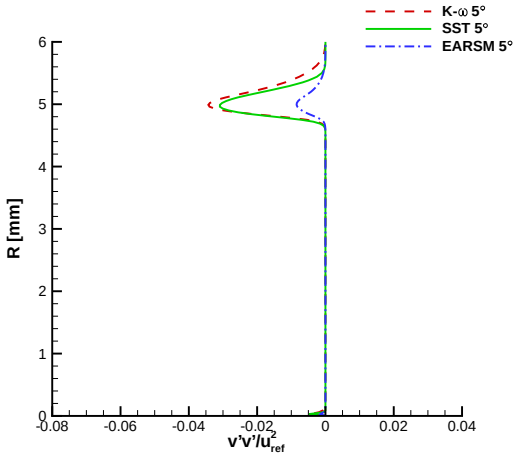

(c) $v'v'/u_{ref}^2$

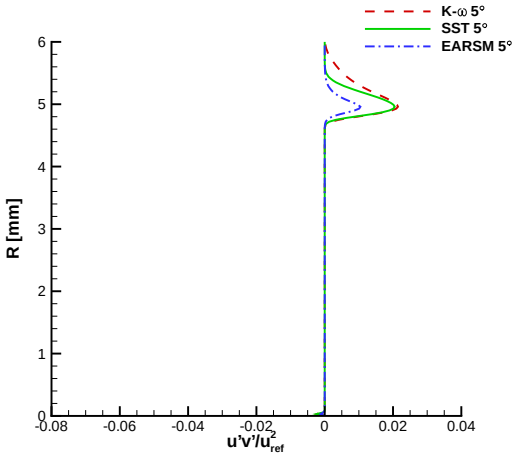

(d) $u'v'/u_{ref}^2$

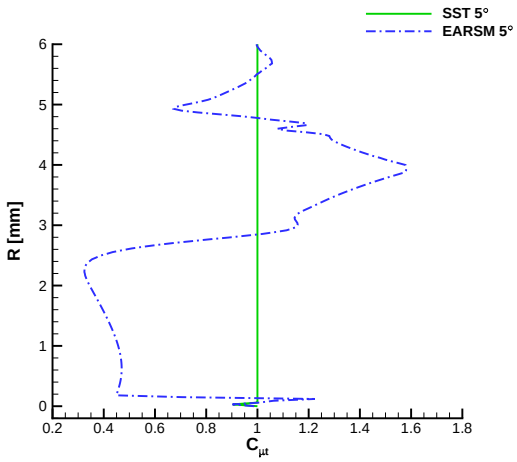

(e) Coefficient of μ_t

Figure 3.26: Mach, Reynolds Stress and coefficient of μ_t profiles without step at 5° for NPR^{-1}=0.257.

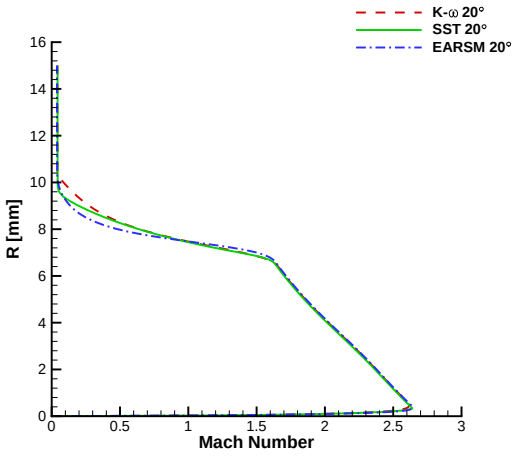

(a) Mach Number

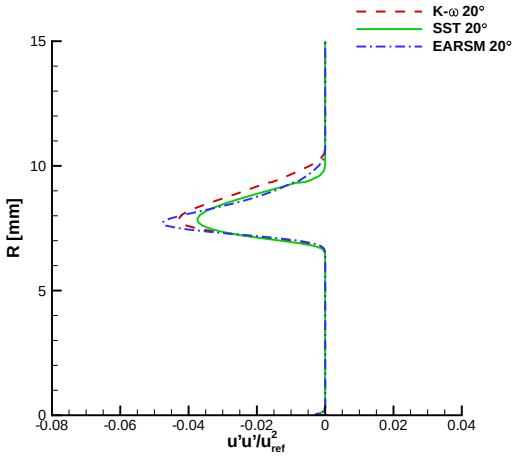

(b) $u'u'/u_{ref}^2$

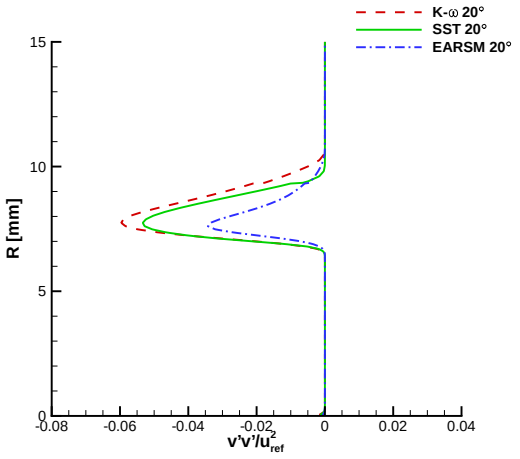

(c) $v'v'/u_{ref}^2$

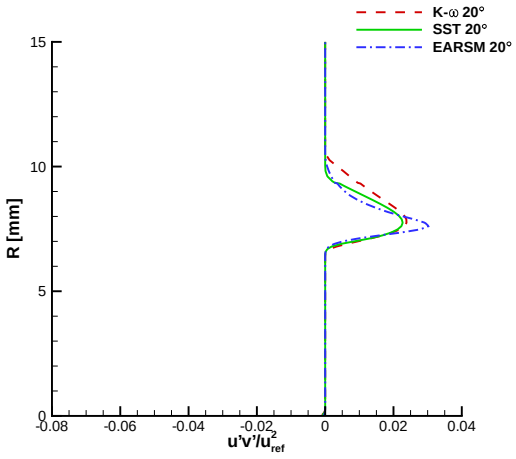

(d) $u'v'/u_{ref}^2$

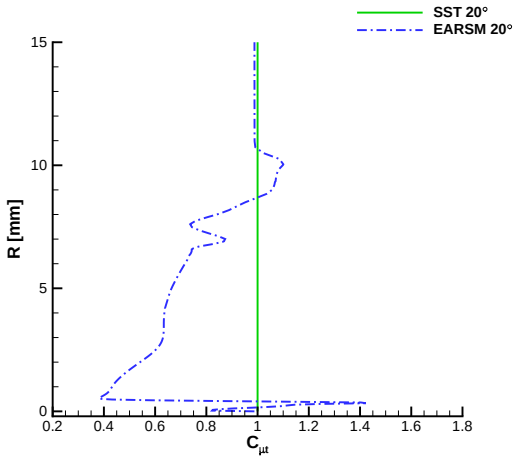

(e) Coefficient of μ_t

Figure 3.27: Mach, Reynolds Stress and coefficient of μ_t profiles without step at 20° for NPR^{-1}=0.257.

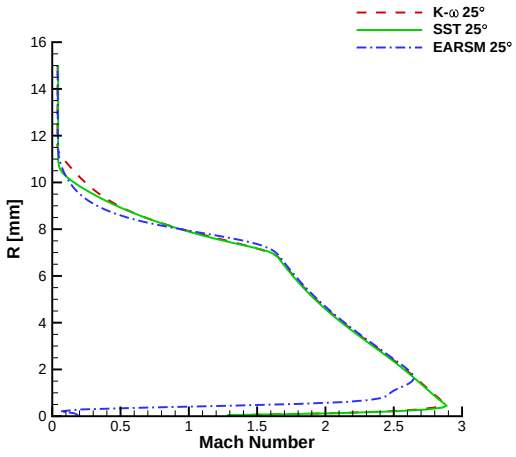

(a) Mach Number

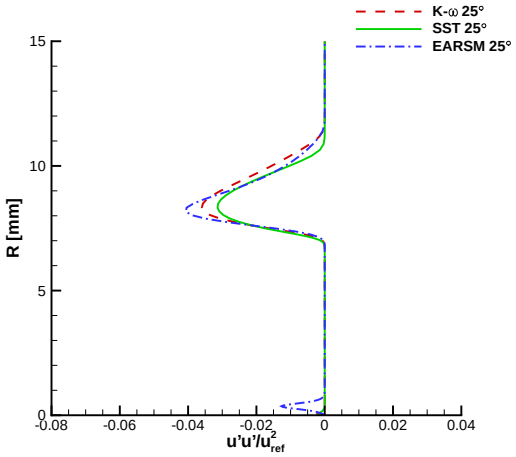

(b) $u'u'/u_{ref}^2$

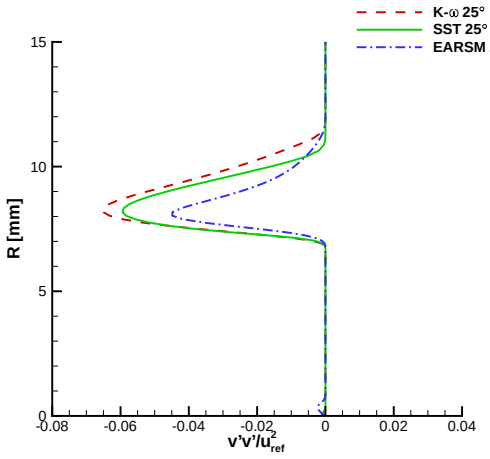

(c) $v'v'/u_{ref}^2$

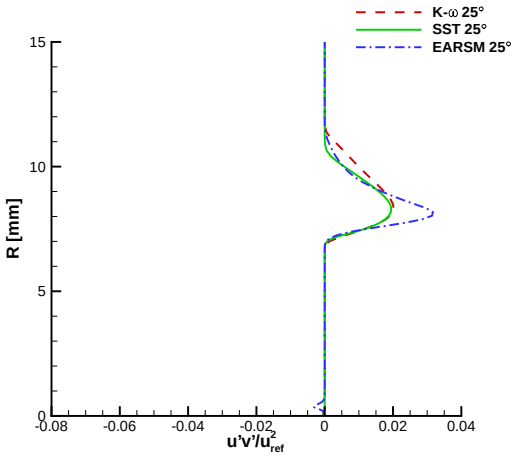

(d) $u'v'/u_{ref}^2$

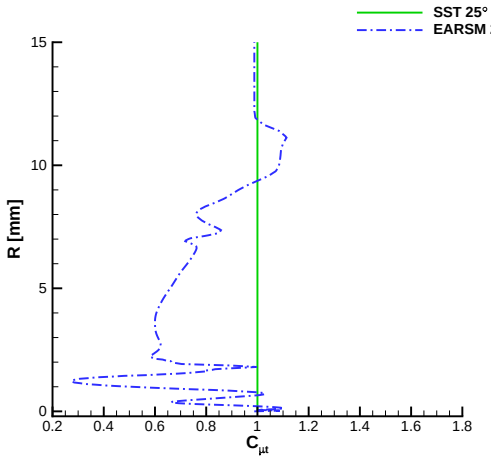

(e) Coefficient of μ_t

Figure 3.28: Mach, Reynolds Stress and coefficient of μ_t profiles without step at 25° for NPR^{-1}=0.257.

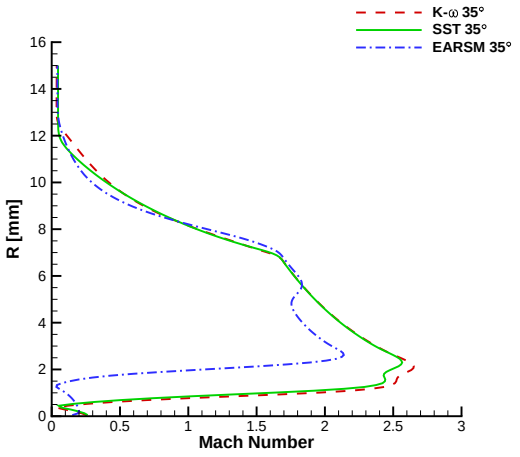

(a) Mach Number

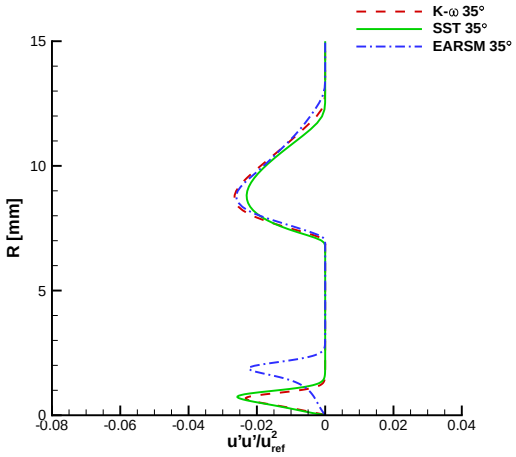

(b) $u'u'/u^2_{ref}$

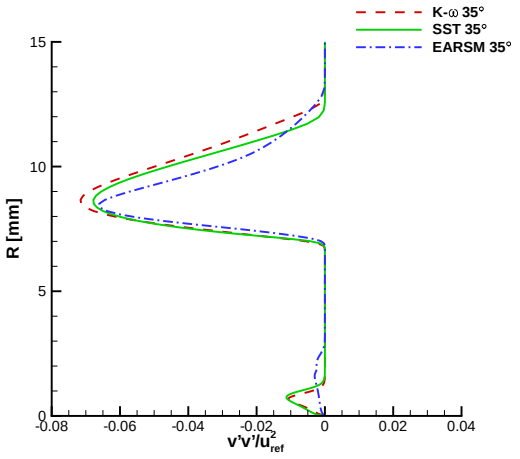

(c) $v'v'/u^2_{ref}$

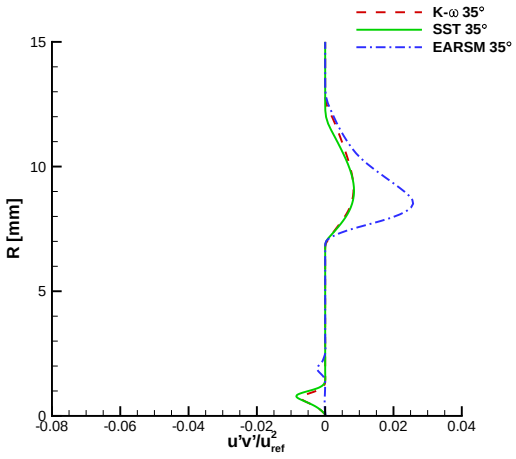

(d) $u'v'/u^2_{ref}$

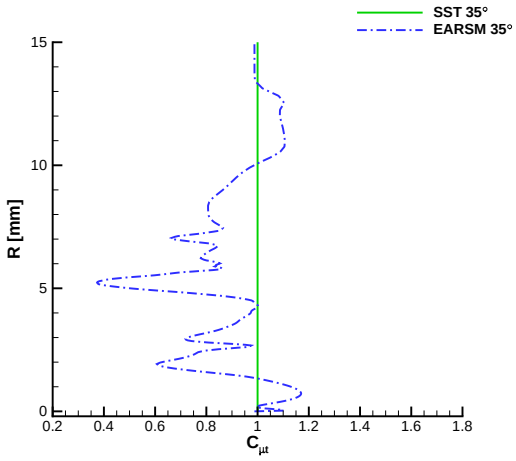

(e) Coefficient of μ_t

Figure 3.29: Mach, Reynolds Stress and coefficient of μ_t profiles without step at 35° for NPR^{-1}=0.257.

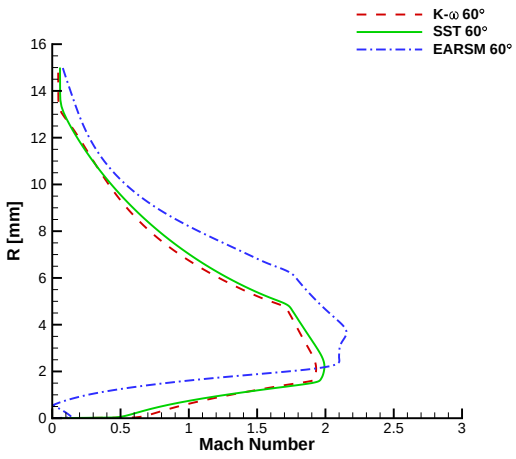

(a) Mach Number

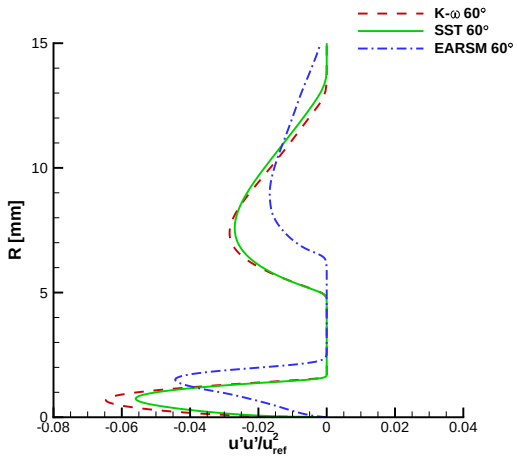

(b) $u'u'/u_{ref}^2$

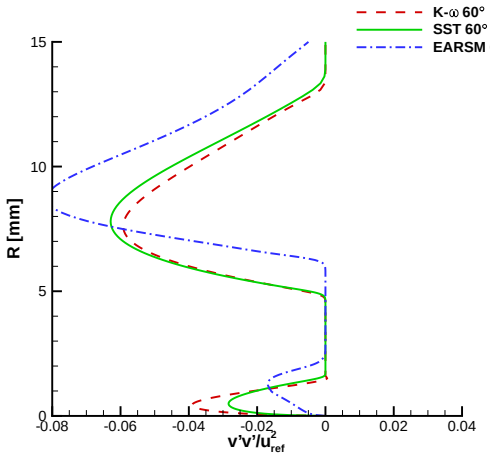

(c) $v'v'/u_{ref}^2$

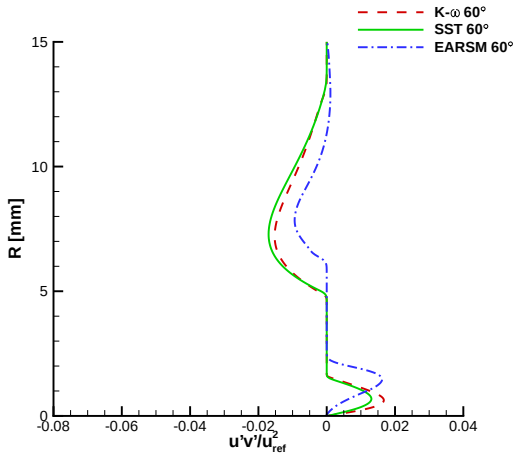

(d) $u'v'/u_{ref}^2$

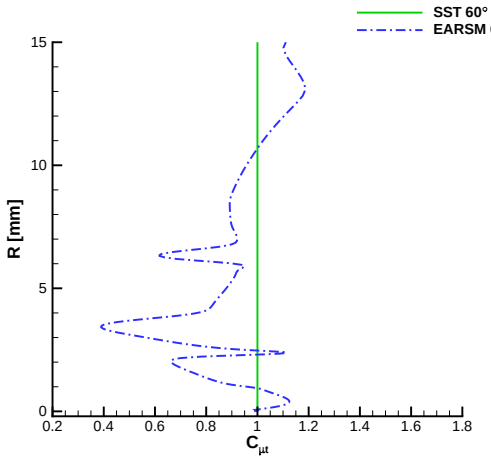

(e) Coefficient of μ_t

Figure 3.30: Mach, Reynolds Stress and coefficient of μ_t profiles without step at 60° for NPR^{-1}=0.257.

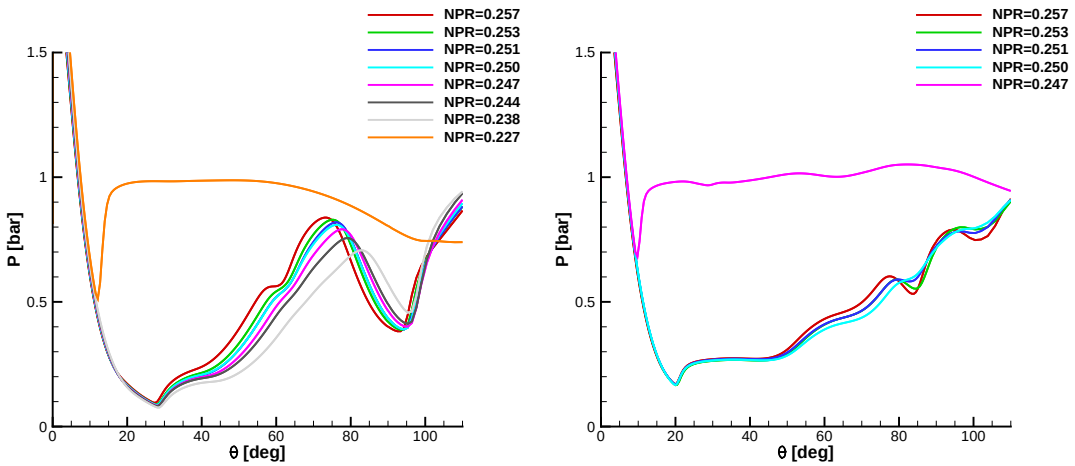

(a) SST

(b) EARSM

Figure 3.31: Surface pressures at successive nozzle pressure ratios until detachment. Unstepped model $h = 4.15mm$, $R = 30mm$. Experimental detachment occurred at $NPR^{-1} = 0.251$.

attachment and detachment. This hysteresis may also be present in the cases considered here, however the modelling of this behaviour has not been conducted.

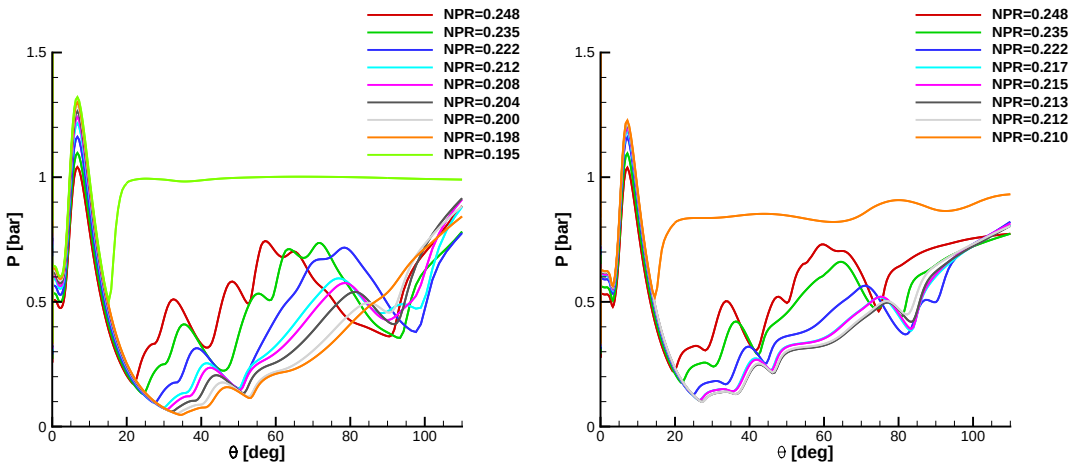

(a) SST (b) EARSM

Figure 3.32: Surface pressures at successive nozzle pressure ratios until detachment. Stepped model $h = 4mm$, $s = 1.5mm$, $R = 30mm$ Experimental detachment occurred at $NPR^{-1} = 0.203$.

3.3 Summary of Results

This chapter contained investigations into the simulation of supersonic Coanda jets for two different geometries. The first provided comparisons against experiments conducted for a circulation control wing at freestream speeds up to $M = 0.8$. In addition a study of the modelling of supersonic Coanda jets with and without a step was conducted.

For the transonic test case, the surface pressures on the Coanda surface are in reasonably good agreement with the experimental results. However the shock position on the upper surface of the main aerofoil section was predicted fairly poorly. As a result of the poor shock prediction and movement of the shock with respect to blowing, the slope of the drag response to blowing was positive in the CFD predictions while it was negative in experiments.

The results showed that modelling this experiment in 3D, including the effects of the splitter plate at the wing root, gave the best agreement with the experiment with regards to shock position on the upper surface and and pressure distribution on the lower surface. In the experiment a trip strip was used, which could (partially) explain the discrepancies with the CFD predictions, as the CFD results are consistent with a thinner boundary layer than in the experiment. For blowing however the shock was found to move too far aft in the CFD simulations. The pressure distribution on the Coanda were generally found to agree well with the experiment for moderate blowing rates.

Without more detailed experimental measurements, it is difficult to identify the culprit for this poor agreement. The transition position of the boundary layer may

be affecting the boundary layer thickness and therefore the shock position. The shock position on this model is sensitive to leading edge geometry and freestream conditions. This was demonstrated in the experimental study by Schlecht and Anders [9], where a small changes in the leading edge radius and camber affected the shock position by approximately 25%. Numerical simulations on this model with a jet flap in transonic conditions by Cruz and Anders [96] showed a sensitivity in shock position by a 1% change in free steam Mach number. Although for a different test case, recent aero elastic simulations replicating an experiment performed in the NASA TDT found that it was necessary to use an accurate CAD model of the tunnel and also allow flow to pass through the slotted walls in order to predict the shock position correctly [98].

For the supersonic Coanda jet cases without a freestream, the EARSM gave the most reliable results in terms of surface pressure predictions. This was due to the location of the initial separation bubble on the surface of the Coanda being predicted with a smaller error. It is unclear from the results whether this improved prediction is due to the boundary layer modelling, shear layer modelling or a combination of these differences with the traditional two equation k-ω models. Again here, experimental studies of supersonic Coanda jets with measurements of flowfield properties and Reynolds Stresses such as the experiments performed in Refs 52, 101 would be extremely valuable. For transonic freestreams, it would appear that these differences in modelling the supersonic Coanda jet using the EARSM do not cause a major effect in the prediction of the flow over the aerofoil, as shown in Fig. 3.14. The apparent increase in accuracy due to the EARSM was achieved with an approximately 15%-20% increase in computational cost relative to the SST model.

Both the SST and EARSM models predicted the detachment of the Coanda jet with reasonable accuracy, the SST predicted a detachment at higher plenum pressures than the EARSM. Without a freestream k-ω model failed to predict a detached jet for the conditions considered here. The k-ω and SST models performed similarly over the full Coanda surface in terms of Reynolds Stresses. The EARSM predictions of the Reynolds Stresses showed anisotropy in the free shear layer near the slot, but also varied the coefficient of μ_t which changed the predictions of the shock boundary layer interactions and, as plenum pressures were increased, changed the prediction of the jet detachment.

Chapter 4

Design Study of Coanda Devices for Transonic CC

This chapter is contained within of Ref. 102, preliminary results were also presented in Ref. 95. Here we intend to consider CC as applied to a supercritical aerofoil section, which has not been conducted so far at transonic conditions. Firstly, the predictions of the flow over the aerofoil with and without a simply hinged aileron will be compared against experimental results published in the AGARD database [103]. The same aerofoil model will then be modified to allow for a comparison of different CC devices and their effectiveness when compared with a traditional control device.

4.1 Transonic Flow Over a Supercritical Aerofoil with Aileron Deflection

The supercritical McDonnell Douglas DLBA032 aerofoil section (Fig. 4.1) was chosen from the AGARD CFD validation database [103] due to the availability of experimental data with an aileron deflection in a transonic freestream. The DLBA032 is a supercrit-

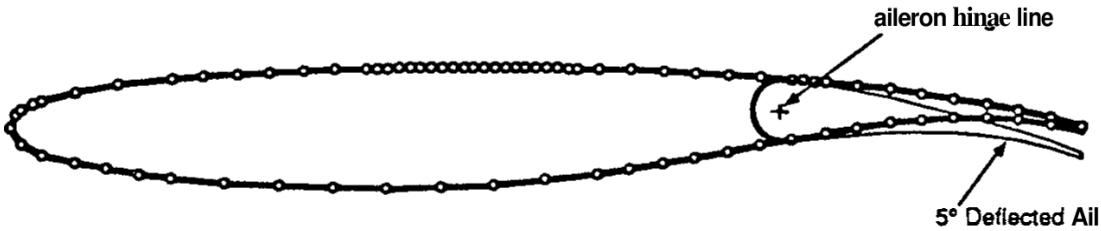

Figure 4.1: Douglas DLBA032 geometry [103].

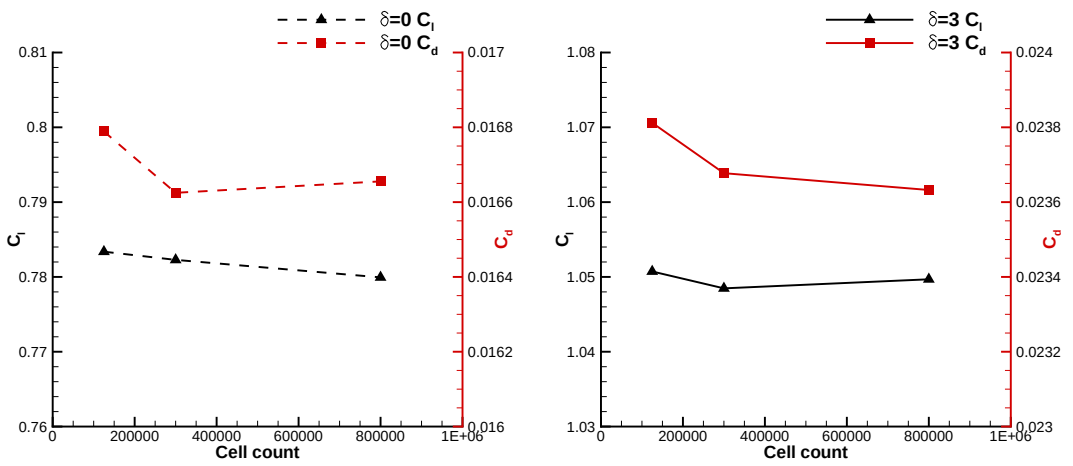

Figure 4.2: Effect of grid refinement on lift and drag for simulations of the DLBA032 with (solid lines) and without (dashed) a $\delta = 3°$ aileron deflection. Here $M \approx 0.715$, $Re = 5 \times 10^6$ at angles of attack of $\alpha = 1.183°$ with deflection and $\alpha = 1.342°$ without aileron deflection.

ical aerofoil with a thickness of 12% chord and an aileron of 25% chord length. Experiments were conducted at a Reynolds number range of $Re = 5 \times 10^6$ to $Re = 25 \times 10^6$, an aileron deflection of $\delta = -5°$ to $\delta = 5°$ and $M \approx 0.72$. To promote transition in the experiments, a boundary layer trip was placed at $x/c = 0.15$ and $x/c = 0.28$ on the upper and lower aerofoil surfaces, respectively. This trip was not taken into account for the present simulations, where a fully turbulent flow was assumed.

Two dimensional simulations were conducted on this geometry since the original dataset was reported to be suitable for such modelling approaches [103]. The data presented in the AGARD report included corrections regarding the wind tunnel interference. Grids were built using mesh densities and refinement strategies using conclusions from preliminary grid refinement studies of the DLBA032 with flap deflection, which is summarised in Fig. 4.2. The conclusions of this grid refinement study, indicated that approximately 300,000 cells were sufficient to produce grid independent results for both deflected and undeflected aileron cases. The following cases apply these findings with grids generated such that $y^+ \approx 1$ initial grid spacing in the wall normal direction is applied, as required by the $k - \omega$-type turbulence models employed.

Figure 4.3 shows the pressure distributions for the DLBA032 with an un-deflected aileron (Fig. 4.3a) and a deflection of 3° (Fig. 4.3b). Without the deflection the lower surface pressure distribution predictions agree well with the experimental data, and the shock location is within 5% chord (Fig. 4.3a). The upper surface suction is greater than the experiment, however the overall trend agrees. Table 4.1 shows that with the SST model, the change in lift is approximately 3% above the measured lift from the experiment.

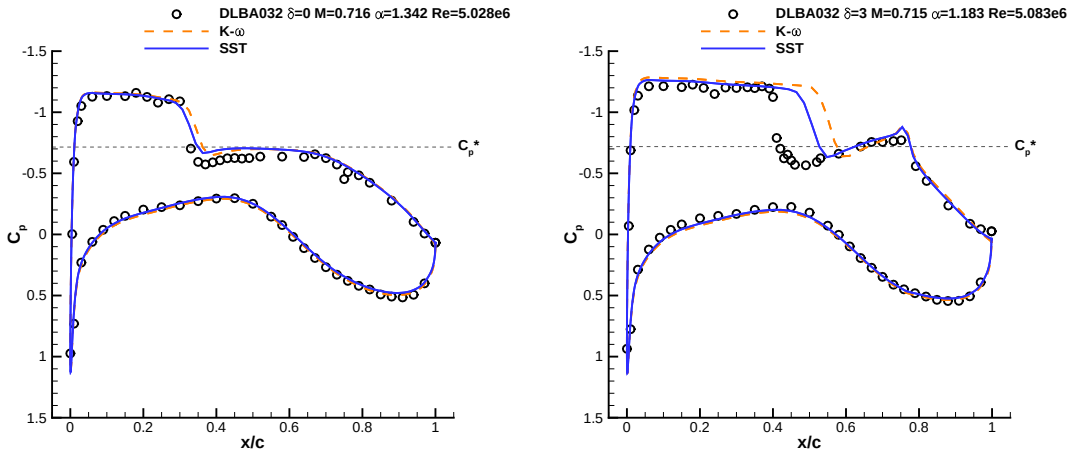

(a) Without deflection, $\alpha = 1.342°$.

(b) 3° aileron deflection, $\alpha = 1.183°$.

Figure 4.3: Experimental and predicted pressure distribution for the DLBA032 with and without aileron deflection at $M \approx 0.715$, $Re = 5 \times 10^6$.

With the deflected aileron, the suction near the leading edge is over-predicted, and the shock is predicted approximately 15% aft of the experiment, as shown in Fig. 4.3b. A similar finding was found by Londenberg [104] for $Re = 5 \times 10^6$ with a 2° aileron deflection. The agreement in the lift coefficient as shown in Table 4.1 is approximately 11% above the experimental data, due to the poor prediction of the shock location.

The data provided within the AGARD dataset used here was provided having been corrected for floor, ceiling effects and sidewall boundary layer effects. It is emphasised however in the AGARD report that there is some uncertainty about the correction methods employed and that the dataset should be taken for qualitative trends [103]. The conditions used in simulations here use the angle of attack, Mach and Reynolds numbers as given in the dataset.

Table 4.1: Comparing sectional lift, drag, and pitching moment behaviour of the DLBA032 at $M \approx 0.715$ and $Re \approx 5 \times 10^6$ with and without aileron deflection.

Configuration	Turbulence model	C_l	C_d	C_m
EXP $\alpha = 1.342°$ $\delta = 0°$		0.7311	0.01044	-0.1518
CFD $\alpha = 1.342°$ $\delta = 0°$	k-ω	0.7823	0.0167	-0.1614
CFD $\alpha = 1.342°$ $\delta = 0°$	SST	0.7593	0.0158	-0.1567
CFD Unblown Coanda $\alpha = 1.342°$	k-ω	0.8251	0.0183	-0.1710
CFD Unblown Coanda $\alpha = 1.342°$	SST	0.8071	0.0175	-0.1672
EXP $\alpha = 1.183°$ $\delta = 3°$		0.8931	0.01416	-0.1787
CFD $\alpha = 1.183°$ $\delta = 3°$	k-ω	1.0460	0.0236	-0.2073
CFD $\alpha = 1.183°$ $\delta = 3°$	SST	0.9942	0.0221	-0.1962

4.2 Evaluation of Coanda Designs in Transonic Flow

The DLBA032 was modified to include a Coanda device by increasing the thickness of the trailing edge along the camber line. The rear 30% of the aerofoil was thickened symmetrically around the camber line, changing the trailing edge thickness from 0.55% in the baseline aerofoil to 1.23% to accommodate a Coanda surface. Figure 4.4 shows the modified aerofoil geometry with a CC device.

The first CC device considered here used a circular Coanda surface with a 0.5% chord radius and 0.05% chord slot height (10:1 Coanda radius to slot height ratio). The design allowed for slots on the upper and lower surface, however the current investigations use upper slot blowing exclusively, see inset Fig. 4.4. Between the slot and upper surface of the aerofoil, a thickness of $t = 0.06\%$ chord was applied as a skin thickness. This skin thickness was maintained for all subsequent shape modifications to ensure comparisons between geometries which were not affected by a change in this parameter.

This sensitivity study considers four different Coanda designs to evaluate the effects of shock boundary layer interactions and the radius of curvature induced detachment of the jet. To assess the influence of the curvature at the slot exit, a Coanda geometry was designed with a larger Coanda radius to slot height ratio (21:1). Converging and converging-diverging nozzles were used to assess the effects of underexpanded and fully expanded Coanda jets on CC. In addition, a stepped geometry with a converging nozzle was investigated to assess whether findings by Gregory-Smith and Carpenter [10, 11] can be applied to CC with a transonic freestream. The descriptions of the Coanda devices used in this study are summarised in Table 4.2 and Fig. 4.5, all other geometric features remain the same between the four designs.

To establish that the modifications made to the DLBA032 did not significantly change the behaviour of the aerofoil, the unblown case was compared with the undeflected aileron over a range of angles of attack. Figure 4.6 shows the pressure coefficients and drag polars for the DLBA032 without aileron deflection and with an unblown CC device fitted as shown in Fig. 4.4. The shock position of the CC geometry is slightly further aft which induces greater lift than the original shape as shown in Table 4.1. The shape of the lift-drag polar in Fig. 4.6b suggests that the effects of the

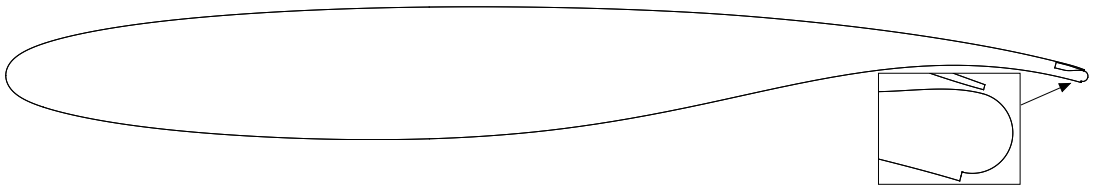

Figure 4.4: Modified geometry with CC device.

Table 4.2: Trailing edge device details (dimensions in % chord).

CC Device	Radius (r)	Slot Height (h)	Step Height (s)	Skin (t)	Nozzle Type
10:1 Convg	0.500%	0.050%	0.000%	0.060%	Converging
21:1 Convg	0.525%	0.025%	0.000%	0.060%	Converging
21:1 Condi7	0.525%	0.025%	0.000%	0.060%	Converging–diverging designed for NPR=7
20:1:1 Step	0.500%	0.025%	0.025%	0.060%	Converging with step

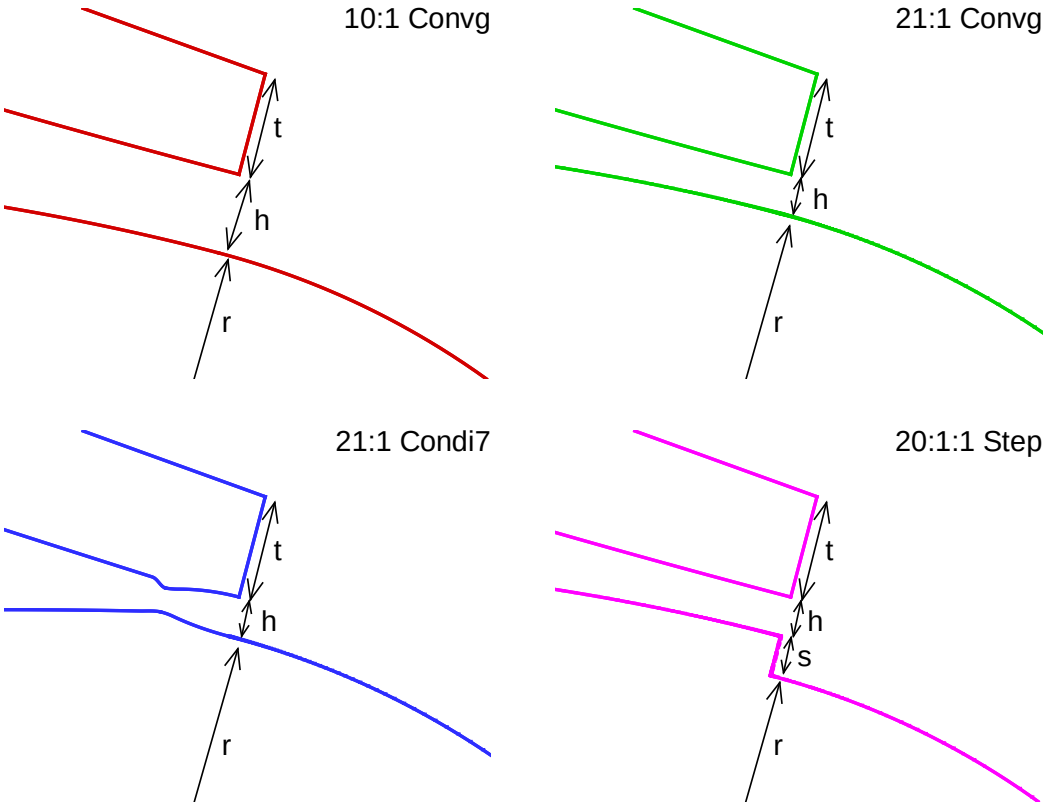

Figure 4.5: Diagrams of trailing edge devices.

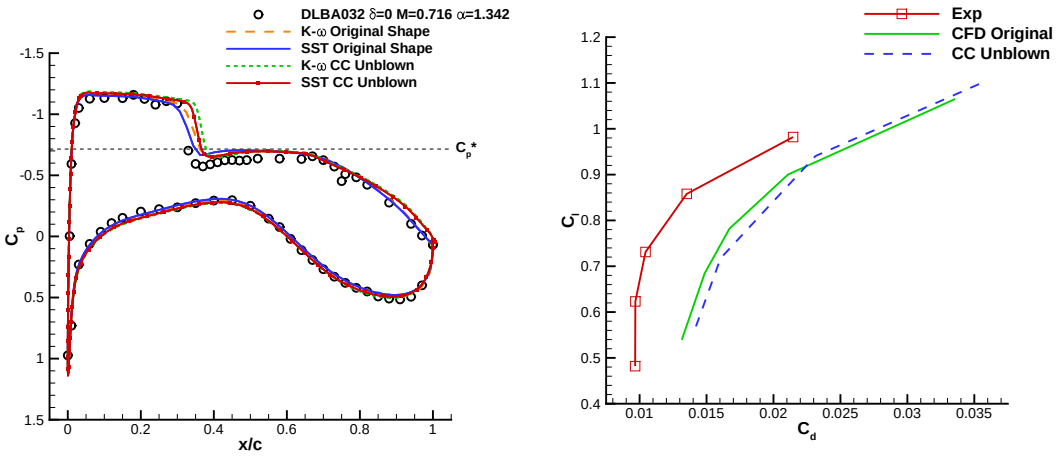

(a) Pressure coefficients.

(b) Lift-drag polar using simulations from the standard k-ω model.

Figure 4.6: Comparing unblown CC DLBA032 with original shape without aileron deflection.

thickened trailing edge and CC device are small, with an approximate 0.001 increase in the drag coefficient. However the characteristics of the lift-drag polar from the original aerofoil geometry were effectively maintained.

Each CC case considered below was simulated at a freestream value of $\alpha = 1.342°$, $M = 0.716$ and $Re = 5.028 \times 10^6$.

4.2.1 Grid refinement

Four grids were built with cell counts between approximately 100,000 and 900,000. Each finer grid was uniformly refined across the entire domain. An initial grid spacing of $y^+ \approx 1$ in the wall normal directions was used for all grids, where y^+ was calculated based on the freestream Reynolds number. For a circular Coanda shape with a 21:1 radius to slot height ratio, the effect of grid refinement on the lift and drag on the aerofoil was assessed at the conditions described above with blowing at $NPR = 4.0$

Figure 4.7 shows the effect of the grid size on the DLBA032 section with CC. Figure 4.7a shows the Mach profile of the jet and aerofoil boundary layer at the trailing edge, taken $3.0h$ from the slot exit. Minor differences occur in the jet profiles between the "Fine" and "V. Fine" grids with 400,000 and 900,000 cells, respectively. These differences, however, do not have a significant effect on the surface pressures on the Coanda nor the main aerofoil surface (Figs. 4.7b and 4.7c). As a result the Fine grid is within 0.01% of the lift and 0.1% of the drag coefficients from the solution using the finest grid (V.Fine on Fig. 4.7), as shown in Fig. 4.7d, suggesting that the 400,000 cell grid produces sufficiently grid-independent results.

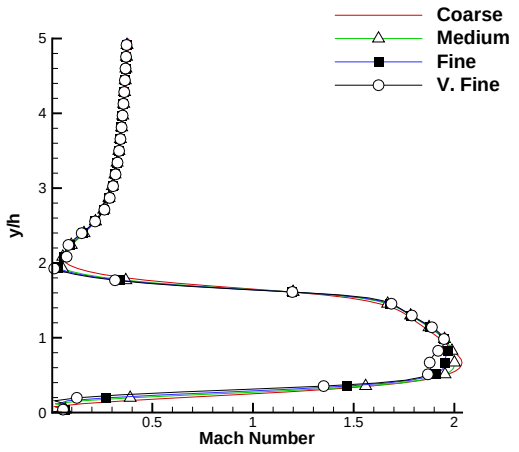

(a) Mach profile normal to Coanda surface at $3.0h$ from the slot exit.

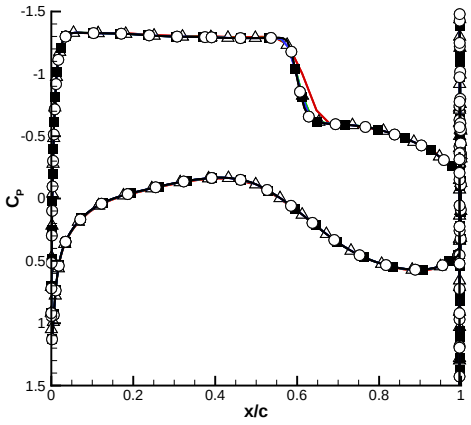

(b) Coefficient of surface pressure on the aerofoil surface.

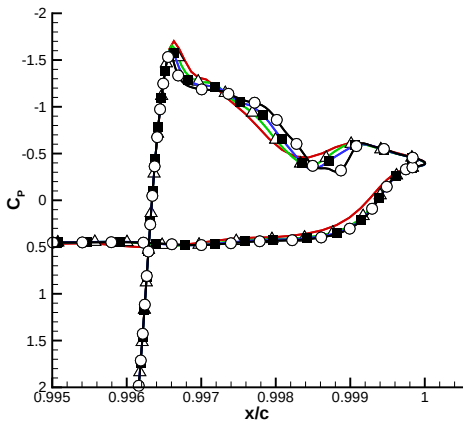

(c) Coefficient of surface pressure on the Coanda surface.

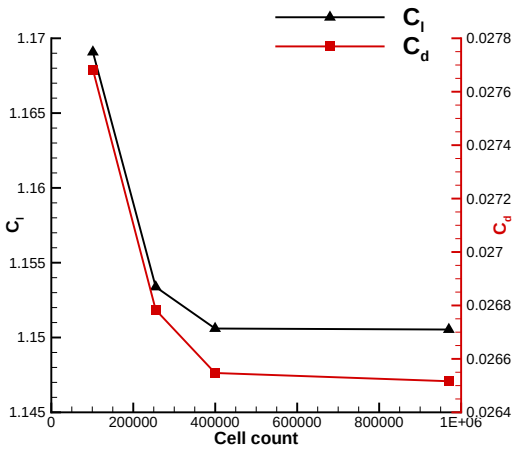

(d) C_l and C_d

Figure 4.7: Effect of grid refinement on the 21:1 Coanda device at $NPR = 4.0$.

4.2.2 Converging nozzle with 10:1 radius to slot ratio (10:1 Convg)

The simulated pressure coefficients for the DLBA032 aerofoil with a circular Coanda device with 10:1 radius to slot ratio are compared with an aileron deflection of 3° in Fig. 4.8. As with the NASA 6% elliptical CC aerofoil results, the shock moves aft with blowing which is consistent with an increase in lift and circulation. The symbols in Fig. 4.8 represent the simulated results of the aileron deflection case at the same conditions.

Comparing the predicted results of the aileron deflection and blowing over the 10:1 configuration at $C_\mu = 0.003$, the lower surface and the front section of the aerofoil have similar pressure distributions. The rear section of the aerofoil with blowing has more suction, and does not have the characteristic peak in suction at the hinge line. This

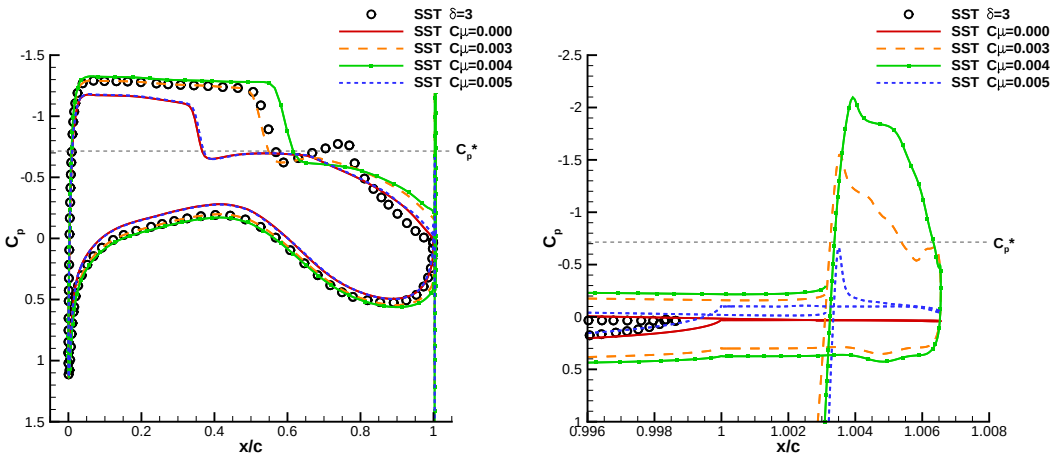

Figure 4.8: Predicted pressure coefficients for Douglas DLBA032 at $\alpha = 1.342°$, $M = 0.716$ and $Re = 5.028 \times 10^6$ for an aileron deflection and with blowing at $C_\mu \approx 0.003$, $C_\mu \approx 0.004$ and $C_\mu \approx 0.005$ for the 10:1 configuration. Symbols here represent the simulated pressure distribution of the deflected aileron case at the same freestream conditions and turbulence model.

additional suction towards the trailing edge generates an increase in the 'nose down' pitching moment compared to that of a 3° aileron, Fig. 4.9.

With increased blowing, the sectional lift, drag and pitching moment coefficients on the aerofoil increase. Figure 4.9 shows the behaviour of the loads due to blowing, also shown are predicted loads for the aerofoil at a range of aileron deflection angles. At a similar lift coefficient to that of a deflected aileron of 3°, blowing over the 10:1 configuration at $C_\mu = 0.003$ resulted in a smaller drag increase.

Additional blowing results in separation of the jet from the Coanda surface, due to the increased underexpansion of the jet. For $C_\mu = 0.004$ the jet separated from the Coanda surface, however in this case the jet re-attached to the surface. This re-attachment may be due to the low pressure within the separated bubble, as shown in Fig. 4.10a. In Fig. 4.10b, Mach contours using a moderately higher blowing rate of $C_\mu = 0.005$ are shown, where the jet is detached. The shock impinging on the Coanda surface is too strong for the flow to re-attach to the Coanda. As seen in Fig. 4.10b, the separation bubble does not form and so the mechanism to re-attach the jet is not present.

The lift characteristics for blowing at $C_\mu = 0.003$ suggest that it is possible to replicate the lift achieved with a 3° aileron deflection using CC in this flight regime, with a reduction in the drag and an increase in the pitching moment, as shown in Fig. 4.9. For this configuration, a blowing rate of $C_\mu = 0.005$ caused detachment of the jet. While the jet remains attached, a lift augmentation ratio of $\Delta C_l / C_\mu = 84$ was achieved.

4.2.3 Converging nozzle with 21:1 radius to slot ratio (21:1 Convg)

The effect of changing the slot height to radius ratio was investigated by halving the slot height of the 10:1 Coanda trailing edge device, resulting in a surface with a radius and slot height of 0.525% and 0.025% chord lengths respectively, and a 21:1 Coanda radius to slot ratio. Using the plenum pressure ratio of 5.0 was found to detach the jet from the 10:1 geometry, while with the 21:1 radius the jet remained attached.

Figure 4.9 shows that at $C_\mu = 0.002$ (NPR=4.0), the SST predictions gave comparable performance to the converging nozzle over the 10:1 surface at $C_\mu = 0.003$ (NPR=3.0) and also the aileron deflection of 3°. For the same blowing rate, the 21:1 device produced approximately 50% higher lift augmentation ratio than the 10:1 CC device, resulting in a $\Delta C_l/C_\mu = 134$.

Similarly to the 10:1 configuration, further blowing detached the jet due to the strongly under-expanded jet flow at $C_\mu = 0.0035$ (NPR=7.0).

By increasing the radius of curvature near the slot exit, the boundary layer within the jet experiences a weaker adverse pressure ratio. As a result the jet boundary layer is able to cope with a stronger shock associated with underexpansion at a higher pressure ratio when using the 21:1 configuration compared with the 10:1, above.

4.2.4 Converging-diverging nozzle with 21:1 radius to slot ratio (21:1 Condi7)

Bevilaqua and Lee's [13] method of characteristics approach fixes a desired irrotational vortex profile along the slot. The two dimensional characteristics equations are solved to determine the nozzle wall profiles from the slot exit to the nozzle throat for a given pressure ratio and Coanda radius. This method of characteristics procedure was applied to the nozzle walls of the 21:1 configuration to design a nozzle to perform at $NPR = 7.0$. At this pressure ratio, flow from a purely converging nozzle failed to attach, as described in Section 4.2.3 above. The resulting asymmetrically contoured converging-diverging nozzle is shown in Fig. 4.5. In designing the nozzle, the exit slot height from the 21:1 Convg device is retained at 0.025% chord. The contouring of the nozzle gave an effective throat height of 0.015% chord, resulting in an expansion ratio of 1.67. For choked conditions, this results in a reduced mass flow rate.

Figure 4.10c shows the converging diverging nozzle operating at the design condition $NPR = 7$. A relatively weak shock occurs at the slot exit, followed by a small separation bubble on the Coanda surface at approximately $x = 1.004$.

Although the nozzle was designed to fully expand the jet, the used method of characteristics did not account for the boundary layer. The effective nozzle contour as seen by the flow, due to the displacement thickness, was found to significantly reduce the expansion rate and so the jet was under-expanded. This can be seen from the

Mach number profile at a station at the slot exit in Fig. 4.11, where the theoretical irrotational vortex profile is also shown. The SST model predicted a thinner boundary layer than that of the k-ω, however both models gave a slope similar to the idealised profile at a reduced value for the mean Mach number.

For a pressure ratio of 9.0, the jet emanating from the converging-diverging nozzle under-expands, however the magnitude of under-expansion is lessened by the nozzle. This allows the jet to adhere to the Coanda surface and gives a lift increment of $\Delta C_l = 0.4077$ using the SST model. An approximate linear change in the lift and drag coefficients using the converging-diverging Coanda until $C_\mu \approx 0.004$ is shown in Fig. 4.9. Again, due to underexpansion, the jet eventually detached from the Coanda at $C_\mu \approx 0.006$ (NPR=13.0).

Figure 4.12 shows the differences between the jet profiles using the converging and the converging-diverging nozzles at $NPR = 4$ and $NPR = 7$ both with a 21:1 Coanda radius to slot height ratio. At $NPR = 4$, the C_μ of the converging nozzle was approximately 10% higher than that from the converging-diverging nozzle, however the ΔC_l was 54% higher using the converging nozzle as shown in Fig. 4.9. The reduction in ΔC_l at the same NPR is possibly due to the reduction in mass flow rate through the shorter throat height of the converging diverging nozzle. The underexpansion of the jet from the 21:1 Convg device appears to entrain more of the freestream than when using the 21:1 Condi7 nozzle at the same conditions. This underexpansion is an impediment at higher nozzle pressure ratios however, since it also brings about shock induced separation of the Coanda boundary layer. By expanding the flow, the extent of the separation is reduced and detachment occurs later.

Figure 4.10d shows contours of Mach number for an over-expanded nozzle on the DLBA032. Although the flow separated inside the nozzle, the jet remained largely attached to the Coanda surface for NPR=3.0 ($C_\mu = 0.0014$).

In all over-expanded cases ($C_\mu < 0.003$) using this nozzle designed for NPR=7, a reduction in lift augmentation ratio and thus efficiency was observed. Comparing this with the same radius to slot height ratio, $\Delta C_l/C_\mu$ with 21:1 Condi7 was 75% of the augmentation ratio achieved from the convergent only nozzle 21:1 Convg.

In contrast to the other designs, the gradient of the ΔC_l vs C_μ plot for the 21:1 Condi7 in Fig. 4.9 initially increases as C_μ increases. Up until the design condition at $C_\mu = 0.0032$ a maximum $\Delta C_l/C_\mu = 105$ was found. Following from the design point, the slope of ΔC_l vs C_μ begins to diminish.

4.2.5 Converging nozzle with a 20:1:1 radius to slot to step ratio (20:1:1 Step)

Using the initial 21:1 purely converging configuration as described above (Section 4.2.3), the radius of the Coanda was decreased by 0.025% chord to give a radius of slot height of 0.5% chord while maintaining the 0.025% chord slot height. This produced a step between the exit of the converging nozzle and the Coanda surface.

Figure 4.10e shows the behaviour of the under-expanded jet at $C_\mu = 0.0027$, the shock cell structure can be seen which begins to follow the Coanda surface. At $NPR = 7$ ($C_\mu = 0.0035$), the flow from the same nozzle caused the jet to detach from the 21:1 configuration (described above), while including the step promoted attachment to the Coanda surface. Attachment of the jet remains up to $NPR = 11.0$ ($C_\mu = 0.0057$). As shown in Fig. 4.9, the behaviour of the jet over the stepped Coanda follows the same behaviour as that of the converging-diverging nozzle. A maximum $\Delta C_l/C_\mu = 108$ up to $C_\mu = 0.0038$ was found when using the stepped Coanda. Below the design point of the 21:1 Condi7 nozzle, the stepped geometry gave a greater $\Delta C_l/C_\mu$. At $NPR = 11.0$, the jet underexpands such that a shock boundary layer interaction with the Coanda is strong enough to separate the jet, despite the step (Fig. 4.10f).

4.2.6 Effect of angle of attack

To assess the range of operability of CC in transonic flow, two representative CC cases are compared here with a deflected aileron case. The effect of increasing shock strength on the upper surface of the aerofoil is investigated by operating at steeper angles of attack. Figure 4.13 shows the effect of varying the angle of attack on the lift characteristics of CC and a 3° aileron deflection. The two CC cases shown are the 21:1 Convg and the 20:1:1 Step running at $C_\mu = 0.0020$ and $C_\mu = 0.0027$, respectively. Independent of trailing edge geometry each case undergoes a stall as α increases, due to the stronger shock on the upper surface causing the boundary layer to separate and so a progressively smaller ΔC_l as α increased. This gradual reduction in ΔC_l is due to a strong shock wave separating the boundary layer on the upper surface of the aerofoil. The rate at which ΔC_l degraded was approximately constant between the CC and aileron deflection cases as shown in Fig. 4.13b, where the difference between circulation control cases and the 3° aileron are presented. These results suggest that the behaviour of CC is similar to that of a deflected aileron at the higher angles of attack considered. At higher angles of attack, degradation of the mean flow rather than the CC system appears to be the limiting factor in retaining control of the forces and moments. Such a result may mean that the well understood principles of using ailerons in transonic flows could be applied to the use of CC.

Figure 4.14 shows the effect of the aileron deflection and CC have on the flowfield

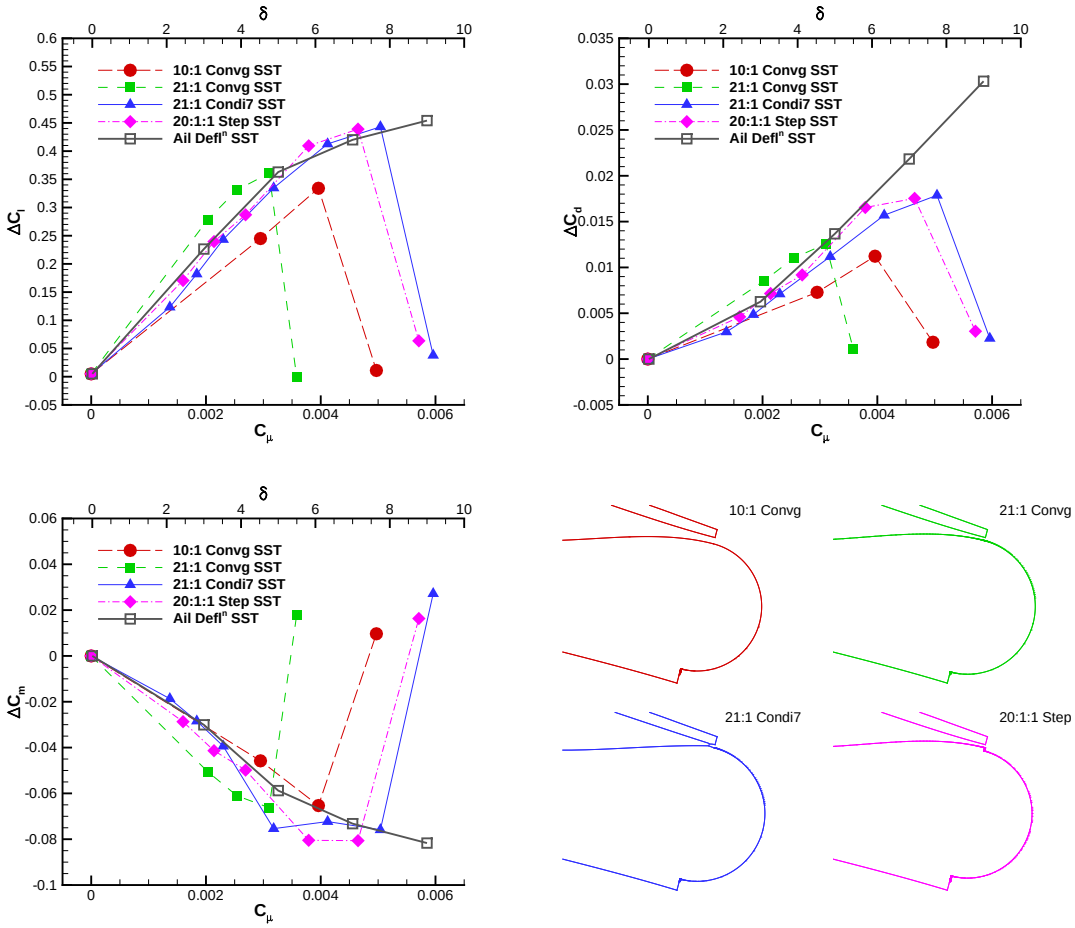

Figure 4.9: Comparing lift, drag and pitching moment coefficient characteristics with blowing over various Coanda surfaces against aileron deflection on the DLBA032 at $M = 0.716$, $\alpha = 1.342°$ and $Re = 5.028 \times 10^6$.

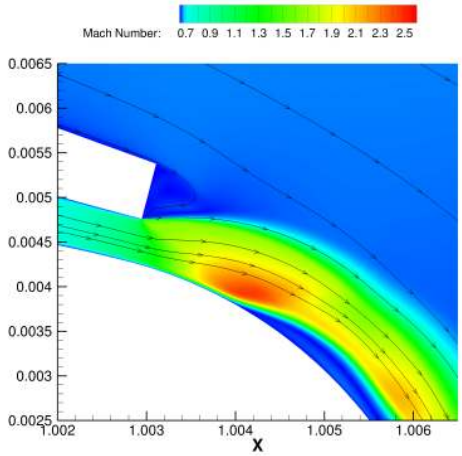

(a) 10:1 Convg NPR=4. $C_\mu = 0.0040$.

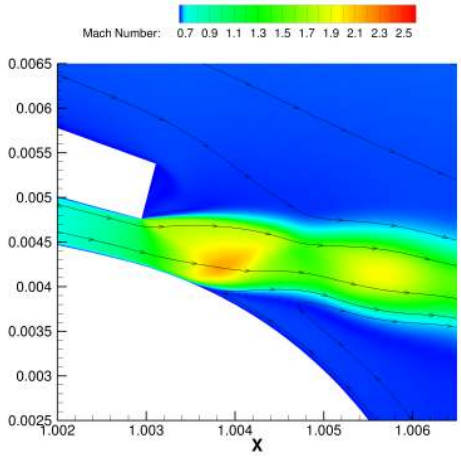

(b) 10:1 Convg NPR=5. $C_\mu = 0.0050$.

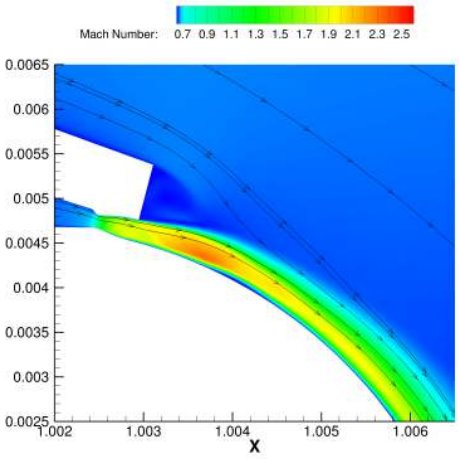

(c) 21:1 Condi7 NPR=7. $C_\mu = 0.0032$.

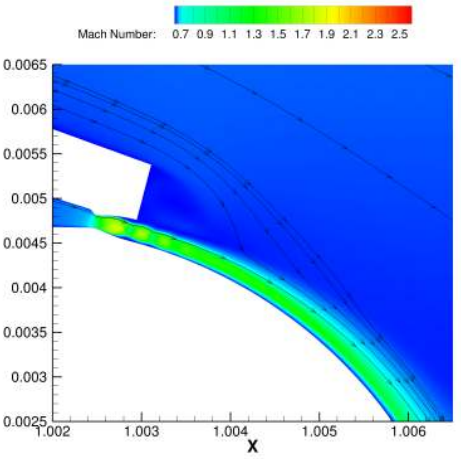

(d) 21:1 Condi7 NPR=3. $C_\mu = 0.0014$.

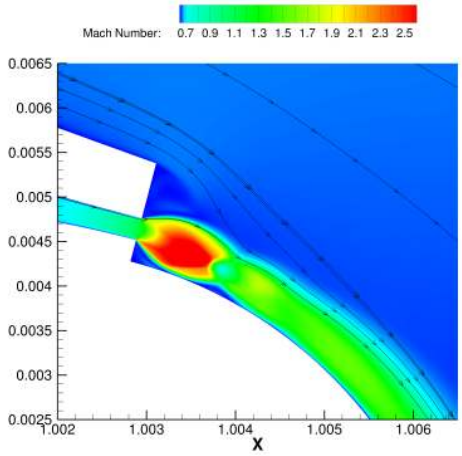

(e) 20:1:1 Step NPR=5. $C_\mu = 0.0027$.

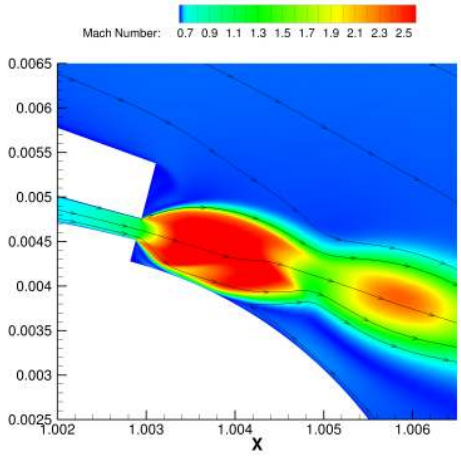

(f) 20:1:1 Step NPR=11. $C_\mu = 0.0057$.

Figure 4.10: Contours of Mach number for various Coanda designs using the k-ω SST turbulence model.

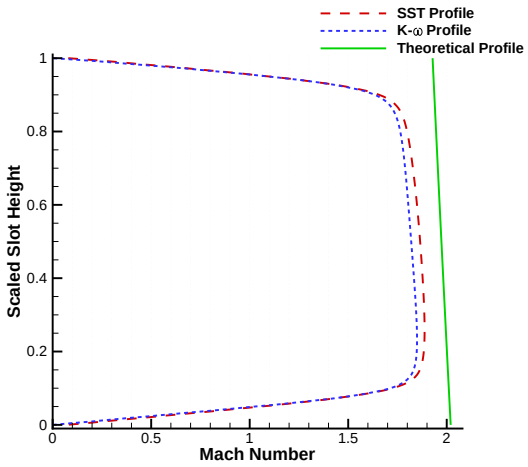

Figure 4.11: Profile of Mach numbers for the SST and k-ω models at the slot exit for the converging diverging configuration with a 21:1 radius to slot ratio at design condition for blowing at PR7.

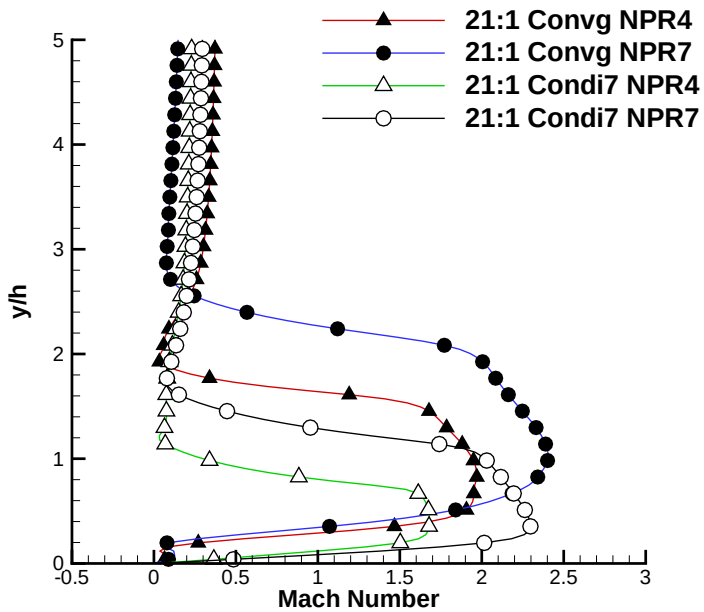

Figure 4.12: Mach profile normal to Coanda surface at 3.0h from the slot exit.

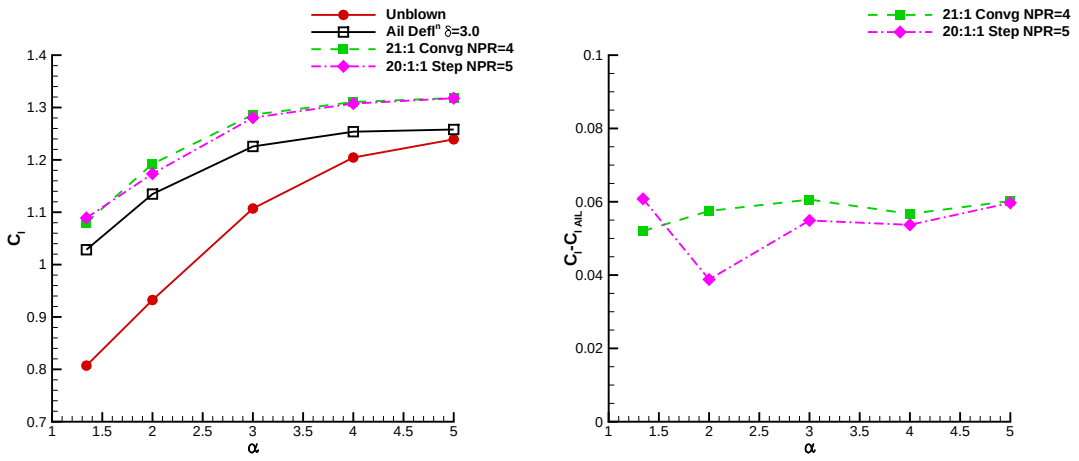

(a) C_l (b) ΔC_l with respect to the aileron deflection.

Figure 4.13: Effect of angle of attack on C_l at $M = 0.716$ and $Re = 5 \times 10^6$.

at the trailing edge of the aerofoil. In both cases a strong shock boundary layer interaction occurred at approximately 55% chord, with the shock further aft for the CC case from the increased circulation generating additional lift. With CC the trailing edge separation is reduced in severity due to the additional boundary layer momentum from jet entrainment and a favourable pressure gradient due to blowing. Although not investigated here, it may be possible that CC may offer some shock buffet onset alleviation.

4.3 Summary of Results

An increase in the ratio between the radius of curvature and the slot height increased the CC effectiveness by providing an increase in total lift and also the lift augmentation ratio. This finding is in line with conclusions from experimental studies described in Section 1.3, where the local radius of curvature at the slot exit was increased by altering the eccentricity of elliptical Coanda devices [3, 4]. Here we have confirmed that an increase in the ratio between the Coanda radius and slot height resulted in an increase in overall lift achievable due to delayed jet detachment.

The limiting detachment pressure ratio can be extended by using a suitably designed converging-diverging nozzle. In the cases considered in this chapter, the converging-diverging nozzle was designed for the operating condition for which the jet detached using a convergent only Coanda device at the same radius to slot height ratio. Further extension may be possible by designing the converging-diverging nozzle for higher pressure ratios, however a further reduction in efficiency is likely be observed.

Introducing a step between the Coanda surface and the slot exit also promoted a delay in detachment for CC with a transonic freestream. This was due to the shock

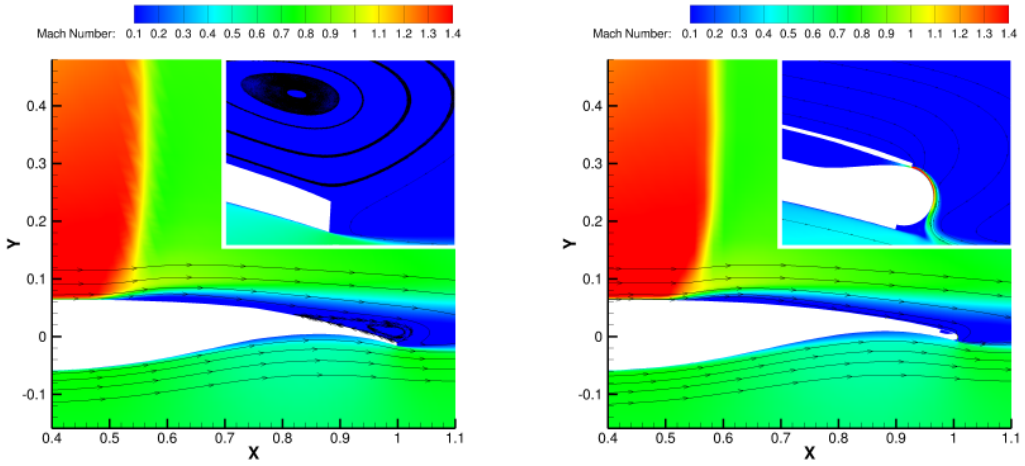

(a) 3° aileron deflection.

(b) 21:1 Convg at NPR=4.

Figure 4.14: Mach contours at the trailing edge of aileron deflection and CC cases at $\alpha = 5°$, $M = 0.716$ and $Re = 5 \times 10^6$. Inset shows detail of the trailing edges, at the same scale in both images.

boundary layer interaction being replaced by a shock shear interaction. For very highly underexpanded stepped Coanda jets, the reattachment shock was the cause of separation.

As shown in Fig. 4.9 each of the designs can be compared to an aileron deflection angle, the 10:1 Convg and 21:1 Convg devices achieved a maximum ΔC_l equivalent to that of approximately 4° and 5° aileron deflection, respectively. Both converging-diverging and stepped devices gave an equivalent aileron deflection of approximately $7.5 - 8°$ before detachment.

Chapter 5

Optimisation

The results within this chapter were presented in Refs 105 and 106.

This chapter presents the results of an optimisation study using the solution of the Adjoint Navier-Stokes equations as described in Sections 2.3 and 2.6. Here, the focus is upon improving the lift augmentation of an unstepped Coanda with a converging nozzle for transonic flows, which will be achieved by modifying the contour of the Coanda surface for a fixed C_μ and nozzle geometry.

Firstly, the optimisation of the Coanda surface for the design point of transonic cruise at $NPR = 4$ will be conducted (called as HSOPT). This will be followed by a similar optimisation for a low speed condition at $M = 0.4$ and $NPR = 4$ (LSOPT). Finally a multipoint optimisation will be conducted using the above two conditions in addition to a transonic cruise condition at $NPR = 6$ (MPOPT).

5.1 Parametrisation

The Coanda surface was parametrised by a radial function varying with the angle, θ from the jet exit (see Fig. 5.1a). The parametrisation was chosen such that the Coanda contour was smooth and without small peaks and troughs that may have presented convergence issues with the simulation, but also to retain feasibility from a manufacturing perspective. A requirement was placed that each of the design variables had equal weighting and were of the same order of magnitude in size. For example, a simple polynomial function would likely have an unbalanced sensitivity to changes in coefficients of the linear and quartic terms.

The radial function chosen is based on the summation of Bernstein polynomials,

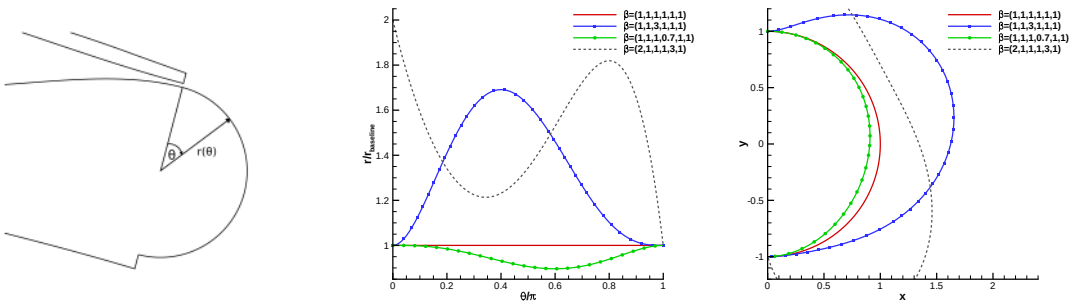

(a) Definition of parameters r and θ.

(b) Radial functions of sample Bernstein polynomials.

(c) Effective Coanda shape due to functions in (b).

Figure 5.1: Parametrisation of Coanda surface by a radial distribution of Bernstein polynomials.

given by;

$$r(\theta) = B_n\left(\frac{\theta}{\pi}\right) = \sum_{\nu=0}^{n} \beta_\nu b_{\nu,n}\left(\frac{\theta}{\pi}\right) , \tag{5.1}$$

where

$$b_{\nu,n}(t) = \binom{n}{\nu} t^\nu \left(1-t\right)^{n-\nu} , \quad t \in [0,1]. \tag{5.2}$$

Using Bernstein polynomials allows for a perfectly circular surface when using equal values of the Bernstein coefficients β_ν, which is shown in Fig. 5.1b where choosing all $\beta_\nu = 1$ gives a line at $r = 1$ and a circle in Fig. 5.1c.

The vector of coefficients β_ν is fixed such that $\beta_0 = \beta_1 = \beta_{n-1} = \beta_n = 1.0$. Limiting the coefficients at the slot exit(s) in this way forces the surface contours to be continuously differentiable at the exit. Figures 5.1b and 5.1c demonstrate this necessity, with β_0 or $\beta_n \neq 1.0$ the Coanda surface does not meet the slot exit, while β_1 or $\beta_{n-1} \neq 1.0$ creates a discontinuity in curvature. A resulting Coanda surface defined by n design variables (given by the design vector $\boldsymbol{x}$) will require $n + 4$ β-coefficients.

For each of the cases considered here, the Coanda surface was parametrised by a summation of 9 Bernstein polynomials defining the local radius of the Coanda. Coefficients of each Bernstein polynomial were used as design variables, with the limitation that the curvature at the slot exit was continuous with the contour of the nozzle as described above. As such, 5 design variables were employed. Figure 5.2 shows an illustration of the parametrised (Fig. 5.2a) and physical representation (Fig. 5.2b) of the limits within the optimisation, here $\mathbf{x}_{min} = [0.70, 0.70, 0.70, 0.70, 0.70]$ and $\mathbf{x}_{max} = [1.10, 1.30, 2.50, 1.30, 1.10]$.

To enforce a constant blowing rate C_μ, the slot exit height, NPR and plenum shape were also fixed. Considering the choked condition in the throat this will fix C_μ. A maximisation of the lift coefficient at these conditions was performed, as such a minimisation of the objective function $I = -C_l$ was sought by the optimiser.

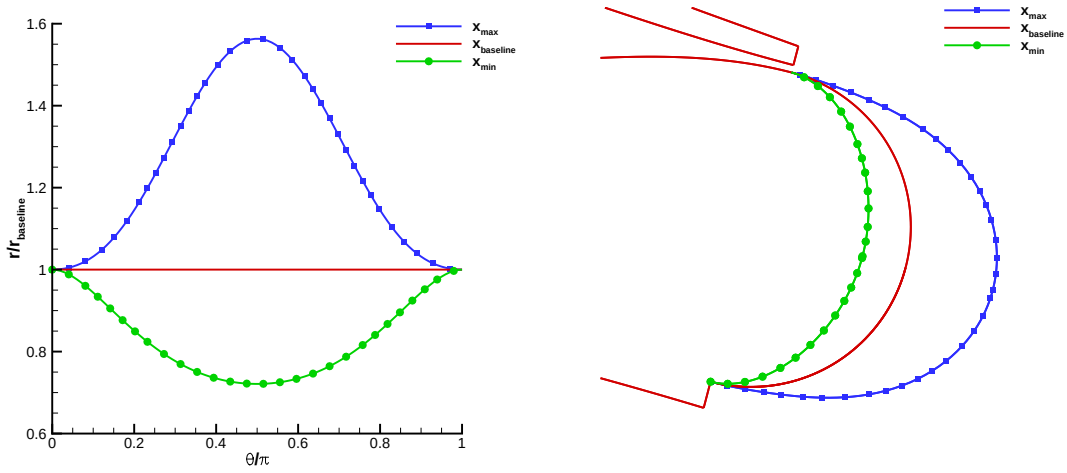

(a) Bernstein polynomial representation.

(b) Physical representation of parameters on Coanda surface.

Figure 5.2: Schematic of the baseline and design variable limit parameters.

5.2 Baseline Circular Coanda

The initial reference geometry for optimisation was the 21:1 radius to slot height circular Coanda surface applied to the DLBA032 aerofoil section [103]. This geometry is equivalent to the 21:1 Convg as studied in Section 4.2.3.

For the present simulations, a moderately coarser grid was used than was used in the previous design study. Here, a grid with 254,822 cells was used during the optimisation, which gave C_l and C_d to within 0.25% and 1% of the grid converged results, as shown in Fig. 5.3.

5.3 Single Point Optimisation

5.3.1 High speed case (HSOPT)

For $M = 0.716$, $Re = 5 \times 10^6$, $\alpha = 1.342°$ and $NPR = 4.0$, several single point optimisations were conducted. To remove the influence of the starting design, several initial design shapes were considered: An optimisation was carried out for each of the minimum, maximum (as shown in Fig. 5.2b), the baseline circular and quasi-elliptical designs.

By blowing over the initial baseline circular Coanda shape at the conditions above a lift coefficient of $C_{l\,baseline} = 1.1527$ was achieved, which corresponds to $\Delta C_{l\,baseline} = 0.33$. The optimisation was initialised with this circular Coanda shape (design variables $\mathbf{x}_{baseline} = [1.00, 1.00, 1.00, 1.00, 1.00]$). After 15 evaluations of the objective function it was found that the resulting 'optimised' surface was relatively unchanged from the

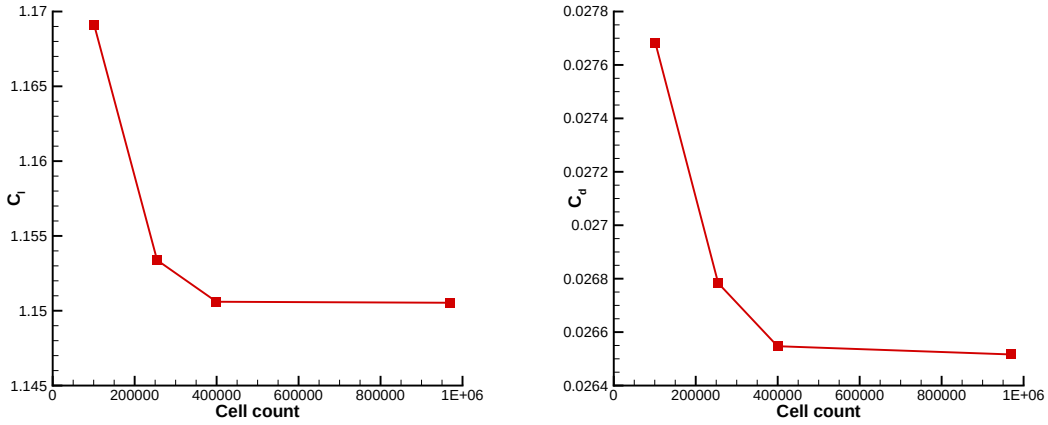

Figure 5.3: Effect of grid refinement on C_l and C_d at $M = 0.716$, $Re = 5 \times 10^6$, $\alpha = 1.342°$ and $NPR = 4.0$.

initial ($\mathbf{x}_{opt} = [1.010, 1.003, 0.997, 0.996, 1.002]$). For this configuration, small overall increase in the lift coefficient was observed, $C_l - C_{l\,baseine} = 0.0015$ and $\Delta C_l / \Delta C_{l\,baseline} = 1.0045$. It was concluded that the circular Coanda surface is within a local minimum of the design space and that an alternative starting point should be used.

Instead, starting from a quasi-elliptical shape with $\mathbf{x}_{initial} = [1.00, 1.00, 2.00, 1.00, 1.00]$ (Fig. 5.4a) successfully increased the lift from $C_{l\,initial} = 1.1138$ for the quasi-elliptical Coanda shape to $C_l = 1.2105$, after 46 evaluations of the objective function. Figure 5.5 shows the relative change in ΔC_l per objective function evaluation with respect to the ΔC_l achieved using the circular Coanda. It is shown that a 16% increase in ΔC_l was found over the $\Delta C_{l\,baseline}$, despite the quasi-elliptical Coanda initially performing at a reduced efficiency compared with the baseline circular shape. Appendix A includes the parameters that were applied at every evaluation of the objective function (one CFD simulation).

At several stages during the optimisation, the Coanda surface was prescribed a shape that caused the jet to detach. As a result, the circulation did not increase and so gave a $\Delta C_l \approx 0$. Such detachments create discontinuities in the design space, which typically present challenges to gradient based optimisation algorithms. In this instance, however, the SLSQP routine successfully found an optimum solution.

Figure 5.4 shows the effect of the optimisation on the location of separation of the Coanda jet. For the the final shape (Fig. 5.4b) the jet remained attached much longer to the Coanda, increasing the circulation and effective camber of the aerofoil. While not shown here, the shock position due to this effective change in camber was moved towards the trailing edge by approximately 10% chord.

Table 5.1 shows a summary of the effect of using different initial Coanda shapes on with a single point optimisation and the final shapes due to the optimisation are

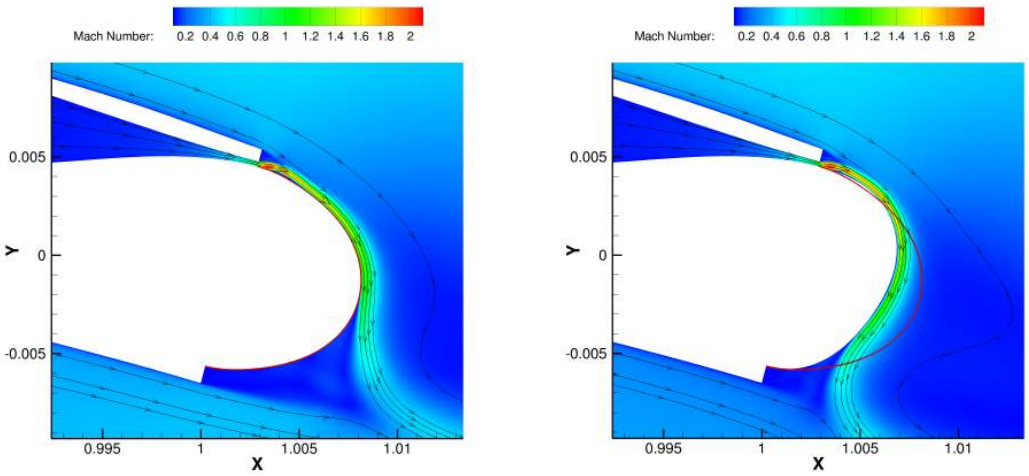

(a) Initial quasi-elliptical Coanda shape, C_l = 1.1138.

(b) Final single point HSOPT shape, C_l = 1.2105.

Figure 5.4: Contours of Mach number at the trailing edge of the aerofoil, a red line indicates the contour of the initial quasi–elliptical Coanda shape.

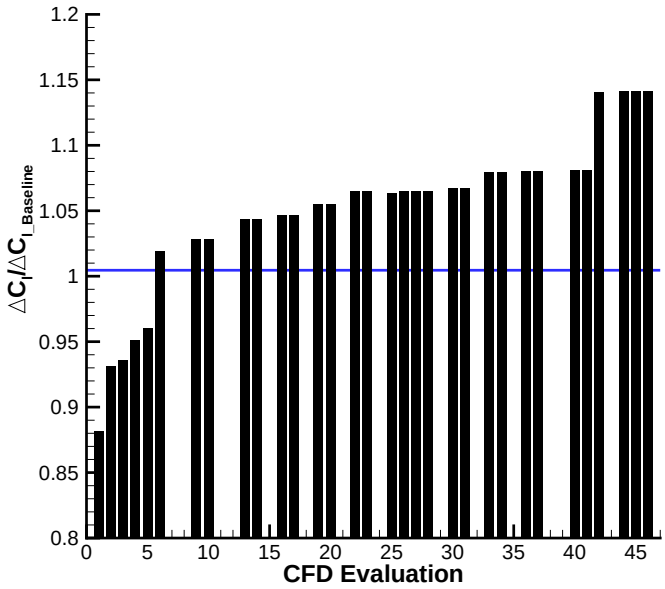

Figure 5.5: Relative change in lift coefficient increase with respect to every HSOPT objective function call evaluation from the initial quasi-elliptical shape. The change is relative to the baseline circular $\Delta C_{l\,baseline} = 0.33$. The horizontal line indicates the maximum achieved when starting HSOPT from a circular shape.

shown in Fig. 5.6. Although the minimum of the design space and quasi-elliptical initial shapes were significantly different in shape, the optimiser converged to a similar optimum design for both cases.

Table 5.1: Summary of results from the single point high speed optimisation.

Initial shape	Baseline	Min	Max	Quasi-elliptical
CFD solutions needed	15	55	51	46
Initial $\mathbf{x}^{\mathrm{T}}$	$\begin{pmatrix}1.000\\1.000\\1.000\\1.000\\1.000\end{pmatrix}$	$\begin{pmatrix}0.700\\0.700\\0.700\\0.700\\0.700\end{pmatrix}$	$\begin{pmatrix}1.100\\1.300\\2.500\\1.300\\1.100\end{pmatrix}$	$\begin{pmatrix}1.000\\1.000\\2.000\\1.000\\1.000\end{pmatrix}$
Initial C_l	1.1527	1.1048	1.1199	1.1138
Final $\mathbf{x}^{\mathrm{T}}$	$\begin{pmatrix}1.010\\1.003\\0.997\\0.996\\1.002\end{pmatrix}$	$\begin{pmatrix}1.061\\0.944\\0.881\\0.700\\0.700\end{pmatrix}$	$\begin{pmatrix}1.100\\1.300\\1.667\\0.775\\0.873\end{pmatrix}$	$\begin{pmatrix}1.057\\1.300\\0.756\\0.776\\1.100\end{pmatrix}$
Final C_l	1.1542	1.2085	1.1395	1.2105

5.3.2 Low speed case (LSOPT)

A similar single point optimisation study was conducted for a low speed freestream condition. For this the LSOPT optimisation was conducted at $M = 0.3$, $Re = 5 \times 10^6$, $\alpha = 1.342$ and for a blowing rate of NPR=4. For a circular Coanda at these conditions, $\Delta C_l = 0.69$ from the unblown $C_l = 0.62$.

Two initial designs corresponding to the minimum of the design space and the quasi-elliptical shapes. After 15 optimisation steps using an initial quasi-elliptical shape, the ΔC_l increased from $\Delta C_l = 0.71$ to $\Delta C_l = 0.83$, which is shown in Fig. 5.7 as a 12% increase compared with the baseline circular shape. The final shape for this LSOPT was still approximately elliptical, with design parameters $\mathbf{x} = [1.10, 0.95, 1.75, 1.12, 1.10]$. This LSOPT final shape will be shown within the discussion of the multi-point optimisation, below.

5.4 Multi-Point Optimisation (MPOPT)

Three design points were considered which focused on the optimisation of blowing over the Coanda at transonic freestream speeds, but also included a subsonic case. In the cruise regime ($M = 0.716$), blowing rates of $NPR = 4$ and $NPR = 6$ are considered to improve the efficiency of circulation control equivalent to moderate flap deflections. To ensure that at low speeds the design is capable of being used as a high lift device,

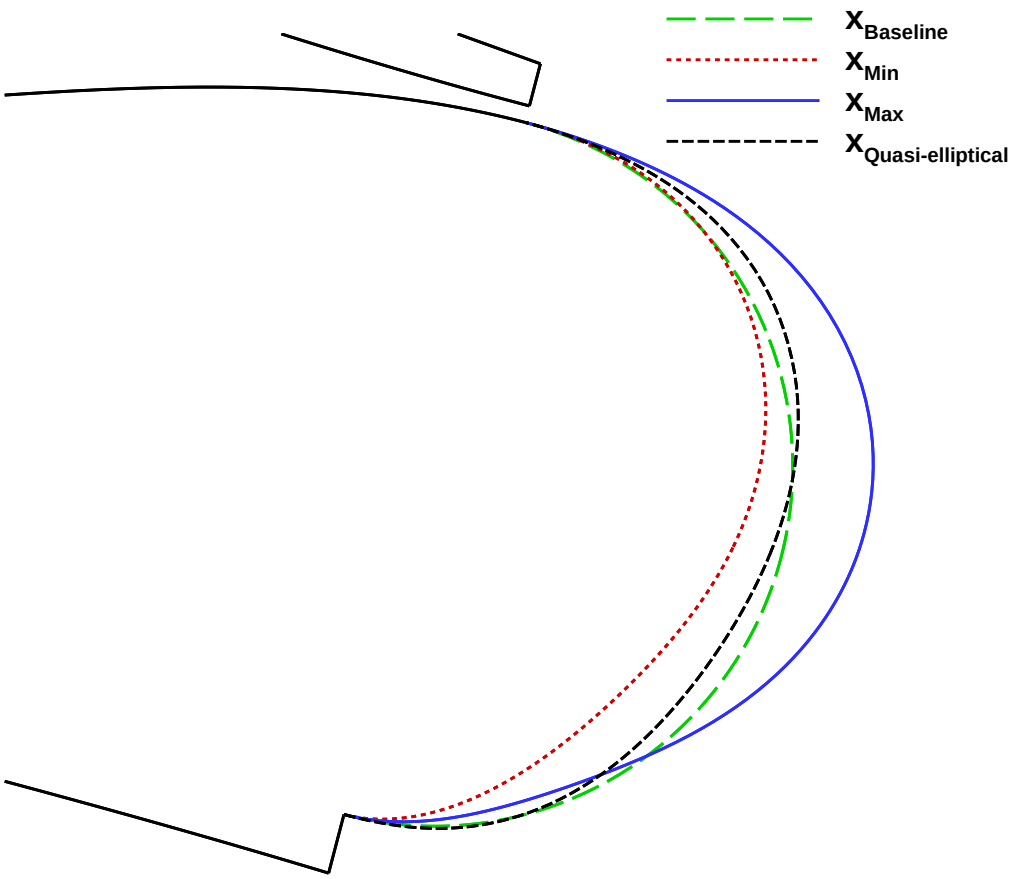

Figure 5.6: Final Coanda geometries following several HSOPT optimisation routines with different initial geometries as given by Table 5.1.

a design point of $M = 0.4$ and $NPR = 4$ is included, which corresponds to $\Delta C_l \approx 0.7$ for the baseline circular case.

Since the focus of the current study is on optimising a design for high speed transonic freestream flows, the weights λ_i were set to favour the high speed cases as shown in Table 5.2. As outlined in Eq. (2.60), the multipoint procedure here aims to minimise the weighted sum of the objective functions for the three conditions in Table 5.2, namely $F = \sum_{i=1}^{n} \lambda_i I_i$, where $-I_i$ is the lift coefficient for each design point.

Table 5.2: Weights used in the multipoint optimisation.

Case	$M = 0.7$ $NPR = 4$	$M = 0.7$ $NPR = 6$	$M = 0.4$ $NPR = 4$
λ_i	1.0	1.0	0.3

Figure 5.8 shows the history of the lift coefficient for each of the three design points and the relative objective function considered in the multipoint optimisation. Comparisons are also made against the single point high speed and low speed optimisation final

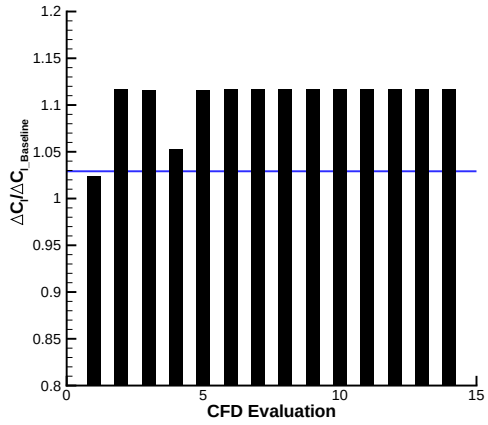

Figure 5.7: Relative change in lift coefficient increase with respect to every LSOPT objective function call evaluation from the initial quasi-elliptical shape. The change is relative to the baseline circular $\Delta C_{l\,baseline} = 0.69$. The horizontal line indicates the maximum achieved when starting LSOPT from the minimum of the design space.

results.

Due to the weighting in favour of the two high speed cases the MPOPT design converged to a similar shape as the HSOPT result, this is shown in Fig. 5.9. The parameters for the final multipoint design were $\mathbf{x} = [1.037, 1.263, 0.936, 0.700, 0.700]$, which gave a shape that was similar to the HSOPT for the first 90° of the Coanda. Despite the MPOPT shape under performing at the conditions considered in the LSOPT and the HSOPT cases (Figs. 5.8a and 5.8b), the overall performance defined by F (Fig. 5.8d) shows that the resulting design is an improvement over both the baseline and the HSOPT designs.

5.5 Off-Design Behaviour

Figure 5.10a shows the behaviour of the three optimised and the baseline designs described above over a range of nozzle pressure ratios. Here the freestream Mach number, angle of attack and Reynolds number are kept at the HSOPT design condition. Throughout the range considered, both HSOPT and MPOPT designs outperformed the baseline circular shape in terms of both ΔC_l and the nozzle pressure ratio for which the jet remains attached. For $NPR = 7$, unsteady calculations were necessary due to unsteadiness within the shear layer between the jet and freestream. Although the LSOPT design gave a lower value of ΔC_l than the baseline, the operating range of pressure ratios was also increased.

Simulations were also conducted to assess the behaviour of the optimised designs at a range of Mach numbers, as shown in Fig. 5.10b. For $M = 0.8$, shock induced

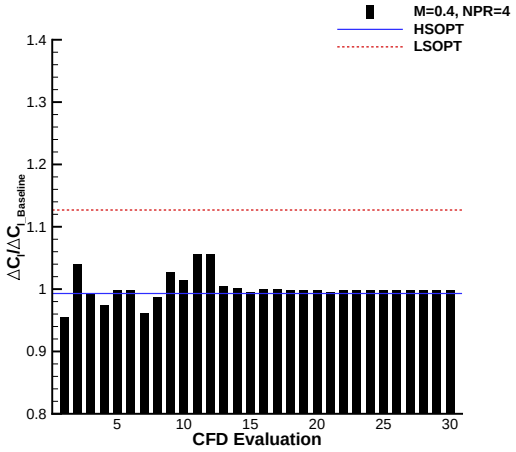

(a) $M = 0.4,\ NPR = 4$

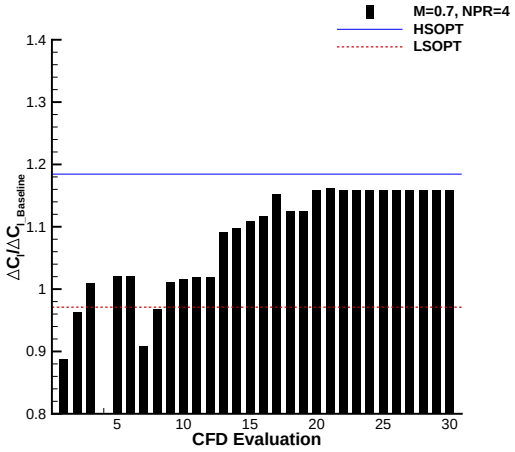

(b) $M = 0.716,\ NPR = 4$

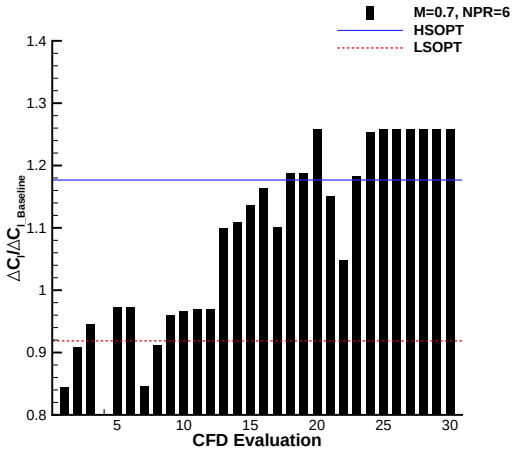

(c) $M = 0.716,\ NPR = 6$

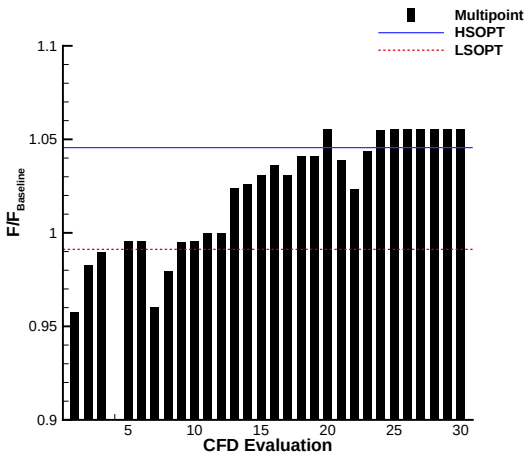

(d) Weighted sum of multipoint design conditions

Figure 5.8: Multipoint optimisation history showing: $\Delta C_l/\Delta C_{lbaseline}$ for $M = 0.4$, $NPR = 4$ (a), $M = 0.716$, $NPR = 4$ (b) and $M = 0.716$, $NPR = 6$ (c) and $F/F_{baseline}$ (d) with comparisons against the results from the single point optimisation studies.

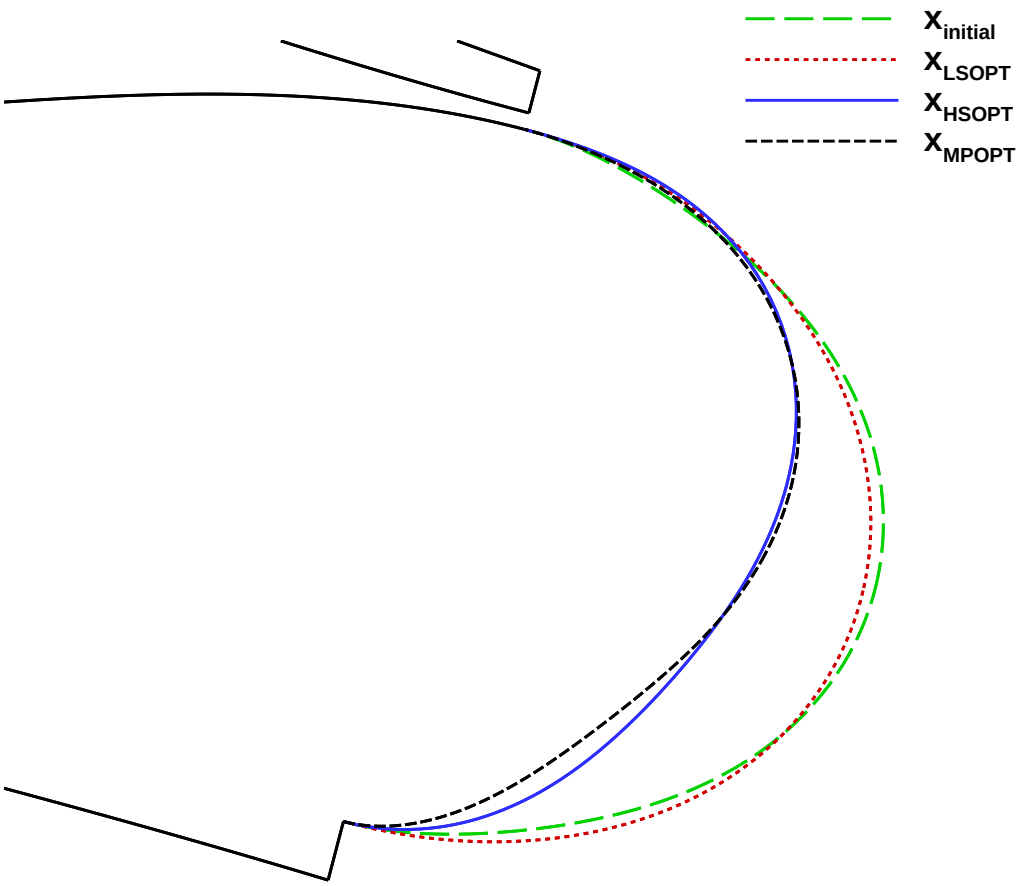

Figure 5.9: Coanda geometry the initial quasi–ellipse and resulting low speed (LSOPT), high speed (HSOPT) and multipoint (MPOPT) optimisation designs.

separation on the upper surface prevented the jets over both the circular shape and the optimised designs from altering the circulation. At $M = 0.6$ the difference between the circular and optimised solutions is $C_l = 0.034$, compared with $C_l = 0.058$ at the design Mach number ($M = 0.716$).

Decreasing the Mach number further resulted in the circular Coanda design outperforming the HSOPT single point optimised. At $M = 0.4$, a crossover occurs in the lift increase, where the circular, HSOPT and MPOPT optimised shapes perform similarly. Here, the LSOPT was at the design condition so performed more favourably to the circular shape.

5.6 Surface Sensitivities

Using an adjoint solution, it is possible to quantify the effect displacing individual surface grid points has on the value of the objective function. The surface sensitivities

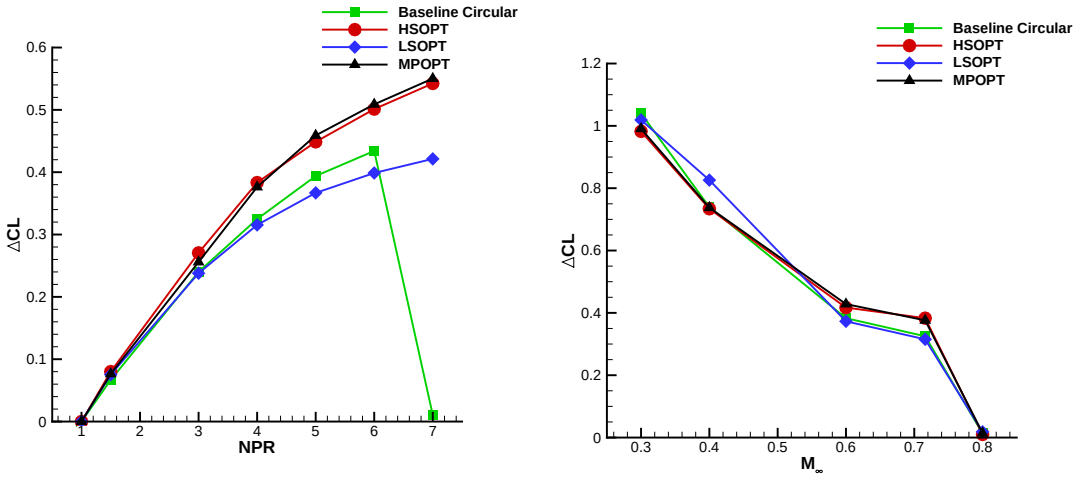

(a) Effect of changing NPR for fixed $M = 0.716$.

(b) Effect of changing M for fixed $NPR = 4$.

Figure 5.10: Comparing the ΔC_l of the single point optimised design with the circular shape at off-design conditions, $\alpha = 1.342$, $Re = 5 \times 10^6$.

shown in Fig. 5.11 show the relative change in C_l with respect to a normal displacement of grid points on the Coanda surface. In these plots, a higher value of $dC_l/dX_\mathbf{n}$ suggests that displacing the grid point in the outwards wall-normal direction would increase C_l, while lower values suggest that an increase in C_l would be achieved by moving the local surface inwards. A comparison of the surface sensitivities between the initial quasi-elliptical, LSOPT, HSOPT and MPOPT results are shown for the three design points considered in the multipoint.

The high sensitivity over the entire quasi-elliptical Coanda shape at $M = 0.4$ and $NPR = 4$ suggest that the quasi-elliptical shape is a poor design for low speed circulation control. Optimising this design at $M = 0.4$ and $NPR = 4$ in the low speed single point optimisation significantly altered the sensitivities for this point by a factor of approximately 100; the average $dC_l/dX_\mathbf{n}$ for the quasi-elliptical was approximately 200, while the low speed optimised design has an overall average of less than 20.

While the LSOPT design performed well on-design, at transonic freestream speeds the improvement over the quasi-elliptical was marginal. This is shown in Fig. 5.11 with both the small change in ΔC_l and also the relatively unchanged surface sensitivities.

Despite the relatively similar designs of the MPOPT and the HSOPT, the sensitivities at $M = 0.716$ and $NPR = 4$ differ considerably. This may be due to the multipoint design sacrificing the performance of the HSOPT design condition in favour of the LSOPT and higher blowing rate conditions. Evidence of this can be seen in the delayed jet separation at $M = 0.716$ and $NPR = 6$ between the HSOPT and MPOPT in Fig. 5.11.

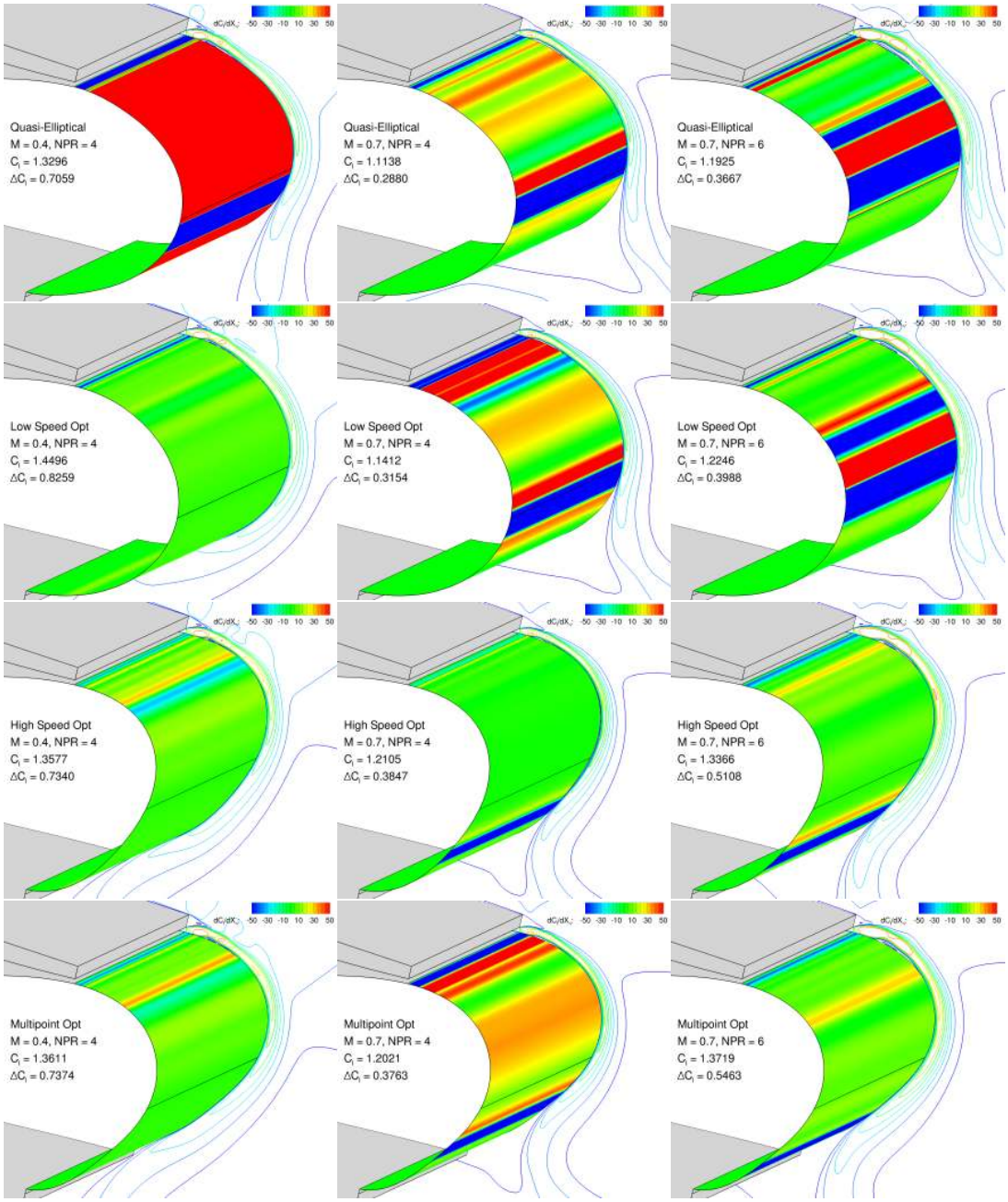

Figure 5.11: Mach contour lines and surface sensitivities ($dC_l/dX_\mathbf{n}$) at conditions $M = 0.4$, $NPR = 4$ (left), $M = 0.716$, $NPR = 4$ (middle) and $M = 0.716$, $NPR = 6$ (right). Top row: Initial quasi–elliptical shape. Second row: Single point optimisation for the low speed design condition $M = 0.4$, $NPR = 4$. Third row: Single point optimisation for the high speed design condition $M = 0.716$, $NPR = 4$. Fourth row: Multipoint optimisation.

5.7 Summary of Results

Several single point and a multipoint aerodynamic optimisation studies were conducted on a Coanda surface as applied to the trailing edge of the two–dimensional supercritical McDonnell Douglas DLBA032 aerofoil. It was shown that the design space for transonic circulation control lacks smoothness; several shapes caused the jet to detach while similar shapes promoted attachment. However, the gradient based optimiser was able to overcome this lack of smoothness. Additionally the design space was found to have many local minima, starting the single point optimisation routines at different initial designs produced different results.

The multipoint optimisation conducted here resulted in shapes which were similar to the better performing shape from the high speed single point optimisation. This may be due to a strong bias towards the high speed cases. The resulting multipoint designed shape did perform more favourably at high blowing rates, however over the remainder of the cases considered the performance was comparable to the single point design. From a cost perspective, the multipoint optimisation required more than twice the number of flow solutions to arrive at essentially the same result. The differences between the low speed behaviour of all cases suggest that a multipoint optimisation at several high speed conditions may be more beneficial with additional verification that the low speed behaviour is still favourable.

Chapter 6

SACCON

Preliminary findings for this chapter were presented in Ref. 107 using half span simulations, while the more recent full span results included here have been presented in meetings as part of the AVT-239 group.

The previous chapters have focussed so far upon the design and optimisation of Coanda devices on a two-dimensional aerofoil model. This chapter will therefore now aim to investigate the use of CC for a representative UCAV configuration in transonic flow. To do this, the SACCON UCAV demonstrator will be used since it has a range of experimental data for traditional control surfaces and is a test case that is actively being studied in the flow control community.

Previous work on circulation control and the SACCON was performed by Hoholis *et. al.* [63], who used CC with subsonic blowing to induce a rolling moment to the SACCON at low freestream speeds ($M = 0.145$). In this chapter, two circulation control device designs are applied to the SACCON at transonic speeds, the first is the same geometry that was considered by Hoholis, and the second uses the same ratios as the stepped Coanda from the design study in Chapter 4. Comparisons with numerical [61] and experimental [108] investigations using physical flaps for the SACCON at $M = 0.7$ are made.

6.1 SACCON Geometry and Grid

The DLR-F17 model as tested at BAE Systems' High Speed Wind Tunnel (HSWT) is shown in Fig. 6.1 [108]. The trailing edge of the wing was modified in the current CFD computations to accommodate a circulation control device for simulations, as shown by Hoholis [63]. For the current study, blowing over the inboard half of a Coanda (IBC) surface spanning the wing is conducted with spanwise slot locations coinciding with the

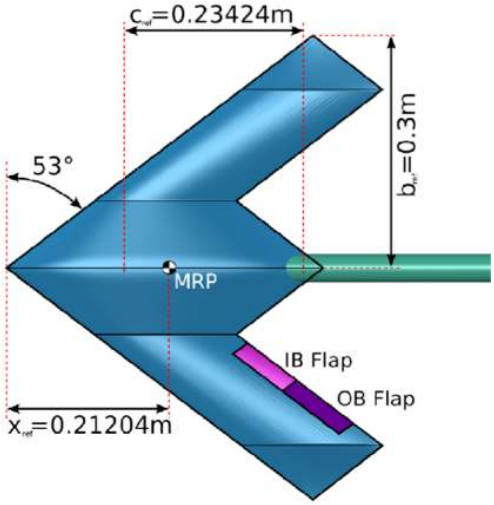

Figure 6.1: SACCON F17 geometry and reference lengths. [60]

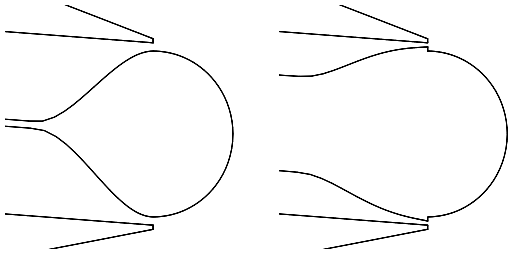

(a) Without step. (b) With step.

Figure 6.2: Diagram of inboard Coanda (IBC) geometries.

location of the flaps as shown in Fig. 6.1.

The two geometries investigated are an unstepped circulation control device with 10:1 Coanda radius to slot height ratio, and a model including a step with a 20:1:1 radius to slot to step ratio as illustrated in Fig. 6.2. For both geometries, the Coanda radius is $0.4\%C_{ref}$ at the wing root and $0.3\%C_{ref}$ at the tip, where $C_{ref} = 0.23424$m, defined in Fig. 6.1 and Table 6.1.

Initial half span simulations were conducted on the SACCON with CC, since simulations by Coppin [60] on the flapped configuration suggested that this was appropriate for angles of attack below 15° up to $M = 0.9$. A grid refinement study was conducted on this half span grid, and the resulting grid was then mirrored to create a full span grid.

Figure 6.3 shows the grid used for simulations of circulation control with the SACCON. The baseline grid has approximately 12×10^6 cell volumes in the half span domain. From this a coarser and a finer grid were made for a grid refinement study. Initial spacings and dimensions were similar to that from Kennett [61], however it was necessary to include additional cells to account for the refinement required near the Coanda surface.

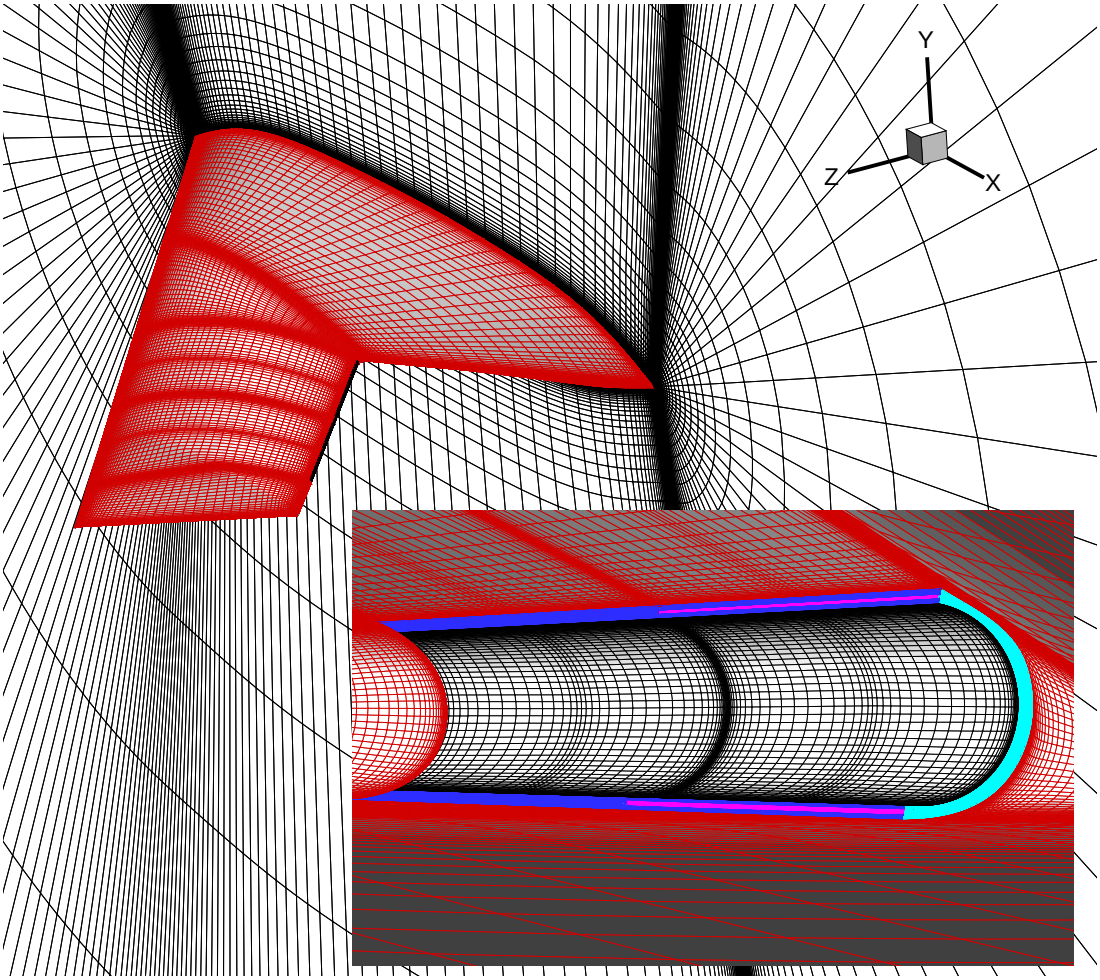

Figure 6.3: Half span grid. Inset shows detail of the trailing edge across the wingspan.

The grid was built such that a stepped geometry can be incorporated using the same mesh topology. Inset into Fig. 6.3 shows in detail the grid around the Coanda, with pink highlighting the jet slot exit associated with the stepped configuration.

Table 6.1: Reference values of the SACCON F17.

Description	Symbol	Value
Area	A (m^2)	0.1173
Semispan	b_{ref} (m)	0.3
Mean Aerodynamic Chord	c_{ref} (m)	0.23424
Moment Reference Point	MRP (x,y,z) (m)	(0.21204,0,0)
Mach Number	M	0.7
Reynolds number per m	Re/m	18.81×10^6

6.1.1 Half span force reduction

To calculate the forces for comparisons with the full span experiments using the left hand half span simulations, forces and moments with CC were combined with mirrored forces and moments for the unblown configuration. Coppin [60] demonstrated that this assumption produced reliable results for simulations on the high speed SACCON with physical flaps. As such, the drag, lift and pitching moment between left hand side CC and left hand side "clean" cases were summed. For the side force, roll and yaw; the total forces were calculated by taking the difference between the two cases. This procedure is summarised in Eq. (6.1). Reference values are given in Table 6.1.

$$
\begin{aligned}
C_D &= (F_x + F_{x,clean})/q_\infty A \\
C_L &= (F_y + F_{y,clean})/q_\infty A \\
C_S &= (F_z - F_{z,clean})/q_\infty A \\
C_l &= (M_l - M_{l,clean})/q_\infty A b_{ref} \\
C_m &= (M_m + M_{m,clean})/q_\infty A c_{ref} \\
C_n &= (M_n - M_{n,clean})/q_\infty A b_{ref}
\end{aligned}
\tag{6.1}
$$

6.2 Grid Convergence

Table 6.2 shows the effects of grid refinement of the stepped configuration on the coefficients of forces and moments. Here blowing was from the upper slot at NPR=3, $C_\mu = 2.2 \times 10^{-4}$ over the half span grid at $M = 0.7$ and $\alpha = 0°$. A Richardson extrapolation was performed to estimate the coefficients on an "infinite" grid by $C_{\text{cont}} = C_{42\text{m}} + (C_{42\text{m}} - C_{12\text{m}})/(r^2 - 1)$, where $r = 1.5$. For all coefficients other than the rolling moment coefficient, the grid with 12.7×10^6 cells produced results that were less than 3% of the continuum estimate. For the roll the medium grid is approximately

Table 6.2: Effect of half-span grid resolution on coefficients of forces and moments for 20:1:1 stepped CC with IBC+ blowing at $C_\mu = 2.2 \times 10^{-4}$.

Cell count	1.7×10^6	12.7×10^6	42×10^6	Continuum
C_D	6.39×10^{-3}	5.55×10^{-3}	5.50×10^{-3}	5.46×10^{-3}
C_L	1.12×10^{-2}	9.74×10^{-3}	9.66×10^{-3}	9.60×10^{-3}
C_S	1.21×10^{-2}	1.24×10^{-2}	1.24×10^{-2}	1.25×10^{-2}
C_l	-4.56×10^{-4}	-1.14×10^{-3}	-1.21×10^{-3}	-1.26×10^{-3}
C_m	2.50×10^{-3}	2.46×10^{-3}	2.46×10^{-3}	2.47×10^{-3}
C_n	-3.95×10^{-3}	-3.52×10^{-3}	-3.47×10^{-3}	-3.42×10^{-3}

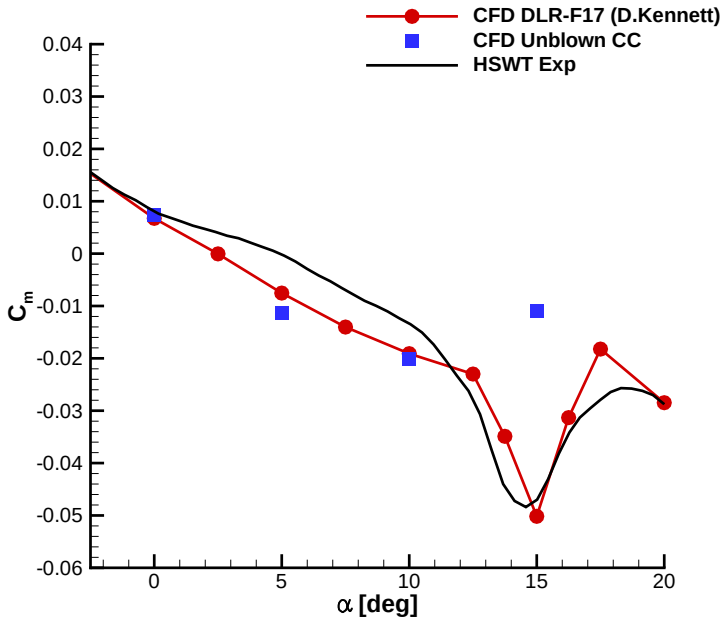

Figure 6.4: α vs C_m for unblown CC, simulated and experimental without flaps.

5% away from the finest grid. From these results, it was concluded that the medium grid gave reasonably accurate results while being computationally cost effective.

6.3 SACCON Pitch-up Behaviour

The SACCON was designed to produce challenging flows for numerical simulations. It has become well known for the strong pitch break as the angle of attack increases, which is due to the highly vortical flow from the combination of rounded and sharp leading edge contouring.

Figure 6.4 shows the predicted pitching moment for the SACCON without blowing, compared with the undeflected flap simulations and experiments. Here the unblown CC case uses a full span grid with approximately 25.4×10^6 cell volumes. The modifications to the geometry to accommodate the CC device appear to have had little effect on the

response in the lift to angle of attack variations for $\alpha < 10°$. The peak in pitch at $\alpha = 17.5°$ for the original unmodified geometry occurred at $\alpha = 15°$ for the unblown CC. This is largely due to the differences in turbulence model chosen, since Kennett used a k-ω model with a vortex limiter and the CC simulations here are with the k-ω SST without a vortex limiter. Small differences in the pitch up behaviour due to the modified trailing edge may also be expected. However, these results provide confidence that meaningful comparisons between CC and flaps for the SACCON for $\alpha < 10°$ can be made.

6.4 Jet Attachment

Simulations here were conducted on the half span grid, and results from blowing were combined with unblown as given in Eq. (6.1) to give a first order estimation of the forces and moments.

6.4.1 Coanda without step

The case without the step is geometrically identical to the circulation control geometry as investigated at low speeds by Hoholis [63], with the exception of reference lengths and moment reference points differing between the low speed DLR-F19 and high speed DLR-F17. Here, blowing over the unstepped case is considered at $\alpha = 0$, $NPR = 2.0$.

As shown in Fig. 6.5a, blowing at $NPR = 2.0$ ($C_\mu = 2.6 \times 10^{-4}$) caused the underexpanded jet to detach from the Coanda surface. This detachment was due to a shock-boundary layer interaction near the slot exit. As a result the circulation control device failed to generate any substantial changes in the forces and moments, as would be found with a physical flap. This result compares well to the findings from Chapter 4, where a 10:1 radius to slot height Coanda was also not favourable for CC at transonic conditions.

The combined efficiencies (with loads given in Eq. (6.1)) for the full UCAV with blowing over the left wing only were $\Delta C_D/C_\mu = -0.6542$, $\Delta C_L/C_\mu = 12.0122$, $\Delta C_S/C_\mu = 0.0297$, $\Delta C_l/C_\mu = 5.8867$, $\Delta C_n/C_\mu = 0.3511$, and $\Delta C_m/C_\mu = 5.0910$ for $C_\mu = 2.6 \times 10^{-4}$.

6.4.2 Coanda with step

The stepped configuration uses the same Coanda radius as the above, but with a slot and step both having 50% the height of the slot from the unstepped case (see Fig. 6.2). With blowing at $NPR = 3$ ($C_\mu = 2.2 \times 10^{-4}$) the underexpansion of the jet did not cause separation, since the shock-boundary layer interaction was replaced with a shock-shear interaction by introduction of the step. Figure 6.5b shows that the jet attached

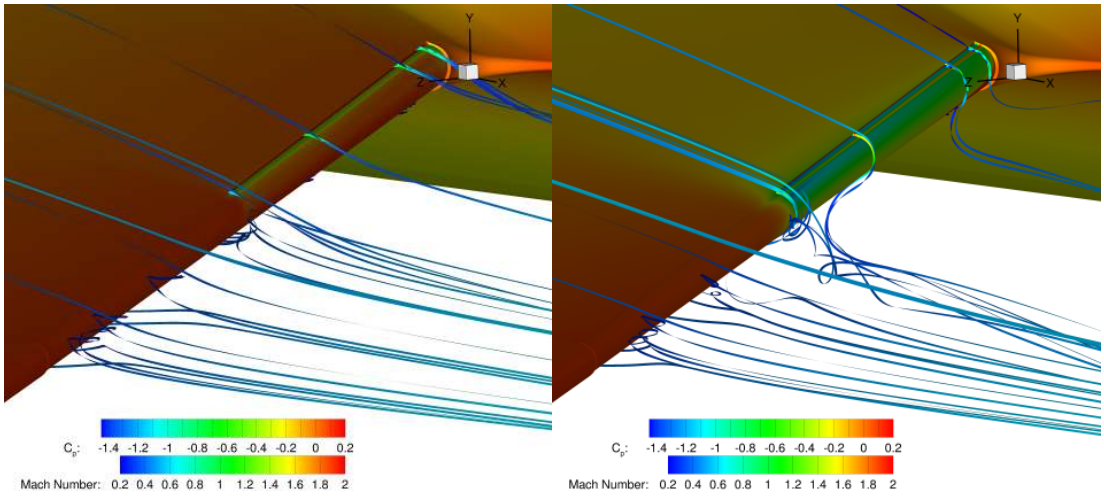

(a) Unstepped IBC+ at $C_\mu = 2.6 \times 10^{-4}$ ($NPR = 2$).

(b) Stepped IBC+ at $C_\mu = 2.2 \times 10^{-4}$ ($NPR = 3$).

Figure 6.5: Contours of surface pressure with streamtrace ribbons coloured with Mach contours at the trailing edge.

to the Coanda surface and entrained the upper surface flow, which is evident by the reduction in C_p on the surface and an increase in M as coloured on the streamline ribbons.

In contrast to the unstepped case above the efficiencies achieved for blowing at $C_\mu = 2.2 \times 10^{-4}$ over the stepped IBC+ configuration was $\Delta C_D/C_\mu = 0.8903$, $\Delta C_L/C_\mu = 101.5760$, $\Delta C_S/C_\mu = -4.9332$, $\Delta C_l/C_\mu = 49.4335$, $\Delta C_n/C_\mu = 1.9336$, and $\Delta C_m/C_\mu = -41.6764$. The lift, roll and pitch changes for the stepped case at a lower C_μ are approximately 8 times greater then the unstepped case. In comparison with the 2D study in Chapter 4, the change in sectional lift coefficient due to blowing was ≈ 100, while the change in sectional pitching moment coefficient was ≈ 20 in the nose down direction.

Additional blowing over the upper slot of the left hand side inboard Coanda (IBC+) resulted in attachment of the jet until $NPR = 4.0$ ($C_\mu = 3.0 \times 10^{-4}$). At blowing rates above $NPR = 4.5$ ($C_\mu = 3.4 \times 10^{-4}$) the jet detached from the upper surface. As shown in Figs. 6.6 and 6.7, the effect of the detachment caused a significant drop in the loads and moments generated by the circulation control device. Blowing over the lower slot (IBC-) gave an approximately symmetric shift in the loads and moments. In Figs. 6.6 and 6.7, negative C_μ corresponds to blowing over the lower surface of the Coanda.

At $C_\mu = (-)3.0 \times 10^{-4}$ (lower slot) the jet starts to detach from the Coanda surface towards the root of the slot. The effect on the loads and moments are most evident in Figs. 6.6 and 6.7 at 5° angle of attack. Figure 6.8d shows that the jet remained attached only to the middle section of the inboard Coanda with blowing at $C_\mu = (-)3.0 \times 10^{-4}$ and $\alpha = 5°$.

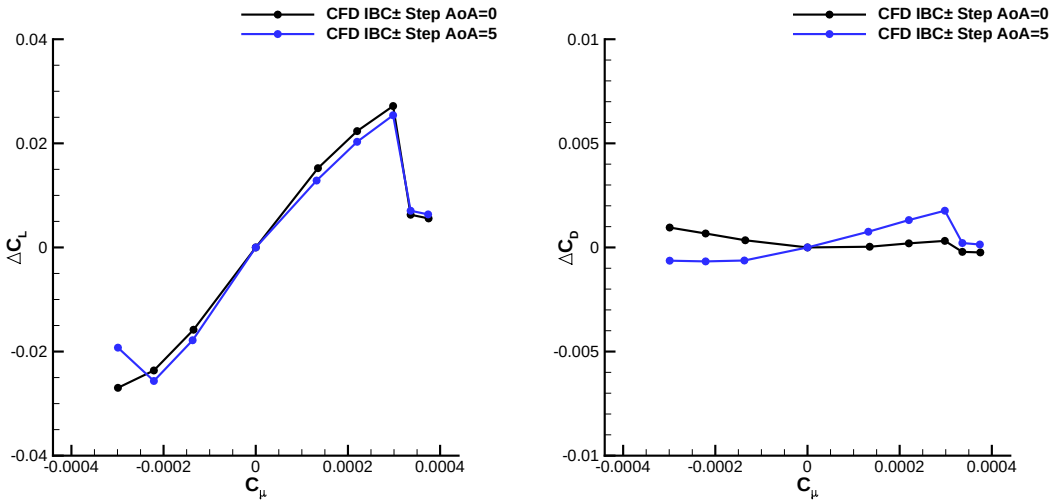

Figure 6.6: ΔC_L and ΔC_D with respect to blowing over from the circulation control device at the inboard of the left wing (lower slot negative C_μ).

6.5 Comparison of Stepped CC with Flaps

Numerical simulations CC here use the full span grid with blowing only over the left hand wing, in line with the experiments. Comparisons are made between the SACCON with an inboard flap at 10° positive and negative deflection angles (IB+10, IB-10 respectively) and the stepped inboard Coanda (IBC) device blowing from the upper, lower and both slots at NPR+3, NPR-3 and NPR±3, respectively. This corresponds to $C_\mu = 2.2 \times 10^{-4}$, and $C_\mu = 4.4 \times 10^{-4}$ when using both slots. Experimental results of flaps are taken from the BAE Systems' HSWT data set [108], while the CFD flapped results are from Kennett [61].

The circulation induced by blowing over either slot of the stepped Coanda on the inboard half of the wing resulted in a change in lift and drag in excess of simulations of an inboard flap deflected by 10° for $\alpha < 10°$ as shown in Fig. 6.9. Blowing over both slots had a negligible effect on the lift, and a small negative change in the drag coefficient.

For $C_\mu = 2.2 \times 10^{-4}$ the device outperforms the representative flap deflection for use as a roll effector. This is shown in Fig. 6.10 which compares the pitch, roll and yaw changes generated in the experiment, simulations by Kennett and the range of moments by the stepped IBC device. The effect on pitch when blowing over one side of the Coanda surface is similar to the flap deflection.

Blowing over both upper and lower LIBC slots at a total $C_\mu = 4.4 \times 10^{-4}$ ($NPR = \pm 3$) also here had negligible effects on the pitch and roll over the angle of attack range, while an effective thrust from the left hand wing produced a constant positive yaw moment of approximately $\Delta C_n = 3 \times 10^{-4}$ (nose right). Figure 6.11 shows the

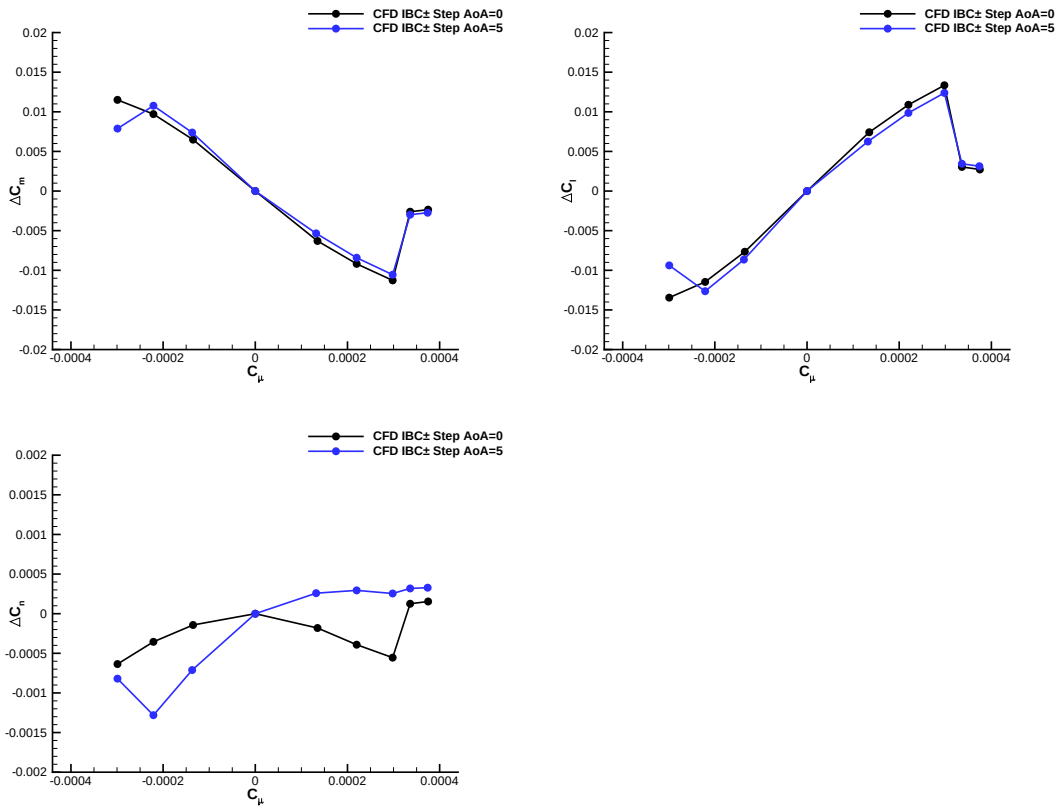

Figure 6.7: Pitch (C_m), roll (C_l) and yaw (C_n) with respect to blowing at the inboard of the left wing (lower slot negative C_μ).

jets remained attached to the Coanda at this blowing rate until approximately 90° from the slot exits, where the jets meet and then separate. The experiment found $\Delta C_n = -5 \times 10^{-4}$ using LOB±10 split flaps for $\alpha < 5°$ [108]. The ratio between the distance from the centre of the outboard and the centre of the inboard flaps to the moment reference point is approximately OB/IB=1.5. Applying this factor to the yaw from blowing over both LIBC slots suggests that blowing over similar LOBC slots would produce approximately the same yaw moment as a ROB±10 split flap. For detached jets at higher blowing rates, it is likely that the yaw due to blowing over both slots can be increased further. For low speeds, Hoholis found that blowing from upper and lower slots over the full span gave enough yaw control to trim the aircraft [109].

Figures 6.12 and 6.13 shows the effect of blowing over the lower Coanda surface has on the C_p over the entire aircraft. Here, the ΔC_p is shown with respect to the unblown configuration. At $\alpha = 0°$, blowing over the lower surface (Fig. 6.12a) gives an approximately symmetric response in the flow compared with blowing over the upper surface (Fig. 6.13a). The majority of the change in surface pressures due to blowing occurs local to the Coanda surface, however the tip vortex on the lower left hand side is altered as an effect of blowing.

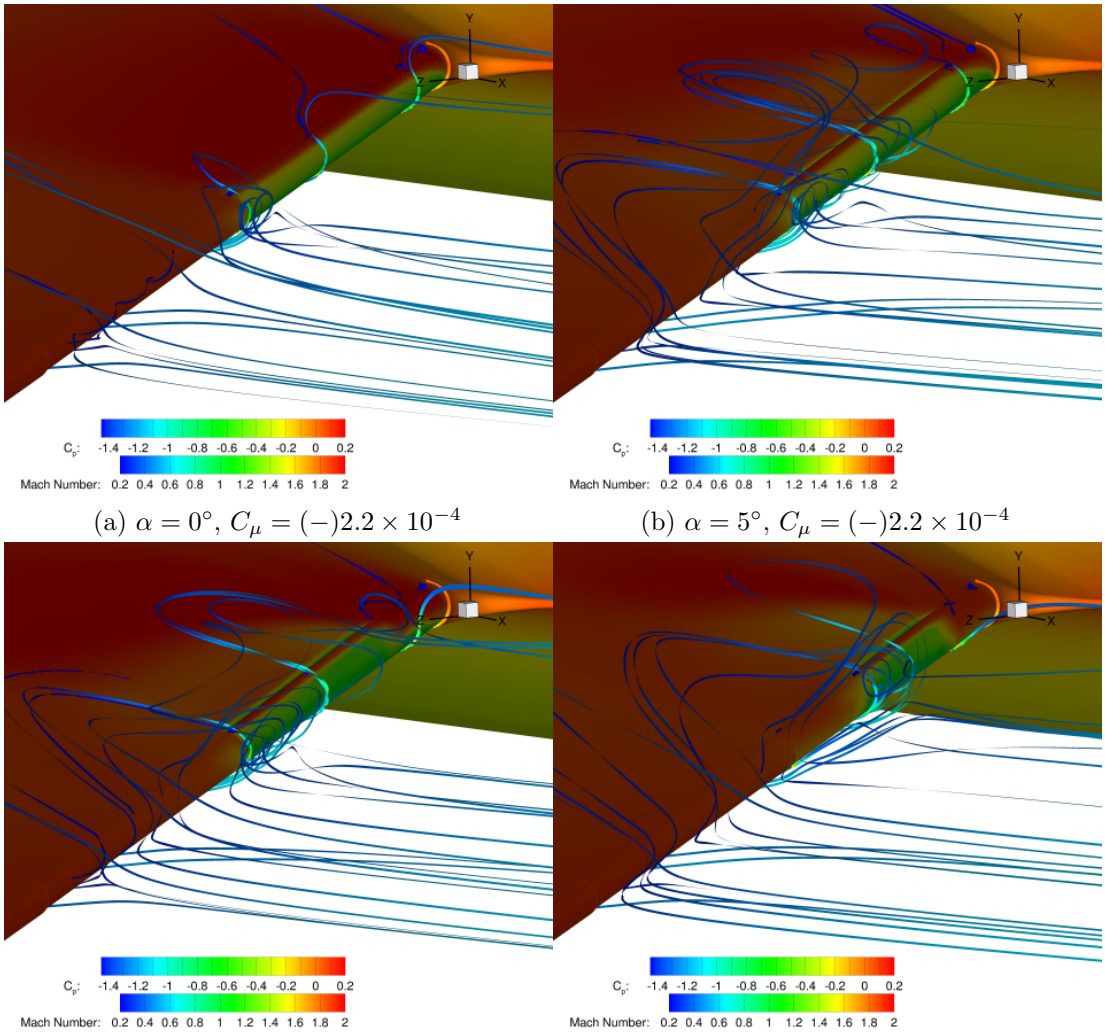

(a) $\alpha = 0°$, $C_\mu = (-)2.2 \times 10^{-4}$

(b) $\alpha = 5°$, $C_\mu = (-)2.2 \times 10^{-4}$

(c) $\alpha = 0°$, $C_\mu = (-)3.0 \times 10^{-4}$

(d) $\alpha = 5°$, $C_\mu = (-)3.0 \times 10^{-4}$

Figure 6.8: Streamtrace ribbons and surface C_p with over lower Coanda (IBC-).

At $\alpha = 10°$, blowing over the lower surface produced a large negative (nose left) response in the yaw moment, as shown in Fig. 6.10. This is possibly due to the jet wrapping onto the upper surface and increasing the size of the separated flow near the trailing edge of the upper surface, as shown in Fig. 6.14. This behaviour was also observed in Fig. 6.8 for $\alpha = 5°$ In addition the tip vortex, which sits on the upper surface at $\alpha = 10°$ is increased in strength (Fig. 6.15). Due to the long moment arm at the tip, a small increase in drag leads to relatively large changes in yaw.

The mean flow broke down for $\alpha = 15°$, such that the jet did not attach when blowing over the lower surface and so had diminished control power. However the predicted loads and moments were similar to those from the flaps.

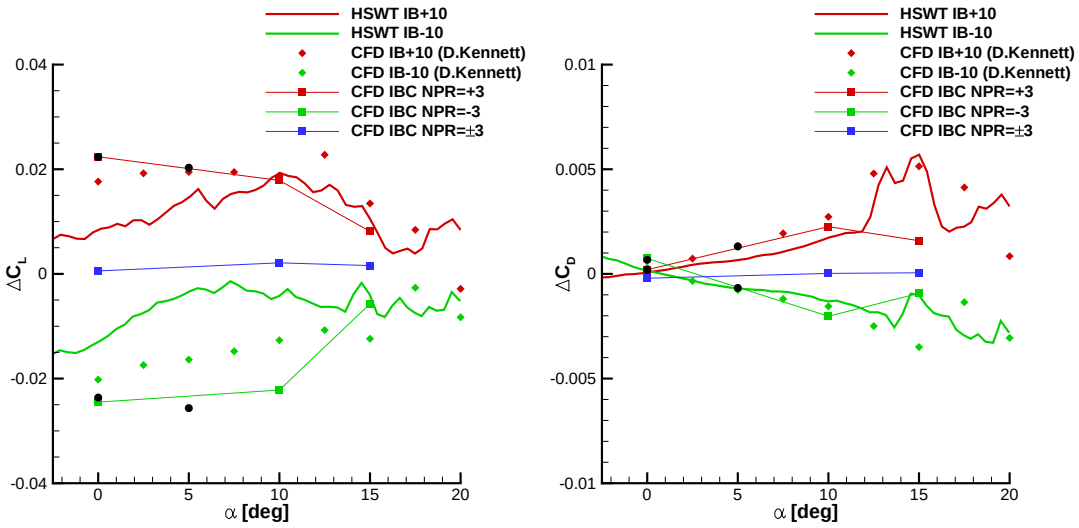

Figure 6.9: ΔC_L and ΔC_D achieved with blowing compared with experiment and CFD with flaps. Both simulations and experiment were conducted with actuation on the left inboard only. Here black circles represent results from half span simulations of CC merged with unblown half span, while connected squares are with the full span grid.

6.6 CC for Roll, Pitch and Yaw Control

Using the half span simulations, an estimate for the response in the forces and moments for blowing over both left and right hand wings was made. Table 6.3 shows the changes in force and moment coefficients with respect to blowing at NPR=3 for IBC blowing from both slots on the left wing (using full span simulation), blowing from the upper slot on both wings and blowing from opposite slots on both wings. As shown in Figs. 6.9 and 6.10, blowing over upper and lower surface simultaneously generated a small decrease in drag and a small yaw moment contribution. The effect on pitch and roll was of the same order of magnitude to the yaw, suggesting that a yaw moment manoeuvre using CC is not completely decoupled here. For blowing over both upper IBC slots using two half span simulations, a large increase in the lift and nose down pitching moment was observed. Due to the procedure in Eq. (6.1) the side force, roll and yaw are estimated to be exactly 0, however a full span simulation would be expected to give small, non-zero values here. A roll manoeuvre using LIBC+ and RIBC- at NPR=3 gave a large response to the roll, with relatively small responses in the other moments and loads. As with the yaw moment, a larger control power could be achieved using less momentum by blowing over outboard slots.

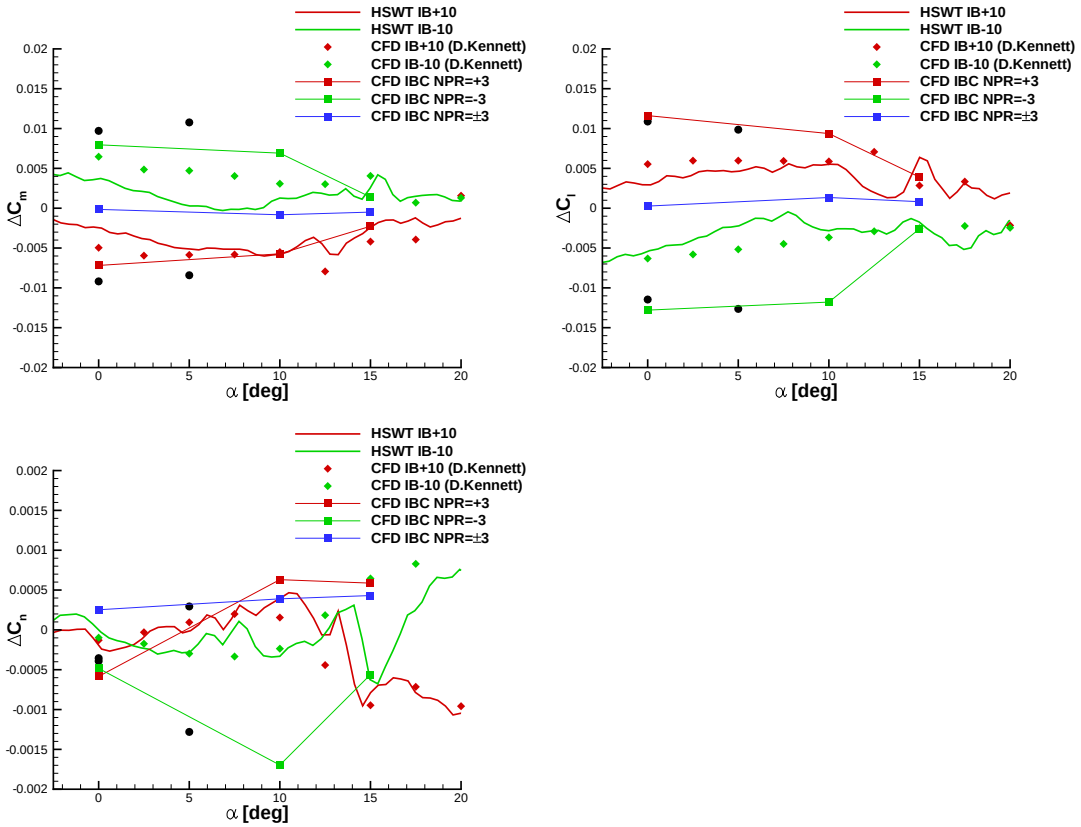

Figure 6.10: Pitch (C_m), roll (C_l) and yaw (C_n) at a constant rate of blowing over a range of angles of attack. Here black circles represent results from half span simulations of CC merged with unblown half span, while connected squares are with the full span grid.

6.7 Summary of Results

The capabilities of using circulation control as a replacement for an inboard flap on the SACCON UCAV demonstrator have been demonstrated. The jet over a 10:1 Coanda surface did not attach to the surface and the CC system could not generate the forces and moments needed to be used for control. However when using a step it was found that with blowing over the Coanda on the inboard half of the left wing the loads and moments generated by circulation control can exceed those of a 10° flap deflection at $M = 0.7$ for low to moderate angles of attack. For situations when the mean flow breaks down due to shock boundary layer interactions, severely separated and highly vortical flows; it appears that CC is limited in it's control effectiveness. However, the effectiveness was comparable to that of a conventional control surface.

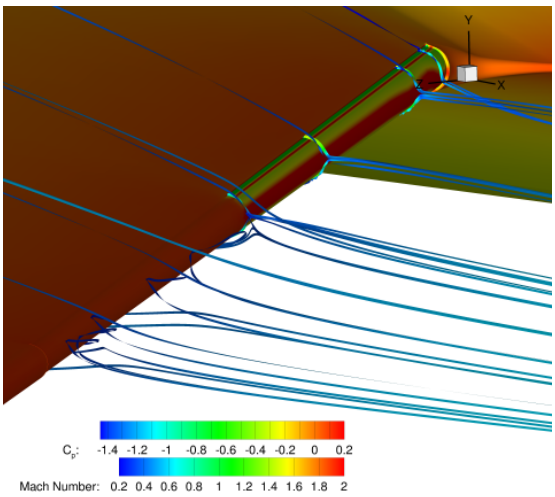

Figure 6.11: Streamtrace ribbons and surface C_p with over both Coanda slots (IBC±).

Table 6.3: First order estimate for yaw, pitch and roll manoeuvre blowing at a total $C_\mu = 4.4 \times 10^{-4}$ and $\alpha = 0$.

Config.	LIBC±	LIBC+ RIBC+	LIBC+ RIBC-
$\Delta C_D/C_\mu$	-0.47	0.89	1.97
$\Delta C_L/C_\mu$	1.28	101.58	-2.92
$\Delta C_S/C_\mu$	0.31	0.00	-2.85
$\Delta C_l/C_\mu$	0.60	0.00	50.76
$\Delta C_m/C_\mu$	0.34	-41.68	1.20
$\Delta C_n/C_\mu$	0.45	0.00	-0.15

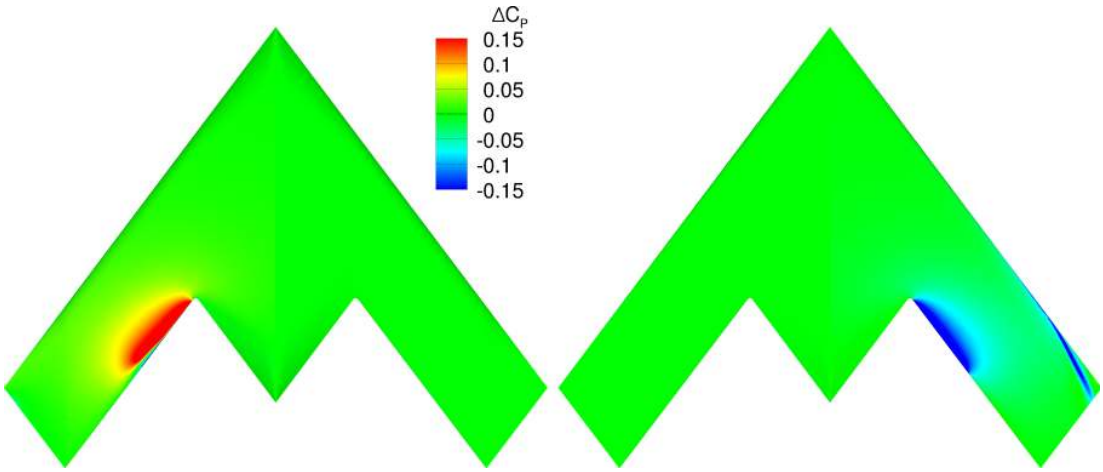

(a) $\alpha = 0°$

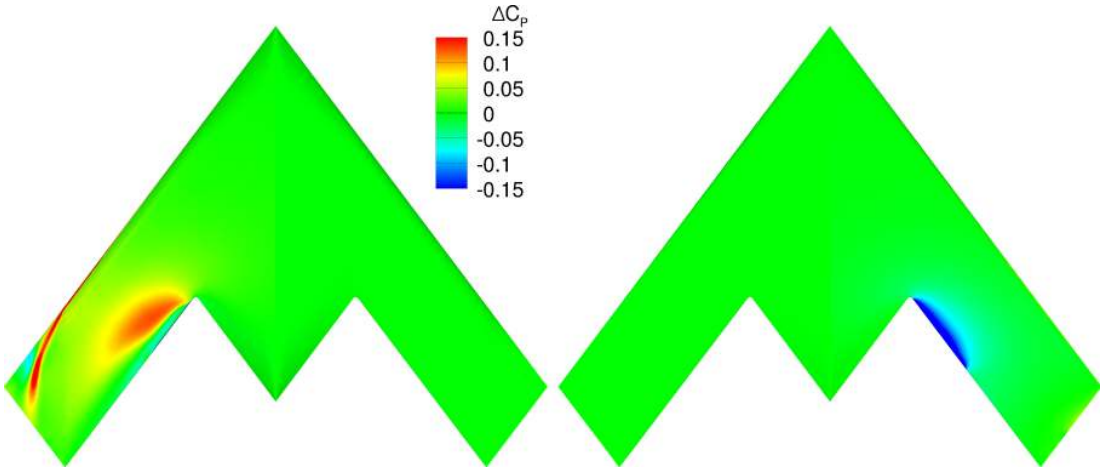

(b) $\alpha = 10°$

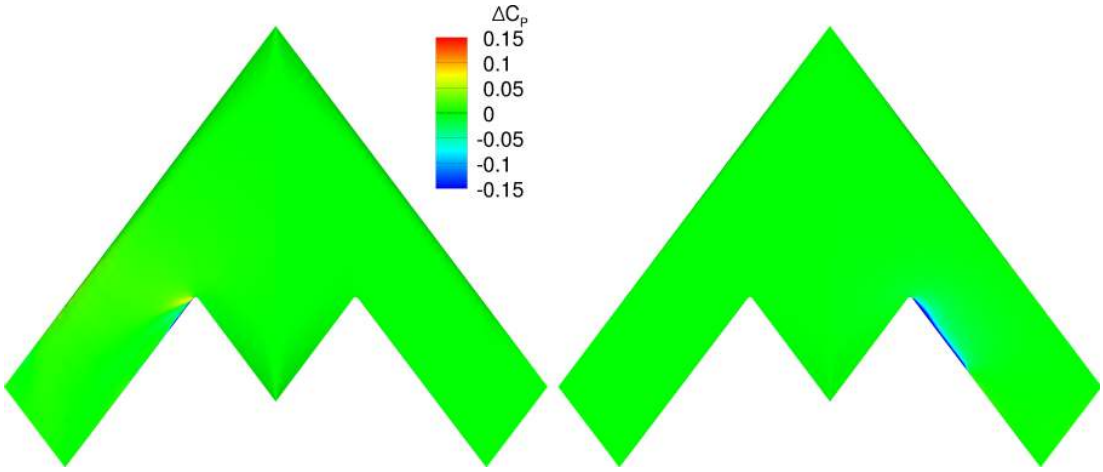

(c) $\alpha = 15°$

Figure 6.12: Difference in C_p with unblown case for blowing over LIBC- at NPR=3, $C_\mu = -2.2 \times 10^{-4}$. The left image shows the upper surface, while the right shows the lower.

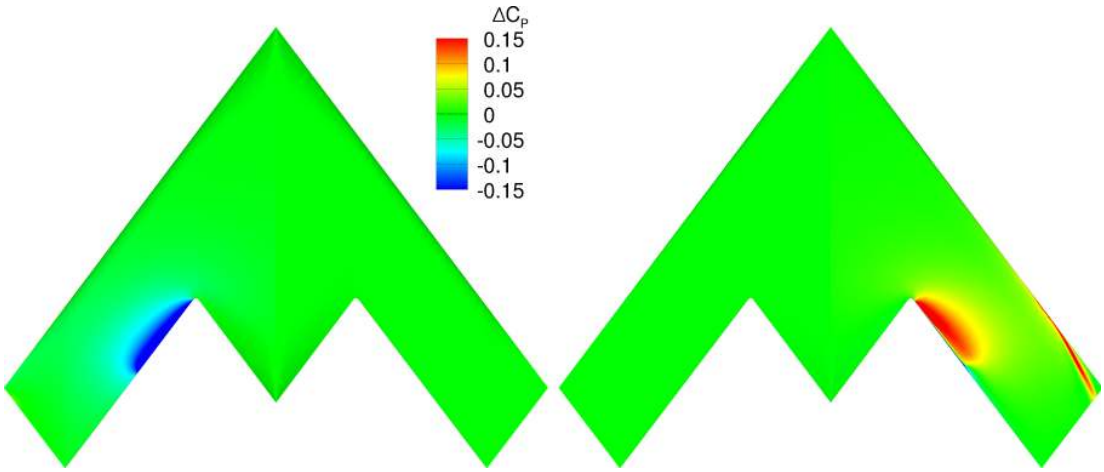

(a) $\alpha = 0°$

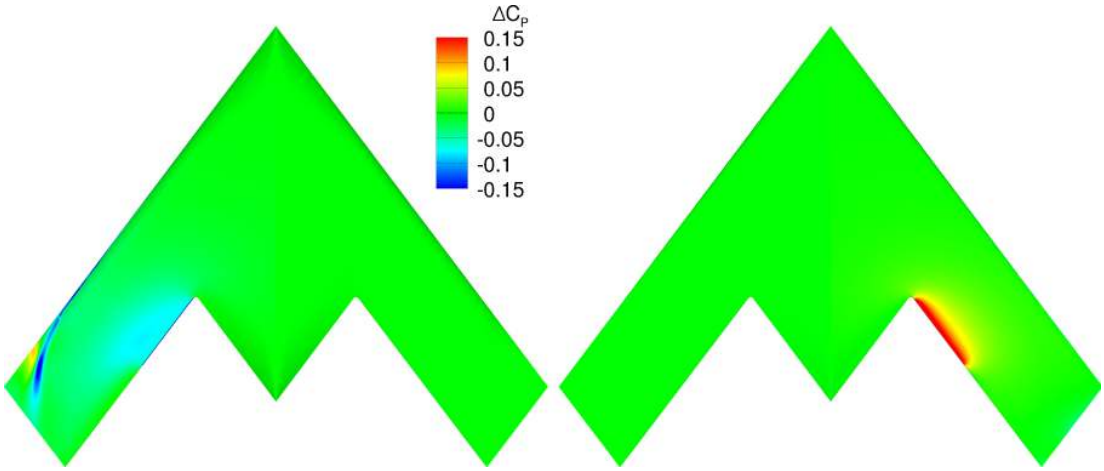

(b) $\alpha = 10°$

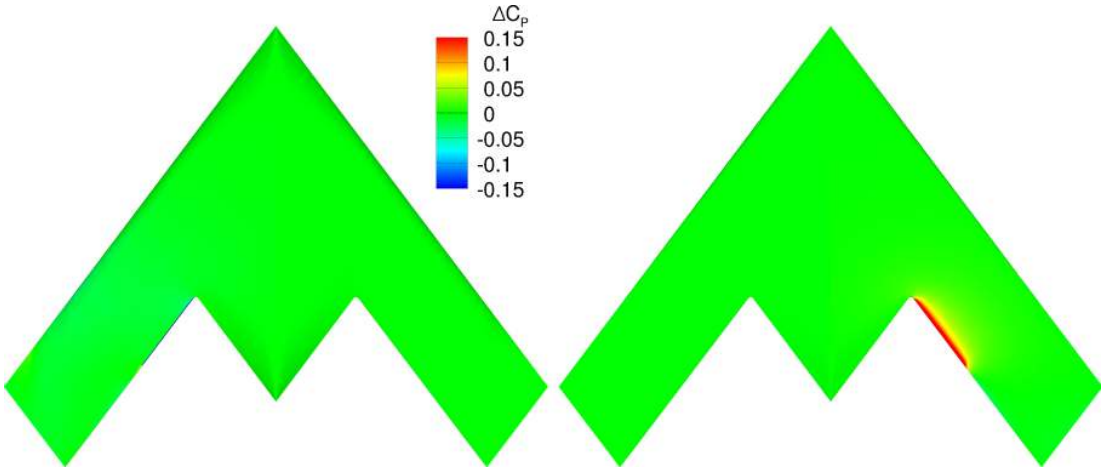

(c) $\alpha = 15°$

Figure 6.13: Difference in C_p with unblown case for blowing over LIBC+ at NPR=3, $C_\mu = 2.2 \times 10^{-4}$. The left image shows the upper surface, while the right shows the lower.

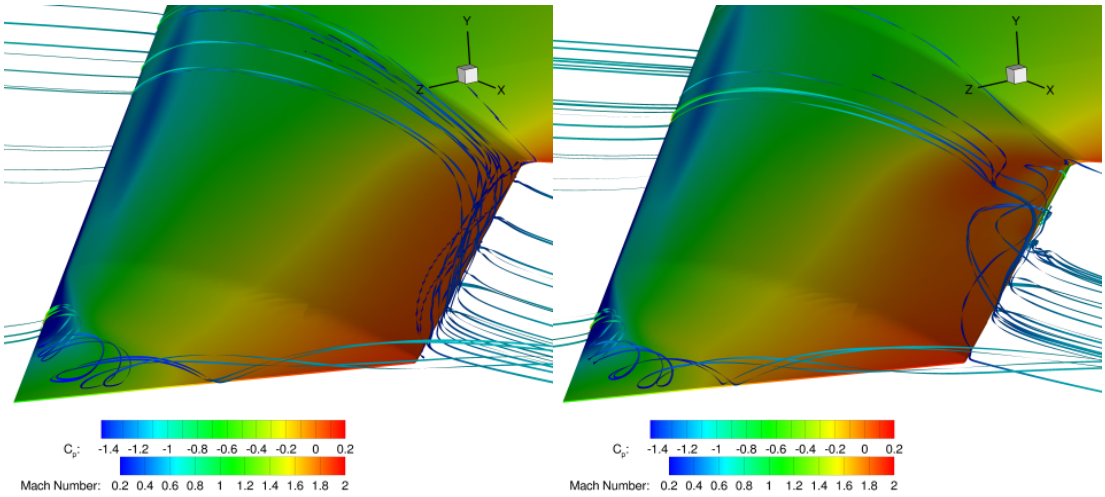

(a) Unblown. (b) IBC- at $C_\mu = -2.2 \times 10^{-4}$ ($NPR = 3$).

Figure 6.14: Contours of surface pressure with streamtrace ribbons coloured with Mach contours at $\alpha = 10°$.

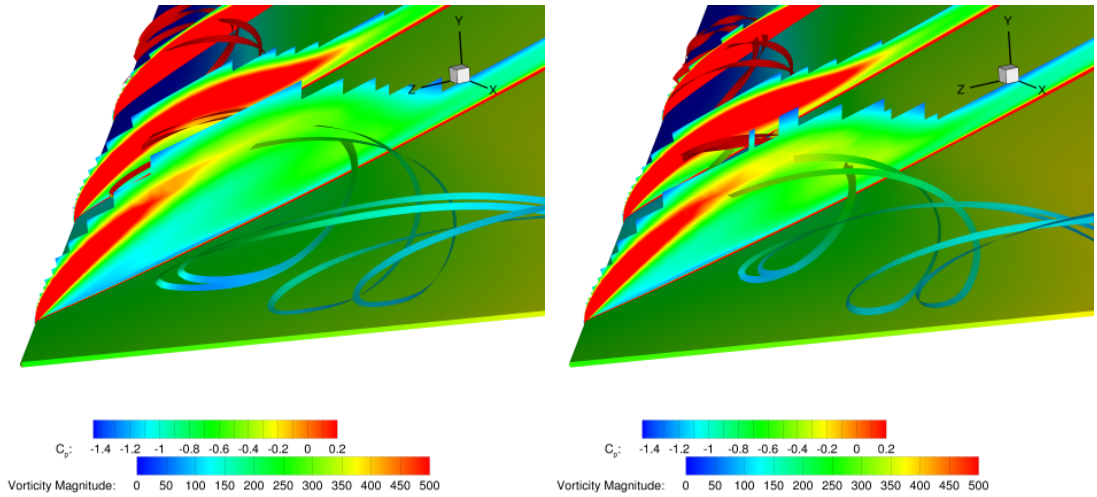

(a) Unblown. (b) IBC- at $C_\mu = -2.2 \times 10^{-4}$ ($NPR = 3$).

Figure 6.15: Tip vortex at $\alpha = 10°$.

Chapter 7

Conclusions

The fundamental aim of this thesis was to increase the understanding of circulation control in transonic flows using a supersonic Coanda jet.

Following a review of the literature, an assessment into the use of RANS simulations for transonic circulation control and supersonic Coanda jets were made. Here, use of the methods were compared with experimental data to establish the modelling requirements. A design study and an optimisation of the Coanda surface for transonic circulation control on a representative supercritical aerofoil section were conducted. The literature survey had suggested that well-designed converging-diverging nozzles and converging nozzles with a step promote supersonic Coanda jet attachment for cases without a freestream. It was found that such devices also promote attachment for transonic circulation control and increase the control power available. Circulation control as applied to a research transonic UCAV demonstrator was then investigated. In line with the findings from two dimensional studies, circulation control was able to match the performance of traditional physical control surfaces for benign transonic flows.

This chapter provides concluding remarks from the separate parts of the investigation and makes recommendations for future research.

7.1 Validation

From the validation cases considered, the results suggest that RANS based CFD capabilities can give reasonably reliable results for design purposes. In terms of surface pressures, loads and moments, the k-ω, SST and EARSM all performed similarly from a "global" perspective. At finer details such as on the Coanda surface for supersonic jets, with and without a transonic freestream the EARSM did give an improved prediction of the surface pressures and separation bubble size and locations.

7.2 2D Design Study of Coanda Surfaces

The design study involved different nozzles, nozzle exit geometries and Coanda surfaces to investigate which design performs most consistently over a range of blowing coefficients. It was found that replicating the lift, drag and moment characteristics of a 25% chord aileron at $\delta = 4.0°$ is possible with a converging nozzle and a Coanda radius to slot height ratio of 10:1. However, a wider range of operating pressure ratios were found for a 21:1 ratio. For the converging nozzle the limiting factor was the strong shock-induced separation created by the under-expansion of the nozzle flow.

The results for converging-diverging nozzles showed that, as expected, the under-expansion related shock-induced separation can be delayed to higher pressure ratios. Furthermore, for the converging nozzle, it was found that the shock-induced separation can be delayed by applying a small step in the geometry between the nozzle exit and the Coanda surface. It was shown that using either the converging-diverging or the stepped Coanda geometry can perform equivalently to an aileron deflection angle of up to 8°.

The effects of angle of attack were in addition considered with a comparison between circulation control and a 3° deflected aileron. The performance of the CC devices at a constant blowing rate performed similarly to the deflected aileron. Each device considered lost effectiveness at the same rate, due to the mean flow and upper surface boundary layer separating from a strong shock boundary layer interaction.

7.3 Optimisation

The findings from the optimisation study showed that relatively small changes to a simply parametrised Coanda surface can give significant improvements to the efficiency of transonic circulation control. Here the optimisation algorithm converged to a design which had a large radius of curvature at the slot exit but turned the jet more than a purely elliptical Coanda surface would.

The Coanda shape designed for one NPR at transonic conditions not only performed well on design, but also at off-design conditions. In addition the multipoint optimisation found a shape that was the same as the single point result. These results suggest that is may be advisable to perform Coanda shape optimisation only for a transonic case with supersonic blowing, and that it is likely to offer performance improvements in off-design conditions, which would significantly reduce the expense of performing such optimisation studies.

The optimisation study did however only focus upon blowing over the upper Coanda surface, and in addition the multipoint optimisation weighted in favour of the transonic conditions. Future optimisation studies are recommended to first perform a mission

analysis to identify the proportion of flight regimes with which to weigh design points.

7.4 SACCON

The results from transonic circulation control on the SACCON UCAV demonstrator have shown that Coanda design recommendations from 2D studies give good insights into their performance for 3D delta wing type flows. This finding is similar to that of Wood, who assessed the applicability of simple sweep theory to circulation control.

An important finding from the assessment of circulation control against traditional devices for the SACCON have suggested that circulation control has the potential to offer similar performance to flaps for roll, pitch and yaw control. The performance of conventional controls was matched on the SACCON with CC when the mean flow was largely attached and where the flow separation and highly vortical flows did not dominate.

7.5 Recommendations for Further Work

The studies on supersonic Coanda jets without a freestream highlighted interesting details related to the jet attachment and unsteadiness. Future numerical studies may consider investigating the three-dimensionality of these flows in order to assess the spanwise instabilities of the shear layer. An understanding of these instabilities may in turn identify geometric details, such as the sawtooth slot profile which increases the NPR range for attachment and also minimises acoustic effects.

Further research into the use of anisotropic RANS turbulence models for predicting supersonic Coanda jet flows is recommended. For modelling the shear layer instabilities, sawtooth and acoustic effects of supersonic Coanda jets and transonic CC may require higher fidelity models such as DES or LES.

For circulation control, an investigation into the effectiveness of the sizing of Coanda devices in transonic flows is recommended for future studies. In doing so it may be possible to minimise further the drag penalty due to the bluntness of the Coanda device.

From the 2D comparisons between CC and the aileron deflection, blowing removed the detachment region seen at the trailing edge when using a deflected aileron. It is possible that control of this separation using blowing from circulation control could have implications for controlling shock buffet.

An assessment into the behaviour the optimised Coanda should be applied to a full UCAV configuration to assess the effect of a 2D optimised shape on the 3D flow behaviour associated with UCAV wings. From the findings between the design study and 3D UCAV case, it is expected that the 2D optimised Coanda will also perform comparatively on a 3D geometry. It may also be beneficial to instead optimise the

baseline aerofoil profile to accommodate a circulation control device more effectively. In addition, optimisation of combinations of nozzles, Coanda surfaces and steps would be an interesting contribution to the literature.

For three dimensional configurations with circulation control, investigations into extending the operating range in terms of angles of attack, sideslip, Mach and Reynolds numbers are recommended. Here it may be possible that combining CC with other flow control devices which control the flow separation and vortical flow features on the main aircraft body would be advantageous.

Bibliography

[1] Paterson, E. G., Baker, W. J., Kunz, R. F., and Peltier, L. J., "RANS and Detached-Eddy Simulation of the NCCR Airfoil," *31st Annual International Symposium on Computer Architecture*, 2004, pp. 112–122.

[2] Gatski, T. B., Rumsey, C. L., and Manceau, R., "Current trends in modelling research for turbulent aerodynamic flows," *Philosophical Transactions of the Royal Society A: Mathematical, Physical and Engineering Sciences*, Vol. 365, No. 1859, October 15 2007, pp. 2389–2418.

[3] Alexander, M. G., Anders, S. G., Johnson, S. K., Florance, J. P., and Keller, D. F., "Trailing Edge Blowing on a Two-Dimensional Six-Percent Thick Elliptical Circulation Control Airfoil up to Transonic Conditions," Tech. Rep. TM-2005-213545, NASA, 2005.

[4] Englar, R. J., "Two-Dimensional Transonic Wind Tunnel Tests of Three 15-Percent Thick Circulation Control Airfoils," Tech. Rep. AD882075, DTNSRDC, 1970.

[5] Wilkerson, J. B. and Montana, P. S., "Transonic Wind Tunnel Test of a 16-Percent-Thick Circulation Control Airfoil With One-Percent Asymmetric Camber," Tech. Rep. ASED-82/03, DTNSRDC, 1982.

[6] Carpenter, P. W. and Green, P. N., "The Aeroacoustics and Aerodynamics of High-Speed Coanda Devices, Part 1: Conventional Arrangement of Exit Nozzle and Surface," *Journal of Sound and Vibration*, Vol. 208, No. 5, 1997, pp. 777–801.

[7] Sawada, K. and Asami, K., "Numerical Study on the Underexpanded Coanda Jet," *Journal of Aircraft*, Vol. 34, No. 5, 1997, pp. 641–647.

[8] Abramson, J. and Rogers, E. O., "High Speed Characteristics of Circulation Control Airfoils," *AIAA 21st Aerospace Sciences Meeting*, AIAA, 1983, p. 265.

[9] Schlecht, R. and Anders, S. G., "Parametric Evaluation of Thin, Transonic Circulation-Control Airfoils," *45th AIAA Aerospace Sciences Meeting*, AIAA, 2007, p. 272.

[10] Carpenter, P. W. and Smith, C., "The Aeroacoustics and Aerodynamics of High-Speed Coanda Devices, Part 2: Effects of Modifications for Flow Control and Noise Reduction," *Journal of Sound and Vibration*, Vol. 208, No. 5, 1997, pp. 803–822.

[11] Gregory-Smith, D. G. and Senior, P., "The Effects of Base Steps and Axisymmetry on Supersonic Jets Over Coanda Surfaces," *International Journal of Heat and Fluid Flow*, Vol. 15, No. 4, 1994, pp. 291–298.

[12] Cornelius, K. C. and Lucius, G. A., "Physics of Coanda Jet Detachment at High-Pressure Ratio," *Journal of Aircraft*, Vol. 31, No. 3, 1994, pp. 591–596.

[13] Bevilaqua, P. M. and Lee, J. D., "Design of Supersonic Coanda Jet Nozzles," *NASA. Ames Research Center Proceedings of the Circulation-Control Workshop*, NASA, 01 May 1987, pp. 289–312.

[14] Von Glahn, U. H., "Use of the Coanda effect for jet deflection and vertical lift with multiple-flat-plate and curved-plate deflection surfaces," Tech. Rep. TN-4377, NACA, 1958.

[15] Dvorak, F. A. and Choi, D. H., "Analysis of Circulation-Controlled Airfoils in Transonic Flow," *Journal of Aircraft*, Vol. 20, No. 4, 1983, pp. 331–337.

[16] Couluris, G. J., Signor, D., and Phillips, J., "Cruise-Efficient Short Takeoff and Landing (CESTOL): Potential Impact on Air Traffic Operations," Tech. Rep. CR-2010-216392, NASA, 2010.

[17] Cook, M. V., Buonanno, A., and Erbslöh, S. D., "A Circulation Control Actuator for Flapless Flight Control," *Aeronautical Journal*, Vol. 112, No. 1134, 2008, pp. 483–489.

[18] Lin, J. C., Andino, M. Y., Alexander, M. G., Whalen, E. A., Spoor, M. A., Tran, J. T., and Wygnanski, I. J., "An Overview of Active Flow Control Enhanced Vertical Tail Technology Development," *54th AIAA Aerospace Sciences Meeting*, AIAA, 2016, p. 56.

[19] Whalen, E., Shmilovich, A., Spoor, M., Tran, J., Vijgen, P., Lin, J., and Andino, M., "Flight Test of an AFC Enhanced Vertical Tail," *8th AIAA Flow Control Conference*, AIAA, 2016, p. 3927.

[20] Milholen II, W. E., Jones, G. S., Chan, D. T., Goodliff, S. L., Anders, S. G., Melton, L. P., Carter, M. B., Allan, B. G., and Capone, F. J., "Enhancements to the FAST-MAC Circulation Control Model and Recent High-Reynolds Number Testing in the National Transonic Facility," *31st AIAA Applied Aerodynamics Conference*, AIAA, 2013, p. 2794.

[21] Goeksel, B., Rechenberg, I., Greenblatt, D., and Paschereit, C., "Steady and Unsteady Plasma Wall Jets for Separation and Circulation Control," *3rd AIAA Flow Control Conference*, AIAA, 2006, p. 3686.

[22] Abramson, J., "Two-Dimensional Subsonic Wind Tunnel Evaluation of Two Related Cambered 15-Percent Thick Circulation Control Airfoils," Tech. Rep. ASED-373, DTNSRDC, 1977.

[23] Jones, G. S., Yao, C. S., and Allan, B. G., "Experimental Investigation of a 2D Supercritical Circulation-Control Airfoil Using Particle Image Velocimetry," *3rd AIAA Flow Control Conference*, AIAA, 2006, p. 3009.

[24] Wetzel, D. A., Griffin, J., and Cattafesta III, L. N., "Experiments on an Elliptic Circulation Control Aerofoil," *Journal of Fluid Mechanics*, Vol. 730, 2013, pp. 99–144.

[25] Englar, R. J., Jones, G. S., Allan, B. G., and Lin, J. C., "2-D Circulation Control Airfoil Benchmark Experiments Intended for CFD Code Validation," *47th AIAA Aerospace Sciences Meeting*, AIAA, 2009, p. 902.

[26] Wood, N. J. and Conlon, J. A., "Performance of a Circulation Control Airfoil at Transonic Speeds," *AIAA 21st Aerospace Sciences Meeting.*, AIAA, 1983, p. 83.

[27] Pulliam, T. H., Jespersen, D. C., and Barth, T. J., "Navier-Stokes Computations for Circulation Control Airfoils," *Von Karman Inst. for Fluid Dynamics Numerical Techniques for Viscous Flow Calculations in Turbomachinery Bladings*, Vol. 1, No. N86-30988, 1986, pp. 22–34.

[28] York, B., Dvorak, F., Strash, D., and Dash, S., "Improved Algorithms for Circulation-Control Airfoils in Transonic Flow," *25th AIAA Aerospace Sciences Meeting*, AIAA, 1987, p. 154.

[29] Dvorak, F. A. and Dash, S. M., "Wall Jet Analysis for Circulation Control Aerodynamics Part II: Zonal Modeling Concepts for Wall Jet/Potential Flow Coupling." *Proceedings of the Circulation-Control Workshop 1986.*, NASA, Washington, DC, USA, 1987, pp. 165–181.

[30] Shrewsbury, G., "Numerical Evaluation of Circulation Control Airfoil Performance Using Navier-Stokes Methods." *AIAA 24th Aerospace Sciences Meeting.*, AIAA, 1986, p. 286.

[31] Spaid, F. W. and Keener, E. R., "Boundary-Layer and Wake Measurements on a Swept, Circulation-Control Wing," *Proceedings of the Circulation-Control Workshop 1986.*, NASA, Washington, DC, USA, 1987, pp. 239–266.

[32] Tai, T., "The Determination of Drag of a Circulation Control Airfoil Tested in the 7-10-Foot Transonic Wind Tunnel," Tech. Rep. ADA152-162, DTIC Document, 1981.

[33] Gregory-Smith, D. G. and Gilchrist, A. R., "The Compressible Coanda Wall Jet-an Experimental Study of Jet Structure and Breakaway," *International Journal of Heat and Fluid Flow*, Vol. 8, No. 2, 1987, pp. 156–164.

[34] Bradshaw, P., "Effects of Streamline Curvature on Turbulent Flow," Tech. Rep. AG-169, AGARD, 1973.

[35] Spaid, F. W. and Keener, E. R., "Boundary-Layer and Wake Measurements on a Swept, Circulation-Control Wing," *Journal of Aircraft*, Vol. 28, No. 11, 1991.

[36] Wood, N., "Section Characteristics of a Finite, Swept Circulation Control Airfoil," *Journal of Aircraft*, Vol. 24, No. 1, 1987, pp. 38–44.

[37] Swanson, R. C., Rumsey, C. L., and Anders, S. G., "Aspects of Numerical Simulation of Circulation Control Airfoils," *AIAA Progress in Astronautics and Aeronautics*, Vol. 214, 2006, pp. 469–498.

[38] Hoholis, G., Steijl, R., and Badcock, K., "Circulation Control as a Roll Effector for Unmanned Combat Aerial Vehicles," *Journal of Aircraft*, Vol. 53, No. 6, 2016, pp. 1875–1889.

[39] Rumsey, C. L. and Nishino, T., "Numerical Study Comparing RANS and LES Approaches on a Circulation Control Airfoil," *International Journal of Heat and Fluid Flow*, Vol. 32, No. 5, 2011, pp. 847–864.

[40] Loth, J. L. and Boasson, M., "Circulation Controlled STOL Wing Optimization," *Journal of Aircraft*, Vol. 21, No. 2, 1984, pp. 128–134.

[41] Meunier, M., "Simulation and Optimization of Flow Control Strategies for Novel High-Lift Configurations," *AIAA Journal*, Vol. 47, No. 5, Jan-1 2009, pp. 1145–1157.

[42] Djojodihardjo, H., Majid, A. A., Laila, D., Romli, F. I., Basri, S., Hamid, A., and Faisal, M., "Numerical Simulation and Analysis of Coanda Effect Circulation Control for Wind-Turbine Application Considerations," *IIUM Engineering Journal*, Vol. 12, No. 3, 2011, pp. 19–42.

[43] Zhang, M. and He, L., "Combining Shaping and Flow Control for Aerodynamic Optimization," *AIAA Journal*, Vol. 53, No. 4, 2015, pp. 888–901.

[44] Tai, T. C., Kidwell, G. H., and Vanderplaats, G. N., "Numerical Optimization of Circulation Control Airfoils." *Journal of Aircraft*, Vol. 19, No. 2, 1982, pp. 145–150.

[45] Tai, T. C. and Kidwell, G. H., "Numerical Optimization of Circulation Control Airfoil at High Subsonic Speed." *Journal of Aircraft*, Vol. 22, No. 10, 1985, pp. 869–874.

[46] Papamoschou, D. and Roshko, A., "Observations of Supersonic Free Shear Layers," *Sadhana*, Vol. 12, No. 1-2, 1988, pp. 1–14.

[47] Slessor, M. D., Zhuang, M., and Dimotakis, P. E., "Turbulent Shear-Layer Mixing: Growth-Rate Compressibility Scaling," *Journal of Fluid Mechanics*, Vol. 414, 2000, pp. 35–45.

[48] Vreman, A. W., Sandham, N. D., and Luo, K. H., "Compressible Mixing Layer Growth Rate and Turbulence Characteristics," *Journal of Fluid Mechanics*, Vol. 320, 1996, pp. 235–258.

[49] Gomez, C. A. and Girimaji, S. S., "Explicit Algebraic Reynolds Stress Model (EARSM) For Compressible Shear Flows," *Theoretical and Computational Fluid Dynamics*, Vol. 28, No. 2, 2014, pp. 171–196.

[50] Goebel, S. G. and Dutton, J. C., "Experimental Study of Compressible Turbulent Mixing Layers," *AIAA Journal*, Vol. 29, No. 4, 1991, pp. 538–546.

[51] Rodionov, A. V., "On the Use of Boussinesq Approximation in Turbulent Supersonic Jet Modeling," *International Journal of Heat and Mass Transfer*, Vol. 53, No. 5-6, 2009, pp. 889–901.

[52] DeBonis, J. R., Oberkampf, W. L., Wolf, R. T., Orkwis, P. D., Turner, M. G., Babinsky, H., and Benek, J. A., "Assessment of Computational Fluid Dynamics and Experimental Data for Shock Boundary-Layer Interactions," *AIAA Journal*, Vol. 50, No. 4, Jan-1 2012, pp. 891–903.

[53] Georgiadis, N. J. and Yoder, D. A., "Recalibration of the Shear Stress Transport Model to Improve Calculation of Shock Separated Flows," Tech. Rep. 2013-217851, NASA, 2013.

[54] Barakos, G. and Drikakis, D., "Investigation of Nonlinear Eddy-Viscosity Turbulence Models in Shock/Boundary-Layer Interaction," *AIAA Journal*, Vol. 38, No. 3, 2000, pp. 461–469.

[55] NATO, "AVT-161 Assessment of Stability and Control Prediction Methods for NATO Air & Sea Vehicles," `https://www.cso.nato.int/ACTIVITY_META.asp?ACT=929`, 2012, Accessed: 12th Jan 2016.

[56] Cummings, R. M., "Introduction: SACCON Unihabited Combat Aerial Vehicle Experimental and Numerical Simulations," *Journal of Aircraft*, Vol. 49, No. 6, 2012, pp. 1541–1541.

[57] NATO, "AVT-201 Extended Assessment of Reliable Stability & Control Prediction Methods for NATO Air Vehicles," `https://www.cso.nato.int/ACTIVITY_META.asp?ACT=2060`, 2015, Accessed: 12th Jan 2016.

[58] Cummings, R. M. and Schütte, A., "The NATO STO Task Group AVT-201 on Extended Assessment of Stability and Control Prediction Methods for NATO Air Vehicles," *32nd AIAA Applied Aerodynamics Conference*, AIAA, 2014, p. 2394.

[59] Rein, M., Irving, J. P., Rigby, G., and Birch, T. J., "High Speed Static Experimental Investigations to Estimate Control Device Effectiveness and S&C Capabilities," *32nd AIAA Applied Aerodynamics Conference*, AIAA, 2014, p. 2004.

[60] Coppin, J. and Birch, T. J., "CFD Predictions of Control Effectiveness for a Generic Highly Swept UCAV Configuration," *32nd AIAA Applied Aerodynamics Conference*, AIAA, 2014, p. 2135.

[61] Kennett, D., Hoholis, G., and Badcock, K., "Numerical Simulation of Control Surface Deflections over a Generic UCAV Configuration at Off-design Flow Conditions," *32nd AIAA Applied Aerodynamics Conference*, AIAA, 2014, p. 2134.

[62] NATO, "AVT-239 Innovative Control Effectors for Manoeuvring of Air Vehicles," `https://www.cso.nato.int/ACTIVITY_META.asp?ACT=4343`, 2013, Accessed: 15th Dec 2015.

[63] Hoholis, G., Steijl, R., and Badcock, K., "The Application of Trailing Edge Circulation Control as a Roll Effector for Unmanned Combat Aerial Vehicles," *Royal Aeronautical Society Applied Aerodynamics Conference*, 2014, p. 19.

[64] Steijl, R., Barakos, G., and Badcock, K., "A Framework for CFD Analysis of Helicopter Rotors in Hover and Forward Flight," *Int. J. Numer. Meth. Fluids*, Vol. 51, 2006, pp. 819–847.

[65] Steijl, R. and Barakos, G., "Sliding Mesh Algorithm for CFD Analysis of Helicopter Roto-Fuselage Aerodynamics," *Int. J. Numer. Meth. Fluids*, Vol. 58, 2008, pp. 527–549.

[66] Badcock, K., Richards, B., and Woodgate, M., "Elements of Computational Fluid Dynamics on Block Structured Grids Using Implicit Solvers," *Progress in Aerospace Sciences*, Vol. 36, 2000, pp. 351–392.

[67] Barakos, G., Steijl, R., Badcock, K., and Brocklehurst, A., "Development of CFD Capability for Full Helicopter Engineering Analysis." 31st European Rotorcraft Forum, 13-15 September 2005, Florence, Italy, 2005.

[68] Carrión, M., Woodgate, M., Steijl, R., Barakos, G., Gomez-Iradi, S., and Munduate, X., "Understanding Wind-Turbine Wake breakdown Using Computational Fluid Dynamics," *AIAA Journal*, Vol. 53, No. 3, 2014, pp. 588–602.

[69] Lawson, S. and Barakos, G., "Evaluation of DES for Weapons Bays in UCAVs," *Aerospace Science and Technology*, Vol. 14, No. 6, 2010, pp. 397–414.

[70] Wilcox, D. C., "Reassessment of the Scale-Determining Equation for Advanced Turbulence Models," *AIAA Journal*, Vol. 26, No. 11, Jan-1 1988, pp. 1299–1310.

[71] Menter, F. R., "Two-equation Eddy-viscosity Turbulence Models for Engineering Applications," *AIAA Journal*, Vol. 32, No. 8, Jan-1 1994, pp. 1598–1605.

[72] Wilcox, D. C., "Formulation of the k-ω Turbulence Model Revisited," *AIAA Journal*, Vol. 46, No. 11, 2008, pp. 2823–2838.

[73] Spalart, P. and Allmaras, S. R., "One-equation Turbulence Model for Aerodynamic Flows," *Recherche aerospatiale*, Jan-1 1994, pp. 5–21.

[74] Wallin, S. and Johansson, A. V., "An Explicit Algebraic Reynolds Stress Model for Incompressible and Compressible Turbulent Flows," *Journal of Fluid Mechanics*, Vol. 403, 2000, pp. 89–132.

[75] Grigoriev, I. A., Wallin, S., Brethouwer, G., and Johansson, A. V., "A Realizable Explicit Algebraic Reynolds Stress Model for Compressible Turbulent Flow With Significant Mean Dilatation," *Physics of Fluids*, Vol. 25, No. 10, 2013.

[76] Jameson, A., "Time Dependent Calculations Using Multigrid, with Applications to Unsteady Flows past Airfoils and Wings," *10th Computational Fluid Dynamics Conference*, AIAA, 1991, p. 1596.

[77] Biava, M., Woodgate, M., and Barakos, G. N., "Fully Implicit Discrete Adjoint Methods for Rotorcraft Applications," *AIAA Journal*, Vol. 54, No. 2, 2016, pp. 735–749.

[78] Tannehill, J. C., Anderson, D. D. A., and Pletcher, R. H., *Computational Fluid Mechanics and Heat Transfer, Second Edition*, Taylor & Francis Group, 1997.

[79] Hellsten, A. K., "New Advanced k-ω Turbulence Model for High-Lift Aerodynamics," *AIAA Journal*, Vol. 43, No. 9, 2005, pp. 1857–1869.

[80] Limache, A. C. and Cliff, E. M., "Aerodynamic Sensitivity Theory for Rotary Stability Derivatives," *Journal of Aircraft*, Vol. 37, No. 4, 2000, pp. 676–683.

[81] Mader, C. A. and Martins, J. R. R. A., "Computation of Aircraft Stability Derivatives using an Automatic Differentiation Adjoint Approach," *AIAA Journal*, Vol. 49, No. 12, 2011, pp. 2737–2750.

[82] Nemec, M., Zingg, D. W., and Pulliam, T. H., "Multipoint and Multi-Objective Aerodynamic Shape Optimization," *AIAA Journal*, Vol. 42, No. 6, 2004, pp. 1057–1065.

[83] Jameson, A., Martinelli, L., and Pierce, N. A., "Optimum Aerodynamic Design Using the Navier-Stokes Equations," *Theoretical and Computational Fluid Dynamics*, Vol. 10, No. 1-4, 1998, pp. 213–237.

[84] Kim, H. J., Sasaki, D., Obayashi, S., and Nakahashi, K., "Aerodynamic Optimization of Supersonic Transport Wing Using Unstructured Adjoint Method," *AIAA Journal*, Vol. 39, No. 6, 2001, pp. 1011–1020.

[85] Giraud, L., Gratton, S., Pinel, X., and Vasseur, X., "Flexible GMRES with Deflated Restarting," *SIAM Journal on Scientific Computing*, Vol. 32, No. 4, 2010, pp. 1858–1878.

[86] Saad, Y. and Schultz, M. H., "GMRES: A Generalized Minimal Residual Algorithm for Solving Nonsymmetric Linear Systems," *SIAM Journal on Scientific and Statistical Computing*, Vol. 7, No. 3, 1986, pp. 856–869.

[87] Morgan, R. B., "GMRES with Deflated Restarting," *SIAM Journal on Scientific Computing*, Vol. 24, No. 1, 2003, pp. 20–37.

[88] Benzi, M., "Preconditioning Techniques for Large Linear Systems: a Survey," *Journal of Computational Physics*, Vol. 182, No. 2, 2002, pp. 418–477.

[89] Min, B. Y., Lee, W., Englar, R., and Sankar, L. N., "Numerical Investigation of Circulation Control Airfoils," *Journal of Aircraft*, Vol. 46, No. 4, 2009, pp. 1403–1410.

[90] Kraft, D. et al., "A Software Package for Sequential Quadratic Programming," Tech. Rep. DFVLR-FB 88-28, Institut für Dynamik der Flugsysteme, Oberpfaffenhofen, Germany, 1988.

[91] Kraft, D., "Algorithm 733: TOMP–Fortran Modules for Optimal Control Calculations," *ACM Transactions on Mathematical Software (TOMS)*, Vol. 20, No. 3, 1994, pp. 262–281.

[92] Johnson, S. G., "The NLopt Nonlinear-optimization Package," `http://ab-initio.mit.edu/nlopt`, 2014, Accessed: Jan 2015.

[93] Reuther, J. J., Jameson, A., Alonso, J. J., Rimlinger, M. J., and Saunders, D., "Constrained Multipoint Aerodynamic Shape Optimization using an Adjoint Formulation and Parallel Computers, Part 1," *Journal of Aircraft*, Vol. 36, No. 1, 1999, pp. 51–60.

[94] Shepard, D., "A Two-dimensional Interpolation Function for Irregularly-spaced Data," *Proceedings of the 1968 23rd ACM National Conference*, ACM '68, ACM, New York, NY, USA, 1968, pp. 517–524.

[95] Forster, M. and Steijl, R., "Numerical Simulation of Transonic Circulation Control," *53rd AIAA Aerospace Sciences Meeting*, AIAA, 2015, p. 1709.

[96] Cruz, J. and Anders, S. G., "Assessment of an Unstructured-Grid Method for Predicting Aerodynamic Performance of Jet Flaps," *24th AIAA Applied Aerodynamics Conference*, AIAA, 2006, p. 3868.

[97] Launder, B. E. and Spalding, D. B., "The Numerical Computation of Turbulent Flows," *Computer Methods in Applied Mechanics and Engineering*, Vol. 3, No. 2, Jan-1 1974, pp. 269–289.

[98] Chawalowski, P., Silva, W. A., Wieseman, C. D., and Heeg, J., "CFD Model of the Transonic Dynamics Tunnel with Applications," *IFASD 2017, Como Italy*, International Forum on Aeroelasticity and Structural Dynamics, June 2017.

[99] Gilchrist, A. R., *The Development and Breakaway of a Compressible Air Jet with Streamline Curvature and its Application to the Coanda Flare*, Ph.D. thesis, Durham University, 1985.

[100] Carlson, J.-R., "Inflow/Outflow Boundary Conditions with Application to FUN3D," Tech. Rep. NASA/TM-2011-217181, NASA Langley, 2011.

[101] Hortensius, R., Dutton, J. C., and Elliott, G. S., "Near Field of an Axisymmetric Underexpanded Jet and an Adjacent Parallel Surface," *AIAA Journal*, Vol. 55, No. 8, 2017, pp. 2489–2502.

[102] Forster, M. and Steijl, R., "Design Study of Coanda Devices for Transonic Circulation Control," *The Aeronautical Journal*, 2017, pp. 1–24, 10.1017/aer.2017.65.

[103] Elsenaar, A., Waggoner, E. G., and Ashill, P. R., "A Selection of Experimental Test Cases for the Validation of CFD Codes," Tech. Rep. AR-303, AGARD, 1994.

[104] Londenberg, W., "Turbulence Model Evaluation for the Prediction of Flows Over a Supercritical Airfoil With Deflected Aileron at High Reynolds Number," *31st Aerospace Sciences Meeting and Exhibit*, AIAA, 1993, p. 191.

[105] Forster, M., Biava, M., and Steijl, R., "Optimisation of Coanda Surfaces for Transonic Circulation Control," *6th European Conference for AeroSpace Sciences*, EUCASS, July 2015.

[106] Forster, M., Biava, M., and Steijl, R., "Multipoint Optimisation of Coanda Surfaces for Transonic Circulation Control using the Adjoint Method," *8th AIAA Flow Control Conference, Washington DC*, AIAA, 2016, p. 3773.

[107] Forster, M. and Steijl, R., "Circulation Control for High-Speed Unmanned Combat Air Vehicles," *Royal Aeronautical Society Applied Aerodynamics Conference*, July 2016.

[108] Fairhurst, D. J., "A Summary of SACCON DLR-F17E Tests carried out on model RA234 in the Warton 1.2m High Speed Wind Tunnel," Tech. Rep. BAE-WEIS-RP-ASF-WTD-119741, BAE Systems, 2012.

[109] Hoholis, G., *Assessment of Fluidic Control Effectors using Computational Fluid Dynamics*, Ph.D. thesis, University of Liverpool, 2016.

Appendix A

Table of single point optimisation parameters

Table A.1 shows the history of the HSOPT optimisation study, as shown in Fig. 5.5. During the one–dimensional line search within an optimisation step, such as at CFD step 8 and 9 in Table A.1, the gradient of the objective function was not required and so to reduce computational expense the solution of the Adjoint equations were not computed for these steps. Such cases are denoted by 'F', where cases using both function and gradient are labelled as 'FG' in the table. At the end of the line search, the gradients are required to update the estimate of the Hessian. Note that step 10 has the same parameters and objective function as step 9, where here the gradient is computed and the steady flow solution taken from the converged answer of step 9.

Table A.1: History of HSOPT when initialising from the quasi–elliptical shape. F/FG = function/function and gradient. x_i is the i'th optimisation parameter.

CFD Step	Opt Step	C_l	F/FG	x_1	x_2	x_3	x_4	x_5
1	1	1.1138	FG	1.000e+00	1.000e+00	2.000e+00	1.000e+00	1.000e+00
2	2	1.1302	FG	1.100e+00	1.026e+00	1.978e+00	9.943e-01	1.019e+00
3	3	1.1315	FG	1.100e+00	1.038e+00	1.960e+00	9.942e-01	1.038e+00
4	4	1.1367	FG	1.100e+00	1.089e+00	1.896e+00	9.996e-01	1.100e+00
5	5	1.1396	FG	1.100e+00	1.116e+00	1.841e+00	1.002e+00	1.100e+00
6	6	1.1590	FG	1.100e+00	1.263e+00	1.538e+00	1.026e+00	1.100e+00
7	7	0.9442	FG	1.100e+00	1.300e+00	7.000e-01	1.007e+00	1.100e+00
8		0.9553	F	1.100e+00	1.272e+00	1.328e+00	1.022e+00	1.100e+00
9		1.1619	F	1.100e+00	1.264e+00	1.516e+00	1.023e+00	1.100e+00
10	8	1.1619	FG	1.100e+00	1.264e+00	1.516e+00	1.023e+00	1.100e+00
11	9	0.9443	FG	1.100e+00	1.300e+00	7.000e-01	9.215e-01	1.072e+00
12		0.9543	F	1.100e+00	1.274e+00	1.279e+00	9.956e-01	1.092e+00
13		1.1668	F	1.100e+00	1.265e+00	1.481e+00	1.021e+00	1.099e+00
14	10	1.1668	FG	1.100e+00	1.265e+00	1.481e+00	1.021e+00	1.099e+00
15	10	0.9558	FG	1.089e+00	1.160e+00	1.306e+00	7.781e-01	1.100e+00
16		1.1680	F	1.099e+00	1.255e+00	1.464e+00	9.971e-01	1.099e+00
17	11	1.1680	FG	1.099e+00	1.255e+00	1.464e+00	9.971e-01	1.099e+00
18	12	0.9530	FG	1.078e+00	1.108e+00	1.063e+00	7.000e-01	1.100e+00
19		1.1706	F	1.097e+00	1.240e+00	1.424e+00	9.674e-01	1.099e+00
20	13	1.1706	FG	1.097e+00	1.240e+00	1.424e+00	9.674e-01	1.099e+00
21	14	0.9523	FG	1.076e+00	1.078e+00	9.948e-01	7.000e-01	1.100e+00
22		1.1738	F	1.095e+00	1.224e+00	1.381e+00	9.407e-01	1.099e+00
23	15	1.1738	FG	1.095e+00	1.224e+00	1.381e+00	9.407e-01	1.099e+00
24	16	0.9562	FG	1.094e+00	1.272e+00	1.223e+00	1.300e+00	1.100e+00
25		1.1735	F	1.095e+00	1.228e+00	1.365e+00	9.766e-01	1.099e+00
26		1.1738	F	1.095e+00	1.226e+00	1.374e+00	9.560e-01	1.099e+00
27		1.1738	F	1.095e+00	1.224e+00	1.381e+00	9.408e-01	1.099e+00
28	17	1.1738	FG	1.095e+00	1.224e+00	1.381e+00	9.408e-01	1.099e+00
29	18	0.9558	FG	1.088e+00	1.205e+00	1.268e+00	9.244e-01	1.100e+00
30		1.1746	F	1.094e+00	1.222e+00	1.370e+00	9.392e-01	1.099e+00
31	19	1.1746	FG	1.094e+00	1.222e+00	1.370e+00	9.392e-01	1.099e+00
32	20	0.8894	FG	1.055e+00	1.163e+00	7.000e-01	8.087e-01	1.100e+00
33		1.1786	F	1.090e+00	1.216e+00	1.303e+00	9.261e-01	1.099e+00
34	21	1.1786	FG	1.090e+00	1.216e+00	1.303e+00	9.261e-01	1.099e+00
35	22	0.9551	FG	1.086e+00	1.227e+00	1.236e+00	9.184e-01	1.100e+00
36		1.1790	F	1.090e+00	1.217e+00	1.296e+00	9.254e-01	1.099e+00
37	23	1.1790	FG	1.090e+00	1.217e+00	1.296e+00	9.254e-01	1.099e+00
38	24	0.9507	FG	1.064e+00	1.279e+00	8.709e-01	8.462e-01	1.093e+00
39		0.9553	F	1.087e+00	1.223e+00	1.254e+00	9.174e-01	1.099e+00
40		1.1792	F	1.089e+00	1.218e+00	1.292e+00	9.246e-01	1.099e+00
41	25	1.1792	FG	1.089e+00	1.218e+00	1.292e+00	9.246e-01	1.099e+00
42	26	1.2102	FG	1.054e+00	1.300e+00	7.000e-01	7.778e-01	1.100e+00
43		0.9501	F	1.063e+00	1.296e+00	8.446e-01	8.252e-01	1.100e+00
44		1.2104	F	1.055e+00	1.300e+00	7.145e-01	7.825e-01	1.100e+00
45	27	1.2104	FG	1.055e+00	1.300e+00	7.145e-01	7.825e-01	1.100e+00
46	28	1.2105	FG	1.057e+00	1.300e+00	7.560e-01	7.762e-01	1.100e+00